INAUGURAL-DISSERTATION
zur
Erlangung der Doktorwürde
der
Naturwissenschaftlich-Mathematischen
Gesamtfakultät
der Ruprecht-Karls-Universität
Heidelberg

vorgelegt von
Dipl.-Phys. Stefan Bartzsch
aus Jena

Tag der mündlichen Prüfung: 5. November 2014

Microbeam Radiation Therapy – physical and biological aspects of a new cancer therapy and development of a treatment planning system

Mikrostrahltherapie – Studien zu physikalischen und biologischen Aspekten einer neuen Krebstherapie und Entwicklung eines Therapieplanungssystems

Gutachter: **Prof. Dr. Uwe Oelfke**

Prof. Dr. Peter Bachert

Zusammenfassung: Die Mikrostrahltherapie (MRT) ist ein neuer Ansatz in der Krebstherapie. Hoch brillante Synchrotronstrahlung wird zu parallelen, wenige Mikrometer breiten, ebenen Strahlenbündeln kollimiert und mit hohen Dosisraten auf das Tumorgewebe gerichtet. Dabei sind die applizierten Peakdosen wesentlich höher als in der konventionellen Strahlentherapie. Die Niedrigdosisbereiche zwischen den Strahlen bleiben jedoch unterhalb der gewohnten Gewebetoleranz. Die bisherige Forschung hat gezeigt, dass derartige Strahlgeometrien das gesunde Gewebe schonen, während Tumore erfolgreich zurückgedrängt werden.

In der vorliegenden Arbeit werden physikalische und biologische Aspekte der Therapie untersucht. Es wird ein Therapieplanungssystem für die ersten klinischen Behandlungen an der Europäischen Synchrotronstrahlenquelle in Grenoble (Frankreich) entwickelt und ein Dosimetrieverfahren auf der Basis radiochromer Filme erarbeitet, um geplante Dosen im Mikrometerbereich experimentell zu validieren. Schließlich werden Experimente auf zellulärer Ebene durchgeführt, um physikalisch geplante Dosen und biologische Schäden zu korrelieren.

Die Unterschiede zwischen Monte-Carlo-Dosis und Messung sind geringer als 10% im Niedrig- und 5% im Peakdosisbereich. Alternativ entwickelte schnellere Dosisberechnungsverfahren weichen von den rechenintensiven Monte-Carlo-Simulationen um weniger als 15% ab und bestimmen die Dosis innerhalb weniger Minuten. In den zellbiologischen Experimenten zeigt sich, dass interzelluläre Signale maßgeblich über das Zellüberleben an Strahlengrenzen entscheiden. Diese Beobachtung ist nicht nur für MRT sondern auch für die konventionelle Strahlentherapie von Bedeutung.

Abstract: Microbeam Radiation Therapy (MRT) is a novel treatment strategy against cancer. Highly brilliant synchrotron radiation is collimated to parallel, a few micrometre wide, planar beams and used to irradiate malignant tissues with high doses. The applied peak doses are considerably higher than in conventional radiotherapy, but valley doses between the beams remain underneath the established tissue tolerance. Previous research has shown that these beam geometries spare normal tissue, while being effective in tumour ablation.

In this work physical and biological aspects of the therapy were investigated. A therapy planning system was developed for the first clinical treatments at the European Synchrotron Radiation Facility in Grenoble (France) and a dosimetry method based on radiochromic films was created to validate planned doses with measurements on a micrometre scale. Finally, experiments were carried out on a cellular level in order to correlate the physically planned doses with the biological damage caused in the tissue.

The differences between Monte Carlo dose and dosimetry are less than 10% in the valley and 5% in the peak regions. Developed alternative faster dose calculation methods deviate from the computational intensive MC simulations by less than 15% and are able to determine the dose within a few minutes. The experiments in cell biology revealed an significant influence of intercellular signalling on the survival of cells close to radiation boundaries. These observations may not only be important for MRT but also for conventional radiotherapy.

Preface

Usually a PhD thesis does not stand alone, but colleagues, students and collaborators make contributions, carry out preparatory work, develop ideas further or help with the experiments with their expertise and equipment. So it is with this work and I see it as an indispensable matter of course to acknowledge this at the beginning. Without the people that were involved in the work that I present in the following this thesis would be unimaginable.

My work started in October 2011 and was carried out for the most part at the German Cancer Research Centre (DKFZ) in Heidelberg in the group "physical models in radiation oncology" lead by Prof. Dr Uwe Oelfke who greatly supported me in my work with advice, ideas but also financially. Despite his tight timetable he was always open to suggestions and discussions. With his call to the Institute of Cancer Research (ICR) in London I moved to London myself in October 2013.

Microbeam Radiation Therapy (MRT) uses synchrotron radiation and so we have a close collaboration with the biomedical beamline ID17 at the European Synchrotron Radiation Facility (ESRF) in Grenoble. Experiments that required the synchrotron beam were conducted there. This applies especially to the dosimetry presented in chapter 4 and some of the cell culture experiments in chapter 5. I thank Dr Alberto Bravin, who is responsible for the beamline ID17 and also the biomedical group around Dr Geraldine Le Duc. Especially I want to emphasise the outstanding support by Dr Elke Bräuer-Krisch, who knows the MRT experiment at the ESRF better than anybody else. With her talent to organise, her expertise and her persistence she incredibly helped me with my work. Moreover it was a great pleasure to work with her.

For all biological experiments I am grateful to Dr Nathan Brady who leads a junior research group on "system biology of cell death mechanisms" at the German Cancer Research Centre in Heidelberg. He granted me access to his laboratory and allowed me to use all the consumables and equipment there. He and his former PhD student Silu Chen-Lindner helped me with protocols and methods in molecular biology and gave me essential advise for cell culture experiments.

So far this work led to two publications in Medical Physics with first authorship:

- Stefan Bartzsch and Uwe Oelfke. A new concept of pencil beam dose calculation for 40-200 keV photons using analytic dose kernels. Med. Phys., 40(11), October 2013

- Stefan Bartzsch, Michael Lerch, Marco Petasecca, Elke Bräuer-Krisch, and Uwe Oelfke. Influence of polarization and a source model for dose calculation in MRT. Med. Phys., 41(4), April 2014

Chapter 2 contains some texts and figures from the second article with kind permission of the American Association of Physicists in Medicine (AAPM). My thanks are given to Dr Michael Lerch and Dr Marco Petasecca, who measured the anisotropic beam absorption due to the polarisation of synchrotron radiation and facilitated a benchmarking of calculations with measured data.

Work from this thesis also contributed to articles of other authors for example in Jean A. Laissue et al., "Response of the rat spinal cord to X-ray microbeams", Radiotherapy and Oncology

(2013), Elisabeth Schültke et al., "Pencilbeam Irradiation Technique for Whole Brain Radiotherapy: Technical and Biological Challenges in a Small Animal Model", PLoS ONE (2013) and Raphaël Serduc et al., "Synchrotron X Ray Induced Axonal Transections in the Brain of Rats Assessed by High-Field Diffusion Tensor Imaging Tractography", PLoS ONE (2014).

During my thesis I supervised several students who did their master thesis, bachelor thesis or just a short project ("HiWi") in the field of MRT. Charlotte Debus implemented the point kernel algorithms presented in chapter 3 in C++ and linked them to a professional treatment planning system and Jennifer Kieselmann worked on a kernel based dose calculation algorithm in curved space which will also be discussed in chapter 3. Andreas Merrem investigated in his project the affect of microbeams on a synthetic vascular network (see chapter 5). Vincent Lami developed an analytic representation of polarised photon scatter kernels. Katrin Welsch and Johanna Lott both worked on radiochromic film dosimetry and were involved in the development of a densitometric film readout with an optical microscope. Their work contributed to chapter 4. Marc Bisch worked on a wavelet-transform algorithm for automated foci detection which is important for the cell analysis in chapter 5. Moritz Beutel implemented a sophisticated interface for an automated processing of fluorescence microscope images.

A very exceptional contribution to this work was given by Stephan Eismann. He constructed in his Bachelor's project an automated cell culturing device that performs molecular biological staining protocols and reduces the influence of the experimentalist on experimental outcomes. But far beyond his own project he accompanied and supported me for the radiobiological experiments at the ESRF (chapter 5) and for a research stay at the STTARR facility in Toronto (Canada). I thank him for all his work, professional advice, help, text revisions and company. Outstanding and invaluable was his friendship and council in a moving time.

Stefan Bartzsch

Contents

Chapter 1

Introduction

1.1 Cancer therapy and Microbeam Radiation Therapy (MRT)

The bodies of humans and animals are in a way a society or ecosystem of thousands of cells. The human body contains in the order of 10^{14} cells that work together. Each cell has its place and function. One very important property of these cells is "altruism". Cells subordinate themselves to the well-being of the organism and even kill themselves if the organism signals them to do so. A complex regulatory system exists in tissues and organs to control cell proliferation (cell division), cell silencing and cell death. Cancer is associated with the escape of one or very few cells from this regulatory system. It has its origin in a microevolution in the body. Certain mutations in the genome can withdraw a cell from the regulatory system and give it a proliferative advantage compared to others. In a way one could say the altruism is exchanged against egoism and the mutated cell and its descendants start to drive out healthy cells. This pathogenic evolution is the initiator of cancer, one of the most frequent deadly diseases in the western society. In Germany the number of new cancer cases in 2010 was 477,300[1]. The incidence rates of cancer depend on many factors and vary between different regions in the world. Age, gender and lifestyle have a mayor influence on the occurrence of cancer, but genetic disposition is also an important factor. Certain exogenous causes and carcinogenic compounds have been identified. Some but not all of them induce mutations in the genome.

Not all cancer cells of a tumour have the ability to proliferate infinitely. Similar to normal tissue only a small percentage of cells can renew themselves, differentiate and create fast, but limited dividing daughter cells. These cells are called (tumour) stem cells[2,3]. For a successful cancer treatment it is commonly accepted that the stem cells of the tumour need to be eradicated. In this sense cancer treatment means (up to now) a removal of cancer cells and especially of cancer stem cells. Hence all cancer treatments have the problem of specificity. While directed to kill tumour cells a therapy needs to spare normal tissue.

Radiotherapy is the second most successful treatment strategy against cancer after surgery and is followed by chemotherapy[2]. It kills cancer cells with ionising radiation, usually x-rays and gains specificity from the fact that cancer cells are usually more sensitive to radiation than normal tissue cells. This opens a therapeutic window between survival of normal tissue and tumour control. Different approaches have been used to widen this therapeutic window further. For example a combination of radiotherapy and treatment with radiosensitizers is applied or one tries to increase the oxygen level in tumour cells which in turn increases the radiosensitivity of often hypoxic tumours.

The radiation dose in terms of energy per mass is used as a physical measure for normal tissue and tumour survival. Hence a very common approach in radiotherapy is dose conformality. A high dose level is delivered to the entire malignant tissue with the aim to destroy all tumour stem cells, while the dose to the healthy tissue is kept as low as possible to avoid normal tissue

complications. By irradiating from different directions it is possible to increase the dose given to the tumour and to reduce at the same time the dose to the surrounding normal tissue. This technique is very successfully applied in stereotactic radiation therapy (SRS or SBRT) and intensity modulated radiation therapy (IMRT) . Dose conformality to the tumour can be further increased by using protons or heavy ions. These particles show a strongly decreasing interaction probability with increasing kinetic energy. Therefore the particle beams lose most of their energy close to the end of their range in matter and create there a peaked dose distribution with a sharp decrease in depth, the so called Bragg peak. The position of this Bragg peak can be adjusted by changing the particle energy. Thus the dose to the normal tissue along the beam path can be significantly reduced. Already a few years after the discovery of x-rays by Wilhelm Röntgen in 1894 these new beams were used for medical purposes and in particular for cancer treatment. In 1909 Alban Köhler was treating tumours with radiation from an x-ray tube. He was facing the problem that the dose required to control deeper seated tumours was exceeding the tolerance of the skin. The necessary dose to control the tumour led to necrotic skin burns. Therefore he used an iron grid with 1 mm thick wires and 2 to 2.5 mm squared stitches to protect the skin. The grid was pressed directly against the skin. He described his discovery in the words "The metal grid on the skin enables us to apply an unconventionally high dose without risking an incurable x-ray ulcer."[4]. With this technique he was able to detain or cure large and deep seated tumours. He realised that with the grid some healthy cells and vessels were left around the wound that enabled rapid healing. The method had the primary aim to protect the skin. The very divergent beams of an x-ray tube and the large size of the focal spot lead to a soon blurring and loss of protection with depth. The technique known as grid therapy was used afterwards as a palliative treatment for large tumours[5].

Many years later the idea was picked up again in radiotherapy after the observation that very narrow beams of high doses are extraordinarily tolerated by normal tissue. These observations were made in the 1960s while studying the effects of cosmic radiations on the organism. Circular deuteron microbeams of 25 μm diameter with a dose of 4,000 Gy were delivered to the brain of mice[6,7]. Nevertheless the tissue was still intact and only in the microbeam paths there was a reduction of neurons observable. In contrast a 1 mm diameter beam of 140 Gy lead to complete destruction and necrosis of the tissue[8]. More than 20 years later with the development of large synchrotron radiation sources the potentially clinical use of this effect was pursued. This was the beginning of Microbeam Radiation Therapy (MRT).

Microbeam Radiation Therapy (MRT) is a treatment strategy in radiation oncology that employs arrays of micrometre sized beams with 25 to 100 μm width and with several hundred micrometre spacing from beam centre to beam centre. It is based on the dose-volume relation which was formulated in 1988 by Rodney Withers et al.[9]: "Threshold absorbed doses for damage to normal tissue increase as irradiated macroscopic tissue volumes are made smaller." In order to treat patients with these beams great demands are placed on the radiation source that are currently only met by 3rd generation synchrotrons.

1.1.1 The European Synchrotron Radiation Facility

The work in this thesis was carried out in cooperation with the European Synchrotron Radiation Facility (ESRF) in Grenoble (France). It has a 844 m circumference storage ring for electrons with an energy of 6 GeV. More than 30 beamlines use the synchrotron radiation produced in wigglers and undulators in the periphery of the ring. It is the most powerful synchrotron radiation source in Europe and a joint facility used by 19 contributing countries. The biomedical beamline ID17 deals with projects in imaging such as diffraction enhanced imaging (DEI) and radiotherapy.

The ESRF produces extremely brilliant radiation, i.e. radiation with a high photon flow per area and solid angle in a narrow wavelength band. Dose rates of up to 16,000 Gy/s can be

reached with a very small divergence of 1 mrad horizontally and 0.1 mrad vertically[10]. The high dose rate presents a particular challenge in the beam application. The switching of the beam has to be very fast and accurately timed. The dose rate is necessary, though, in order to avoid dose blurring caused by respiratory or cardiovascular motions which could easily destroy the fine dose profiles.

For MRT a wiggler produces synchrotron radiation 41.7 m upstream from the multislit collimator (MSC)[11]. This collimator is the central part for the creation of microbeams and shapes in its current design for the first clinical trials 50 μm wide vertical beams with 400 μm centre to centre spacing (ctc). Between wiggler and MSC a number of filters modify the spectrum of the beam: 0.5 mm beryllium, 1.5 mm carbon, 1.5 mm aluminium, 1.0 mm copper[12,13]. The photon spectrum for MRT at the ESRF has its maximum intensity at 83 keV and a mean energy of 100 keV[14,15].

So far only preclinical studies were performed with MRT. However, MRT is now moving forward to clinical trials. To that end different elements have been added to the beam line and a safety system "PASS" (PAtient Safety System) was set up. The system collects information on the state of the filters and the beam. Apart from the existing filters a Kr-gas filled absorber was introduced as a pre-absorber that protects the main absorbers from heat. At 160 mbar pressure in the Kr gas pipe, in case of a leak, the pressure would increase and the pipe would be filled additionally with air. The pressure is monitored by the PASS and the beam will trip if there is a pressure change[16].

The sample (phantom, animal or patient) is located on a goniometer. Unlike in normal radiation therapy the source cannot move around the target but the target has to be rotated and moved. Several motors adjust the target position and irradiation angle. The maximum field size is 41 mm in width and 2.5 mm in height. In order to increase the vertical field size the sample is scanned vertically through the beam. Thereby the absorbed dose is determined by the vertical collimator slit size h (52 μm or 520 μm), the dose rate and the scanning speed v which can be varied from approximately 10 to 100 mm/s. The dose rate itself scales linearly with the current in the storage ring and hence the absorbed dose for a broad field can be calculated via

$$D = \frac{\dot{D} \cdot h \cdot I}{v} \tag{1.1}$$

where $\dot{D}$ is the dose rate per current and I the current in the storage ring. $\dot{D}$ is in the order of 70 Gy/mA/s and is measured before the exposure with ionisation chambers (see for example Prezado et al.[17]).

A Taper FReLoN CCD camera for imaging was added to the beam line. The camera is located opposite to the MSC.

The efficiency of tumour ablation can be increased by microbeam exposures from different directions ("multiple ports")[10,12,18]. With an interlaced geometry the dose in the target regions can be increased while there is still a high protection of the surrounding healthy tissue. Only the accurate alignment of the beams is problematic. The brain can move up to 2 mm/s due to perfusion. Serduc et al.[10] did, however, not find alignment problems after irradiating rat brains from four different ports with 200 μm spaced 50 μm wide microbeams. They showed that a precise, interlaced radiosurgical exposure of certain areas of the brain can reduce spontaneous seizures of epilepsy in genetic absence epilepsy rats. Nevertheless they suggest to trigger the exposure in multiport irradiations with the heart beat to limit the risk.

1.1.2 Biological evidence

The remarkable resistance of normal tissue to microbeams was shown for the first time for neutron microbeams in the 1960s[7,19–21]. In the 1990s this resistance was confirmed by a great number

of experiments with synchrotron radiation[12,22–24]. Slatkin et al.[25] studied the brain damage after microbeam irradiations of rats with skin entrance doses between 312 and 10,000 Gy at the National Synchrotron Light Source (NSLS) in Brookhaven (USA). They observed a loss of neuronal and astrocytic nuclei for doses of 1,250 Gy and above. However, except for some of the rats exposed to 10,000 Gy peak entrance dose they did not find tissue necrosis or other kinds of brain damage. Also the behaviour of the rats seemed to be normal up to 1 month after exposure. When compared to seamless irradiations, doses of above 100 Gy led to death within days.

The response of larger animals to ionising radiation was examined by Laissue et al.[22]. They irradiated the cerebellum of weanling piglets with 25 μm wide and 210 μm spaced microbeams of 150, 300, 425 and 600 Gy peak entrance dose. After exposure there was no difference observed in the magnetic resonance (MR) images or in the weight when compared to unirradiated littermates. Subsequent to the treatment the animals were kept on a farm in Switzerland. Farmers and veterinary scientists were not able to distinguish the animals by their behaviour. 15 months after treatment no traces of haemorrhage were found and the ratio of cerebellum to total brain weight was identical in treated and untreated animals. The only difference was the occurrence of stripes marking the microbeam paths. The group confronts their results to those of van den Aardweg et al.[26] who found that 27 Gy seamless irradiation of ^{60}Co γ-rays leads in 50% of the cases to leg paralysis 7 to 16 weeks after exposure.

MRT has also shown to be effective against brain tumours. Bräuer-Krisch et al.[27] reported a therapeutic index for the treatment of 9L gliosarcoma (9LGS) with MRT of around 5. This index is defined as the minimum dose required for tumour control to the maximum dose tolerated by normal tissue. This is much better than for seamless irradiations.

Laissue et al.[28] and Bouchet et al.[12] treated a few weeks old Fischer rats bearing a 9LGS tumour in the stratum and nucleus with microbeams and found a reduced tumour growth and even tumour regression. In the experiments by Laissue et al.[28] 22 of 36 rats had no brain tumour after treatment with 625 Gy (unidirectional and bidirectional) peak entrance dose microbeams with 25 μm width and 100 μm spacing. However, the adjacent tissue was considerably damaged. Bouchet et al.[12] used 400 Gy for 50 μm wide and 200 μm spaced microbeams. The mean survival time increased from 20 days in control rats to 65 days in the irradiated rats. 15 days after exposure 2 out of 9 rats were without tumour and mice with tumour showed a reduced tumour cell density and proliferation rate in the irradiated regions.

Miura et al.[18] compared microbeams with 35 μm beam width and 200 μm spacing at 422, 625 and 884 Gy and microbeams with 70 μm beam width and 200 μm spacing at 442 Gy in a rather large field of 16×15 mm^2 size. They found that the most effective tumour palliation was given by 35 μm wide beams at 884 Gy peak entrance dose. Although the 70 μm wide beams showed the second best tumour control, they exhibited at the same time the most substantial damage. This damage is presumably caused by the high valley dose. The ratio of peak to valley dose (PVDR) is to a large extend determined by the field size and the ratio of beam spacing to beam width. Large fields and small ratios of beam spacing to beam width lead to a lower PVDR.

A similar observation was made by Regnard et al.[29] in Fisher rats that had an implanted 9LGS tumour. They irradiated either 100 μm or 200 μm spaced 25 μm wide microbeams with a peak entrance dose of 625 Gy. Although there was a longer mean survival time and a larger fraction of long term survivors for the 100 μm spaced beams the side effects were considerable. Rats irradiated with 100 μm beam spacing did not gain weight after treatment and micro calcifications in the beam path revealed substantial brain damage.

Schültke et al.[30] analysed the memory of C6 glioma bearing Wistar rats and F98 bearing Fisher rats after treatment with 200 μm spaced and 25 μm wide microbeams at 350 Gy peak entrance dose. For some of the rats they added the radiosensitizer buthionine-SR-sulfoximine (BSO). They found a significant loss of memory 1 month after treatment. However, there was a marked improvement 1 year post irradiation. For MRT alone the memory dysfunction was much

less than for combined therapy of MRT and BSO.

MRT has a variety of treatment parameters. Their influence on treatment outcome has physical and biological origins. From the physical point of view it seems to be favourable to keep the valley doses as low and the peak doses as high as possible, i.e. a high PVDR. Furthermore the beam penumbras should be small and the mean free path of the beam needs to be high if deep seeded tumours should be treated. Obviously increasing the beam spacing and decreasing the beam width will lead to higher PVDRs. The spectrum has an important influence on both, beam penumbra and photon mean free path. Low energy photons produce in general low energy secondary electrons with a short range (details will be discussed later). Furthermore photon scattering is reduced at low energies which leads to a lower valley dose. However, low energy photons have a high absorption coefficient and therefore a low mean free path. High energy photons produce longer ranged electrons. These will travel out of the beam and blur the dose profiles. Hence a compromise between low and high photon energies is needed[14].

Under the assumption that the valley dose is crucial for normal tissue survival Serduc et al.[31] investigated the effect of 25, 50 and 75 μm wide and 200 μm spaced beams when used for treatment of 9LGS tumours in rats for a constant valley dose of 18 Gy. Although the longest survival was found when treating with 25 μm wide beams the mean survival time was not different to untreated controls. 50 μm beam width seemed to provide the best therapeutic index as a compromise between small beams with very high doses in the target and larger beams with brain damage and oedema formation. For larger animals they proposed to increase the beam width rather than the dose. Their findings promoted the arrangement of 50 μm wide beams of 400 μm inter beam spacing for the first veterinary trials at the ESRF. This arrangement was further encourage by the fact that wider beams have the advantage that the MSC with regular slits is easier to fabricate and also the dose calculation and measurement is less difficult, in contrast to the 25 μm wide beams with 200 μm spacing used before in experiments at the NSLS in Brookhaven.

1.1.3 Biological Mechanisms of MRT

So far the biological mechanisms behind the tissue sparing observed after high dose MRT treatment have not been elucidated. Different mechanisms were proposed to have an influence. Most authors agree with the theory that repair is mediated by the large interfaces between irradiated and non-irradiated tissues[27]. Manifold experimental evidence suggests an important role of blood vessels[12,25,28,32].

The lack of haemorrhage after high dose microbeam exposure is one of the astonishing observations made already at the very beginning of MRT research. Defects caused by hectograys of dose must be repaired very quickly[33]. One of the main complications after brain irradiations is acute cerebral oedema. After microbeam exposure with 312 and 1,000 Gy only a transient oedema was observed that disappeared within the first week after exposure[24]. Bouchet et al.[12] did not observe residual damage after MRT in blood vessels and hypothesised a very rapid repair of blood vessels after MRT treatment. They found especially a high level of vascular endothelial growth factor (VEGF) expression in treated normal brain tissue. This is a signalling protein that stimulates vascularisation. A faster repair of blood vessels as compared to broad beam exposure was confirmed by observations of Sabatasso et al.[32]. The vascular volume and the capillary density does not change after exposure with microbeam fields whereas fractionated stereotactic radiotherapy of brain tumours causes significant blood volume changes in the adjacent tissue[23,34].

While larger vessels are unaffected by high doses of narrow beams, the destroyed microvasculature is quickly repaired. An exposure of the chicken embryo chorio amniotic membrane (CAM) with a single 25 μm wide beam of 2,500 Gy did not cause lesions in large vessels while the microvascular plexus was damaged[33]. The irradiation with arrays of microbeams with doses

between 300 and 1,200 Gy revealed an uninterrupted blood flow and showed vascular bridges across areas situated in the beam path[33]. A high tolerance of small arteries to very high dose microbeams was also reported by van der Sanden et al.[35].

A high resistance to small injuries of vessels is supported by the work of Reidy and Schwartz[36]. They report a rapid reendothelialisation after small areas of a mouse aorta had been injured. Furthermore they realised a directional dependence. If the wound was circumferential a recovery was seen after 8 hours whereas injury oriented parallel to the vessel axis was only repaired after 48 hours. Lost endothelial cells seem to be quickly replaced either by repopulation from the low dose zones or by neighbouring cells that increase their surface[33].

Possibly the little radiation damage in MRT is related to geometrical sparing as well. Ischemia, i.e. a deficit in blood supply, can be one complication after radiotherapy. Therefore it was suggested that sparing of sufficient capillaries located outside the microbeam paths keeps up the supply of normal tissue with oxygen and thereby enables fast repair[8,32]. In our group the master project of Andreas Merrem[37] was dedicated to the simulation of radiation damage to a vessel system after an exposure with microbeams. He could show that spatial fractionation of dose in microplanar beams can increase the survival fraction of vessels by a factor of three.

The differential effect of microbeams to normal tissue and tumours could be caused by differences in the microvasculature. Risser et al.[38] compared normal and tumour vascular networks in primate and rat brains. They found that vessels in normal tissue have fractal properties for vessel diameters from 1.4 up to approximately 50 μm. For larger vessel diameters the network is homogeneous. In contrast tumour vasculature remains fractal to much higher scales and exhibits also a higher fractal dimension. The latter observation is probably related to a higher blood supply to fast proliferating tumour cells.

Tissue maturation plays a central role for the sensitivity to radiation damage. Sabatasso et al.[32] irradiated chick chorioallantoic membrane (CAM) at days 8 and 12 of the embryo development. While the vasculature of the CAM is still immature consisting of naked capillaries at day 8 it has significantly matured at day 12 possessing a hierarchical organisation and in particular protecting, multifunctional pericytes. They compared exposures with MRT fields with 200 or 300 Gy peak entrance dose and seamless exposures between 5 and 40 Gy. 12 day old CAM showed after treatment with 200 and 300 Gy microbeams significantly less damage than CAM at day 8. They observed in the more mature 12 day old CAM that the fraction of unperfused microvasculature is much lower 6 hours after exposure and that the vascular transpermeability returns to a normal level a few hours after irradiation. Much higher damage was inflicted in homogeneous irradiations. At 20 Gy only few supplying arterioles were spared and at 40 Gy the vasculature was completely destroyed. Sabatasso et al.[32] propose therefore that pericyte coverage increases the resistance to ionising radiation. In fact pericytes have various functions such as stabilisation, blood flow regulation and angiogenesis. The vascular systems of tumours show a higher tortuosity, increased vessel diameters and permeability and resemble in many aspects an immature vasculature[12,39,40].

Another explanation of the MRT principles is cell communication. Various surprising findings have recently challenged traditional views on radiobiology. Not only cells that are directly hit by radiation show stress related responses but also unexposed adjacent cells. These effects are called bystander responses (one of many good reviews can be found in Prise et al.[41]). Not only neighbouring cells, but even cells of other organisms can be affected by bystander signals. Mothersill et al.[42] observed bystander effects in unexposed fish swimming with exposed fish or in the water that was previously occupied by irradiated fish. It is difficult to judge whether these bystander effects are detrimental or advantageous.

As demonstrated by Smith et al.[43] there are differences in the proteom after MRT and homogeneous radiation exposures. After analysing the proteom in 2D gel electrophoresis they came to the conclusion that microbeams activated bystander effect proteom responses may be

anti-tumorigenic, while most of the changes by homogeneous irradiations were associated with tumourigenesis. In this work we investigated the influence of bystander effects in MRT and our results document a strong influence of cell-cell communication. This will be presented in chapter 5 where we will discuss these fascinating effects in more detail on a molecular biological basis.

1.2 Challenges and focus of this work

An understanding of the biological effects and parameters in MRT is just one prerequisite before moving towards a clinical application. MRT also demands for a high accuracy in the beam exposure when high doses are delivered in fractions of a second. In cross firing irradiations an exact aiming to the target is indispensable and any motion of the patient has to be reduced to a minimum between the exposures from two ports. Furthermore the dose distribution in the patient needs to be estimated in advance. Here dosimetry and dose calculation strategies are required that meet the demands set by some of the extraordinary parameters in MRT. In contrast to conventional radiotherapy MRT stands out due to the following properties:

- A spectrum in the keV photon energy range with a mean energy of approximately 100 keV and a maximal intensity at 83 keV
- A beam that is linearly polarised in the plane of the storage ring
- Extremely high dose rates of up to 16,000 Gy/s
- A high dynamic range of treatment relevant doses, from around 5 Gy in the valley to 1000 Gy in the peak region
- High dose gradients
- A bulky radiation source which cannot be placed in a normal hospital environment and which delivers the beam always in the same direction.

This work focuses on two main topics. The topic in the first part is treatment planning in MRT which will be covered in the chapters 2, 3 and 4. Chapter 5 deals with the effect of spatially fractionated doses on living cells.

Prior to a clinical treatment with MRT the physician sets certain objectives for an exposure. Typical objectives may be the peak dose in the tumour region or upper limits for the valley dose in organs at risk (OARs). In order two achieve these goals the irradiation direction, the field size and the peak entrance dose can be manipulated. Although not yet possible one could also imagine to adjust beam widths, ctc, the energy spectrum (by changing the filter set) or to add more irradiation ports in order to influence the dose distribution in the patient. A variety of equipment and tools have been developed to control the parameters of the exposure and to simulate the treatment objectives.

We have developed a treatment planning system for MRT that is incorporated into the user interface VIRTUOS. VIRTUOS is a platform for 3D radiotherapy planning that was developed at the German Cancer Research Centre (DKFZ) in Heidelberg[44]. The therapist can use it to import patient data (CT, MR, PET and ultrasound images) and contour target volumes and organs at risk (OARs) on the three dimensional patient model. Treatment plans can be created in a plan mode and several of the just mentioned treatment parameters can be specified. Among these parameters are the irradiation direction, characterised by couch, gantry and collimator angle, the width of the microbeams and the ctc.

The central part of the treatment planning is the dose calculation which will be discussed in chapter 3. We developed two independent algorithms that calculate peak and valley doses

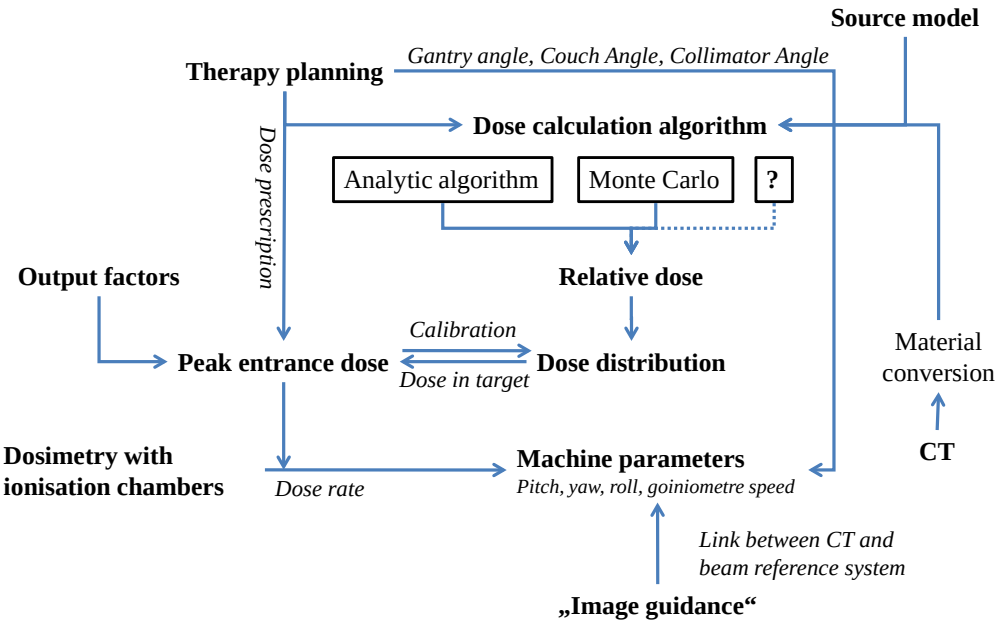

Figure 1.1 – A concept of therapy planning in MRT.

on the CT-voxel based grid. One algorithm is based on Monte Carlo simulations and will be presented in chapter 3.2. The other algorithm is based on analytically derived kernels and the superposition of these kernels weighted by the total energy released per mass (TERMA). Two realisations of this algorithm will be discussed in chapter 3.3.

Both, the kernel based dose calculation and the Monte Carlo simulations require information about the radiation source and the materials in the patient. The transformation of the information in the CT provided in the form of Hounsfield units (HU) to material parameters such as density and elemental mass fractions is based on the work of Schneider et al. [45]. A brief analysis of the uncertainties introduced by these transformations will be discussed in chapter 3.4.

The radiation source is characterised by the physics of synchrotron radiation and various beam modifying elements such as filters and collimators. We dedicate the description of the source a separate chapter, chapter 2. The linear polarisation of the photon beam, a particular property of synchrotron radiation, and its effects on the dose absorption is analysed there. Furthermore a model is developed that accurately describes the radiation source and serves as an input for all dose calculation methods.

The result of the dose calculation is a distribution of relative dose values. These have to be calibrated and translated into machine parameters, such as collimator height and goniometer speed (see above). The dose of a broad beam radiation field at a certain depth in homogeneous water is determined by the goniometer speed, the vertical collimator slit height h, the current in the storage ring and equation 1.1. The dose in a microbeam is, however, smaller, because of a lacking electronic equilibrium at the beam centre. The beam entrance dose of a microbeam can be derived by scaling the homogeneous beam entrance dose with a beam size dependent output factor OF.

Output factors need to be determined by measurements and Monte Carlo simulations. Furthermore dosimetric validations of the calculated dose distributions are essential before a clinical application of MRT. Dosimetry in MRT is a very challenging task due to several factors: the high resolution required, extremely high dose rates, the high dynamic range of relevant doses

(approximately 5 to 1000 Gy), the required accuracy and the energy dependence of most dosimeters at low photon energies. We developed a dosimetry protocol with radiochromic films and readout with light microscopy. In chapter 4 the dosimetry protocol is presented. It is applied to the measurement of output factors (chapters 4.2.7 and 4.3.4) and to measurements of various beam geometries. There results from dosimetry and dose calculations will be compared.

Dose measurements serve as calibration for the relative dose calculations of the treatment planning. Irradiation angles in the therapy planning system also need to be benchmarked with the treatment system. To this end markers are added during CT-imaging. They can also be visualised in low dose projection images from different ports by the FReLoN CCD camera at the beam line. The subsequent determination of the correct goniometer angles to fulfil the treatment plan was worked out by Mattia Donzelli [his Master thesis will be submitted in Heidelberg soon]. In figure 1.1 therapy planning in MRT is illustrated in a structure chart.

Chapter 5 leaves the area of treatment planning and presents some fascinating results of radiobiological experiments in vitro with spatially modulated radiation fields. It pursues the question whether signal exchange between neighbouring cells influences the response of tissues to ionising radiation in MRT. We show evidence for gap junction and soluble factor mediated signals and demonstrate that bystander effects influence the cell cycle. Furthermore some of our results suggest that the vicinity of high dose regions to low dose regions facilitates damage repair in the high dose region. The chapter is supposed to establish a link between the physical doses and the biological effect. However, due to the complexity of this topic we cannot give a final answer to the relation between dose, dose distribution and biological damage.

The final chapter 6 summarises the main results and presents conclusions.

Chapter 2

Characterisation of the radiation source

2.1 Introduction

This chapter is dedicated to the description of the radiation source in MRT.[i] The analysis is confined to the set-up at the biomedical beamline ID17 of the ESRF. With this in mind this chapter is not generally applicable to other centres in the world that conduct research in the field of MRT. Yet, some of the analysed properties such as the beam polarisation or the low beam divergence are common properties of synchrotron radiation and apply to other sources as well. The source characterisation was achieved with the aid of Monte Carlo simulations. Dose calculation was performed with different Monte Carlo codes in the past, for example Geant4[47], EGS4[48,49] and PENELOPE[15] and there is the question of comparability. Here the Geant4 tool set is used. De Felici et al.[50] carried out a code comparison for MRT between different Monte Carlo codes including Geant4 and did not find significant differences. This gives confidence in the use of Geant4, although clearly results should be interpreted with the appropriate care and should not be taken as an ground truth. Some of the limitations of Geant4 will be discussed in the final section of this chapter.

For a long time microbeams have been assumed to be ideal parallel beams. Nettelbeck et al.[51] studied as one of the first the influence of the collimator and the divergence of the beams. They found an increase in the penumbral dose of up to 26% when incorporating the divergence of the beams compared to calculations with ideal parallel microbeams. In the peak and midvalley, however, differences disappeared. Including inclined incidence on the collimator at the field edges produced up to 30% differences in the penumbra doses and lead to a variation of the full width half maximum (FWHM) of the microbeams of up to 4 μm. However, collimator scattering was found to be of no importance within the 2% uncertainties of the Monte Carlo simulations. Martínez-Rovira et al.[13] have performed a complete simulation of the beamline from the wiggler source down to the MSC. But a detailed study of the influence of the gathered phase space information and the important parameters on the dose distribution in MRT was still missing and is presented here.

Another particular property of synchrotron radiation is its linear polarisation. The polarisation effect has been a matter of debate in the past and its influence has not been totally clarified. Orion et al.[49] used for the first time Compton and Rayleigh scattering cross sections (DCS) for polarised photons in the EGS4[52] Monte Carlo code for the dose calculation of microbeams. De Felici et al.[53] also used an EGS4 version to analyse the polarisation influence on PVDRs. They calculated 3×3 cm^2 microbeam fields with 25 μm wide beams and 200 μm spacing in a 16 cm long and 16 cm diameter water cylinder and found in 7 to 8 cm depth a dose change of (1 ± 1)%

[i] A large part of the work in this chapter was published in Bartzsch et al.[46] and some of the figures and texts are taken from the article with kind permission from the American Association of Physicists in Medicine. Especially texts in the sections 2.1 and 2.3 are borrowed with slight changes.

in the field centre, $(3 \pm 3)\%$ at the field edge and $(10 \pm 2)\%$ outside the field when rotating the polarisation direction by 90°. Hence they concluded that polarisation is of minor importance for therapy planning. They also investigated the asymmetric dose absorption around a pencil beam from 0 to 150 μm distance from the beam centre and found between 7% and 18% direction depending differences. However, they did not analyse asymmetric dose absorption outside this range. The importance of the photon polarisation for the dose prediction in treatment planning was emphasised by Hugtenburg et al.[54], though. They concluded that the distortions emerging from the photon polarisation are beyond the usual criterion in conventional radiation therapy and hence that it will be essential to take photon polarisation into account for any future MRT therapy planning.

In this chapter we study the influence of the source model and the polarisation on the dose distribution in MRT in a water phantom. Results of Monte Carlo simulations are compared with dosimetric measurements. We develop a source model of parallel microbeams with corrections motivated by our analysis that shows agreement to dose calculations with complete source simulations within the measurement uncertainties. This model simplifies Monte Carlo dose calculations and facilitates the application of alternative dose calculation methods such as kernel based algorithms. Here we show the applicability of the developed model exemplarily for a semi-adjoint Monte Carlo simulation, but more applications of the model will be presented in chapter 3

2.1.1 Polarisation states and Stokes parameters

Electromagnetic waves in free space are transversal waves. The wave-vector $\vec{k}$, electric field vector $\vec{E}$ and magnetic field vector $\vec{B}$ are pairwise perpendicular to each other. This follows directly from the Maxwell equations. The polarisation of an electromagnetic wave is defined by the electric field of the wave. Polarisation can be described best in a photon bound reference frame. Geant4[55] and PENELOPE[56] distinguish between the laboratory frame and the particle frame. In the particle frame the z-axis points towards the propagation direction and the x-axis of the particle frame is in the x-y-plane of the laboratory frame. The y-axis of the particle frame is the remaining axis to obtain a right-handed system $\vec{e}_x, \vec{e}_y, \vec{e}_z$.

The electric field of a monochromatic, plane, electromagnetic wave can be described in the beam system by

$$\vec{E} = E\Re\left[\begin{pmatrix} \epsilon_x \\ \epsilon_y \end{pmatrix} e^{-i(\omega t - kz)}\right] \qquad \text{with } |\epsilon_x|^2 + |\epsilon_y|^2 = 1 \tag{2.1}$$

Here ϵ_x and ϵ_y are complex amplitudes, ω is the the frequency, k the wave number, t the time and E the electric field intensity. The function $\Re$ returns the real part of its complex argument. We define the complex polarisation vector $\vec{q}$ as

$$\vec{q} = \epsilon_x \vec{e}_x + \epsilon_y \vec{e}_y. \tag{2.2}$$

Its general representation except for an irrelevant phase can be written as

$$\vec{q} = \begin{pmatrix} \cos(\alpha) \\ \sin(\alpha) e^{i\delta} \end{pmatrix} \tag{2.3}$$

with the angles α and δ. The amplitudes in x and y are $\hat{E}_x = E\cos(\alpha)$ and $\hat{E}_y = E\sin(\alpha)$. In the x-y-plane at any $z = z_0$ of the particle frame the electric field vector moves on an ellipse. We define the phase as $\phi = \omega t - kz_0$ and find for the components of the electric field vector

$$\begin{aligned} E_x &= \hat{E}_x \cos(\phi), \\ E_y &= \hat{E}_y \cos(\phi + \delta). \end{aligned} \tag{2.4}$$

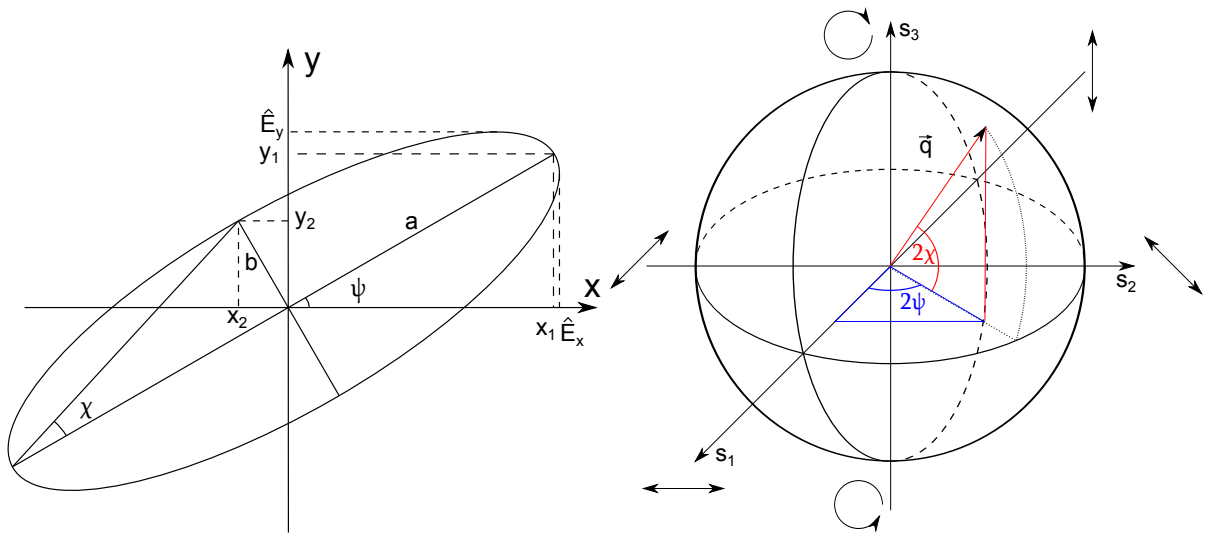

Figure 2.1 – The trajectory of the electric field vector describes an ellipse, the polarisation ellipse (left). The polarisation vector $\vec{q}$ can be illustrated on the Poincaré sphere (right). The radius of the sphere is the polarisation degree.

Hence the polarisation state of a plane monochromatic wave is completely determined by the amplitudes $\hat{E}_x$, $\hat{E}_y$ and the phase difference δ. However, the polarisation is preferably described by the Stokes vector $S = (1, s_1, s_2, s_3)$[ii] with the parameters

$$\begin{aligned} s_0 &= \left\langle E_x^2 + E_y^2 \right\rangle \\ s_1 &= \left\langle E_x^2 - E_y^2 \right\rangle / s_0 \\ s_2 &= \left\langle 2E_x E_y \cos\delta \right\rangle / s_0 \\ s_3 &= \left\langle 2E_x E_y \sin\delta \right\rangle / s_0 \end{aligned} \tag{2.5}$$

The angle brackets indicate an averaging over time. For a totally polarised wave we have $s_1^2 + s_2^2 + s_3^2 = 1$. A geometric interpretation of the Stokes vector can be obtained by writing the parameters depending on the angles χ and ψ shown in figure 2.1 (left). At the vector orientations (x_1, y_1) and (x_2, y_2) the relations

$$\begin{aligned} x_1 &= \hat{E}_x \cos(\phi) &&= a\cos\psi \\ y_1 &= \hat{E}_y \cos(\phi+\delta) &&= a\sin\psi \\ x_2 &= -\hat{E}_x \sin(\phi) &&= -b\sin\psi \\ y_2 &= -\hat{E}_y \sin(\phi+\delta) &&= b\cos\psi \end{aligned} \tag{2.6}$$

apply. It follows that $a^2 + b^2 = \hat{E}_x^2 + \hat{E}_y^2$. A transformation of these equations regarding that $\tan\chi = b/a$ yields

$$\begin{aligned} s_1 &= s_0 \cdot \cos(2\chi)\cos(2\psi) \\ s_2 &= s_0 \cdot \cos(2\chi)\sin(2\psi) \\ s_3 &= s_0 \cdot \sin(2\chi) \end{aligned} \tag{2.7}$$

This result can be visualised in a Poincaré sphere and is illustrated in figure 2.1 (right). Linearly polarised light is defined by $\chi = 0$. ψ defines the orientation of the polarisation. The Stokes

[ii] Sometimes the Stokes vector is defined as $S = (s_0, s_1 \cdot s_0, s_2 \cdot s_0, s_3 \cdot s_0)$ where s_0 gives the total beam intensity. We follow here the definition in Geant4 where the polarisation state is defined by the parameters (s_1, s_2, s_3) only. Care has to be taken when interpreting data from other Monte Carlo codes. Whereas Geant4 uses the optical order of Stokes parameters, PENELOPE uses a different order of the Stokes parameters (s_3, s_1, s_2) which follows from the quantum mechanical treatment (see below).

vector $(1,1,0,0)$ refers to an in x linearly polarised wave, $(1,-1,0,0)$ is linearly polarised in y. If χ is increased the polarisation becomes elliptical and reaches finally circular polarisation for $\chi = \pm\pi/4$ at the poles of the Poincaré sphere. The sign of χ decides upon right or left handed circular or elliptical polarisation.

In quantum mechanics the polarisation state of a single photon is a linear combination of a polarisation in x and y.

$$|E\rangle = \epsilon_x |e_x\rangle + \epsilon_y |e_y\rangle = \begin{pmatrix} \epsilon_x \\ \epsilon_y \end{pmatrix} \tag{2.8}$$

defines the quantum state of the photon with complex amplitudes ϵ_x and ϵ_y. The probability to find the photon in one of the two states is 1 and hence $|\epsilon_x|^2 + |\epsilon_y|^2 = 1$. As discussed for the classical description of the monochromatic plane wave the single photon has again one of the pure polarisation states. For an ensemble of many photons with states $|E_i\rangle$ the polarisation state of the beam can be described by the density matrix

$$\rho = \sum_i p_i |E_i\rangle \langle E_i| , \tag{2.9}$$

where p_i is the relative frequency of the state $|E_i\rangle$ (with $\sum_i p_i = 1$). The density matrix may be represented in any basis,

$$\rho_{jk} = \sum_i p_i \langle e_j|E_i\rangle \langle E_i|e_k\rangle , \tag{2.10}$$

e.g. in the bases of ($|e_x\rangle$, $|e_y\rangle$). For a pure polarisation the representation in this basis is

$$\rho = \begin{pmatrix} \epsilon_x\epsilon_x^* & \epsilon_x\epsilon_y^* \\ \epsilon_x^*\epsilon_y & \epsilon_y\epsilon_y^* \end{pmatrix} = \begin{pmatrix} \cos^2(\alpha) & \cos(\alpha)\sin(\alpha)\, e^{-i\delta} \\ \cos(\alpha)\sin(\alpha)\, e^{i\delta} & \sin^2(\alpha) \end{pmatrix} . \tag{2.11}$$

Here we used the parametrisation of the polarisation vector in equation 2.3. ρ is hermitian, i.e. $\rho^\dagger = \rho$ and its trace is one. The bases of all hermitian 2×2 matrices are the Pauli matrices σ_1, σ_2, σ_3 and the diagonal matrix $\mathbb{1}_2$. With respect to equation 2.11 one finds

$$\rho = \frac{1}{2}(\mathbb{1}_2 + S_3\sigma_1 + S_1\sigma_2 + S_2\sigma_3). \tag{2.12}$$

This is the quantum mechanical representation of the Stokes vector. A measurement of the polarisation of the system is the trace of the product of density matrix with the observable. For example S_1 can be measured by

$$S_1 = \mathrm{tr}(\rho\sigma_2). \tag{2.13}$$

The vector (S_3, S_1, S_2) is equivalent to the spin vector of spin-$\frac{1}{2}$-particles. Each photon has a fixed polarisation and $S_1^2 + S_2^2 + S_3^2 = 1$. However, usually a beam is a mixture of photons with different polarisations and hence does not exhibit a pure polarisation. An unpolarised beam has the Stokes vector $S = (1,0,0,0)$. The polarisation degree is defined as

$$P = \sqrt{S_1^2 + S_2^2 + S_3^2}. \tag{2.14}$$

In general a beam will be partially polarised with $0 < P < 1$. These beams can be regarded as an incoherent mixture of an unpolarised and a polarised beam. The density matrix is composed of two parts,

$$\rho = (1-P)\frac{1}{2}\mathbb{1}_2 + P\frac{1}{2}\left(\mathbb{1}_2 + \frac{S_3}{P}\sigma_1 + \frac{S_1}{P}\sigma_2 + \frac{S_2}{P}\sigma_3\right). \tag{2.15}$$

The first matrix is the density matrix of an unpolarised beam and the second is that of a purely polarised beam.

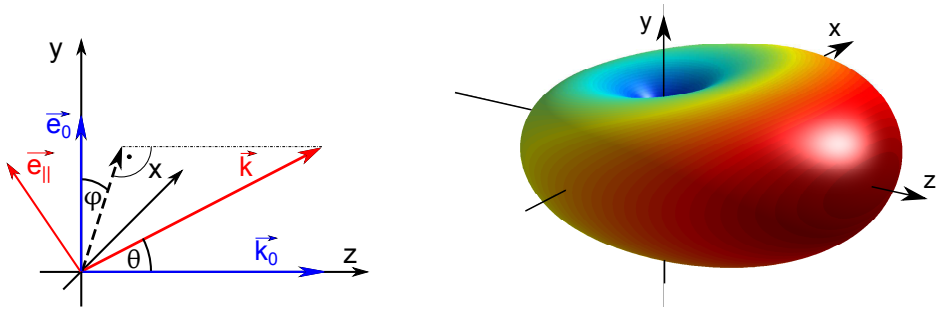

Figure 2.2 – Left: Angle relations for the polarised Compton scattering are illustrated. The incoming wave vector $\vec{k}_0$ points along the z-axis, and the polarisation of the incoming photon $\vec{e}_0$ points along the y-axis. $\vec{k}$ is the wave vector of the scattered photon, it forms with $\vec{k}_0$ the scattering angle θ. The angle between the $\vec{e}_0$-$\vec{k}_0$-plane and the $\vec{k}$-$\vec{k}_0$-plane is denoted with ϕ. The parallel component of the scattered polarisation vector $\vec{e}_{||}$ lies in the $\vec{e}_0$-$\vec{k}_0$-plane (y-z-plane) and is perpendicular to $\vec{k}$. Right: Graphical illustration of the differential scattering cross section for a photon with 100 keV energy. The axis are defined as on the left. The colours (blue-low, red-high) and the distance from the origin shall give an illustration of the scattering probability. Scattering into the direction of the primary photon polarisation is less likely than perpendicular to it.

2.1.2 Compton scattering of polarised photons

Several photon and electron interactions depend on the particle polarisation state or produce polarised particles. The two most important photon interactions at the for MRT relevant energies, photoelectric absorption and Compton scattering, are both influenced by the polarisation state of the photon. For the photoelectric absorption the angle of the emitted photoelectron depends on the polarisation of the incoming photon. Most electrons are ejected in the direction of the primary photon polarisation. However, due to the frequent scattering of electrons this does not play an important part for the energy absorption.

The Compton interaction of a linearly polarised photon with a free electron is schematically illustrated in figure 2.2. An incoming photon with the energy E_0 and polarisation $\vec{e}_0$ transfers a part of its energy to an electron and is scattered off with an energy $E < E_0$ and a polarisation $\vec{e}$. The wave vector of the incoming photon $\vec{k}_0$ and the outgoing photon $\vec{k}$ form the scattering angle θ. The angle between the plane containing $\vec{k}_0$ and $\vec{e}_0$ and that containing $\vec{k}$ and $\vec{k}_0$ is ϕ. Energy and momentum conservation yield the relation

$$E = \frac{E_0}{1 + \frac{E_0}{m_0 c^2}(1 - \cos\theta)}, \tag{2.16}$$

where m_0 is the electron rest mass and c the velocity of light. The differential scattering cross-section was first derived by Klein-Nishina[57] from quantum electrodynamics. A comprehensive derivation can be found in Heitler[58]. The scattering cross-section reads

$$\frac{d\sigma}{d\Omega} = \frac{1}{4} r_0^2 \frac{E^2}{E_0^2} \left[\frac{E_0}{E} + \frac{E}{E_0} - 2 + 4\cos^2\Theta \right]. \tag{2.17}$$

Here r_0 is the classical electron radius and Θ is the angle between the polarisation of the incoming photon and the polarisation of the scattered photon. To further analyse this formula it is useful to decompose the polarisation vector $\vec{e}$ of the scattered photon into a component $\vec{e}_\perp$ perpendicular to $\vec{e}_0$ and another component $\vec{e}_{||}$ in the plane of $\vec{k}$ and $\vec{e}_0$. From figure 2.2 we use that $\vec{e}_0 = \vec{e}_y$, $\vec{k}_0 = k_0 \vec{e}_z$ and

$$\vec{k} = k \begin{pmatrix} \sin\theta \sin\phi \\ \sin\theta \cos\phi \\ \cos\theta \end{pmatrix}. \tag{2.18}$$

For the component $e_\perp \cos\Theta$ is 0 and disappears. $\vec{e}_\parallel$ can be calculated from

$$\vec{e}_\parallel = \frac{(\hat{\vec{k}} \times \vec{e}_0) \times \hat{\vec{k}}}{|(\hat{\vec{k}} \times \vec{e}_0) \times \hat{\vec{k}}|} = \frac{\left(\vec{e}_0 |\vec{k}|^2 - \hat{\vec{k}} \cdot (\hat{\vec{k}} \cdot \vec{e}_0)\right)}{\sqrt{1 - \sin^2\theta \cos^2\phi}}, \tag{2.19}$$

where $\hat{\vec{k}} = \vec{k}/|\vec{k}|$. Therefore we obtain for $\cos\Theta$

$$\cos\Theta = 1 - \sin^2\theta \cos^2\phi. \tag{2.20}$$

In the non-relativistic case E_0 and E are approximately equal (from equation 2.16 for $E_0 \ll m_0c^2$). Therefore the scattering cross section becomes

$$\frac{d\sigma_\perp}{d\Omega} = 0 \tag{2.21}$$

for the perpendicular component and for the parallel component

$$\frac{d\sigma}{d\Omega} = r_0^2(1 - \sin^2\theta \cos^2\phi). \tag{2.22}$$

In the non relativistic case a linearly polarised primary photon produces a completely linearly polarised scattered photon. In the ultra relativistic case, i.e. $E_0 \gg m_0c^2$ one needs to differentiate between small and large scattering angles. For small angles $E \approx E_0$ again holds true and therefore the scattering cross section is identical to that of the non-relativistic case. For large scattering angles there is $E_0 \gg E$ and the scattering cross-section for the two final polarisation components $\vec{e}_\perp$ and $\vec{e}_\parallel$ are identical,

$$\frac{d\sigma_\perp}{d\Omega} = \frac{d\sigma_\parallel}{d\Omega} = \frac{r_0^2 E}{4E_0} \tag{2.23}$$

Scattering into a single direction irrespective of the final polarisation state is given by the sum of $d\sigma_\perp/d\Omega$ and $d\sigma_\parallel/d\Omega$,

$$\frac{d\sigma}{d\Omega} = \frac{1}{2} r_0^2 \frac{E^2}{E_0^2} \left[\frac{E_0}{E} + \frac{E}{E_0} - 2\sin^2\theta \cos^2\phi\right]. \tag{2.24}$$

This scattering cross-section is illustrated in figure 2.2 (right) for a primary photon energy of 100 keV. If the primary beam is unpolarised averaging over ϕ yields

$$\frac{d\sigma}{d\Omega} = \frac{1}{2} r_0^2 \frac{E^2}{E_0^2} \left[\frac{E_0}{E} + \frac{E}{E_0} - \sin^2\theta\right]. \tag{2.25}$$

2.2 Methods

Monte Carlo simulations were performed in the Geant4 toolkit version 9.3.p2 using the Livermore low-energy polarised physics libraries. These libraries incorporate the polarised Compton scattering and also polarised electron interactions. In the simulation Compton scattering, Rayleigh scattering and photoelectric absorption were activated for photons. Electron processes were multiple scattering, ionisation and bremsstrahlung. All dose comparisons were carried out in cuboid homogeneous water phantoms with dimensions similar to those used for dosimetry experiments with $30\times30\times12$ cm^3 side lengths. Energies of the simulated photons were distributed according to the previously measured spectrum (see e.g. Slatkin et al.[14], Siegbahn et al.[15]). In order

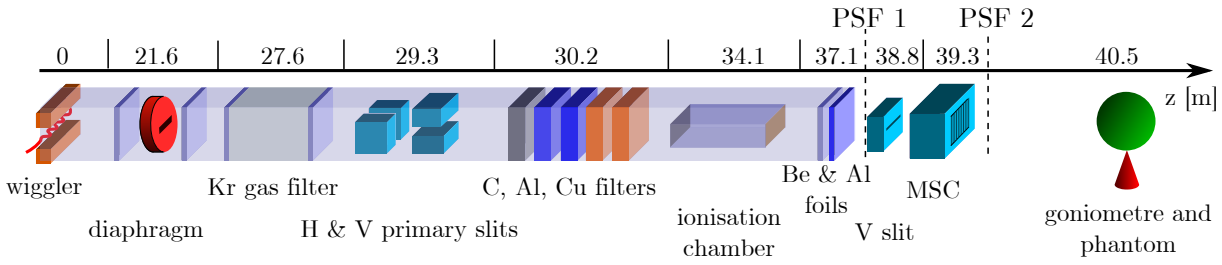

Figure 2.3 – Sketch of all beam modifying elements. This image was adapted from Martínez-Rovira et al. [13].

to accelerate the Monte Carlo simulations and to enhance the statistics adjoint Monte Carlo techniques were employed apart from forward simulations (see chapter 3.2.3).

The study consists of two parts. In one part of the analysis the effect of the phase space on the dose absorption in the phantom is considered. In Monte Carlo simulations the radiation source was defined to deliver either perfectly parallel microbeams, to produce photons following the source phase space or according to a developed source model. The phase space of the source at the ID17 of the ESRF was completely characterised by Martínez-Rovira et al. [13]. They simulated the particle transport from the wiggler to a plane (phase space plane 1) in front of the vertical slit 38.8 m from the source with the ray tracing program Shadow [59] and the Monte Carlo code PENELOPE [56,60]. For all photon trajectories that passed the phase space plane 1, direction, polarisation state and energy of the photons were stored in a phase space file (PSF 1). The location of the plane in the beamline ID17 (in MRT mode) and all filters, beam modifying elements and the phantom are illustrated in figure 2.3. Three different primary vertical slit apertures of 1, 2 and 3 cm width were used by Martínez-Rovira et al. [13] for the generation of PSF 1 with a beam height of 1 mm. The number of photon trajectories was $5.2 \cdot 10^7$, $6.3 \cdot 10^7$ and $12.5 \cdot 10^7$ at 1, 2 and 3 cm aperture respectively. Technical details on the simulations can be found in the work of Martínez-Rovira et al. [13].

The simulations with the complete set of phase space information was performed in two steps. In a first step photons were created in the phase space plane 1 according to the information in the PSF 1 and passed through the horizontal slit and the multislit collimator (MSC), i.e. the photon trajectories were continued. In a plane directly behind the MSC, the phase space plane 2, the residual particle trajectories were stored again in a second phase space file, PSF 2. The MSC and the horizontal gap absorb the majority of photons from the PSF 1. Therefore the particle yield behind the absorber is pretty low and not sufficient for a reliable simulation in the patient geometry. For that reason these particles were reused and 10^{10} photons were created from the PSF 2. The intrinsic uncertainties of PSF 2 are of course still present in the final simulation. However, the statistics of dose absorption in the phantom could be significantly enhanced.

These simulations with the complete phase space information were compared to simulations with ideal microbeams. To ideal microbeams we refer as perfectly parallel planar beams with 100% intensity in the beam and no photon fluence in the valley region. The centre to centre distance and the beam width were set to those at the phantom surface, deduced from the beam divergence in the PSF and the slit sizes of the MSC, 412.3 and 51.5 μm. For these simulations it was convenient to use adjoint Monte Carlo techniques.

In another part of this study the polarisation effect was investigated by simulating an infinitesimally narrow beam in the water phantom which was 100% linearly polarised. Dose was scored in a cylindrical detector geometry shown in figure 2.4. While the slice spacing along the beam and also the angles are equidistant, the radii of the detector segments increase exponentially. The detector geometry allowed both, studying the absorption of electrons created in primary interactions close to the beam and the scattered photon absorption extending to a larger

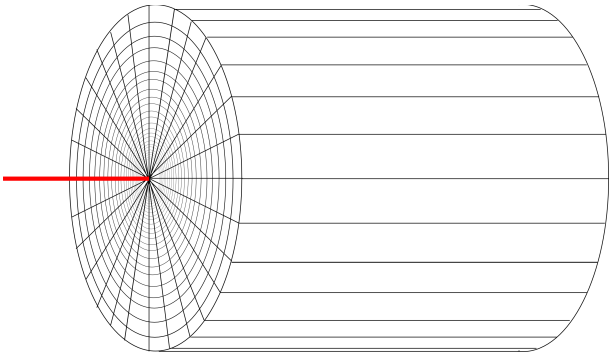

Figure 2.4 – Detector geometry to score an infinitely small microbeam in homogeneous water[46].

distance from the beam. Nonetheless the number of particle histories required for statistically significant results remained reasonable.

The simulation results were benchmarked against experimental data. The data was collected by Michael Lerch and Elke Bräuer-Krisch at the biomedical beamline ID17 of the ESRF. Measurements were performed under standard MRT conditions for filters and the wiggler gap size. A homogeneous 2×2 cm^2 field was radiated onto a phantom with stacked 30×30 cm^2 solid water slabs of various thickness (figure 2.5) by vertically moving the phantom through the 20 mm wide and 0.051 or 0.52 mm high beam. The phantom was set approximately 42.9 m from the wiggler source. A PTW semiflex ionisation chamber (IC) in combination with a PTW UNIDOS electrometer (model T10002) served as detectors. The electrometer was operated at 400 V. Dosimetry followed the IAEA dosimetry protocol[61] no. 398.

The advantage of using the semiflex IC is its excellent response uniformity with photon energy for the spectral range in MRT. A major challenge of dosimetry in MRT is the dose rate dependency. For measurements in the beam the dose rate was reduced by using the narrower 0.052 mm high slit. Therefore the speed of the goniometer can be reduced and thus the effective dose rate at the IC. Previous studies[62] showed that measurements at this slit height require only a very small correction for ion recombination effects, while for the out-of field dose no correction is necessary.

The measurements were carried out at 0, 2 and 4 cm distance from the beam axis in two orientations. One measurement was done in the plane of the storage ring, i.e. the plane of polarisation and one perpendicular to it. The depths in the phantom were chosen in a range between 5 and 120 mm. The thickness of the backscattering material was always kept constant.

2.3 Results

2.3.1 Polarisation effects

For a monoenergetic pencil beam of 150 keV figure 2.6A shows profiles perpendicular and parallel to the polarisation direction. Scattering of a photon perpendicular to its polarisation direction is more likely than parallel to it. In the profile there are clearly three domains in distance from the primary beam visible, separated by steep dose fall-offs (compare Spiga et al.[63]). The first domain forms a region of approximately 10 μm radius around the beam. Photoelectric absorption and Compton scattering produce electrons in the central beam. At low energies the Compton electrons get just around 20% of the primary photon energy, whereas a photoelectron gets, neglecting binding energies, the whole photon energy. Hence the range of photoelectrons is much larger than that of Compton electrons. For a few tens of keV the electron range is in the order of a few microns, where as the electron CSDA range at 150 keV is around 280 μm[64].

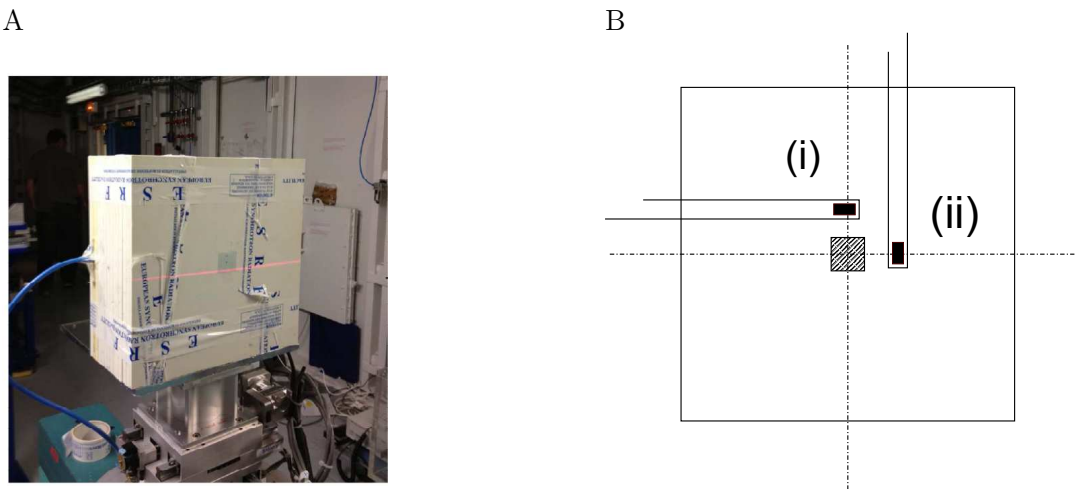

Figure 2.5 – A: Photo of the experimental set-up at the ESRF. B: Schematic diagram showing the orientation of the ionisation chamber for measuring the (i) vertical and (ii) lateral out-of-field dose components. The radiation field is indicated by the hashed region [46].

Energy absorption in the first 10 μm around the central beam is therefore mediated by Compton electrons. Momentum conservation implies that electrons scatter off opposite to the scattered photons and hence they are mainly produced in the plane perpendicular to the polarisation. In a distance between 10 and 200 μm from the beam the region of photoelectrons can be found. The photoelectric absorption is independent of the photon polarisation and thus there are no directional differences observed. Figure 2.6B shows the ratio between the profile perpendicular and parallel to the polarisation. In the second domain from 10 to 200 μm the ratio is almost 1 whereas inside the 10 μm radius a strong directional dependency can be seen. Electrons become maximal ionising at the end of their path. Hence at the end of the Compton electron range the polarisation effect is strongest and the ratio is peaked there.

Beyond 200 μm energy absorption is mediated by scattered Compton photons. Primary photons are preferentially scattered perpendicular to their polarisation. The difference between the dose deposited perpendicular and parallel to the primary polarisation direction is around 60%. This difference is almost independent of depth and distance from the beam. Only at very shallow depths the difference increases slightly with distance.

Looking at this data we expected a strong influence of the polarisation on the dose distribution in MRT in patients. The simulated pencil beam was used to calculate the dose in an MRT field of 2×2 or 3×3 cm^2 size, 400 μm ctc and 50 μm beam width. Figure 2.7 compares the calculation results with those without polarisation. The dose differences are up to 45% outside the microbeam field (figure 2.7A and 2.7B). Within the field, differences between polarised and non-polarised treatment appear in a narrow region at the microbeam penumbras (figure 2.7D). These regions have a width of around 20 μm and the differences can be as high as 9%. They are caused by the polarisation sensitive Compton electrons and doses in the beam penumbras are lower for polarised photons. Differences in the peak doses are very small, though. The peak dose differences are smaller than 0.1% throughout the whole field. The valley dose difference between calculations with and without polarisation is lowest in the centre and increases towards the field edges. If polarisation is taken into account, valley dose values are a bit lower, but the deviations remain below 3% for a 3×3 cm^2 field except for a 3 mm wide field edge. In the centre the polarisation has an effect of around 1%. For other field sizes, e.g. a 2×2 cm^2 microbeam field deviations are very similar (results are not shown here).

In the beam set-up at the ESRF in Grenoble the polarisation is perpendicular to the alignment

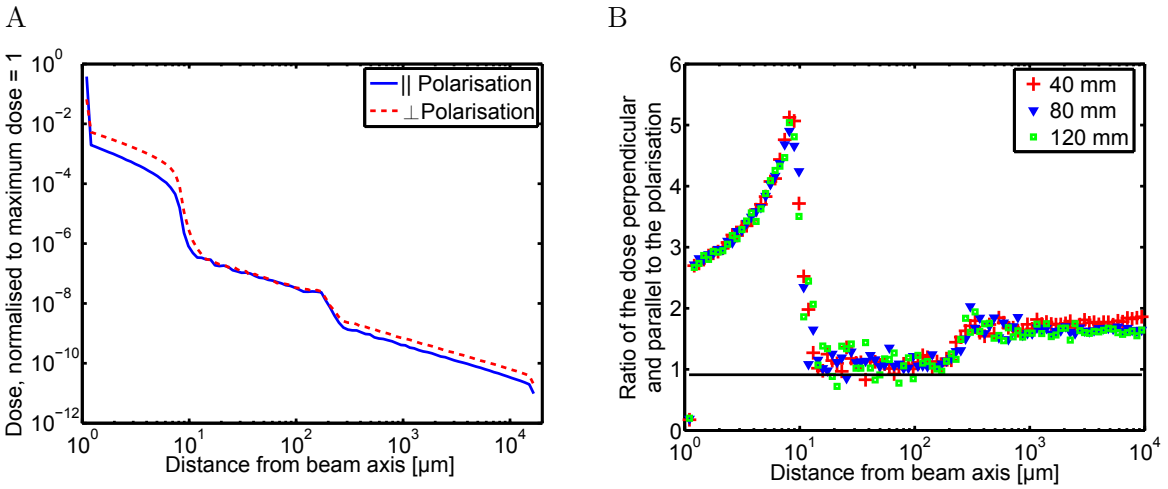

Figure 2.6 – (A) shows the lateral dose profile from the beam axis parallel and perpendicular to the polarisation direction for a photon pencilbeam of 150 keV. In (B) the ratio between the profile perpendicular to the polarisation direction and parallel to the polarisation direction is plotted. There are three different regions distinguishable [46].

of the microbeams. This means that scattering perpendicular to the microbeams in the direction of the valley regions is less frequent than parallel to the microbeams. Amazingly, this does not necessarily lead to a constantly lower valley dose. In order to understand this effect we need to consider the microbeam field as a whole. The total scattering cross section does not depend on the photon polarisation. Going from non-polarised to polarised photons only the distribution of scattering angles changes. With linear polarisation in a plane perpendicular to the beam the scattering is no longer isotropic but has a quadrupole structure. Its minima are placed on a line perpendicular to the microbeams and its maxima parallel to it. In a point in the centre of a large field the dose is determined by interactions homogeneously distributed around. Positive and negative parts of the quadrupoles cancel each other and hence the absorbed dose does not differ from the dose of isotropically scattering non-polarised photons. Close to the beam edges, there are fewer interactions in a certain direction. This is true for polarised and non-polarised photons. However, for polarised photons the orientation of the edge is important. If the off-beam region is located in the direction of the positive lobe of the quadrupole the decrease will be stronger, because the lacking dose of back scattering particles is higher. Whereas an off-beam region in direction of the negative lobe of the quadrupole implies a less pronounced dose decrease towards the beam edge, because particles from this direction did anyway contribute less to the dose.

In the peak dose region for instance there are only electron producing photon interactions along the microbeam. Perpendicular to the microbeam there are less interactions. The consequence is a slightly higher peak dose close to the peak edge and a dose reduction in the penumbra region just outside the beam. For the valley dose photon scattering is important. In the centre of the field there is an equilibrium of in- and out-scattering photons. Close to the field edge there are less photons scattering in from a particular direction. Polarisation leads to an anisotropic lack of photons compared to non-polarised isotropic scattering. However, the average range of scattered photons is much larger than the field size. Therefore there is no dose increase towards the field edges visible but only the decrease outside the field moving perpendicular to the microbeam direction. Hence in the valley dose the effect leads to the relative differences shown in figure 2.7B(C).

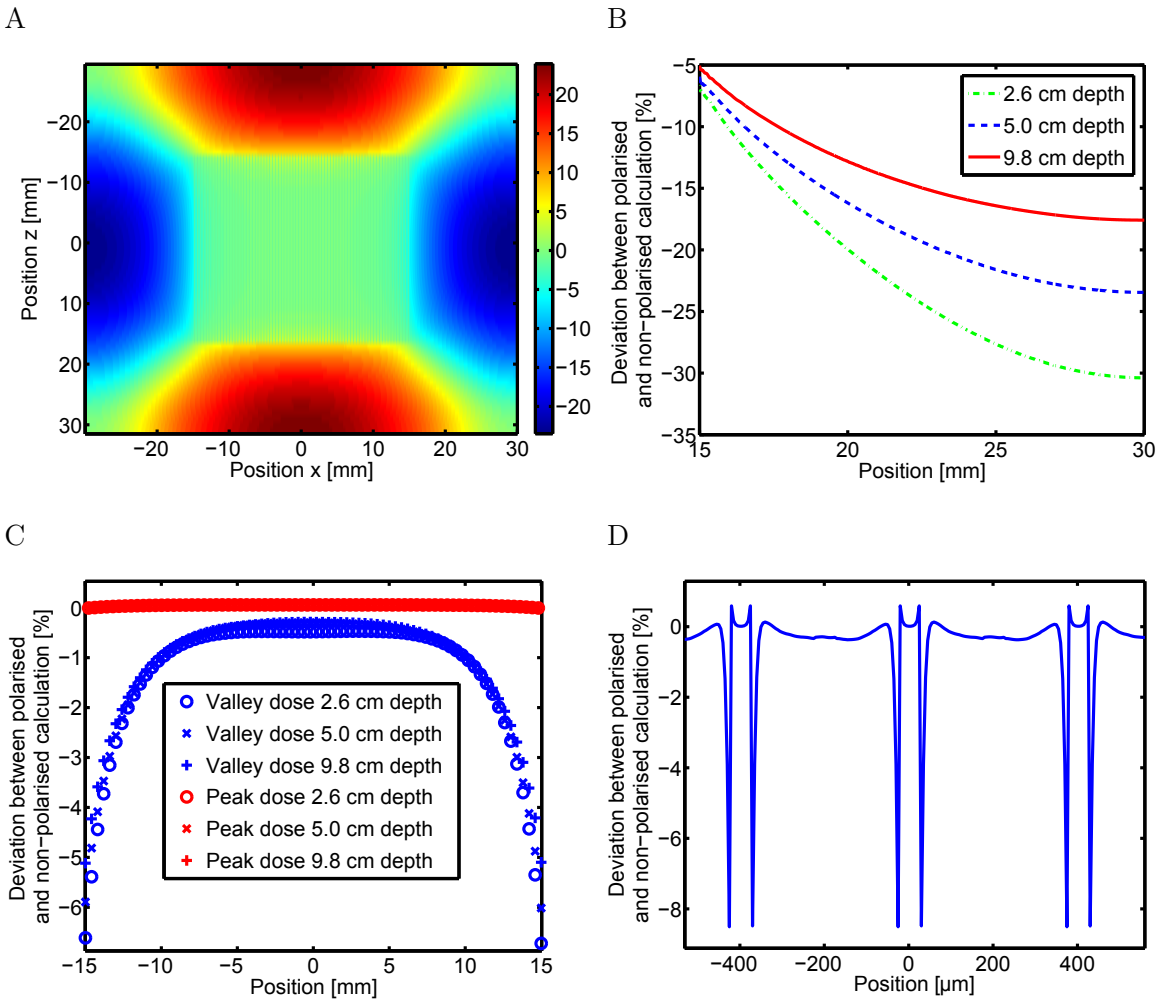

Figure 2.7 – Differences between dose calculations regarding and ignoring photon polarisation in a 3×3 cm^2 microbeam field in a water box. It is positive if the dose of a calculation with polarised photons is higher. Figure (A) shows the whole field in 5 cm depth. The colour coding states the differences in %. Figure (B) shows differences at different depths outside the microbeam field and figure (C) compares peak and valley doses inside the field. In figure (D) differences in the centre of the field for three adjacent microbeams are shown. Except for the overshoot in the beam penumbra difference are very small [46].

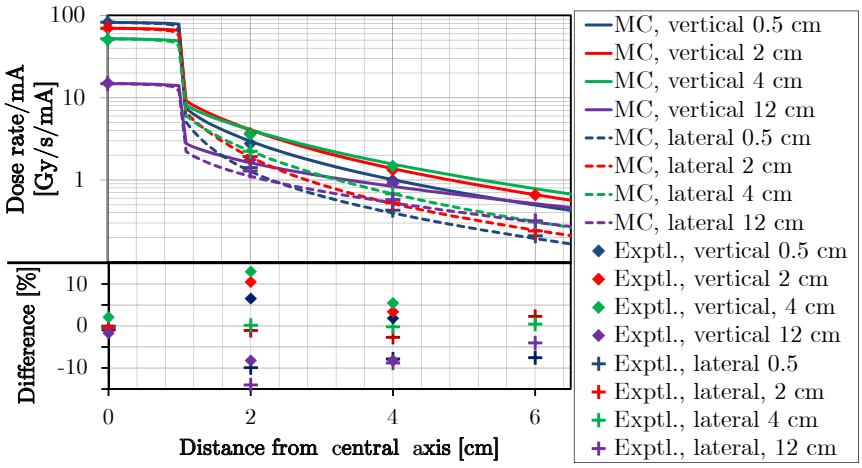

Figure 2.8 – Dose rate per mA of storage current deduced from measured IC response falls off with distance up to 6 cm from the central axis in the vertical (diamonds) and lateral (crosses) direction for the three different depths indicated. Measurements are compared to Monte Carlo (MC) simulations in the vertical (solid lines) and lateral (dashed lines) direction[46].

2.3.2 Comparison with measurements

In the case of MRT the primary photon flux emerging from the superconducting wiggler is well known to be proportional to the current in the synchrotron storage ring. The dose rate was deduced by multiplying the measured dose by the ratio of the speed of the goniometer (typically 20-100 mm/sec) and the slit size that defines the height of the primary photon beam (0.051 mm in this case). As such the dose rate is therefore more specifically the average dose rate for a volume defined within the primary radiation field ($2\times2\ cm^2$ being the standard field size). The semiflex IC has a well documented significant dose rate dependence. In order to minimise this dependence the height of the primary beam was reduced to 0.051 mm (usually 0.520 mm) and the dose was independently checked within the primary field against a pin point IC (no such dose rate dependence) previously[62]. For all measurements made outside the primary radiation field, where the dose rate is orders of magnitude less than that within the primary field, the measured dose scaled within 1% in going between the 0.051 and 0.520 mm slits, which gives confidence to this data. Figure 2.9B shows the deduced dose rate per milliampere of storage ring current.

Figure 2.8 shows how the measured IC response falls off with distance up to 6 cm from the central axis in the vertical (solid lines) and horizontal (dashed lines) direction for four different depths (0.5, 2, 4 and 12 cm). Each measurement at the positions and depths indicated were repeated three times and the measurement uncertainty for the 99% confidence limit is below 5% for all measurement points. The scattered energy deposited outside the $2\times2\ cm^2$ radiation field generally falls off at a double exponential rate, at all depths. The measured dose fall-off with distance from the central axis out to 6 cm, appears to decrease with depth in the solid water phantom. This is due to the contribution to the energy deposition from forward scattered photons which increases with depth, in the case of the photon energy spectrum of the primary MRT radiation field. It can also be seen immediately that the presence of the polarised primary beam effects the vertical and horizontal scattered photon distribution (and hence dose delivered) differently, which is significant for MRT dose planning if the radiation field is near or adjacent to critical organs. For all depths the vertical dose is consistently greater than the horizontal dose, which is consistent with that expected from theory and is in agreement with the Monte Carlo simulations. Monte Carlo simulations conform to the measurements to less than 10% (except for 1 value). Some of the values lie outside the uncertainties provided by the measurement. However,

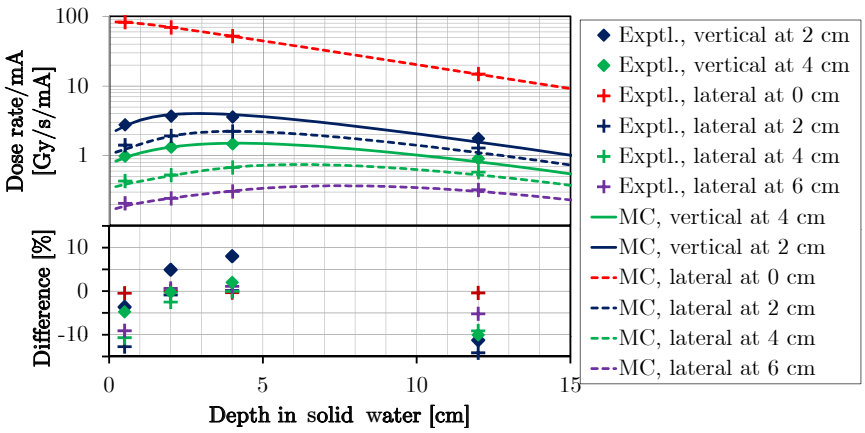

Figure 2.9 – Dose rate fall of with depth measured on the axis and in 2, 4 and 6 cm distance. Measurements are again compared to Monte Carlo (MC) simulations. Measurement uncertainties remain below 5% and differences to MC simulations are, except for one value, below 10% [46].

the scattered dose in contrast to the peak doses depends heavily on collimator scattering and back scattering from surfaces surrounding the phantom that were not taken into account in the Monte Carlo calculations. Hence the agreement between Monte Carlo and measurement in the off-beam, low dose domain is reasonably good.

2.3.3 Source Phase Space

PVDRs calculated with Monte Carlo simulations regarding the phase space information are on average 8% smaller than simulations assuming ideal microbeams. This result can be seen in Figure 2.10C. Although peak doses in the field centre are equal in both simulations, valley doses are substantially lower in calculations with ideal microbeams. Where do these differences originate from? In the following we investigate the physical and technical reasons for these deviations. An analysis was done on the PSF 1 in the phase space plane 1 and on the PSF 2 created directly behind the collimator. In the following y is the propagation direction of the photons, z the direction parallel to the collimator slits and x perpendicular to both. The direction of the photon momentum is denoted by $\vec{u} = (u_x, u_y, u_z)$ with $|\vec{u}| = 1$. We concentrated on the following deviations from ideal microbeams and show that they explain the deviations observed:

1. Geometrical beam divergence of the whole field: Although the collimator is in a distance of 39.3 m from the wiggler source and the field is just a few centimetre in size, there is a measurable geometrical divergence. One consequence is that at the phantom surface 1.2 m from the collimator, ctc and width of the microbeams have slightly increased.

2. Imperfect absorption of the absorber material in the tungsten carbide collimator leads to leakage radiation.

3. Associated with the geometrical divergence could be a more pronounced absorption at the MSC for beams at the field edge, because the beam incidence is inclined towards the collimator walls.

4. The photon fluence is not completely flat. I.e. the photon flux in a plane in front of the MSC is higher at the centre than close to the beam edges.

To estimate the error made by the neglect of the geometrical beam divergence we have plotted phase space points over x and u_x in figure 2.11A. All phase space points are more or less aligned

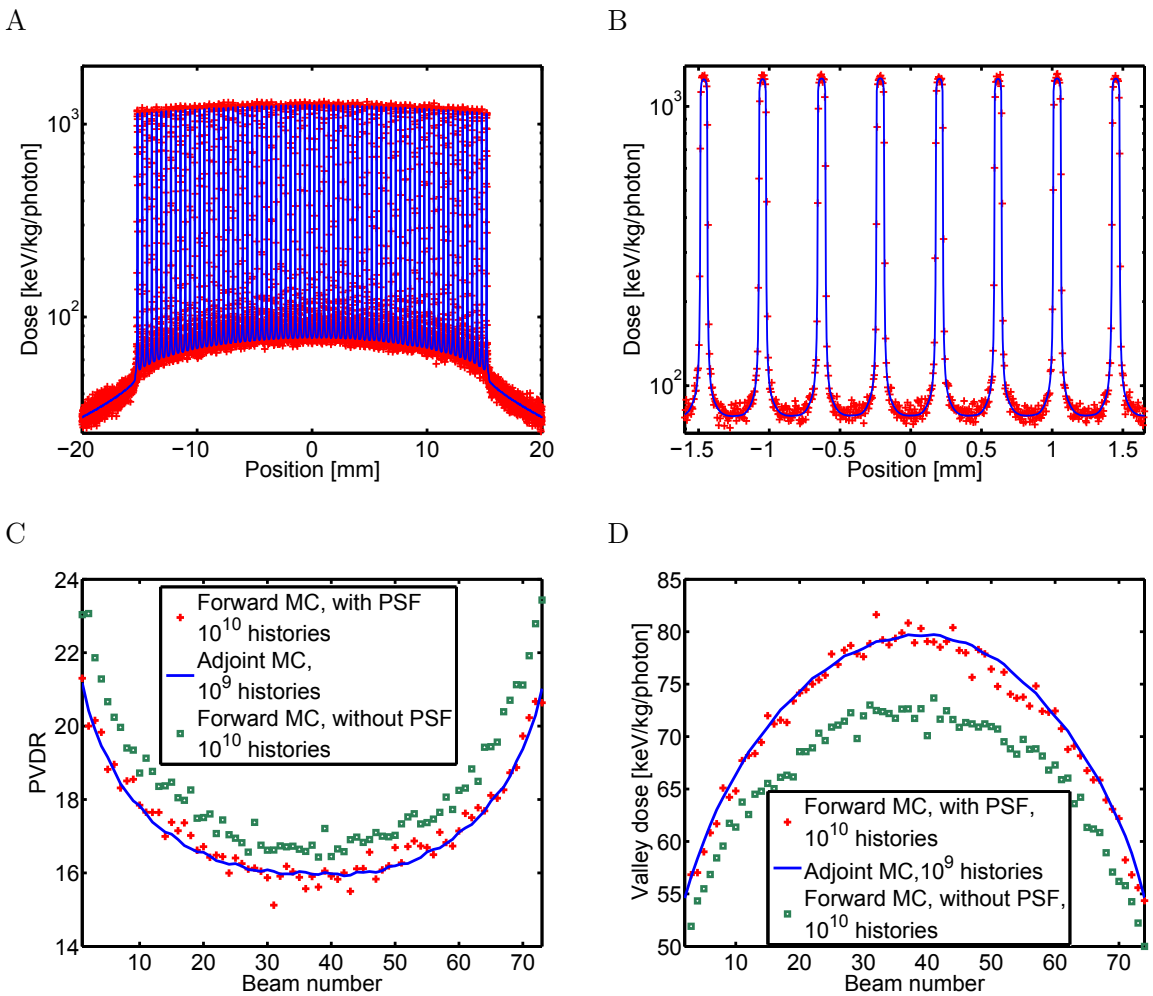

Figure 2.10 – Comparison of calculations with phase space information (red "+"), adjoint Monte Carlo calculations with phase space model (blue line) and calculations without phase space information (green "□"). (A) illustrates the whole field and (B) a few beams in the field centre. In (C) and (D) the PVDR and valley dose is plotted over the beam number[46].

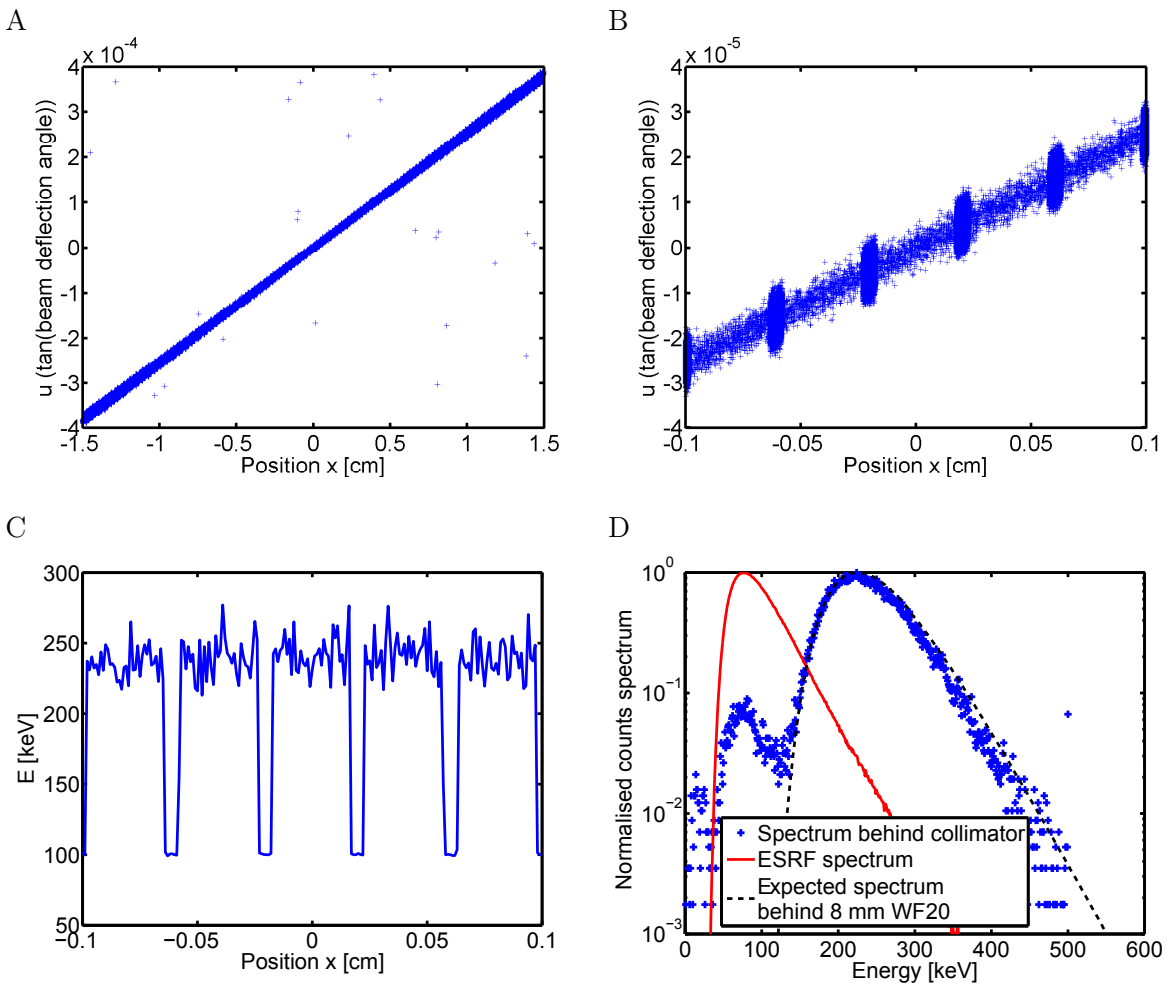

Figure 2.11 – Analysis of the phase space after tracking the photons from the phase space plane through the MSC. Figure (A) shows the tangent of the deflection angle depending on the position in the beam. Figure (B) shows the same graph in detail at the field centre. Graph (C) plots the mean photon energy depending on the position x. There is a considerable energy difference observable between photons in the beam and between the beams. This is shown in more detail in figure (D). As a red line the spectrum in the microbeams is plotted and as blue "+" the photon spectrum behind the absorber material. The black dashed line is the expected spectral shift of the red spectrum after the photons penetrated 8 mm WF20 [46].

along a straight line. As shown before by Martínez-Rovira et al. [13] the linear dependence between x and u_x with the regression coefficient γ is given by

$$u_x = \gamma x = 2.56(4) \cdot 10^{-5} mm^{-1} x. \tag{2.26}$$

The beam divergence remains unchanged after the photons have passed the MSC. The consequence of this divergence is that the beam width of the microbeams has increased from 50 μm to 51.5 μm and the ctc from 400 μm to 412.3 μm when reaching the phantom surface in 120 cm distance from the MSC. The divergence itself inside the phantom is of negligible importance. At the back side of a 20 cm thick phantom the beam parameters have not significantly changed and are 51.8 and 414.4 μm. This difference is hardly measurable and is unlikely to have any clinical impact (compare measurements in chapter 4.).

Apart from this over all geometric divergence there is an intrinsic beam divergence emanating from collimator scattering superimposing the geometrical divergence. Figure 2.11B shows the dependence of x and u_x in the centre of the field in more detail. The actual trajectories in the

phase space scatter around the found linear relation. Each beam has an intrinsic divergence which is given by $u_x = 2 \cdot 10^{-6}$ in the centre of the field and $4.8 \cdot 10^{-6}$ at the field edges. The consequence for the beam shape at the phantoms surface in 120 cm distance from the collimator is that the beam edges are smeared out between 2 and 4.8 μm with a more or less Gaussian distribution. As long as the beam sizes and spacing are much higher than that, there is no substantial influence on the absolute peak and valley dose values to be expected. Therefore the valley dose contribution from collimator scattering is small enough to be neglected.

Higher valley doses, however, could also be a result of imperfect absorption from the collimator material. The collimator material is a tungsten carbide alloy (WF20) containing 39.41% tungsten, 40.72% carbon, 18.11% cobalt, 0.44% vanadium and 1.32% chrome[11]. Its thickness is 8 mm. The photon flux behind the absorber material is around $1.0 \cdot 10^{-3}$ of the flux behind the aperture. However, the average energy of the photons behind the absorber material is about 2.4 times higher than the average photon energy behind the apertures. Figure 2.11C shows the average photon energy depending on the position (x) in a region close to the centre of the field. The average energy in the beam is around 100 keV. In the off-beam region the average photon energy is 240 keV. Due to less particles penetrating the absorber the noise level is higher than in the peaks. In order to confirm that the photon flux behind the collimator is caused by photons of the primary beam passing through the absorber we have calculated the spectral change of the beam after penetrating 8 mm WF20 and compared it with the actual spectrum behind the absorber material in Figure 2.11D. The red curve shows the MRT beam spectrum and the black dashed line is the derived spectrum after the beam has penetrated 8 mm of WF20. The actual observed spectrum is shown with blue plus symbols. The maxima of the spectra are normalised to 1. Calculated and observed spectrum behind the absorber coincide except for energies beneath around 135 keV. The energy contribution of photons with less than 135 keV is 1.35% and can probably be attributed to scattering at the collimator edges. Its small contribution consolidates the finding that collimator scattering into the valley region is of minor importance. Furthermore the divergence of the beam behind the absorber matches that of the microbeams as can be seen from figure 2.11B. So even after penetrating 8 mm absorber material the divergence of the beam has not increased.

In the plane directly behind the MSC the flux per microbeam changes depending on the position of the beam. The flux is highest in the centre of the field and decreases by about 9% to the edge of the field (see figure 2.12B, blue "+"). This deviation consists of two parts. On the one hand the photon flux in the phase space plane is smaller at the field edges than in the field centre. This is shown in figure 2.12A. The photon flux follows the quadratic profile

$$I = I_0(1 - 0.0196\, cm^{-2} x^2), \tag{2.27}$$

where I_0 is the maximum dose in the centre of the field. The caused variations in the photon flux per beam are around 4%. On the other hand the inclined incidence of the beam outside the field centre leads to a partial shielding of the microbeams. Assuming the MSC made of ideal absorbing material (absorption coefficient $\mu \to \infty$) simple geometrical considerations yield for the ratio of actually transmitted photons N to the number of transmitted photons in the field centre N_0

$$\frac{N}{N_0} = 1 - \frac{\gamma(\text{absorber\_thickness})}{(\text{beam\_width})}|x| = 1 - \beta|x|. \tag{2.28}$$

A derivation is provided in appendix A. Using the linear divergence $\gamma = 2.564 \cdot 10^{-5}$ mm^{-1}, the absorber thickness of 8 mm and the beam width of 50 μm gives $\beta = 0.041$ cm^{-1}. However, due to imperfect absorption at the collimator edges the actually observed value is $\beta = 0.030$ cm^{-1}. From the centre to the edge of a 30×30 mm^2 field the number of photons per beam decreases by 5% due to this effect. Taking both effects together the photon numbers per beam can accurately

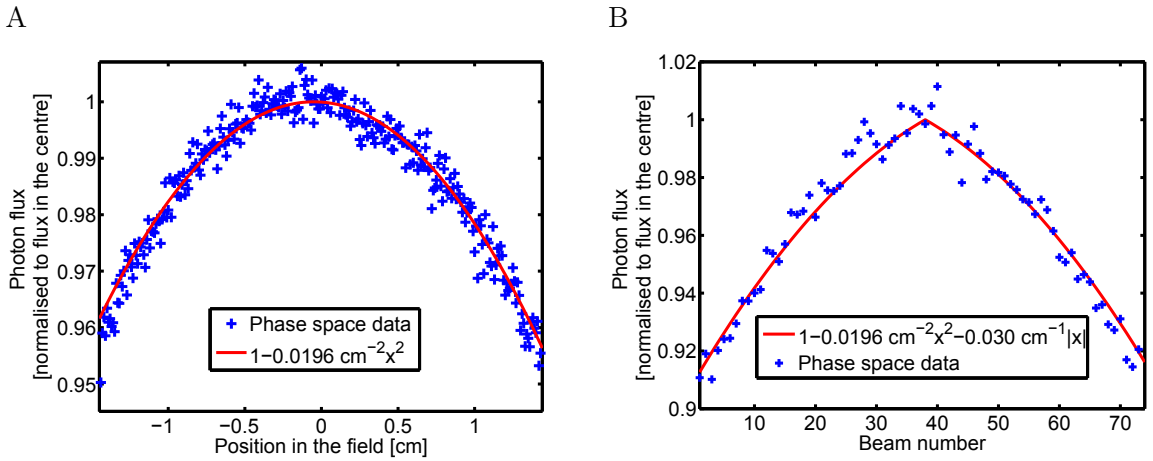

Figure 2.12 – (A) shows the photon flux of the primary field in front of the MSC (blue "+") and a quadratic fit (red line) of this data. (B) shows the relative number of photons per beam (blue "+") and the developed model (red line)[46].

be described as shown in figure 2.12B. The total variations of peak doses are around 9% of the maximum.

Summarizing these findings we established the following simplified source model:

1. Parallel microbeams of 51.5 μm width and 412.3 μm spacing comprised of photons with energies according to the ESRF spectrum impinge the sample.

2. Parallel leakage radiation with an altered spectrum in the spacing between the beams contributes to the valley dose. The photon flux is reduced to 0.10% of the primary beam.

3. The photon flux in the beam varies with the beam position according to $I_0(1-\alpha x^2-\beta|x|)$ with the constants $\alpha = 0.0196cm^{-2}$ and $\beta = 0.030cm^{-1}$.

4. The leakage radiation follows the profile of the primary beam in the phase space plane, $I_0(1-\alpha x^2)$.

This simple source model can easily be implemented in Monte Carlo simulations, but also in other dose calculation techniques. Kernel based dose calculation algorithms especially benefit from the simplification to parallel beams. Only the primary photon fluence needs to be modified. The implementation of the model to the MRT dose calculation algorithms is a subject in chapter 3. The correction for the leakage dose can easily be performed by calculating the photon absorption of a broad parallel field with 0.1% flux of the primary field with the spectrum shown in figure 2.11D. In the following section we describe the usage of the established source model in semi-adjoint Monte Carlo simulations and compare the results with a forward calculation using the complete phase space information.

2.3.4 Semi-Adjoint Monte Carlo simulation

The developed source model can be employed in a semi-adjoint Monte Carlo simulation. The principles of this technique are explained in chapter 3.2.3. We define the adjoint detector in the phase space by the formulae below (there are no directional constraints).

$$\begin{aligned} D(x,y,z,E) &= \Theta_{XZ}(x,z)\Delta(y-y_0)\left(\Theta(w-x \bmod a)(1-\alpha x^2-\beta|x|)+\dots\right. \\ &\quad \left.\dots+\Theta(x \bmod a-w)(1-\alpha x^2)\rho_{Abs}(E)\right). \end{aligned} \tag{2.29}$$

Here we use E as the photon energy, x, y and z are the coordinates as defined before, $w = 51.5\,\mu m$ is the beam width, $a = 412.3\,\mu m$ the centre to centre distance of the beams, y_0 the depth of the detector in water and ρ_{Abs} characterises the transmission of the primary photons through the absorber material. It is defined as number of photons N with energy E that penetrate the absorber per number of primary photons N_0 with energy E, $\rho_{Abs}(E) = e^{-\mu_{WF20}(E)\cdot d}$, with d = 8 mm being the absorber thickness and μ_{WF20} the absorption coefficient of tungsten carbide. The operator mod stands for modulo (remainder of division), the function Θ is one for positive arguments and zero otherwise; and the function Θ_{XZ} is one in the microbeam field and zero otherwise. $\Delta(y - y_0)$ is one in a region around $y = y_0$ and characterises the sampling in y. For the simulations presented here the mesh size in y was chosen to be 4 mm, i.e. $\Delta(y - y_0)$ is one for $y \in [y_0 - 2\,mm, y_0 + 2\,mm]$ and zero otherwise.

The adjoint source is a point source at the surface of the phantom sending a parallel photon pencil beam into the phantom. The photon energy is distributed according to the spectrum of the primary beam (red line in figure 2.11D).

The results of this calculation can be seen in figure 2.10, which compares profiles in 8 cm depth from forward Monte Carlo simulations with PSF and adjoint Monte Carlo using the described detector. In figures 2.10A and 2.10B profiles of the microbeam field are shown in the field centre. Although the forward calculation used 10 times more particles, the statistical uncertainties are much higher than in the adjoint MC. Within the uncertainties both methods, adjoint Monte Carlo simulation and forward Monte Carlo simulation, provide the same results.

In figure 2.10C the PVDR is compared between Monte Carlo simulations with the PSF (red "+"), adjoint Monte Carlo simulation (blue line) and a Monte Carlo simulation with ideal microbeams (green squares). Figure 2.10D shows the valley doses for the same three calculations. The adjoint Monte Carlo coincides with the forward calculation with the PSF. The valley dose for the forward calculation with ideal microbeams is significantly lower. This difference originates from the neglect of leakage photons in the valley region. The peak dose also shows a modulation across the beam (see figure 2.10A). Moving out from the field centre peak doses calculated with our phase space model or the PSFs from Martínez-Rovira et al. [13] decrease, whereas the peak dose for ideal microbeams remains approximately constant.

2.3.5 Comparisons with measurements and unexplained deviations

In figure 2.13 results of the adjoint Monte Carlo simulation are compared with film dosimetry measurements and Monte Carlo simulations from Martínez-Rovira et al. [13]. The comparison is made in a 60×24×60 cm^3 solid water phantom for a 20×20 and a 30×30 mm^2 microbeam field. The results obtained with our model are for most of the measurement points within the uncertainty limits of the experimental data. At shallow depth for the 30×30 mm^2 field PVDRs tend to be slightly lower in the measurement. However, uncertainties of the film dosimetry are too high and more accurate measurements need to be performed to validate this effect. Compared to the Monte Carlo simulations by Martínez-Rovira et al. [13] our calculations are closer to the measurement. The origin of the difference between the two simulations has not yet been resolved.

2.4 Conclusions

In this chapter we developed an understanding of important beam parameters in MRT. A simple approximation of ideal microbeam profiles (see chapter 2.2) leads to considerable differences in the peak and valley doses. However, we were also able to show that a complete simulation of the beamline is not necessary. As key parameters the flux profile across the broad beam, the leakage radiation from the MSC in the valley regions and the diminishing microbeam intensity with increasing beam incidence angle at the field edges were identified. They allow an accurate

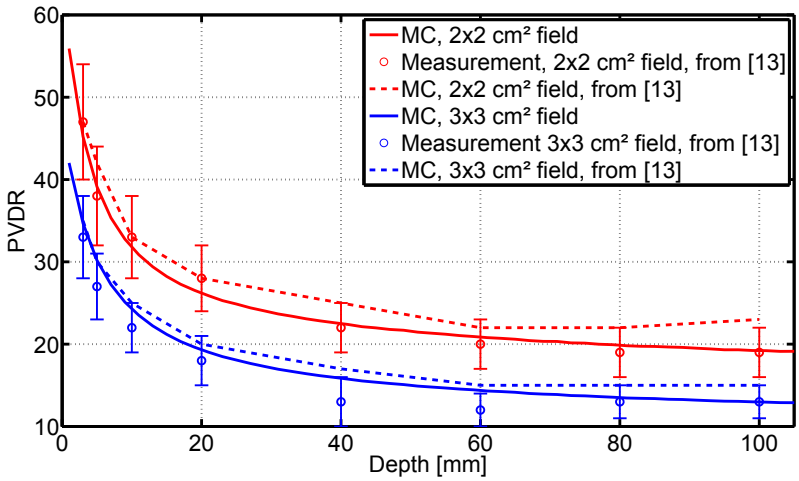

Figure 2.13 – The graph compares PVDRs in depth calculated with the adjoint Monte Carlo simulation using the model developed in this work (solid line) for a 20×20 mm^2 and a 30×30 mm^2 field in water and compares the result with film measurements (circles) and Monte Carlo simulations by Martínez-Rovira et al. [13] (dashed line).

dose calculation with planar perfectly parallel beams if the spacing and width of the beams are adapted to their size at the position of the phantom. Whereas the MSC produces beams with 50 μm width and a ctc of 400 μm the beam divergence leads to slightly larger parameters at the phantom surface. Nevertheless the beam divergence does not seem to affect the dose absorption in the phantom.

These findings were incorporated in a source model. The valid assumption of parallel beams allows the application of many alternatives to inefficient forward Monte Carlo simulations. This was shown for semi-adjoint Monte Carlo techniques as one example (see also chapter 3.2.3). The presented source model is the input for all dose computations within this work. It was incorporated into the Monte Carlo codes as well as the analytic dose calculation algorithm. The exact implementation will be a topic in the respective chapters (e.g. chapter 3.2.2).

Nevertheless it should be noted that the model has several short comings. Scattering from the collimators into the valley regions was found negligible in this study. It should be kept in mind however, that Monte Carlo simulations also rely on necessary simplifications. Surfaces in the collimator are not perfectly plane and there may be sedimentations of atoms and molecules on the surface of the absorber material. An unpublished chemical analysis of the collimator surface revealed significant amounts of copper. Furthermore the fabrication of the MSC leads to variations from beam to beam – although they have drastically improved in recent years [11]. Certain interactions are not incorporated in Monte Carlo simulations. For example diffraction and interference at crystalline structures in the collimator or total external reflection. The refractive index of absorber materials for electromagnetic waves in the x-ray range is slightly smaller than one.

$$n = 1 - \delta - i\beta \tag{2.30}$$

Where β is the absorption and δ the refractive part of the complex refractive index. δ is very small. The measurement of the refractive index is difficult. The imaginary part β can, however, be derived from the photoelectric absorption. Real and imaginary part of the refractive index are related to each other by the Kramers-Kronig relation. Kuznetsov [65] calculates by these means $\delta = 1.27 \cdot 10^{-6}$ at 50 keV and $\delta = 3.20 \cdot 10^{-7}$ at 100 keV photon energy. The critical angle of

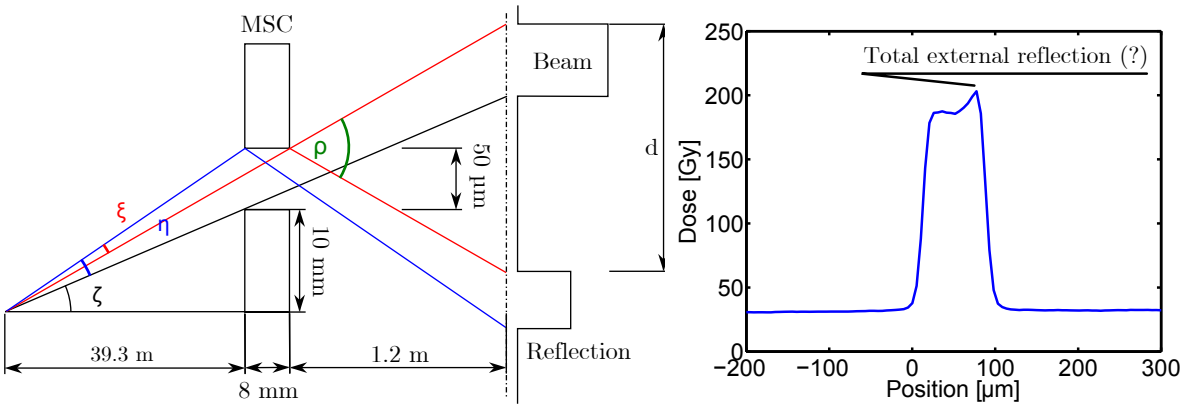

Figure 2.14 – Left: Geometry of the beam incidence to a 50 μm wide slit of the MSC at the edge of a 20 mm wide MRT field. The sketch is not in scale. Right: Film dosimetry of a single 100 μm wide beam. The dose elevation at the beam edge could originate from total external reflection.

total external reflection can be obtained from the Snellius refraction laws,

$$\cos x \approx 1 - \frac{x^2}{2} = 1 - \delta \tag{2.31}$$

where x is the angle between the beam and its projection onto the surface. At 50 and 100 keV the critical angles are 2.3 and 0.8 mrad. This is much higher than the beam divergence angle at the field edges as can be inferred from figure 2.11B. Consequently the synchrotron beams that are hitting the wall of the collimator slits are reflected. We assume for now ideally plane surfaces. What is the effect of these reflections and how do they contribute to the dose? Let us consider the geometry presented in figure 2.14 (left) for a beam at the edge of a 20 mm wide MRT field. For this aperture the beam grazing the inside edge of the collimator and the axis of the synchrotron beam form an angle ζ of 0.254 mrad. In the beams eye view the aperture appears under an angle of $\eta = 1.27$ μrad and the outside edge of the collimator under an angle of $\xi = 0.052$ μrad. This would mean that about 4.1% of the photons reaching this slit are reflected. The position of the reflection can be calculated relative to the outside edge of the beam in the phantom which is in approximately 1.2 m distance from the MSC. The angle ρ is given by

$$\rho = 2 \cdot (\zeta + \eta - \xi) \approx 0.510 \text{ mrad} \tag{2.32}$$

and hence the distance d is approximately 611 μm. The reflection is located outside the beam itself.

However, these reflections have not been observed in dosimetry of MRT fields. The reason is presumably the rough surface of the collimator walls. Similar to light reflected on a rough surface the reflection will be diffuse. Moreover bumps in the surface may increase the incidence angle of the beam towards the surface and therefore the reflected beam intensity may be even less than the predicted 4.1%. Total external reflection will hence to some extend increase the dose in peak and valley and therefore reduce the PVDR.

Although no reflections were observed in the dosimetry of MRT fields we detected an effect when measuring output factors which will be a topic in chapter 4. In these measurements a single aperture was positioned as accurately as possible on the axis of the synchrotron beam. The profile of such a 100 μm wide beam is presented in figure 2.14. On the right side of the beam there is a dose elevation between 5 and 9% of the peak dose observable. The asymmetry is very likely caused by a slight tilting of the collimator. A deviation of 1 μrad is sufficient to cause this kind of asymmetric response and a collimator wall which is located just 100 μm off-axis (perfect parallel alignment) will cause a displacement between reflection and primary beam of about 6

μm. It will be very hard to predict the effect of total external reflection because information on the exact collimator surface quality is necessary. Therefore dose measurements will remain indispensable for the benchmarking of dose calculation methods.

Synchrotron radiation is polarised. The Compton scattering cross section depends on the polarisation state of the primary photon and therefore dose absorption is not isotropic for polarised beams. Especially outside the radiation field in the region of scattered photons the polarisation leads to up to 40% dose differences as compared to unpolarised beams. However, inside the microbeam and therefore in the therapeutically most relevant region we were able to show that the effect of the polarisation is less than 3% for the valley and negligible for the peak doses. Therefore PVDRs may be calculated without regarding the photon polarisation. The phase space model has a much higher influence on the dose calculation. Ignoring the phase space information leads to deviations of approximately 10%. This is important for the interpretation of previous preclinical treatments of animals. Dose calculations that assumed ideal microbeams and neglected photon polarisation differ by less than 15% from the simulations presented here. In view of the high biological uncertainties this is probably not a matter of concern when the data is used as a basis for the first veterinary trials. For human clinical trials, the dose differences outside the radiation field must be correctly taken into account including the polarisation effects, since the dose must be determined accurately for the normal tissue and organs at risk (OAR).

Chapter 3

Dose calculation in MRT

3.1 Introduction

Dose calculation is an important component in therapy planning. The absorbed dose is a surrogate for quantification of tissue tolerance and tumour control. Although the dose response of tumours and normal tissue in MRT is not known it is evident that applied therapy doses crucially determine the therapy outcome. The peak doses are supposed to decide on tumour control whereas valley doses influence the survival of normal tissue.

As it has become clear in the last chapter, beam properties in MRT differ from those in conventional radiotherapy. In this chapter we develop different dose calculation approaches for MRT and integrate them into an existing treatment planning system (TPS). The chapter starts off with some general considerations on dose absorption in MRT. In section 3.2 a slow but relatively accurate Monte Carlo dose calculation algorithm is presented which is integrated into the TPS. Furthermore an alternative, faster Monte Carlo method is presented which places, however, certain demands on the phantom geometry. In section 3.3 we discuss significantly faster but less accurate point kernel methods which are also incorporated into the TPS.

Dose planning is based on the information provided by CT images. Different materials in the organism have different radiological properties and are represented by different Hounsfield Units (HU) in the CT. The conversion of the CT-data into material parameters has of course an important influence on the dose computation. The conversion algorithm and its uncertainties are presented in section 3.4.

In section 3.5 we show some example dose calculations and compare the accuracy of the different calculation methods. We cease the chapter with some final conclusions and remarks.

3.1.1 Physics of dose absorption in MRT

The photon energy spectrum in the current filter set-up for MRT is depicted in figure 2.11D. Between 45 and 175 keV the spectrum has an intensity above 10% of the peak intensity at 80 keV. In this energy range photons interact via Compton scattering, photoelectric absorption and Rayleigh scattering. The interaction probability of these processes depends on both, energy and material composition. At low energy photoelectric absorption becomes dominant and at high energy photons mainly interact via Compton scattering. Rayleigh scattering plays a minor role.

In *photoelectric absorption* an electron in the atomic shell of an atom absorbs the energy of the photon completely. The photon energy is much higher than the binding energy of the electron. Energy in excess of the binding energy is transformed into kinetic energy of the electron. If a photon of energy E_0 interacts with a free electron via *Compton scattering* it transfers a part of its energy to the electron and scatters off with an energy $E < E_0$. The energy fraction transferred to the electron is determined by momentum and energy conservation (compare equation 2.16). For

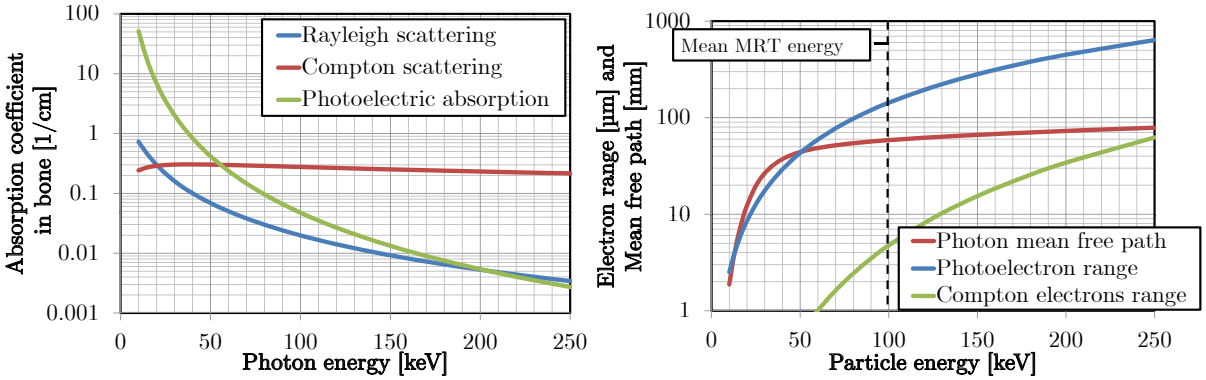

Figure 3.1 – The graph on the left shows the scattering/absorption coefficients for Compton scattering, Rayleigh scattering and photoelectric absorption in bone [source: Berger et al. [64]]. On the right the mean free path in mm for photons is drawn over the photon energy. It is defined as the average distance a photon travels without interacting. The graph shows the CSDA ranges in μm of Compton and photoelectrons as well.

photons in the relevant energy range this fractions is pretty low between 7 and 20%. The fraction increases with energy. The scattered Compton photon may interact again. While photoelectric effect and Compton effect produce secondary electrons, no secondary particles are created in *Rayleigh scattering*. The photon only changes its direction. The absorption and scattering coefficients of these three processes in compact bone are presented in figure 3.1 (left).

The total absorption coefficient of a 100 keV photon beam is much higher than that of MeV photon beams commonly used in conventional radiotherapy treatment where photons are produced in linear accelerators (so called linacs). The average mean free path depth of a photon beam is therefore much lower. In figure 3.1 the mean free path, defined as the average distance a photon travels without interacting, is plotted against the photon energy. While the photon mean free path slowly increases with energy above 40 to 50 keV, there is a strong drop of mean free path with decreasing energy below 40 keV. This is due to the strength of photoelectric absorption at these energies. The photoelectric absorption coefficient possesses a strong energy dependence,

$$\mu_{Ph} \sim E^{-3.27}. \tag{3.1}$$

Electrons produced in primary photon interactions can lose their energy by collisions and radiation. Unlike photons, charged electrons frequently interact with the electric fields of the atoms. At energies below 1 MeV Coulomb scattering is the dominant interaction process. In each interaction just a small fraction of the kinetic energy is transferred to shell electrons in the atoms. However, the frequency of these interaction leads to a rapid slowing down. In interactions with the electric field of the atomic nucleus or shell electrons, secondary electrons may also produce "bremsstrahlung". This radiative energy loss of electrons at around 100 keV kinetic energy is extremely low and can usually be neglected. The electron range is in the order of a few tens of micrometre.

On the one hand the range of secondary electrons at an energy of around 100 keV is a few micrometres. On the other hand the mean free path length of photons is in the order of several centimetres. That means photons travel larger distances without scattering and produce in interactions secondary electrons that are absorbed rather locally. Electrons transfer the energy to the medium and are responsible for the majority of ionisations. The peak dose in an MRT field has a width of just a few microns. Hence the peak dose is built up by electrons produced in interactions of the primary photon beam. We define the order of energy absorption by the number of photon interactions prior to the interaction that created the secondary electron. That means the peak dose is built up by 0^{th} order absorption. If a secondary electron is produced in a photoelectric absorption its energy will be approximately equal to that of the primary photon,

whereas if the electron is produced in a Compton process its energy will be 5 to 20% of the primary photon energy. The range of a Compton electron will therefore be much shorter than that of a photoelectron.

The range of secondary electrons is crucial for high dose gradients between peak and valley regions. The lower the energy of the photons and thus the energy of secondary electrons the steeper is the beam penumbra region. However, the lower the photon energy the smaller gets the photon mean free path. The spectrum in MRT is a trade-off between high photon mean free path and narrow beam penumbras. This is illustrated for water in figure 3.1 (right). The red curve is the photon mean free path. The blue curve represents the photoelectron and the green curve the Compton electron CSDA range. The currently used spectrum has a mean energy of 100 keV. The range of photoelectrons is approximately 150 μm and the photon mean free path has a length of around 6 cm. However, at 100 keV photoelectrons are just of minor importance in water and Compton electrons have a much lower range of approximately 5 μm. Therefore it could be considered to move the spectrum towards higher energies. At 200 keV photon energy the Compton electron range is 25 μm. This should still be small enough for 50 μm wide microbeams. The photon mean free path would be increased by about 25%. Another advantage of going to slightly higher energies is the energy transfer to Compton electrons. The higher the photon energy the higher the energy fraction transferred to Compton electrons. This would increase the ratio of primary energy absorption which builds up the peak dose to the scattered photon absorption which is responsible for the valley dose.

3.2 Dose calculations based on Monte Carlo simulations

3.2.1 Challenges for Monte Carlo techniques in MRT

Monte Carlo algorithms solve numerical problems with random numbers and are widely used for the simulation of radiation transport but also for other applications. In radiation transport Monte Carlo methods treat each particle track as a sequence of stochastic processes, where random numbers determine path lengths, scattering angles etc.. Averaging over many particle tracks allows the estimation of measurable quantities, as for example the dose. The outcome is not exact but deviates with a certain probability from the correct result.

"All problems solved by Monte Carlo are essentially equivalent to integrations."[i] This surprising statement can be understood from the following considerations. Any quantity Q that is computed in Monte Carlo simulations is a function of a certain number N of random numbers $r_1, r_2, ..., r_N$. Without loss of generality these numbers can be assumed to be uniformly distributed. Any other distribution can be obtained by applying transformation rules. Thus $\langle Q \rangle$ is an estimation of the N-dimensional integral

$$\langle Q \rangle = \int_0^1 \int_0^1 \dots \int_0^1 Q(r_1, r_2, \dots, r_N)\, dr_N \dots dr_2\, dr_1. \tag{3.2}$$

Monte Carlo techniques are especially useful in solving high dimensional integrals. The relative error F made by Monte Carlo simulations is proportional to

$$F \sim \frac{\sigma}{\mu\sqrt{M}} \tag{3.3}$$

where M is the number of particle histories, σ the standard deviation and μ the expectation value of a single simulation.

[i] Lux and Koblinger [66], chapter 4, p. 81

There are two main challenges for Monte Carlo techniques in MRT dose calculations. The first challenge is the rapid spatial variation in the dose. Voxel sizes have to be smaller than 5 μm perpendicular to the microbeam planes in order to describe beam penumbras, valley and peak doses accurately. Such small voxels increase the standard deviation σ in equation 3.3. The probability that a particle hits the detector volume is very unlikely. If the volume is hit, the produced dose in this event D_{event} is very high because the voxel volume V_{voxel} is small.

$$D_{\text{event}} = \frac{E}{V_{\text{voxel}}} \tag{3.4}$$

If we consider a Bernoulli process and only look at the probability for the events "voxel hit" p and "voxel not hit" (1-p) then we obtain for the ratio of the standard deviation σ_B to mean μ_B

$$\frac{\sigma_B}{\mu_B} = \sqrt{\frac{1-p}{p}} \approx \sqrt{\frac{1}{p}}. \tag{3.5}$$

For the last approximation it was assumed that $p \ll 1$. The probability for a hit is inversely proportional to the voxel size

$$p \sim \frac{1}{V_{\text{voxel}}}. \tag{3.6}$$

Although the radiation transport is more complicated than a Bernoulli process, we should expect that the ratio σ/μ is more or less proportional to $\sqrt{V_{\text{voxel}}}$. If the voxel size in one dimension is decreased from 1 mm to 5 μm 200 times more particle histories need to be simulated in order to keep the relative simulation error F in equation 3.3 constant. That means a 200 times longer calculation time. If we now also want to compute the dose distribution for an MRT multiport exposure where we require 5 μm voxel side lengths in all three dimensions the number of simulated particle tracks needs to be increased by a factor of $8 \cdot 10^6$. It becomes evident that straightforward Monte Carlo simulations are not reasonable. Apart from the simulation time there is also the problem of data storage and finally visualisation.

The second challenge in MRT is the high dynamic range of doses. Both, peak and valley doses have to be accurately determined, that differ in a factor of 20 or more. In order to achieve a low statistical uncertainty in the valley region, simulations need to precisely predict low scattered dose effects. If in conventional dose calculations 5% accuracy of the maximum dose is required, this means in the MRT valley dose calculation a maximum of 5% uncertainty in an anyhow small scattered dose contribution of 5% or less.

How can we solve these problems? In this section two strategies are pursued that both reduce the ratio $\frac{\sigma}{\mu}$ in equation 3.3. The first approach constrains the information extracted from the simulation and is described in chapter 3.2.2. It is useful to think again about the essential quantities required for treatment planning. Most experiments suggest that the peak dose and the valley dose (or the peak to valley dose ratio, PVDR) are the quantities that decide upon therapy success. A high peak dose is supposed to be crucial for tumour ablation and a low valley dose presumably ensures normal tissue sparing. We therefore developed a Monte Carlo simulation tool that calculates an average peak and an average valley dose on the voxel-grid of a CT.

The second approach artificially increases the scoring volume by partially inverting source and detector geometry. This will be presented in chapter 3.2.3. Unfortunately this approach does only work with certain phantom geometries and is therefore not suitable for dose calculations in general.

3.2.2 Forward Monte Carlo simulations

Monte Carlo simulations were set up in Geant4 version 9.5. The calculations were performed with the interaction models of the Livermore polarised physics libraries. Cut-off ranges for

electrons were set to 1 μm. Activated photon interactions are Compton scattering, photoelectric absorption, Rayleigh scattering and also pair production – although the latter process does not occur at energies below 1 MeV. For electrons multiple electron scattering, ionisations and the production of bremsstrahlung are taken into account.

Set-up of the detector geometry

In Geant4 materials, objects and detectors are defined in a class derived from the class G4UserDetectorConstruction. There elements and compounds can be defined and various tools exist to describe geometries and to align objects. The set of all objects is called the detector. Materials that are assigned to objects in the detector have to be predefined in the storage. Therefore the number of definable materials N_{mat} is limited and is predefined in the beam set-up text file.

The simulation reads in the Hounsfield units (HU) from the CT file, the voxel size and voxel number of the CT. The maximum and the minimum HU values in the CT data is determined. Within these limits equally spaced HU-intervals $I_1, \ldots, I_{N_{mat}}$ are defined according to the number of materials N_{mat}. Each interval is assigned to a material. The necessary material properties mass density and elemental mass fractions of hydrogen, carbon, nitrogen, oxygen, phosphorous and sodium are calculated from the mean HU value of the interval following the method of Schneider et al.[45] (see chapter 3.4).

The detector is set up as a three dimensional array of voxels. Each voxel gets the material definition according to the HU interval it belongs to. The reference system Σ is equivalent to the patient or treatment planning system (x: right-left, y: anterior-posterior, z: head-foot). Each voxel is used as a sensitive volume.

Beam configuration

Whereas the MC simulation is performed in the reference system of the CT-image Σ, the radiation source is defined in a beam reference frame Σ_S spanned by the three pairwise orthogonal unit vectors $\vec{e}_{x_s}$, $\vec{e}_{y_s}$ and $\vec{e}_{z_s}$. This reference frame is at the same time the laboratory frame in which the beam propagates along $\vec{e}_{z_s}$ and the microbeams are parallel to $\vec{e}_{x_s}$. The origin of the reference system is the fixed isocentre of the beam in the patient. This is at the same time the invariant point for all rotational motions of the goniometre motors. Neglecting beam-air interactions, the z-position of the source in Σ_S is not as important, since we assume parallel beams in the source model presented in chapter 2. The patient and laboratory system (Σ and Σ_S) are illustrated in figure 3.2 (left).

The photon source was simulated according to the model developed in chapter 2. The beam width and the ctc were set to 51.5 μm and 412.3 μm, respectively. The photon trajectories start at

$$\begin{aligned} x_s &= W_F^x \cdot (r - \tfrac{1}{2}) \\ y_s &= n_{beam} \cdot \mathrm{ctc} - \tfrac{W_F^y}{2} + q \cdot w \\ z_s &= -d \end{aligned} \tag{3.7}$$

and point into the positive z_s-direction. Here W_F^x, W_F^y are the field sizes in x and y, w the beam width and ctc the beam spacing. q and r are random numbers generated from an uniform distribution with $0 \leq q, r \leq 1$. The number of the beam n_{beam} is selected randomly according to the fluence profile $I = I_0(1 - \alpha y_s^2 - \beta|y_s|)$. This profile can be interpreted as a probability density function $f(y_s)$,

$$f(y_s) = \begin{cases} \dfrac{1-\alpha y_s^2-\beta|y_s|}{\int_{y=-W_F^y/2}^{y=W_F^y/2} 1-\alpha y^2-\beta|y|\, dy} & \text{for } -\frac{W_F^y}{2} < y_s < -\frac{W_F^y}{2} \\ 0 & \text{otherwise} \end{cases} \tag{3.8}$$

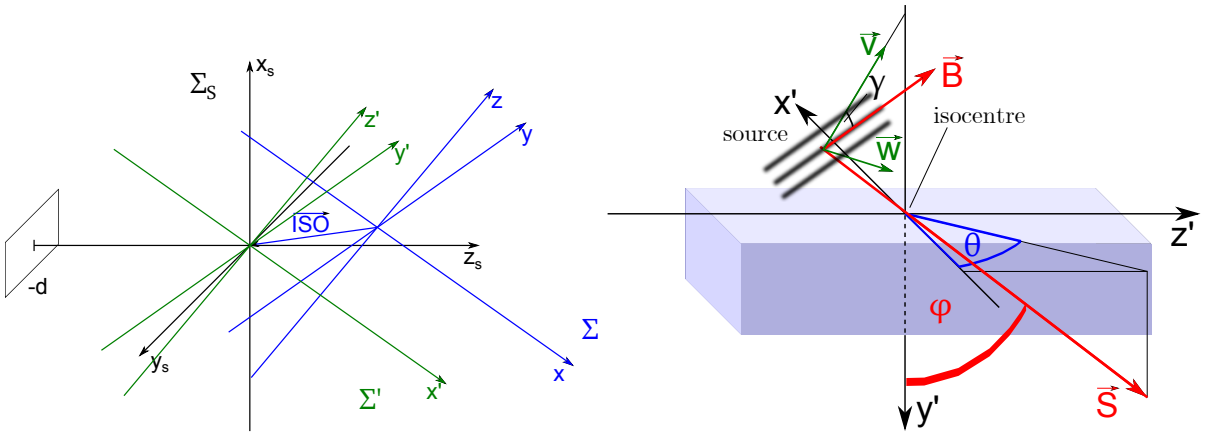

Figure 3.2 – Left: The laboratory system Σ_S, the CT or patient system Σ and the system Σ' which is obtained by translating Σ along the vector $\vec{ISO}$. The origin of Σ_S and Σ' is the beam isocentre. The beam origin in Σ_S is set at $z_s = -d$. Right: The patient system with gantry angle ϕ, couch angle θ and collimator angle γ is shown.

With the corresponding cumulative distribution function

$$F(y_s) = \frac{y_s - \text{sign}(y_s)\frac{b}{2}y_s^2 - \frac{1}{3}y_s^3 + \frac{W_F^y}{2} - b\frac{W_F^{y\,2}}{8} - \frac{aW_F^{y\,3}}{24}}{W_F^y - \frac{bW_F^{y\,2}}{4} - \frac{aW_F^{y\,3}}{12}}, \text{ for } -\frac{W_F^y}{2} \leq y_s \leq \frac{W_F^y}{2} \tag{3.9}$$

it is possible to generate random numbers that follow the intensity profile with the inverse-transform method (see for example Salvat et al.[56] or Ahrens and Dieter[67]): If ξ is a uniform random variable in $[0, 1]$, then the random variable

$$\eta = F^{-1}(\xi) \tag{3.10}$$

follows the distribution described by the probability density function f. The beam number n_{beam} is therefore selected as the integer number that is closest to[ii] $(\eta/\text{ctc} + W_F^y/2)$.

We also use the inverse-transform method to choose the photon energies from a spectrum which is given as intensities $I(E_i)$ at discrete energies $E_1, \ldots, E_N$ in ascending order (i.e. $E_i > E_j$ for $i > j$). The cumulative distribution function at the discrete energies is given by

$$F(E_i) = \sum_{n=1}^{i} I(E_n) / \sum_{n=1}^{N} I(E_n); \tag{3.11}$$

for all other values, $F(E)$ is linearly interpolated.

The leakage photon flux is 0.001 of the primary beam. Therefore a fraction of

$$0.001 \cdot \frac{ctc - w}{w} \tag{3.12}$$

of the photons is simulated to originate from points between the microbeams with a different energy distribution given by the leakage spectrum (see chapter 2). The distribution in x_s is uniform and the distribution in y_s follows the profile $(1 - \alpha y_s^2)$. The coordinates y_s are again sampled with the inverse-transform method.

[ii] Strictly speaking this is an approximation, because the fluence is averaged over a 400 μm wide range around the beam and not just the beam itself. However, it should be kept in mind that the position of the microbeams is anyway not precisely known and presents an experimental uncertainty.

Coordinate transformations

The simulations are performed in the patient reference system. Therefore all vectors of the laboratory frame have to be transformed into the patient system. The necessary information are provided in the VIRTUOS plan file. They are stored in the plan file as gantry angle ϕ, couch angle θ, collimator angle γ and the coordinates of the isocentre $\overrightarrow{\text{ISO}}$ in the patient system. These are the typical parameters in conventional radiotherapy and they are shown in figure 3.2 (right) in a system Σ' which is obtained by translating the patient reference system Σ along the vector $\overrightarrow{\text{ISO}}$ (figure 3.2, left). Gantry and couch angle define the beam direction $\vec{S}$ in Σ'

$$\vec{S} = \begin{pmatrix} -\sin\phi\cos\theta \\ \cos\phi \\ \sin\phi\sin\theta \end{pmatrix}. \tag{3.13}$$

The collimator angle γ describes the tilting of the microbeam direction $\vec{B}$ to the vector $\vec{v}$. $\vec{v}$ is perpendicular to $\vec{S}$ and lies in a plane spanned by the y'-axis and $\vec{S}$. Its representation in the system Σ' is given by

$$\vec{v} = \begin{pmatrix} -\cos\phi\cos\theta \\ -\sin\phi \\ \cos\phi\sin\theta \end{pmatrix}. \tag{3.14}$$

With the vector $\vec{w} = \vec{v} \times \vec{S}$ the microbeam direction can be written as

$$\vec{B} = \cos\gamma\ \vec{v} + \sin\gamma\ \vec{w}. \tag{3.15}$$

The vectors $\vec{B}$ and $\vec{S}$ form the coordinate vectors $\vec{e}_{x_s}$ and $\vec{e}_{z_s}$ of the beam reference system Σ_S. The missing vector $\vec{e}_{y_s}$ is chosen such that the vectors $\vec{e}_{x_s}$, $\vec{e}_{y_s}$ and $\vec{e}_{z_s}$ form a right handed system. Therefore the coordinate matrix M of these three vectors in the reference system Σ' (and also in Σ) is

$$\begin{aligned} M &= (\vec{e}_{x_s}, \vec{e}_{y_s}, \vec{e}_{z_s}) \\ &= \begin{pmatrix} -\cos\phi\cos\theta\cos\gamma + \sin\theta\sin\gamma & \sin\theta\cos\gamma + \cos\phi\cos\theta\sin\gamma & -\sin\phi\cos\theta \\ -\cos\gamma\sin\phi & \sin\phi\sin\gamma & \cos\phi \\ \cos\phi\sin\theta\cos\gamma + \sin\gamma\cos\theta & \cos\theta\cos\gamma - \cos\phi\sin\theta\sin\gamma & \sin\phi\sin\theta \end{pmatrix} \end{aligned} \tag{3.16}$$

The transformation of a vector $\vec{r}_s = (x_s, y_s, z_s)$ in the beam reference system Σ_S into the vector $\vec{r}$ in the patient reference system is therefore described by

$$\vec{r} = M\vec{r}_s + \overrightarrow{\text{ISO}} = x_s\vec{B} + y_s(\vec{S} \times \vec{B}) + z_s\vec{S} + \overrightarrow{\text{ISO}} \tag{3.17}$$

Scoring of peak and valley doses

Dose is scored in voxelised structures based on the CT-grid. Since the microbeams are usually smaller than the voxel size, dose accumulation has to be separated into a peak and a valley part. To achieve this the interaction point $\vec{P}$ is transformed into the beam reference frame by projecting onto the vector $\vec{e}_{x_s}$, $\vec{e}_{y_s}$ and $\vec{e}_{z_s}$,

$$\begin{aligned} x_s &= <\vec{e}_{x_s}, \vec{P}>, \\ y_s &= <\vec{e}_{y_s}, \vec{P}>, \\ z_s &= <\vec{e}_{z_s}, \vec{P}>. \end{aligned} \tag{3.18}$$

The absorbed energy is assigned to the peak if the interaction occurred in a microbeam path and it is assigned to the valley if the interaction occurred in the central 80% of the inter-beam region,

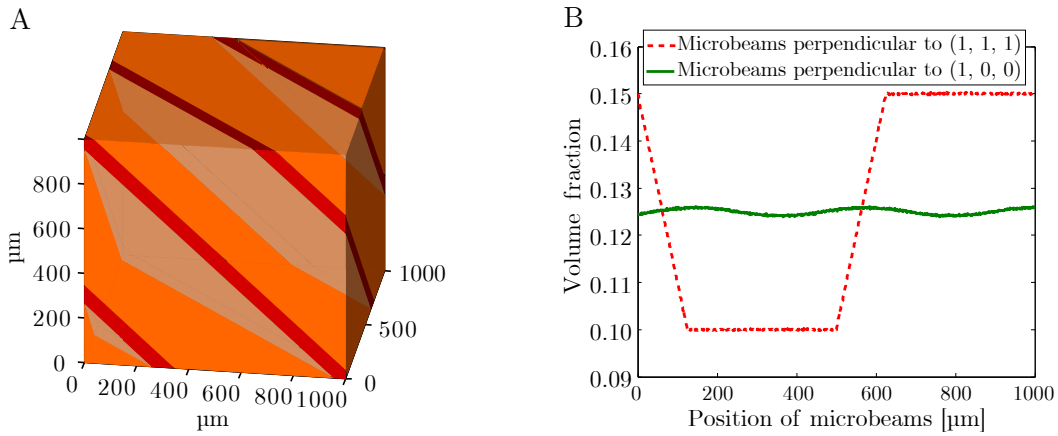

Figure 3.3 – Figure (A): Microbeams intersperse the voxels in the Monte Carlo dose calculation and cut out a certain volume. As an example figure (B) shows the volume fraction for microbeams that are perpendicular to the x-axis and microbeams that are perpendicular to direction $(1, 1, 1)$ as illustrated in (A). The calculation was done for a ctc of $400\,\mu m$ and a beam width of $50\,\mu m$.

avoiding the microbeam penumbras. Furthermore, in order to calculate the dose, the volume V is required for

$$D = \frac{E}{V\rho}, \tag{3.19}$$

where ρ is the mass density of the voxel material. The peak and valley volume in a voxel depend on the size, orientation and position of the voxel in the microbeam field. The problem is visualised in figure 3.3A. The geometric problem is complex and involves an extensive case-by-case analysis. We therefore opted for a numeric, Monte Carlo based volume determination.

All voxels of the CT are equally oriented. In other words the direction of the microbeam incidence is for all voxels the same. For a given irradiation geometry the peak or valley volume fraction depends on the voxel position perpendicular to the microbeam planes modulo ctc only. In the beam reference system this is given by the y_s-coordinate modulo ctc. Figure 3.3B shows the beam volume fraction of a $1{\times}1{\times}1$ mm^3 voxel for two beam directions, a ctc of 400 μm and a beam width of 50 μm. The volume fractions were calculated by randomly choosing points in the voxel from a uniform distribution. The relative number of points that fall inside a microbeam path is a measure for the volume fraction of the peak region. In a similar way the valley volume is estimated.

In the just described scoring peak and valley doses are defined as averages over a certain volume. There are of course other ways to define peak and valley doses. Unfortunately there is no generally agreed definition of peak and valley dose. This has to be regarded when comparing the simulations with measurements and calculations of others.

3.2.3 Semi-adjoint Monte Carlo simulations

Introduction to adjoint Monte Carlo methods

In MRT dose estimates have to be made for very small detector volumes. This is problematic for Monte Carlo simulations because the energy scored in small volumes is low and the statistical noise for the dose in this volume is high. In order to resolve the structure of microbeams classical forward Monte Carlo simulations require a huge amount of particle histories. This leads to long calculation times.

In this chapter a section is presented that circumvents this problem by partly exchanging the detector and the source geometry. It is based on the well-established adjoint Monte Carlo

techniques. These methods have another advantage: The simulation of various source geometries can be handled more efficiently. Whereas studies on source parameters require a repetition of the entire simulation in forward Monte Carlo simulations they can often be performed with a single simulation using adjoint Monte Carlo approaches. One typical example where this is advantageous is the calculation of output factors (see chapter 4).

In the theory of Monte Carlo simulations and partial differential equations, problems with small detector volumes or varying sources are often treated in their adjoint form [68,69]. The idea is that in the adjoint representation of the problem detector and source exchange their position. In this context detector and source have to be understood as pay-off or source functions in the 6 dimensional particle phase space consisting of three spatial and three motion (e.g. momentum) dimensions.

As mentioned before all problems solved by Monte Carlo simulations are essentially equivalent to integrations [70]. For particle transport Monte Carlo calculations integrate the Boltzmann transport equation

$$\vec{\Omega}\vec{\nabla}\Phi^i(\vec{r},\vec{E}) + \Sigma_T^i(\vec{r},\vec{E})\Phi^i(\vec{r},\vec{E}) = S^i(\vec{r},\vec{E}) + \sum_j \int d\vec{E}'\Sigma_S^{ij}(\vec{r},\vec{E}',\vec{E})\Phi^j(\vec{r},\vec{E}') \tag{3.20}$$

(integro-differential form). In this equation $\vec{\Omega} = (\sin\theta, \cos\theta\cos\phi, \cos\theta\sin\phi)$ is the directional vector, Φ^i the flux of particles, S characterises the field of particle sources, Σ_T^i and Σ_S^{ij} determine the particle transport and scattering in the phase space. The vector $\vec{E}$ describes the motion of the particles and consists of $\vec{E} = (E, \phi, \theta)$. The superscript indices indicate the particle type. For low energy photon interactions it may denote photons and electrons. Particles may convert into each other. Therefore the scattering term includes a matrix Σ_S^{ij} coupling the fluxes of different particles to each other. In the following we simplify the notation and skip the superscripts. The particle flux Φ for low energy photon transport can, however, be regarded as a two component vector including photons and electrons[iii]. Therefore we write

$$\vec{\Omega}\vec{\nabla}\Phi(\vec{r},\vec{E}) + \Sigma_T(\vec{r},\vec{E})\Phi(\vec{r},\vec{E}) = S(\vec{r},\vec{E}) + \int d\vec{E}'\Sigma_S(\vec{r},\vec{E}',\vec{E})\Phi(\vec{r},\vec{E}'). \tag{3.21}$$

Instead of solving the forward Boltzmann transport equation, it is also possible to consider the adjoint flux Φ^*. For this purpose we may rewrite equation 3.21 as an operator equation in the form

$$\left[\vec{\Omega}\vec{\nabla} + \Sigma_T(\vec{r},\vec{E}) - \int d\vec{E}'\Sigma_S(\vec{r},\vec{E}',\vec{E})\right]\Phi = S(\vec{r},\vec{E}). \tag{3.22}$$

Scoring of a physical quantity J in Monte Carlo simulations corresponds to calculating the scalar product of the flux Φ with a pay-off detector function D,

$$J(\Phi) = \int d\vec{E}\int d\vec{r}\,\Phi(\vec{r},\vec{E})D(\vec{r},\vec{E}) = \langle D,\Phi\rangle \tag{3.23}$$

For a simple scorer in space with density ρ and scoring volume V_S the function D would have the representation

$$D(\vec{r},\vec{E}) = \begin{cases} E_{Abs}/(\rho V_S) & \vec{r}\in V_S \\ 0 & \vec{r}\notin V_S \end{cases} \tag{3.24}$$

As shown by Marchuk [68] this problem can be reformulated into its adjoint representation. Consider the operator equation

$$A\Phi = S, \tag{3.25}$$

[iii] i.e the source is then also a two component vector, Σ_S is a 2×2 matrix and Σ_T a diagonal 2×2 matrix.

where we are interested in the scalar product

$$J = \langle D, \Phi \rangle \,. \tag{3.26}$$

If we then consider the equation with the adjoint operator A^* for a function Ψ^*

$$A^* \Psi^* = D \tag{3.27}$$

then we realise that

$$J = \langle D, \Phi \rangle = \langle A^* \Psi^*, \Phi \rangle = \langle \Psi^*, A\Phi \rangle = \langle \Psi^*, S \rangle \,. \tag{3.28}$$

Equation 3.27 is called the adjoint equation to 3.25. The adjoint of the Boltzmann transport equation reads

$$\left[-\vec{\Omega}\vec{\nabla} + \Sigma_T^*(\vec{r}, \vec{E}) - \int d\vec{E}' \Sigma_S(\vec{r}, \vec{E}, \vec{E}') \right] \Psi^* = D(\vec{r}, \vec{E}), \tag{3.29}$$

$$J = \langle \Psi^*, S \rangle \,. \tag{3.30}$$

In these two equations source and detector are exchanged. Equation 3.29 is solved once for a certain detector geometry. To that end particles are tracked backwards in time from the detector to the source. Afterwards the quantity J can be determined by simply computing the scalar product between the source function S and the adjoint flux Ψ^*. A small detector volume $D(\vec{r}, \vec{E})$ does not negatively influence the solution of equation 3.29 with Monte Carlo techniques. As long as the source function S covers a sufficiently large phase space volume this adjoint equation can even provide Monte Carlo solutions for a point-like detector.

On the one hand, in MRT dose needs to be scored in a very small geometrical volume since dose is changing on a micrometre scale. On the other hand there are no constraints on the energy and angular dimensions for the detector. The detector scores particles independently of the direction they are coming from and independent of their energy.

For the source this is the other way around. The source volume is comparably large perpendicular to the beam; but the constraints on the angles ϕ and θ are high since the beams are extremely parallel. In this sense both, the forward and the adjoint Monte Carlo simulation face the problem of small detector volumes in the phase space: Small in the spatial directions for forward Monte Carlo simulations and small in the directional dimensions for the adjoint Monte Carlo simulations. Instead of exchanging source and detector in all phase space dimensions it would be favourable to exchange just some dimensions of the source and detector in order to increase the scoring volume in the simulation.

Extension of the adjoint Monte Carlo method

Let us consider the irradiation geometry given in a coordinate system with the x-axis pointing in the direction of the parallel beams and the y- and z-direction perpendicular to the beam (Figure 3.4A). θ is the angle between a particle trajectory and the x-axis. ϕ denotes the angle between the projected trajectory in the y-z-plane and the y-axis. If in the y-z-plane the size of the source is large and the detector size small it would be useful to have a semi-adjoint method that adjoints the Boltzmann equation only in the y-z-plane. Especially if the phase space volume of the source in other dimensions is small a complete adjoint calculation has disadvantages.

We describe a solution of this problem in the situation of a phantom which is homogeneous in y and z and we assume that the radiation source can be described in phase space as

$$S(\vec{r}, \vec{E}) = \delta(x) f_S(y, z) \frac{1}{2\pi \sin\theta} \delta(\theta) f_E(E) = s(x, \vec{E}) f_S(y, z). \tag{3.31}$$

A B

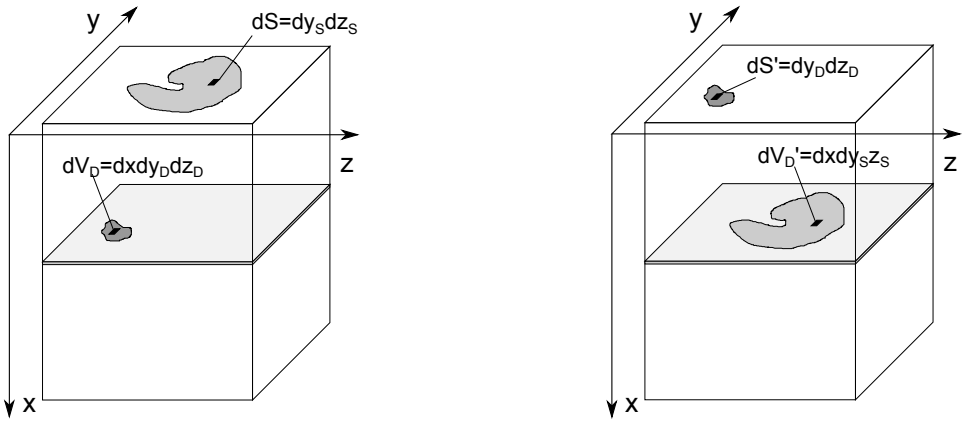

Figure 3.4 – The forward geometry (A) and semi-adjoint geometry (B) are illustrated.

$f_s(y,z)$ describes the aperture of the source or collimator, $f_E(E)$ characterises the spectrum of the source. S integrates over the phase space to 1. The detector can be written as

$$D(\vec{r},\vec{E}) = \Delta(x - x_D) f_D(y,z) = d(x,\vec{E}) f_D(y,z). \tag{3.32}$$

f_D describes the geometry of the detector in the y-z-plane. The function $\Delta(x)$ is the detector shape in the direction of the primary beam. For a scoring mesh Δ will typically look like

$$\Delta(x) = \begin{cases} 1/d & -d/2 < x < d/2 \\ 0 & \text{otherwise} \end{cases}. \tag{3.33}$$

It is now possible to exchange the geometry of detector and source only in y-z-coordinates and keep all other coordinates constant. The homogeneity of the material in the y-z-plane implies

$$\begin{aligned} \Sigma_T(\vec{r},\vec{E}) &= \Sigma_T(x,\vec{E}), \\ \Sigma_S(\vec{r},\vec{E}' \to \vec{E}) &= \Sigma_S(x,\vec{E}' \to \vec{E}). \end{aligned} \tag{3.34}$$

Therefore we find in equation 3.21 one operator acting on the $(x,\vec{E})$ subspace,

$$A_{x,E} = \Omega_x \frac{\partial}{\partial x} + \Sigma_T(x,E) - {}_E\langle \Sigma_S(x,E' \to E) | \tag{3.35}$$

and one operator acting on the (y,z) subspace,

$$B_{y,z} = \Omega_y \frac{\partial}{\partial y} + \Omega_z \frac{\partial}{\partial z}. \tag{3.36}$$

In equation 3.35 we have made use of the convenient bra/ket notation. Thus equation 3.22 can be rewritten as

$$(A_{x,E} + B_{y,z})\,\Phi = s(x,\vec{E}) f_S(y,z). \tag{3.37}$$

The semi-adjoint version of this equation transforms only operators and functions that act on the y-z-subspace. The semi-adjoint flux Ψ^* has to obey the equation

$$\left(A_{x,E} + B^*_{y,z}\right)\Psi^* = s(x,\vec{E}) f_D(y,z). \tag{3.38}$$

The dose or quantity J that we are interested in is then calculated in a scalar product with $d(x,\vec{E})$ and $f_S(y,z)$ (compare equation 3.28),

$$J = \left\langle \Psi^*, d(x,\vec{E}) f_S(y,z) \right\rangle \tag{3.39}$$

The geometric interpretation of the semi-adjoint equation can be seen from figure 3.4. For the same number of simulated particles the dose measured in the detector in figure 3.4A and in the inverted detector in B are going to be the same.

This can be explained by the following argumentation. Let us consider a photon leaving the source element $dS = dy_S dz_S$. This photon has the same expectation of energy absorption dE in the detector volume $dV_D = dx dy_D dz_D$ as a photon in the inverted geometry has, leaving the inverted source element $dS' = dy_D dz_D$ for the energy absorption in the inverted detector element $dV'_D = dx dy_S dz_S$ as long as $dy_S dz_S = dy_D dz_D$ and the geometry is homogeneous in y and z. More complicated detector and source geometries can be considered as composed of infinitesimally small detector and source elements. For each pair of detector and source volume element (dV_{Dj}, dS_i) the equality of energy absorption expectation holds, i.e. $\langle E(dS_i \to dV_{Dj})\rangle = \left\langle E'(dS'_j \to dV'_{Di})\right\rangle$, if each source element emits the same amount of photons. In the forward geometry the total energy absorbed by the detector is the sum over all detector elements dV_{Dj}. For each detector element the absorbed energy is the sum over contributions from all source elements dS_i. Thus obviously absorbed energy in the forward and inverted geometry is equal,

$$E = \sum_i \sum_j \langle E(dS_i \to dV_{Dj})\rangle = \sum_i \sum_j \left\langle E'(dS'_j \to dV'_{Di})\right\rangle = E' \tag{3.40}$$

It is important to note that this equality holds for the same photon fluence of the source. Or, respectively, if the number of particles is identical in both simulations the dose will be the same. The statistics is of course better with the larger detector.

Applications and results

A modified version of MRT are pencilbeam irradiations where small rectangular beams of a few micrometer side length are delivered in two dimensional arrays. The hope is to enable with this technique whole brain irradiations without a breakdown of the therapeutically important peak to valley dose ratio. First studies were done in mice by Schültke et al. [71]. In these experiments arrays of 45×21 beams sized $50{\times}50\mu m^2$ having 400 or 200 μm spacing were created at the ESRF using a step and shoot method. The dose estimations for this study were performed in this work in Monte Carlo simulations of the beams in a water phantom of $16{\times}16{\times}16\ cm^3$ side length employing semi-adjoint instead of forward Monte Carlo simulations. Simulations were carried out in the Geant4 tool set (Version 9.3 p02). The source was a point in the y-z-plane at (y_0, z_0) emitting photons in the x-direction. Energy was scored on a grid of bins sized $5{\times}5$ μm^2 in the y-z-plane and at 0.5 or 4 mm depth from the beam entrance into the phantom. 10^7 photon histories were simulated. The energy that corresponds to the energy scored in the direct simulation in a point at (y_0, z_0) is the scalar product $\langle \Psi_{y_0,z_0}(y,z), d \cdot f_S(y,z)\rangle$ which needs to be evaluated,

$$\sum_y \sum_z f_S(y,z)\Psi(y,z,y_0,z_0). \tag{3.41}$$

$\Psi_{y_0,z_0}(y,z)$ is the fluence[iv] that was created by the adjoint source positioned at y_0, z_0. Due to the homogeneity of the problem in y, z, a shift of the source is equivalent to a shift in the fluence $\Psi_{y_0,z_0}(y,z) = \Psi(y - y_0, z - z_0)$, where Ψ is the fluence with $y_0, z_0 = 0$. Therefore the energy absorption in equation 3.41 can be calculated in a convolution,

$$E(y_0, z_0) = [f_S * \Psi](y_0, z_0) \tag{3.42}$$

and can for example be efficiently evaluated in Fourier space.

[iv] While we refer to the flux φ as the particle density in phase space, the fluence Ψ denotes the number of particles passing through a certain area.

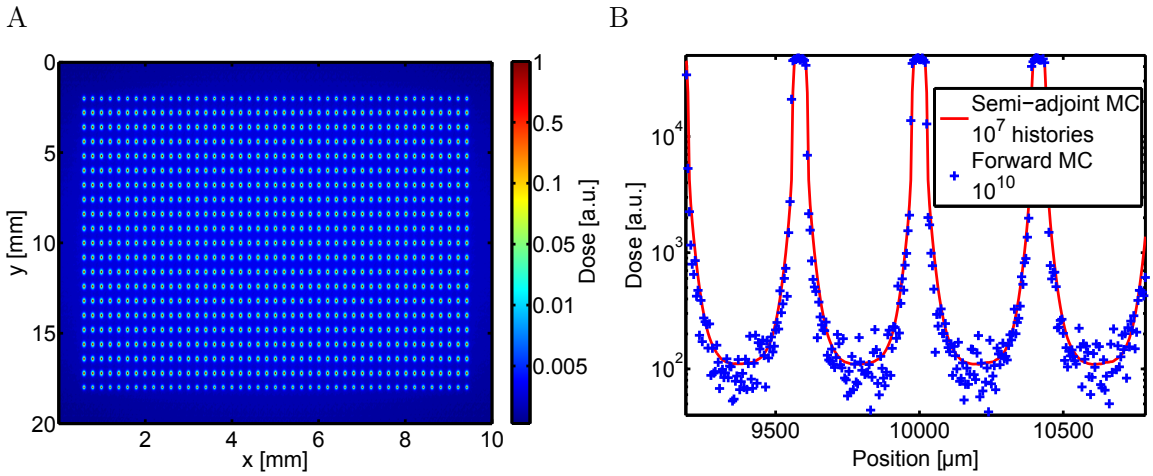

Figure 3.5 – Dose of a pencilbeam field in a cubic water phantom with 16 cm side length in 4 cm depth. (A) shows the dose distribution of the whole field at this depth. The spatial dependency is obtained by convolving the dose of a pencilbeam over the detector shape (equation 3.42). (B) shows a comparison between direct forward calculation with 10^{10} particle histories and the semi-adjoint calculation with 10^7 histories. The statistics is significantly poorer in forward calculations.

Figure 3.5A shows the 2D result of the dose calculation in 4 cm depth. For comparison a forward calculation on the same scoring grid with 10^{10} photons was performed, i.e. with 1000 times more photon histories. Nevertheless the statistical uncertainties of the forward calculation are much higher. A profile through the centre of the field in 4 cm depth is shown in figure 3.5B. The profiles of the direct method and the semi-adjoint method coincide. If the irradiation pattern is changed the forward Monte Carlo simulation has to be repeated. In the inverted geometry only the convolution in equation 3.42 has to be recomputed for the new source shape f_S.

Another very useful application of the semi-adjoint Monte Carlo method is the calculation of output factors. The output factor is the ratio of the peak dose of a collimated beam to the peak dose of a reference field at identical primary particle flux. In forward Monte Carlo calculations each collimator aperture has to be calculated separately. With the semi-adjoint method the Monte Carlo simulation has to be carried out only once and all future computations can be reduced to a single convolution (equation 3.42). The computation and measurement of output factors and a comparison of the results will be presented in chapter 4. The method was also applied to studies where layer structures were assumed, for instance in Laissue et al. [72].

Conclusion and Outlook

The adjoint Monte Carlo technique is a useful approach if the detector has a small and the source a large volume in the phase space or if for various sources the response of the same detector shall be determined. This technique traces particles backwards in time from the detector to the source. In this chapter we have presented a method that adjoints only a part of the simulations. This is especially advantageous in MRT where the detector volume is small perpendicular to the beam, but where also the source volume is small in the momentum subspace. In the semi-adjoint method the exchange of source and detector geometry is only applied to some dimensions and particles are still tracked forward in time.

The method uses the simulated particle tracks more efficiently. For forward Monte Carlo simulations in MRT most of the simulated photon histories are rejected because they do not hit the detector volume. Hence most of the computational power is spent for photon paths that do not actively take part in the determination of the final dose. In the semi-adjoint Monte Carlo method this ratio of actively contributing to simulated photon histories is remarkably enhanced.

Consequently the statistics of the results is significantly better than in forward Monte Carlo simulations. In an example we were able to show that the statistical noise in the result of the adjoint Monte Carlo method was much less than in that of forward Monte Carlo simulations, although 1000 times more photon histories were simulated in the forward Monte Carlo simulation.

Semi-adjoint Monte Carlo methods are used for several studies in this work. Among others it was employed to calculate the effect of polarisation on microbeam fields in homogeneous phantoms in chapter 2, it was used in the calculation of output factors and for the calculation of the absorbed dose in the cell culture experiments presented in chapter 5. Possibly the method could be further developed for more complicated geometries.

3.3 Dose calculation with kernel based techniques

3.3.1 Introduction

Apart from Monte Carlo simulations analytic approaches were developed for dose calculations in MRT. They are based on point kernel superposition algorithms with analytically calculated dose kernels. Given a photon interaction at a certain point (x_0, y_0, z_0) in a radiation field, a point kernel $K_{(x_0,y_0,z_0)}(x, y, z)$ describes the energy distribution by scattering particles around this point. These kernels are superimposed along the primary beam depending on the interaction probabilities. For MeV-photons scattering kernels need to be provided for water only. The dose absorption in other materials can be calculated by applying O'Connors[73] theorem which states that the absorbed dose in materials that differ from water can be obtained by scaling depths and field sizes with the electron density[v]. However, for photons at energies relevant in MRT the theorem is not applicable, due to the higher importance of the photoelectric absorption. Its cross-section scales much stronger with the atomic number Z than that of the Compton effect which dominates at higher photon energies.

The principles of the point kernel algorithm were presented in our previous work[75,76]. The basic idea of the approach is the splitting of electron and photon absorption due to the differences in their ranges. Electrons travel a maximum distance of 100 to 200 μm in the relevant energy domain of around 100 keV, but the photon mean free path in water is about 6 cm (see figure 3.1). Hence, when describing the photon scattering, the energy transport by secondary electrons can be ignored. The assumption of a local energy absorption is reasonable. Nevertheless, electrons produced in primary interactions on the initial beam are responsible for the beam penumbras and need to be regarded because of the micrometre-structure of the radiation field.

Both, photon and electron scattering are described in a point kernel algorithm. The kernels are computed analytically. For electrons the absorption is derived from Bethe's equation of the stopping power S of charged particles[77],

$$S = -\frac{dE}{dx} = \frac{Ze^4 N_A \rho}{8\pi\epsilon_0^2 E M_A} \ln\left(\frac{4E}{I}\right) \tag{3.43}$$

In this equation Z, ρ, M_A and I are material parameters, namely atomic number, density, molecular weight and ionisation energy. e is the electron charge, N_A the Avogadro constant and ϵ_0 the dielectric constant. The equation describes the amount of kinetic energy that a charged particle loses per distance travelled in matter. The equation is valid for non-relativistic energies. At high but non-relativistic photon energies the equation can be approximated by[75]

$$S = KE^{-p}. \tag{3.44}$$

[v] In fact O'Connor limited his analysis to materials that differ from water only in density. His work was extended by others. For more information see for example Pruitt and Loevinger[74]

The quantities K and p can either be derived from material parameters or from data tables listing the stopping power for electrons.

Analytic electron kernels can be obtained with some additional assumptions: Electrons created in a primary photon interaction, i.e. photoelectric absorption or Compton scattering, are assumed to be emitted isotropically in all directions. The unsteady path of the electrons is approximated by a straight line. The production of bremsstrahlung is neglected. The initial electron energy depends on the primary photon energy and on the interaction that created the electron. However, Compton electrons are treated as monoenergetic, irrespective of the scattering angle. Finally it is assumed that the material is homogeneous within the electron range, i.e. within a radius of less than 200 μm. The derived kernels are in reasonable agreement with Monte Carlo simulated electron kernels. Comparisons were carried out previously [75].

Photon kernels are calculated by differentiating between scattering orders. An incoming photon might interact a first time by photoelectric absorption or Compton scattering. We call the energy transferred to electrons in this first interaction as 0^{th} scattering order. In the case of Compton scattering a scattered photon is created that can interact again via the two interaction processes. We call the transferred energy from this scattered photon 1^{st} scattering order and so on. The higher the scattering order the more the energy is spread in space. Therefore the dose decreases with increasing order. If q_i is the fraction of photons that interacts via Compton scattering in i^{th} scattering order,

$$q_i(E) = \frac{\mu_C(E_i)}{\mu_C(E_i) + \mu_{Ph}(E_i)}, \tag{3.45}$$

and if $p_i(E)$ is the fraction of photon energy that is on average transferred to an electron in a Compton scattering event then the fraction of energy absorbed in n^{th} order can be calculated with

$$O_n = (q_n p_n + 1 - q_n) \prod_{i=0}^{n-1} (q_i(1 - p_i)). \tag{3.46}$$

In equation 3.45 μ_C and μ_{Ph} are the total scattering or absorption coefficient of the Compton effect and photoelectric absorption. The spatial distribution of energy in the point kernel is calculated from the differential scattering cross sections of the Compton effect. For different scattering orders the kernels are calculated separately. From the third scattering order an analytical or numerical integration is impossible. The photon scattering is therefore simplified to a random walk process with isotropic scattering. Details on the derivation of the spatial energy distribution can be found in Bartzsch and Oelfke [76]. The final scattering kernel $K_{E,M}(\vec{r})$ for photon energies E and materials M is obtained by adding up contributions of all scattering orders.

Dose calculation itself is performed in a convolution algorithm. Kernels $K_{E,M}(\vec{r})$ are precalculated for various materials M and energies E for the scatter dose (order $n > 0$). Currently implemented are the materials presented in table 3.1 at the photon energies $E_1 = 45$, $E_2 = 55$, $E_3 = 65$, $E_4 = 80$, $E_5 = 105$ and $E_6 = 135\,keV$. As for the Monte Carlo dose calculation algorithm the material conversion from HU to the parameters in table 3.1 is based on the method of Schneider et al. [45].

In the dose calculation first the photon scattering is calculated. The spectral energy is assigned to the six energies $E_1, \ldots, E_6$ and separately at each energy E the "interaction strength" S_E is determined[vi], defined by the equation

$$S_E(x, y, z) = \mu(E, x, y, z) e^{-\int_{x'=0}^{x} \mu(E,x',y,z)\, dx'}, \tag{3.47}$$

[vi] S_E is closely related to TERMA $T(x, y, z)$, as defined by Ahnesjö et al. [78]: $S_E = T\rho/E$.

M	HU	ρ	H	C	N	O	P	Ca
1	-700	0.31	3.86	22.65	50.46	22.00	0	0
2	-350	0.67	8.36	49.07	21.24	20.72	0	0
3	-99	0.93	11.59	68.02	0.28	19.80	0	0
4	99	1.12	9.41	20.59	6.15	62.35	0	0
5	408	1.26	7.77	37.00	2.99	37.75	4.44	9.57
6	617	1.38	6.63	31.40	3.31	39.25	5.96	12.94
7	779	1.48	5.88	27.71	3.51	40.24	6.97	15.16
8	1038	1.63	4.87	22.71	3.80	41.57	8.33	18.16
9	1167	1.71	4.43	20.56	3.92	42.15	8.92	19.46
10	1416	1.86	3.69	16.91	4.12	43.12	9.92	21.65

Table 3.1 – Materials for which kernels are pre-calculated at 45, 55, 65, 80, 105 and 135 keV. The table states the material index M, Hounsfield units (HU), density (ρ) in $g\,cm^{-3}$, and the weight fractions of the elements hydrogen (H), carbon (C), nitrogen (N), oxygen (O), phosphorous (P) and sodium (Ca) in percent.

where x denotes the propagation direction of the beam. The calculation is performed on the macroscopic voxel grid of the CT and each voxel in the phantom is assigned to the most similar kernel material $M = 1, 2, \ldots, 10$ in table 3.1. Afterwards the scattered dose is calculated by convolving the interaction strength S_E and the kernels $K_{E,M}$ in an energy and material dependent manner,

$$D_{E,M}(\vec{r}) = (K_{E,M}(\vec{r}) * S_{E,M}). \tag{3.48}$$

Here we define $D_{E,M}$ as the dose contribution of material M and energy E. $S_{E,M}$ is the interaction strength for the material M, which is S_E for all voxels that are assigned to M and 0 otherwise. After the calculation of all $D_{E,M}$ (currently $6 \cdot 10 = 60$) the total scattered dose is computed as the sum

$$D_{scattered} = \sum_E \sum_M D_{E,M} \tag{3.49}$$

For broad beams the total dose is the sum of scattered and primary dose $D_{scattered} + D_{primary}$, where the primary dose is directly obtained from the "interaction amplitude" S_E and the 0^{th} energy absorption fraction obtained from equation 3.46

$$D_{Primary} = \sum_E S_E \left(q_0(E)p_0(E) + 1 - q_0(E)\right) \frac{E}{m_{Voxel}}. \tag{3.50}$$

In order to calculate the peak and valley dose the microscopic structure of the beams has to be regarded. The valley dose has two components, the scattered photon dose $D_{scatter}$ and electrons that scatter from the peak region into the valley region. The peak dose is almost exclusively defined by the primary dose $D_{primary}$. The structure of the microbeam profile is computed by convolving the electron kernels over the photon fluence pattern $F(y)$. Since we consider planar microbeams it can be assumed that the dose does only vary perpendicular to the microbeam planes, parallel to the y-axis. Therefore the electron kernel is calculated in one dimension as a function of y and reads

$$K^{e^-}(y) = \frac{C}{\sigma} I_\alpha(1 - \frac{y}{\sigma}) \tag{3.51}$$

where[vii]

$$I_\alpha(q) = \int_0^q \frac{r^\alpha}{1-r}\, dr. \tag{3.52}$$

[vii] The derivation can be found in Bartzsch[75] p. 35 ff.

σ and α are material dependent. σ corresponds to the electron range. The constant C is chosen such that K^{e^-} integrates to one. The fluence profile F(y) of primary photons is zero in the valley regions, constant in the peak regions and is normalised that it integrates to one as well. Hence the dose profile in the voxel is obtained in the convolution

$$D(y) = D_{scatter} + D_{primary} \cdot (K^{e^-} * F)(y). \tag{3.53}$$

3.3.2 Implementation of the method, benefits and limitations

The described algorithms were implemented in a C++ program and connected to VIRTUOS by Charlotte Debus[79], a master student at the DKFZ. The program reads in plan files and CTs from VIRTUOS and converts Hounsfield units to material parameters. In contrast to the Monte Carlo calculations presented in chapter 3.2.2 calculations are performed in the beams eye view. The CT is rotated and resampled on a grid such that the beam is parallel to the z-axis. At the end of the dose calculations the calculated dose is rotated back into the CT system.

Similar to the Monte Carlo simulations the source model presented in chapter 2 was included in the dose calculation. The ctc and beam width were set to 412.3 and 51.5 μm respectively. The fluence profile was applied to the calculation of the interaction strength S_E. The leakage radiation dose was calculated from the leakage spectrum and added to the scattered dose.

The calculation time depends on the hardware, on the field size and the CT dimensions. Typical calculation times are in the order of several minutes on a normal modern PC. This is a major advantage over Monte Carlo simulations where typical calculation times are in the order of several weeks, if the processes are not parallelised.

The disadvantage of the analytic dose calculation method is a lower accuracy due to the approximations made. Particularly problematic are interfaces of materials with highly contrasting properties in the phantom. The point kernel algorithm assumes a locally homogeneous environment for the point kernels. The problem is illustrated in figure 3.6 (left) for a bone-water interface. The energy absorption in the scattering kernel in bone is more concentrated at the centre, whereas the kernel in water spreads the energy over a larger volume. In the figure a bone-scattering kernel (blue curve) is added close to the bone-water interface, assuming a homogeneous bone environment. The correct dose contribution of the scattering photons would, however, follow the red curve. There are two effects that are important here: First, the range of the photons is much higher in water, leading to an underestimation of the dose distant to the material interface and secondly the absorption coefficient is lower in water and therefore there is a sudden dose drop at the interface which leads to a lower kernel contribution than predicted by the bone kernel close to the boundary. The consequences are smeared out dose edges in the point kernel algorithm which are in reality much sharper. The effect can be seen in figure 3.6 (right), where a depth dose curve from a 30×30 mm^2 broad beam field is plotted. The phantom consists of water and contains a bone cylinder of 15 mm radius and a 200 mm axis perpendicular to the beam in 35 mm depth (The graph was taken from Bartzsch[75]).

How is it possible to reduce these errors without jeopardizing the speed of the dose calculation? A straight forward procedure would be a ray tracing and a directional scaling of the dose kernels. But this is a very time consuming procedure, because from each interaction point it would be necessary to perform a ray tracing into all beam directions. Instead we took another approach. Similar to the optical path length a radiological distance dL can be defined via

$$dL = \mu ds \tag{3.54}$$

where ds is the geometrical distance and μ the total absorption coefficient. Instead of deforming the kernels a deformation of the geometry in the phantom around the interaction point can be

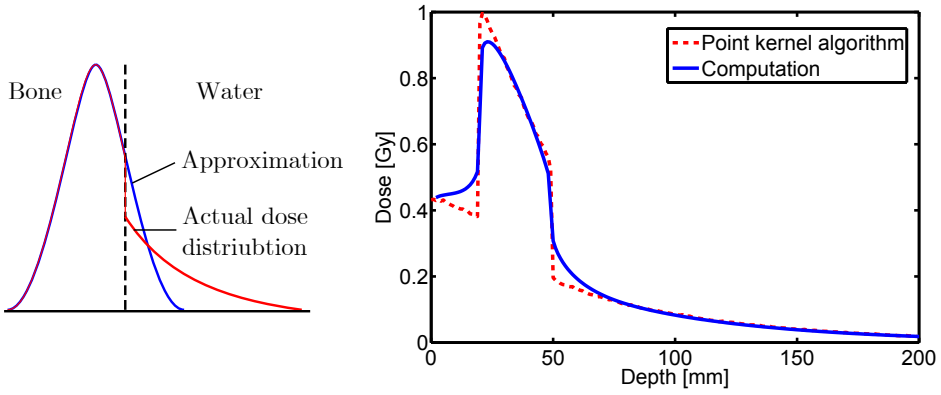

Figure 3.6 – Left: The figure illustrates the dose errors made by the point kernel algorithm at material interface. The drawing shows a bone kernel close to a material interfaces to water. The superposition algorithm assumes a homogeneous bone material around the kernel and therefore the dose contribution at this point follows the blue curve. However, the correct contribution would be the red curve. Right: The consequences are smeared out dose edges as shown in the example of a depth dose curve in a water phantom with a piece of bone.

performed. This leads to a superposition algorithm in curved space. The modified method which is based on differential geometry part of the master thesis of Jennifer Kieselmann[80]. It will be presented in outlines in the next section. As a short hand we refer to the presented method as convolution point kernel algorithm (CPKA) and the method in the next chapter as superposition point kernel algorithm (SPKA).

3.3.3 A superposition algorithm in curved space

In Bartzsch and Oelfke[76] point kernels in homogeneous medium are derived in different scattering orders in the relevant energy range of MRT. In spherical coordinates $\vec{r} = (r, \theta, \phi)$ centred at the primary interaction point, the first scattering order kernel has the principle shape[viii]

$$K_{hom}(\vec{r}) = F(E_0, \theta, \phi) \cdot \frac{\mu}{r^2} q(E_0)(p(E_1)q(E_1) + 1 - q(E_1))e^{-\mu r}, \tag{3.55}$$

where $F(E_0, \theta, \phi)$ is a factor that does not depend on material parameters anymore. Material dependent quantities are the total attenuation coefficient μ and the fraction of Compton interactions for photons, i.e.

$$q = \frac{\mu_C}{\mu}, \tag{3.56}$$

where μ_C is the Compton attenuation coefficient. p is the fraction of energy which is transferred to the electron in a Compton scattering event. While E_0 is the primary photon energy, $E_1 = (1-p)E_0$ is the mean photon energy of the scattered photon. For simplicity we focus on monoenergetic beams in the following and we will not write energy dependencies explicitly. We write q_0 for $q(E_0)$, p_0 for $p(E_0)$, q_1 for $q(E_1)$ and p_1 for $p(E_1)$. As already discussed, polychromatic beams can easily be calculated as a weighted sum over all spectral components.

Moving to inhomogeneous phantoms the kernel becomes

$$K_{inh}(\vec{r}) = F(\theta, \phi) \cdot \frac{\mu(\vec{r})}{r^2} q_0(\vec{0})(p_1(\vec{r})q_1(\vec{r}) + 1 - q_1(\vec{r}))e^{-\int_0^r \mu(r', \phi, \theta)dr'}, \tag{3.57}$$

where we denoted the primary interaction point with $\vec{0}$.

[viii] In this shape the kernel yields the energy in a certain voxel. The dose is obtained by division by the mass density.

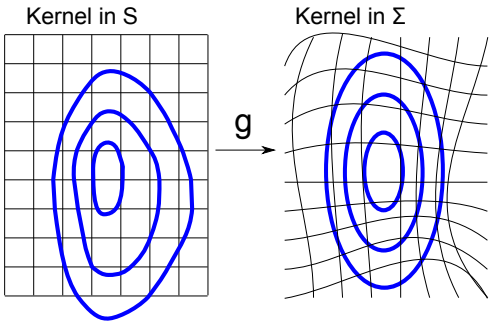

Figure 3.7 – The function g maps the inhomogeneous kernel in the physical system S into a system Σ where the kernel corresponds to the homogeneous water kernel. The blue lines symbolise isodose curves. If the coordinate transformation g is known a ray tracing is unnecessary.

This kernel can be split in four factors: The material independent factor F, the factor $q_0(\vec{0})$ which depends on the material at the primary interaction point only, a factor $p_1(\vec{r})q_1(\vec{r})+1-q_1(\vec{r})$, which depends on the material at the scattering point only and the factor $G = e^{-L}$, which depends on the radiological distance L between primary and scattering point,

$$L(r,\theta,\phi) = \int_0^r \mu(r',\phi,\theta)dr'. \tag{3.58}$$

The inhomogeneous kernel can therefore be obtained from the homogeneous (e.g. water) kernel in the equation

$$K_{inh}(\vec{r}) = K_{hom}\left(\frac{L(r,\theta,\phi)}{\mu_{hom}},\theta,\phi\right)\frac{p_1(\vec{r})q_1(\vec{r})+1-q_1(\vec{r})}{p_{1,hom}q_{1,hom}+1-q_{1,hom}}\cdot\frac{q_0(\vec{0})}{q_{0,hom}} \tag{3.59}$$

Equation 3.59 inspires the following procedure for a dose calculation in an inhomogeneous phantom:

1. The scattering power S_E (see equation 3.47) is modified to $S_E^*(\vec{r}) = S_E(\vec{r})\cdot\frac{q_0(\vec{r})}{q_{0,hom}}$.

2. The homogeneous water kernels are superimposed after deformation in spherical coordinates around $\vec{r}\,'$ with a function $g_{\vec{r}\,'}: (r,\theta,\phi)\rightarrow(L/\mu_{Water},\theta,\phi)$. The superposition is weighted by the modified scattering power S_E^*:

$$D'(\vec{r}) = \sum_{\vec{r}\,'}\left[S_E^*(\vec{r}\,')K_{Water}(g_{\vec{r}\,'}(\vec{r}-\vec{r}\,'))\right] \tag{3.60}$$

   g is determined by the absorption coefficient around the primary interaction point.

3. Finally all dose values are multiplied with $\frac{p_1(\vec{r})q_1(\vec{r})+1-q_1(\vec{r})}{p_{1,hom}q_{1,hom}+1-q_{1,hom}}$.

$$D(\vec{r}) = \left(\frac{p_1(\vec{r})q_1(\vec{r})+1-q_1(\vec{r})}{p_{1,hom}q_{1,hom}+1-q_{1,hom}}\right)D'(\vec{r}) \tag{3.61}$$

Step 2 can be understood as a deformation of the physical space via $g: S\rightarrow\Sigma$, such that the kernel in the inhomogeneous phantom has the shape of a water kernel in Σ. The mapping g allows a transformation to the real physical space. Given the transformation g a ray tracing is no longer required. The procedure is graphically illustrated in figure 3.7. Unfortunately the

transformation

$$g_{\vec{r}'} : (r, \theta, \phi) \rightarrow (L/\mu_{Water}, \theta, \phi) \tag{3.62}$$

is just locally defined and it has to be found individually for all primary interaction points at $\vec{r}'$. It would be tempting to try to find a global transformation of the space, because than the superposition could be carried out as before in a convolution (see equation 3.48). This is, however, not possible since the radiological distance depends on the integration path.

The general metric which describes radiological distances is given by

$$ds^2 = \mu^2(r, \theta, \phi)dr^2 + \mu^2(r, \theta, \phi)r^2 d\theta^2 + \mu^2(r, \theta, \phi)r^2 \sin^2\theta d\phi^2. \tag{3.63}$$

The transformation g is a parametrisation for the arc length in radial direction (i.e. along the photon paths).

Jennifer Kieselmann developed and implemented in her masters project an algorithm to approximate g and superimposing inhomogeneous kernels in a superposition algorithm. This work is now part of the dose calculation in the TPS and its accuracy at material boundaries is significantly improved as compared to the convolution based point kernel algorithm. The price for the higher accuracy is an increase in the calculation time by a factor of around 3, which is still acceptable compared to Monte Carlo simulations. Further details of the method are given in the master thesis[80].

3.4 CT transformations: From HU to material parameters

Apart from the models used, the accuracy in the dose calculation substantially depends on the conversion of Hounsfield units (HU) to material parameters. The method that we used for the point kernel and for the Monte Carlo dose calculation was introduced by Schneider et al.[45].

The conversion of HU to material parameters is not unambiguous. A CT device measures the absorption coefficient of a material. The measured value depends on the spectral energy of the CT. Therefore the absorption measured by a certain device cannot easily be compared with that of other CT-devices. Hounsfield units present a way to compare different devices to each other by the definition of a relative scale. On this scale water gets the value HU = 0 and air HU = -1000 using the formula

$$HU = 1000 \cdot \left(\frac{\mu}{\mu_{H2O}} - 1 \right). \tag{3.64}$$

The Hounsfield unit scale simplifies comparisons between different CT images. But still the relation between HU and material remains device dependent. In fact beam hardening effects may even alter the HU representation of a material within the same CT image. Moreover, two different materials may have the same HU representation because their absorption values are coincidently equal at the photon energy of the source.

Schneider et al.[45] developed an interpolation method for the HU material conversion. They realised that most tissues in the body can be described as a mixture of two main components. The composition and density can therefore be calculated by an interpolation with the material weights W_1 and W_2 of component 1 and component 2. The weight fraction of an element i, ω_i, for example can be interpolated from its weight fractions $\omega_{i,1}$ and $\omega_{i,2}$ in component 1 and component 2 by

$$\omega_i = W_1(\omega_{i,1} - \omega_{i,2}) + \omega_{2,i}. \tag{3.65}$$

Here we exploited the relation $W_1 + W_2 = 1$. Similarly the density can be obtained in

$$\rho = \frac{\rho_1 \rho_2}{W_1(\rho_2 - \rho_1) + \rho_1}. \tag{3.66}$$

Material	density [g/cm^3]	RED	HU	ΔHU
dense bone	1.53	1.456	1044	28
adipose	0.96	0.949	-69	20
lung (exhale)	0.50	0.489	-489	20
liver	1.07	1.052	56	21
trabecular bone	1.16	1.117	286	21
breast	0.99	0.976	-33	21
lung (inhale)	0.20	0.190	-792	21
muscle	1.06	1.043	48	21
Water	1.00	1.000	-5	56
Air	0.0012	0.0011	-998	10

Table 3.2 – The table shows the materials of the electron density reference phantom (model 062, CIRS), the material parameters provided by the company [81] and the HU measurement with the CT device at the AOI. ΔHU states the standard deviation of the HU within the tissue equivalent inlets. Additionally air was added to the list.

From this Schneider et al. [45] derive the following HU-dependent scaling rules

$$\rho = (\alpha + \beta \cdot 10^{-3} HU) \text{ and} \tag{3.67}$$

$$\omega_i = \gamma \cdot \frac{\delta - HU}{\epsilon + \eta HU}(\omega_{i,2} - \omega_{i,1}) + \omega_{i,1}. \tag{3.68}$$

As supporting points for their interpolation they use in the bone domain between 100 and 1524 HU cortical bone (HU = 1524) and a mixture of red and yellow marrow (HU = -22). In the soft tissue domain interpolation is carried out between adipose tissue (HU = -98), adrenal gland (HU = 14), small intestine (HU = 23) and connective tissue (HU = 100). For HU below -98 the material is treated as a mixture of air (-1000) and adipose tissue. These 7 tissues are the base materials for the conversion.

Since the HU representation of tissues is CT-device dependent, a calibration of the material conversion has to be carried out. For the first clinical pet trials at the ESRF CT scans will be carried out at the "Animal Oncology and Imaging centre (AOI)"[ix] in Hünenberg, Switzerland. In order to calibrate the CT an electron density reference phantom (model 062, CIRS, Norfolk, USA) was scanned by Elke Bräuer-Krisch and Barbara Kaser-Hotz at the facility. This phantom is a 330 mm wide an 270 mm high soft tissue equivalent epoxy resin slice with 19 inserts representing various materials in the human body. Table 3.2 presents the insert materials, and the HU seen in the CT. Furthermore density and the relative electron density to water (RED) are listed as provided by the manufacturer.

From this measurement the HU of the seven base materials are selected to achieve a maximum agreement in density and RED for the 10 materials in table 3.2. The calibration curve is presented in appendix B. The calibration uncertainty is on average 8.8 HU and is always smaller than 18 HU. Here we analysed of course just a limited number of materials. Schneider et al. [45] performed a more comprehensive analysis with a total number of 77 naturally occurring tissues. The standard deviation in HU from the calibration curve is 17.3. We assume therefore an uncertainty of approximately 20 HU, taking into account the uncertainty in calibrating the CT-device and the scattering of materials around the calibration.

This HU uncertainty affects the determination of the absorption coefficients and thus the absorbed dose. The uncertainty in the absorption coefficient depends heavily on the HU and the energy and varies between 0.5 and 5%. It is higher for low energies, since the photoelectric

[ix] Homepage of the AOI: http://www.aoicenter.ch/

absorption has a strong dependence on the element composition. In general the uncertainty is decreasing with increasing HU. A graph of the uncertainties over HU for 50, 100 and 150 keV photons is shown in appendix B.

What is the resulting dose uncertainty? As it is apparent from the last paragraphs it is not a simple task to attribute a general uncertainty from the material conversion. This is even more difficult for the dose, because it will depend on the structure of the phantom, the depth in the phantom and the spectrum of the radiation. If we just assume an uncertainty of 2% for the determination of the absorption coefficient, which is approximately the average uncertainty for a material that deviates modestly from the calibration curve, than in a homogeneous phantom the dose uncertainty is

$$\frac{\Delta D}{D} = \frac{(\mu + \Delta\mu)e^{-(\mu \pm \Delta\mu)} - \mu e^{-\mu x}}{\mu e^{-\mu x}} \approx \pm\frac{\Delta\mu}{\mu} \mp \Delta\mu x. \tag{3.69}$$

For an absorption coefficient of $\mu = 20\,m^{-1}$ the expected error in for example 10 cm depth would be 2%.

3.5 Results

At this point we present results for our algorithms and compare the accuracy of the dose calculation methods with each other. Of course benchmarking to measurements at the beamline is indispensable. Dosimetry will be discussed in the next chapter and so we present here only a comparison of dose calculations for two problems discussed in the next chapter: Dose calculation in a homogeneous water phantom and in a human head phantom. In the next chapter measurement results will be compared to Monte Carlo simulations only. Monte Carlo simulations can be expected to be the most accurate dose calculation method and so we justify this limitation with the wish to minimize possible confusions in the data presentation. The reader is, however, invited to return to this chapter for comparisons.

3.5.1 Homogeneous water phantom

The energy absorption of microbeams in a homogeneous water phantom was calculated with Monte Carlo simulations and the point kernel algorithm. To that end a CT was synthetically created with HU = 0 in a 32×32×12 cm^3 cuboid. The size of the CT image was 512×512×200 voxels with a resolution of 1 mm in all directions. Around the cuboid air was simulated with $HU = -1000$. A plan was created in VIRTUOS with a 20×20 mm^2 field of 50 μm wide and 400 μm spaced beams. The beam was directed parallel to the small dimension of the water phantom. Subsequently the dose was calculated with three dose calculation approaches: the convolution based point kernel algorithm (CPKA), the point kernel algorithm based on superposition in curved spaced (SPKA) and Monte Carlo simulations (MC). In the Monte Carlo simulations $2 \cdot 10^7$ photon histories were simulated.

Figure 3.8 shows a comparison between Monte Carlo simulations and point kernel algorithm (PKA) for the depth dose curve and 2 profiles at 30 and 60 mm depth, respectively. In the case of a homogeneous phantom the results of the convolution and the superposition algorithm are essentially the same. The agreement between the peak doses is better than 2% for all depth and therefore the deviation is not plotted. For the valley doses figure 3.8 presents the relative differences between Monte Carlo and point kernel algorithm underneath the dose curves. Monte Carlo simulations still show a not negligible level of noise, which is ignored for quantitative comparison. Between 24 and 120 mm depth the agreement in the depth dose curve is better than 5%. For shallow depth the dose is systematically overestimated by the point kernel algorithm. Between 0 and 8 mm depth the deviation is higher than 20%. In the 30 mm depth profile the

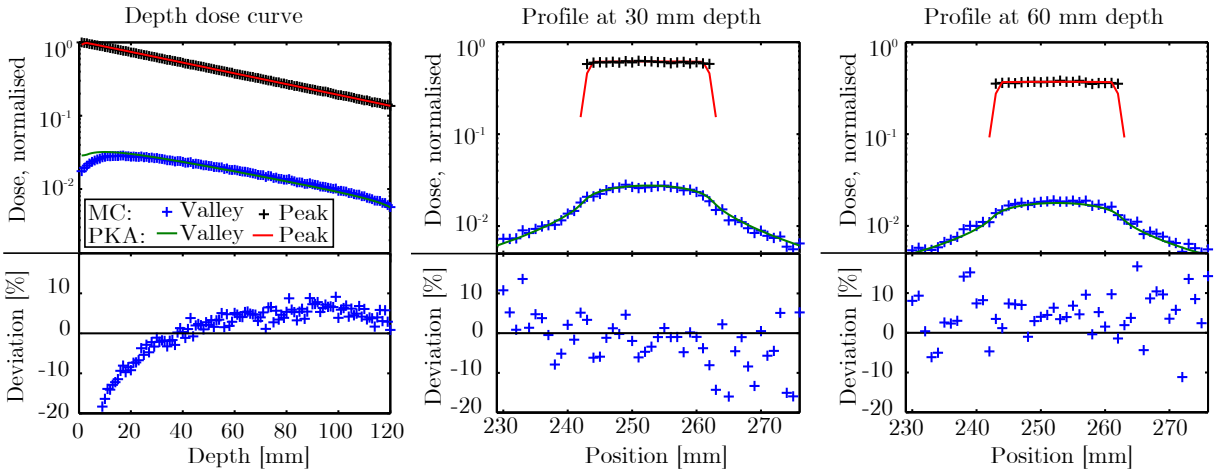

Figure 3.8 – The graphs compare Monte Carlo simulations and kernel based dose calculation in a homogeneous water phantom for a 20×20 mm^2 microbeam field with 50 μm wide and 400 μm spaced beams. From left to right the depth dose curve in the field centre, a profile at 30 mm depth and a profile at 60 mm depth are shown. All figures show the peak and the valley dose on a logarithmic scale. Underneath deviations in the valley dose between both dose calculation methods are provided. The peak dose deviations are less than 2%.

dose is overestimated by 2% and in the 60 mm depth profile it is underestimated by 4.8% on average.

3.5.2 Human head phantom

The dose calculation methods were compared on a CT of an anthropomorphic human head phantom (CIRS, USA). This phantom served also for dose measurements with radiochromic films in the next chapter. Slices of the CT image of the phantom are shown in figure 4.2. The phantom is irradiated from the back with a field sized 20×20 mm^2 consisting of 50 μm wide and 400 μm spaced microbeams. The irradiation plan corresponds to plan 1 presented in chapter 4.2.6 where also further details on the phantom will be given. In order to facilitate an easy comparison with the next chapter we normalised the beams to a beam entrance dose of 100 Gy.

Figure 3.9 shows the depth dose curve in the beam centre and dose profiles at two different depths, 64 and 104 mm. These two depth correspond to the inlay position 1 and 4 for film dosimetry. For all dose curves relative deviations from MC are plotted underneath. The peak depth dose curve agrees very well between MC, CPKA and SPKA. Encountered differences are usually below 5% and only at the skull close to the beam entrance there are higher deviations of up to 10% which are very likely caused by resampling the phantom in the kernel based dose calculation. This is necessary, because kernels were precalculated for 0.5 and 2 mm resolution, only. In the valley dose the differences are higher. In the homogeneous part of soft tissue the dose is underestimated by CPKA and SPKA by between 10 and 15%. Close to the beam entrance the CPKA overestimates the dose by 30% and more. Here the SPKA has a clear advantage and deviations between SPKA and MC remain below 15%.

In the beam profiles again the peak dose is in excellent agreement between MC and the kernel based dose calculation. The reason for the observed deviations seem to be linked to statistical uncertainties in the Monte Carlo rather than physical shortcomings in the models of the point kernel algorithm. Valley doses show again a bit higher uncertainties. Within the field uncertainties are below 15%. There is a tendency of dose underestimation inside the beam and dose overestimation outside the beam. In the Monte Carlo simulation there are two dose spikes visible at approximately 70 and 200 mm lateral position. These dose features are not resolved in the kernel based algorithms. The CPKA assumes of course homogeneous material around

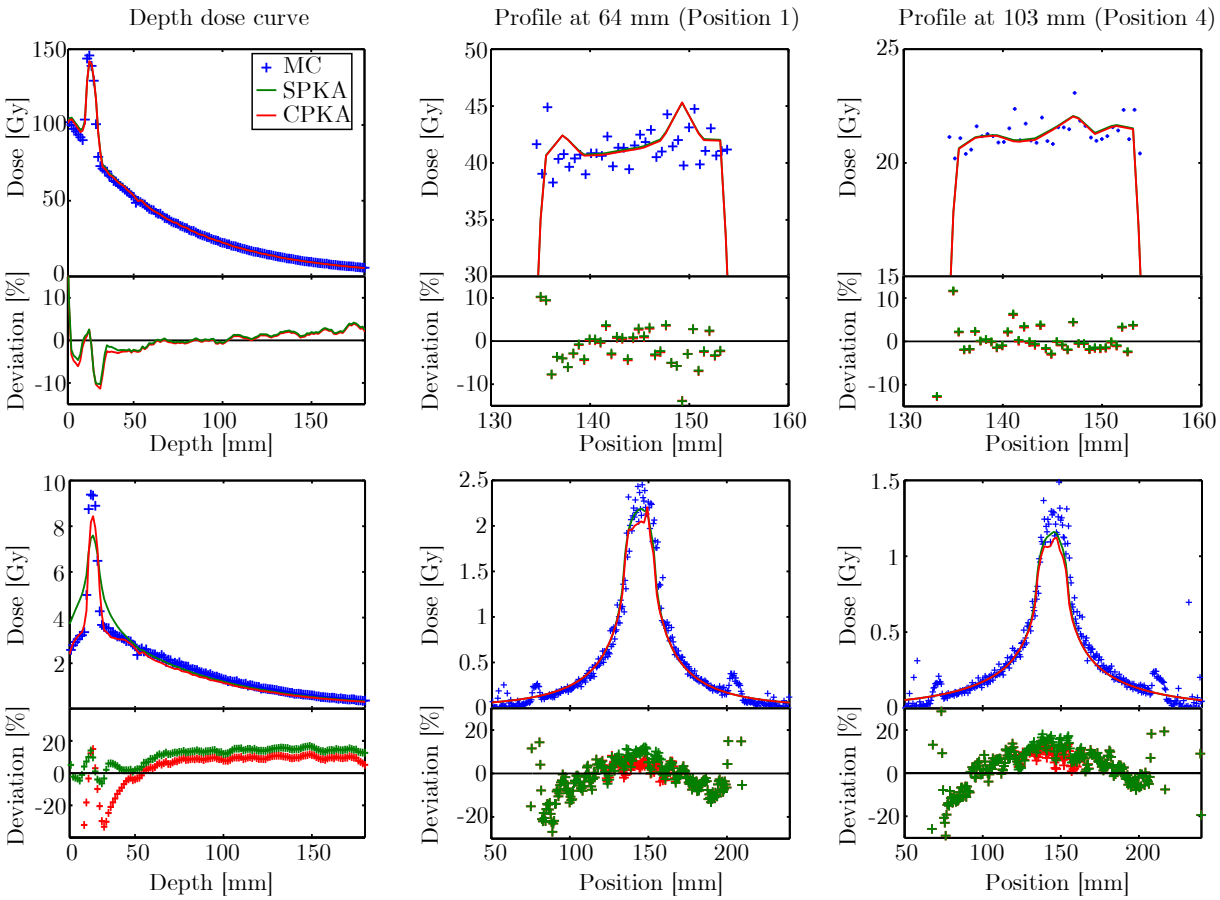

Figure 3.9 – The figure shows a dose calculation comparison for a 20×20 mm^2 microbeam field with 50 μm wide and 400 μm spaced beams in a anthropomorphic human head phantom. The top row shows the peak doses and the bottom row valley doses in a depth dose curve (field centre) and two profiles. The positions correspond to those in the next chapter (e.g. in figure 4.8). Deviations underneath the dose curve state differences to MC simulations.

the primary interaction points. Since this is a feature far outside the primary beam it does not recognise these structures. For the SPKA the structures are outside the region where the superposition in curved space is applied and therefore the algorithm similarly ignores material inhomogeneities there. However, the dose is just approximately 10% of the valley dose inside the field and deviations there are unlikely to have a biological implication.

3.5.3 Optimal photon energy for MRT

Finally we return to the problem addressed at the beginning of this chapter. What is the optimal photon energy for MRT? We created a phantom made of homogeneous water and a thin bone layer of 7 mm thickness imitating the skull in an MRT treatment of the brain. We modified the Monte Carlo simulations presented in chapter 3.2.2 to simulate monoenergetic MRT-fields of 2×2 and 4×4 cm^2 between 50 and 400 keV photon energy. In figure 3.10 the result of the calculation is plotted for PVDRs and valley doses in dependence on the photon energy. Furthermore the peak dose in 10 cm depth is shown. The dose calculation was normalised to 100 Gy peak dose at 2 cm depth.

The PVDR is highest at 150 keV photon energy in water and at 200 keV in bone. Doubling the field size from 2×2 to 4×4 cm^2 drastically reduces the PVDR, but it only slightly shifts the energy upwards at which the PVDR is maximal. The result for the valley dose is very similar.

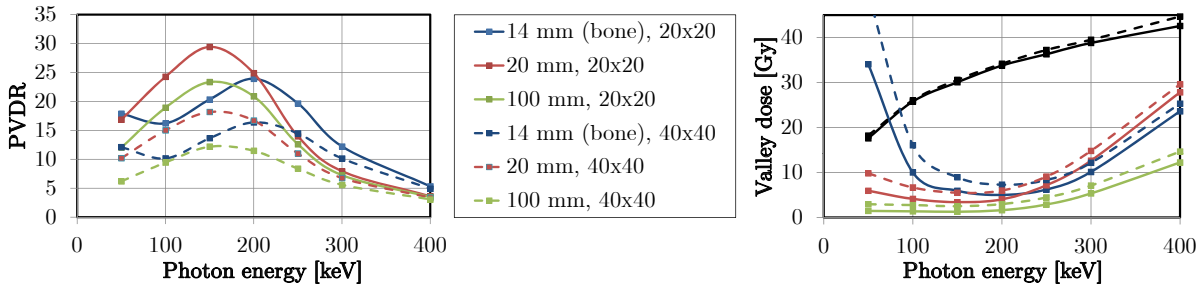

Figure 3.10 – The graph on the left show the PVDR dependence on the photon energy for monoenergetic MRT fields of 2×2 cm^2 (solid lines) and 4×4 cm^2 (dashed lines) at 14 (blue), 20 (red) and 100 mm (green) depth in the phantom. On the right the valley doses are shown. Additionally the peak dose in 10 cm depth is plotted as a black line. Doses on the right are presented for a fixed peak dose of 100 Gy at 2 cm depth.

A minimal valley dose is reached at 150 keV photon energy in water and at 200 keV in bone. Lower photon energies (50 keV) lead to much lower PVDRs and higher valley doses. The effect is particularly severe in bone, where the valley dose at 50 keV is by factor of 3.5 higher than at 100 keV.

The peak dose in 10 cm depth increases with the photon energy. At the current mean energy of the spectrum at ID17 of 100 keV around 26 Gy would be reached in the peak, whereas at 200 keV the dose would be 34 Gy.

These results proof that from a physical point of view a harder photon spectrum would be advantageous. A mean photon energy between 150 and 200 keV would be the best compromise between large mean free path on the one hand and low valley doses in bone and water on the other hand.

3.6 Conclusions

In this chapter we presented various techniques to calculate peak and valley doses in MRT. These techniques are, accept for the semi-adjoint Monte Carlo simulations, linked to a treatment planning system VIRTUOS where all irradiation parameters are set. After planning the dose calculation can be performed in forward Monte Carlo simulations or with point kernel based algorithms. These algorithms are all based on the model of the photon source, which was introduced in chapter 2 and furthermore on the conversion of CT Hounsfield units to material parameters of which methods and uncertainties were analysed in chapter 3.4. Uncertainties from the CT conversion are expected to be around 2%.

Among the dose calculation methods linked to VIRTUOS the forward Monte Carlo technique presented in chapter 3.2.2 can be considered most accurate. However, calculation times are in the order of several weeks for a sufficiently low statistic noise level. Parallelisation can reduce the calculation time. Nevertheless Monte Carlo simulations remain a time consuming approach.

For that reason kernel based dose calculation algorithms were developed and discussed in chapter 3.3. A pure convolution based dose calculation method (CPKA) is the fastest alternative to Monte Carlo simulations. Dose calculations can be performed within 5 to 10 minutes. However, close to material boundaries there are larger deviations observable. This is an intrinsic disadvantage of the method. Around the primary interaction point homogeneous material is assumed and this generates a blurring at material interfaces. Although the deviations are less than 10% in homogeneous parts of the phantom, errors close to irradiation boundaries can be 30% and more (chapter 3.5).

We therefore introduced another method in chapter 3.3.3: Dose calculation in curved space which was implemented as part of a master thesis[80]. The basic idea of this method is that kernels

in first order have the same shape when distances are measured in units of the radiological distance. A mapping from the curved to the physical space depends on the material and is approximated from the total attenuation coefficient around the primary interaction point. This mapping in combination with local and global scaling methods enables the transformation of a homogeneous water kernel in the curved space to the kernel in inhomogeneous material in physical space. The method reduces the error close to material interfaces to less than 15%.

Screenshots of the treatment planning system are provided in appendix B. The methods presented will not finalise the development of dose calculation tools in MRT. There are many improvements and expansions desirable. The kernel based dose calculation approach provides a method to calculate within around 30 minutes the dose with uncertainties of less than 15% in the dose valleys and less than 2% in the dose peaks. This is an acceptable result for the optimisation of treatment parameters and also with respect to the larger uncertainties in biology. Nonetheless the accuracy will not be sufficient for therapy planning in patients and after optimisation of irradiation directions and beam parameters time consuming Monte Carlo simulations will be essential.

What limits the accuracy of the point kernel dose calculations? Respectively, what slows down the speed of Monte Carlo computations? The limiting point for the point kernel algorithms is the computation of scattered photon dose, whereas the limitations of Monte Carlo simulations are the small voxel and beam sizes. The simulation of the photon scatter dose on a macroscopic grid is easy to perform. These considerations suggest a combination of Monte Carlo and kernel based techniques. In a hybrid algorithm the photon scatter dose could be efficiently calculated in Monte Carlo simulations. Several authors report about very fast Monte Carlo codes that run parallelised on GPUs[82–84]. The electron kernel algorithm, however, seems to be accurate enough for the calculation of peak and valley doses. This approach could have the potential to calculate peak and valley doses within minutes and with the accuracy of Monte Carlo simulations that run over several weeks.

Another limiting factor of the developed dose calculation method is the restriction to unilateral ports. In principle the point kernel algorithms have the ability to calculate the dose for any beam geometry. However, work has to be invested into the storage and visualisation of treatment relevant information. For the forward Monte Carlo code presented in chapter 3.2.2 multiport irradiations present a more fundamental problem. Here again hybrid approaches with a combination of Monte Carlo and analytic methods could have the potential to offer an efficient solution.

Chapter 4

Dosimetry of microbeams

4.1 Introduction

Dosimetry for MRT remains a challenge. The use of commercially available detectors is limited due to the extremely high dose rate of up to 16,000 Gy/s, the required micrometer resolution and the dose sensitivity which needs to range from 5 Gy up to 1000 Gy. A further issue in dosimetry is the material equivalence to water. For a future clinical application of MRT doses need to be measured within 3% accuracy. Bräuer-Krisch et al. [85] present several means of dosimetry and analysed their strengths and weaknesses. Among others, solid state detectors are discussed such as flash memory MOSFET detectors, fluorescent nuclear track detectors (FNTD), thermoluminescent dosimeters (TLDs) and silicon strip detectors. These detectors often show dose rate and energy dependencies and the readout process can be difficult. In recent years silicon detectors have become very accurate, though, showing a high resolution, linearity over a wide dose range and allow a microsecond real-time readout [86,87]. However, solid state detectors are usually not water equivalent and may induce distortions in the radiation field. Other more tissue equivalent detectors are MRI Gel dosimeters [88,89]. They possess a high three dimensional resolution, but are usually very sensitive to dose rates.

Radiochromic films that we use here are promising dosimeters in MRT that have shown to be largely dose rate independent and are usable over a wide range of radiation doses. With resolutions of a few micrometre radiochromic films are among the highest resolving dosimeters, they are easy to handle and their use is already established in radiotherapy. Unlike conventional radiographic films radiochromic films darken instantaneously after radiation exposure without chemical processing. Usually the radiosensitive substance is a monomer that polymerizes after exposure to radiation and changes the absorption of the film material at optical wavelengths.

As radiosensitive films we used in this work HD-810 and HD-V2 Gafchromic® films from ISP (Nuclear Associates) and investigated their applicability for our purposes. In table 4.1 some features of the used films are compared to EBT2 films which are most frequently used in the clinical practice but are sensitive to lower doses. So far HD-810 films showed the best performance in terms of sensitivity and resolution in MRT. However, these films are not available any more and are substituted by HD-V2 films. We compare the performance of both film types.

The dynamic range of the films is limited. HD-810 films are sensitive to doses between 5 and 500 Gy HD-V2 films to doses between 10 and 1000 Gy. Hence it is necessary to measure peak and valley doses separately by choosing adequate beam exposure times.

For Gafchromic® films no dose rate dependency was reported. However the independence of the dose rate was only confirmed between [90] 0.34 and 80 Gy min^{-1}. For photon energies beneath 100 keV the film sensitivity becomes energy dependent [91]. This should not impair measurements as long as calibration and measurements use the same spectrum. However, deviations are expected due to beam hardening and differences in the photon energies between peak and valley

Film	HD-V2	HD-810	EBT2
Dose	10 - 1000 Gy	5 - 500 Gy	0.1 - 10 Gy
Resolution	5 μm	2.5 μm	5 μm
Uniformity	$\leq$ 3%	$\leq$ 8%	$\leq$ 3%

Table 4.1 – Comparison of HD-V2, HD-810 and EBT2 Gafchromic® films. Information are taken from the webpage of Radio Product Design, Inc., http://www.rpdinc.com/ (01/05/2014).

regions in MRT-fields.

For all of the used films the optical dose-dependent absorption is strongest in the red light. HD-V2 films have the most sensitive absorption peak at around 675 nm[92]. Due to their crystal structure, Gafchromic® films have polarising properties rendering the readout sensitive to the film orientation[91,93,94] if the read-out light or the detector have any polarization preferences. A disadvantage of radiochromic films is the required time between film exposure and readout. After exposure the films need about 10 hours to darken and only after around 24 hours no significant changes in the optical density can be observed[91]. This renders them unsuitable for online dose measurements.

The main difficulty, however, in using radiochromic films is the film inhomogeneity which can be classified in a microscopic and a macroscopic part[91]. Microscopic fluctuations in the optical density arise due to the granular structure, compositional variations, defects in the film structure, scratches or dust particles. This non-uniformity is of particular concern in high resolution dosimetry considered here. Macroscopic non-uniformity is caused during layer production in the manufacturing process. The overall variations within a film sheet are listed in table 4.1. However, there are also variations between films and between batches.

The readout of the films on a micrometer scale is delicate. In conventional radiotherapy film scanners are used. However, the resolution does not suffice for MRT. Although the nominal scanner resolution is sometimes stated to be higher than 10,000 dpi, the actual optical resolution is much less. At the ESRF a Joyce Loebl microdensitometer which has a much higher spatial resolution is used to resolve the microbeams. Nevertheless its resolution is limited. The modulation transfer function (MTF) of the device was measured and the resolution estimated to be around 25 μm[95]. This is too low for 50 μm wide beams and the measured peak doses may be incorrect. Another disadvantage of the microdensitometer is the lack of reproducibility and its sensitivity to individual adjustments that makes the outcome user-dependent[85].

In this chapter we use a microscope for the readout of films after the exposure to microbeams. Its performance is demonstrated for various phantoms at the beamline ID17 of the ESRF. The results of the dose calculation methods presented in the previous chapter are used for comparisons. Microscopes were used before for dosimetry in MRT by Nariyama et al.[96], who compared HD-810 Gafchromic® film measurements with Monte Carlo simulations for 25 μm wide microbeams. The achieved agreement was better than 20%. For quantitative measurements an appropriate image processing is required. Even for a very good optics the field of view defined by the objective and the camera chip size will not be homogeneously illuminated and flattening corrections are necessary. However, compared to the microdensitometer the microscope is easier to handle and data acquisition over the complete microbeam field is feasible within a reasonable amount of time.

4.2 Methods

4.2.1 Calibration with ionisation chambers

Radiochromic films enable only relative dosimetry. In order to link relative dose measurements to absolute doses a calibration was performed with broad beam irradiations. For these fields conventional dosimetry with ionisation chambers is possible when saturation effects due to the high dose rates are corrected[62]. This way the optical film absorption can be correlated to a physical dose.

Dosimetry of broad beams was performed using a pinpoint chamber TW31014 with a sensitive volume of 0.015 cm^3 and a semiflex chamber T31010 with a volume of 0.125 cm^3 in combination with a Unidos Webline T10022 electrometer; all devices are from PTW Freiburg. The semiflex chamber was chosen due to its response uniformity to the MRT relevant photon energies and the pinpoint chamber due to its small sensitive volume and low dose rate dependency. Cross-checking both dosimters gives confidence in the measurement and its accuracy.

Dose measurements followed the AIEA TRS 398 report[61] guidelines where further calibration details can be found. The absorbed water equivalent dose $D_{w,q}$ is determined by correcting the effective ionisation M_q^* with the beam quality factor k_q and the calibration factor $N_{D,w}$, a chamber dependent factor that converts charge to the associated dose at the reference beam quality,

$$D_{w,q} = M_q^* \cdot N_{D,w} \cdot k_q. \tag{4.1}$$

In order to obtain the effective ionisation the chamber is calibrated to normal pressure p_0 and temperature T_0 and is corrected for recombination effects by k_{recomb} and the chamber polarity by k_{pol},

$$M_q^* = M_q \cdot \frac{p_0 T}{p T_0} \cdot k_{recomb} \cdot k_{pol}. \tag{4.2}$$

The factor k_{pol} can be determined by subjecting the chamber to opposite polarities and reading out the charge M^+ and M^-. The mean charge is assumed to be correct and hence k_{pol} is set to $(M^+ + M^-)/(2M)$ where M is the standard readout polarity. For x-ray beams the effect is usually very small. The recombination correction factor k_{recomb} is obtained from the two voltage method. Further details can be found in Andreo et al.[61].

We are very grateful to Elke Bräuer-Krisch who conducted all the chamber measurements and was an indispensable help due to her knowledge and experience with the ID17 beamline at the ESRF.

4.2.2 Film handling

The 20.32×12.7 cm^2 film sheets were carefully cut into pieces of around 3×3 cm^2 size and were marked with an "R" in the upper right corner to mark the film orientation. For the exposure and the readout the orientation of the films was always kept constant. Film pieces for calibration and measurement were usually taken from the same column of the film sheet since layer variations are usually more prominent perpendicular to the coating application[97].

Except for exposure and readout films were kept in darkness and wrapped in aluminium foil to avoid the absorption of UV light. Films were carefully handled with nitrile gloves to avoid contamination with oil and mechanical damage of the surfaces. However, we did not take extra effort to control temperature or humidity.

4.2.3 Optics, Microscope

Instead of the microdensitometer we used a Zeiss Axio Vert.A1 microscope with EC Plan-Neofluar objective lenses (magnification/numerical aperture of the objective lenses: 5x/0.16, 10x/0.3 and

20x/0.5). In order to guarantee a stable illumination over time the microscope was equipped with an LED light source. The spectral range of the LED extends from 400 to 750 μm and is temperature independent. However, the output is low at longer wave lengths. Since the Gafchromic® films have the highest readout sensitivity in the red light we added a RG 665 Schott low pass filter in the light path that is transmissive for wavelengths over 675 nm. As detector we used an AxioCam MRm Rev. 3 FireWire camera (from Zeiss) with 1388×1040 pixels of 6.45×6.45 μm^2 size. The dynamic range of the 12 bit camera is larger than 1:2200. The quantum efficiency exceeds 20% between 350 and 900 nm and reaches its maximum between 500 and 550 nm.

The microscope was equipped with a scanning table (130×85 mot P) that allows a reproducible positioning within 1 μm accuracy.

A linear response between light intensity and camera signal is very important for quantitative measurements. We therefore validated the linear response of the camera with a photographic step table (Kodak, Photographic Step Table No. 2).

4.2.4 Readout and image processing

The resolution of the smallest objective (NA=0.16, resolution of 1.29 μm with the camera) was sufficient for all film readouts. The objective provides a relatively large field of view of 1.79×1.34 mm^2 and also limits the amount of data acquired per scan. The field of view can be extended by stitching images together. For this purpose we used the Zeiss MosaiX software. To ensure that the film is flat in the focal plane it was clamped between two object plates. An important adjustment at the microscope is the condensor aperture that determines the depth of focus. For the Axio Vert.A1 the depth of field varies approximately between 2 and 45 μm. An optimal setting would mean an illumination of the film's sensitive layer only. We found that the contrast is best if the aperture is 80% opened. Unfortunately the aperture also has a strong influence on the light intensity and thus once adjusted the aperture should not be touched during the measurement. Image brightness can be reproducibly regulated via LED voltage and exposure time of the CCD-camera.

The image intensity is obtained as an integer value (grey value G) between 0 and 4095 (12-bit). Measuring the intensity as a function of LED-voltage or camera exposure time always yielded a linear behaviour up to a grey value of around 2800 (see figure 4.1). Above, the grey value started to saturate. For this reasons we ensured that in all measurements the camera readout did not exceed this value. On the other hand the grey value should be large enough to reduce the noise. If the dynamic range is not sufficient, different exposure times or LED voltages can be used for acquisition and the results be calibrated to each other.

Unfortunately the illumination of the field of view is never completely homogeneous. After image acquisition all single images were shading corrected and imperfections in the film caused by dust and scratches were eliminated. The latter was achieved by excluding pixels that lay outside 5 standard deviations of the surrounding pixels. For the shading correction a reference image R was taken from an unirradiated film and a dark image D where the illumination of the microscope was turned off to account for the average background noise level. The raw image B_{raw} was corrected with the equation

$$B_{corr}(i,j) = \frac{B_{raw}(i,j) - D(i,j)}{R(i,j) - D(i,j)} \langle R - D \rangle . \tag{4.3}$$

The argument (i, j) denotes the pixel position in the images. The angle brackets indicate an averaging over the image. If the exposure time was changed between dark image, reference image and sample image the brightness needs to be calibrated. Due to the linear response of the CCD camera grey values taken at a exposure time t can easily be converted to the grey value at

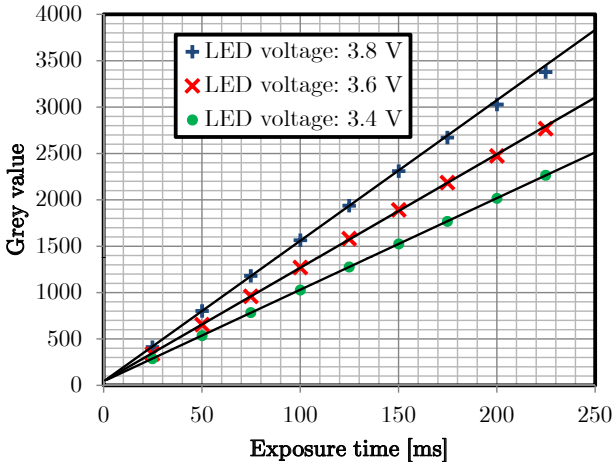

Figure 4.1 – Grey value response of the camera depending on the exposure time for different LED voltages. There is a clear linear behaviour observable. Up to a grey value of 2800 the deviation from the linear response is less than 1%. Above this value the response saturates. In all cases the grey value off-set at exposure time 0 ms is 43.5 presumably due to the dead time of the system and background light/noise.

exposure time t_0 by linear scaling,

$$G_0 = \frac{\alpha t_0 + \beta}{\alpha t + \beta} G. \tag{4.4}$$

Here α and β represent the regression parameters for the grey value dependence on the exposure time (figure 4.1).

The microscope resolution was higher than the resolution actually required and images were averaged over several pixels. Parallel to the microbeams where spatial resolution is not as important averaging took place over 775 pixel (= 1.000 mm) and perpendicular to the microbeams always 4 pixel were summarised (= 5.16 μm).

4.2.5 Calibration curves

For quantitative data the actual measurement films always need to be accompanied by calibration films. It is advisable to take measurement and calibration films from the same row parallel to the coating application.

Calibration films were exposed with homogeneous 2×2 cm^2 fields at a reference depth of 2 cm in a 30×30×12 cm^3 solid water phantom. Under these conditions also the measurements with ionisation chambers were performed. Nevertheless the dose is not completely homogeneous across the field. It is highest in the centre and lowest at the field edges. Therefore after the scan of the calibration films the central, minimal grey value G_0 was approximated by fitting a quadratic function

$$G = G_0 + \alpha(i-a)^2 + \beta(j-b)^2; \tag{4.5}$$

to the acquired image, where i and j are the image coordinates and α, β, a, b are fitting constants.

A calibration curve between film grey values and the dose measured with ionisation chambers was obtained by identifying the parameters p_1, p_2 and p_3 in equation

$$D(G) = p_1 + \frac{p_2}{G - p_3}, \tag{4.6}$$

that fitted the measurement best. Herein we follow the rational fit approach that Lewis [98] proposed.

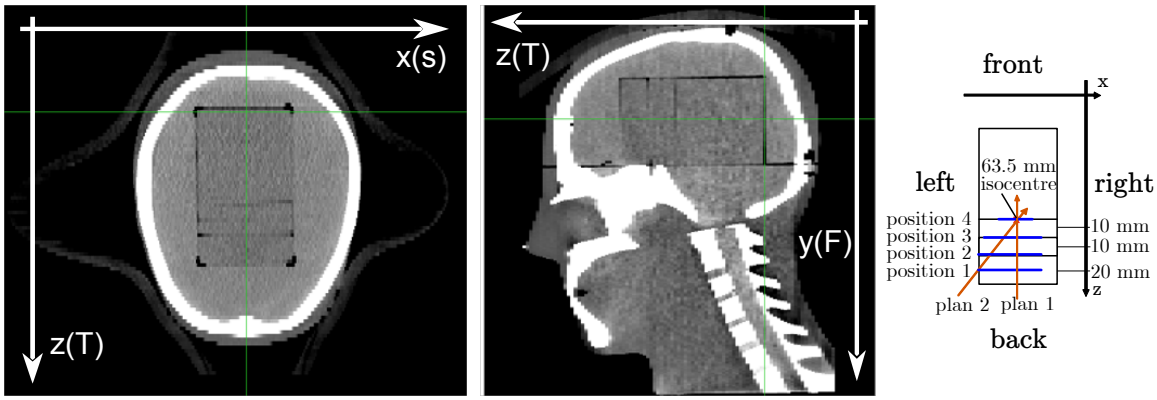

Figure 4.2 – The left two figures show a transversal and a sagittal view of the human head phantom CT scan. On the right a sketch of the inlay and the film positions used for the measurements are shown.

4.2.6 Phantoms and experimental set-up

A homogeneous water phantom

The method was applied at ID17 of the ESRF to measure the dose in a 30×30×12 cm^3 solid water (RW3) phantom, where the short axis was parallel to the beam direction. Both, HD-V2 and HD-810 films were used for the measurement and their performance was compared. Films were positioned at 3, 5, 10, 20, 30, 40, 60 and 80 mm depth and exposed to a 20×20 mm^2 microbeam field formed by the multislit collimator (MSC)[11]. The collimator had 50 μm wide slit apertures with 400 μm pitch. For all measurements the vertical slit upstream the MSC had a 520 μm wide opening. At a storage ring current of approximately 200 mA the irradiation was carried out by moving the target at a constant speed through the beam.

The measurement was done with two different beam set-ups, the preclinical and clinical. For safety reasons and as part of the PASS system (see chapter 1.1.1) additional ionisation chambers were added in the clinical set-up to online monitor the dose rate during irradiation. These additional chambers affect mainly the dose rate but also the spectrum. In the preclinical modus the dose rate per storage ring current was measured as 69.91 Gy/mAs and in the clinical modus 39.37 Gy/mAs.

In order to meet the most sensitive range of the radiochromic films peak doses and valley doses were determined in separate irradiations. Films for the valley dose measurements were irradiated with an 8 times higher peak entrance dose than films for the peak dose measurements.

An anthropomorphic human head phantom

A more realistic set-up was used to validate the therapy planning system. An anthropomorphic human head phantom (CIRS, USA) was first scanned with a CT-scanner and afterwards used for therapy planning in VIRTUOS (see chapter 1.2). The phantom consists of epoxy materials imitating the brain, spinal cord, vertebral disk and soft tissue[i]. CIRS claims that the attenuation coefficients of the materials match those of the real tissue within 1% accuracy between 50 keV and 1 MeV. Figure 4.2 presents CT-scan slices of the phantom. The phantom has got an inlay of 63.5×63.5×104 mm^3 size made up of one 63.5 mm, one 20 mm and two 10 mm high blocks with a width and thickness of 63.5 mm. Between these blocks films can be positioned for measurements.

Two irradiation directions were planned for an exposure with 20×20 mm^2 MRT fields with 50 μm wide and 400 μm spaced microbeams (plan 1 and plan 2). For both exposures the isocentre was in the centre of the inlay in x and y and in z just behind the 63.5 mm high block (see figure

[i]The details can be found on the web page of the company: http://www.cirsinc.com

4.2). Four film positions were used as illustrated in figure 4.2. In plan 1 the field was irradiated from the back and in plan 2 the head was horizontally rotated by 45° compared to plan 1 to obtain a beam entrance from the back left.

Measurements were performed in the preclinical set-up. Calibration and measurement films were always taken from the same row on one film sheet parallel to the coating direction to minimize the effect of the film inhomogeneity. A maximum number of 8 film pieces can be obtained in a row from a single film sheet. The calibration curve was measured with four films at the doses 90, 120, 150 and 180 Gy. The other four films were used to measure peak and valley doses at different depths (positions 1-4, figure 4.2). The peak entrance dose was adjusted in a range between 300 and 10,000 Gy such that the dose to measure was always in the range of the calibration. By varying the scanning speed of the goniometer the different peak entrance doses were obtained (see chapter 1.1). The choice of a rather small calibration range was made to increase the calibration accuracy.

Similar to a real treatment scenario the alignment of the head phantom was carried out on the basis of lead markers located at different positions on the phantom surface. These markers can be identified on the CT image. Prior to the MRT exposure projection images are acquired in situ. On these projections the markers can also easily be located. Mattia Donzelli implemented an algorithm that computes from this information the gantry angles required to deliver the treatment plan.

4.2.7 Measurement of output factors

The dose absorbed in the phantom (patient, animal or sample) is determined by the dose rate and the exposure time. The dose rate for a micrometre wide beam, however, is not directly accessible by absolute dosimetry. Only the dose rate of large field sizes can reliably be measured with ionisation chambers. Output factors link the dose rate of a small beam to that of a large reference field.

The dose calculation of the treatment planning system only provides relative dose values. For a treatment the exposure time (or goniometre speed) needs to be determined from the prescribed dose at a certain depth in the target (usually given as a peak entrance dose at a certain depth), the dose rate measured with ionisation chambers for a large reference field and the output factor that relates both quantities with each other. Furthermore many MRT experiments use non-standard irradiation geometries. One example are pencil beam irradiations[71]. At the moment there is no treatment planning system that allows treatment planning for all possible irradiation patterns. Other standard MRT experiments with mice and rats are lacking complete CT scans. Nevertheless the dose given to the brain of the laboratory animal should be estimated. In all these cases output factors are of outstanding importance. Their measurements with film dosimetry and computation with Monte Carlo methods is, however, delicate.

Due to the small vertical field size and the impossibility to move the source, larger fields can only be created by scanning the sample vertically through the beam (compare chapter 1.1). The dose is determined by the scanning speed v, the slit height h, the electron current I in the storage ring and the specific dose rate $\dot{D}$. $\dot{D}$ is vastly determined by the gap size of the magnetic field of the wiggler, the measuring point in the phantom and the field size. For a certain geometry and field size the dose can be calculated from the equation 1.1

$$D = \frac{\dot{D} \cdot I \cdot h}{v}.$$

The linear relationship between dose and ring current is well established[99,100]. $\dot{D}$ needs to be determined at the beginning of an experiment. For that reason a reference dose rate $\dot{D}_{ref}$ is

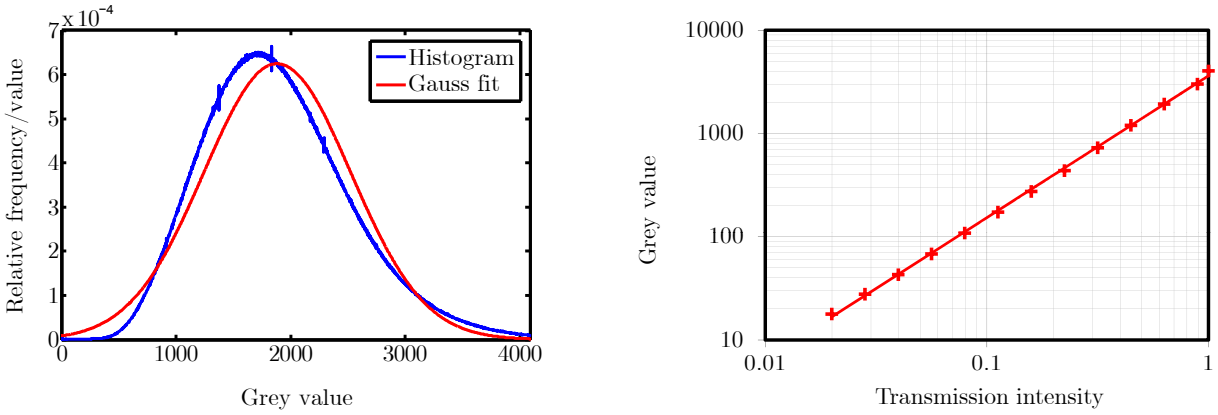

Figure 4.3 – Left: The figure shows a grey value histogram of a homogeneously irradiated film. In comparison to a Gauss distribution (red) the distribution is clearly asymmetric and therefore peak, mean and median grey value differ. Right: The mean grey value exhibits the most linear behaviour over the transmission intensity of a photographic step table, and was hence used in all measurements.

measured under reference conditions for a 20×20 mm^2 field, at 2 cm depth in a large[ii] solid water phantom. The dose for any other field size and depth in a homogeneous phantom can be calculated by multiplication of the reference dose rate with an output factor OF, i.e.

$$D = \frac{\dot{D}_{ref} \cdot I \cdot h}{v} \cdot \mathrm{OF}(\text{field size}, \text{depth}). \tag{4.7}$$

Here we measure output factors for 25, 50, 75, 100, 500 and 1000 μm wide and 20 mm high beams at 2 cm depth in a solid water phantom under preclinical conditions.

The Monte Carlo simulations were carried out with the semi-adjoint approach presented in chapter 3.2.3. The source was defined as a point emitting photons in a single direction. Dose was scored at 2 cm depth in a homogeneous water phantom on a grid with 10 μm bin side length perpendicular to the beam and 1 mm parallel to the beam. As a whole the mesh grid covered an area of 30×30 mm^2 around the beam at 2 cm depth. 10^8 linearly polarised photons were simulated and the interactions were handled as for most other simulations in this work with the Livermore low energy libraries. The photon energy distribution followed the MRT spectrum.

For the determination of output factors the semi-adjoint Monte Carlo approach has the advantage that the calculation for field sizes between 10×10 μm^2 up to 30×30 mm^2 can be handled with a single simulation.

4.3 Results

4.3.1 Calibration curves

Grey values of the microscope film scans scatter over a broad range. A typical histogram of a homogeneously irradiated film is presented in figure 4.3 (left). The grey values do not follow a normal distribution (red curve) but are asymmetrically distributed; mean and maximum do not coincide. We scanned a photographic step tablet (KODAK, Photographic Step Tablets No. 2) with the microscope and plotted the logarithm of the grey value against the optical density. The optical density (OD) is defined as

$$OD = -\log_{10}(I/I_0), \tag{4.8}$$

[ii] Ideally would be a solid water phantom of infinite size. In this sense "large" refers to a size where the change in the backscattering contribution due to the phantom limitations can be neglected.

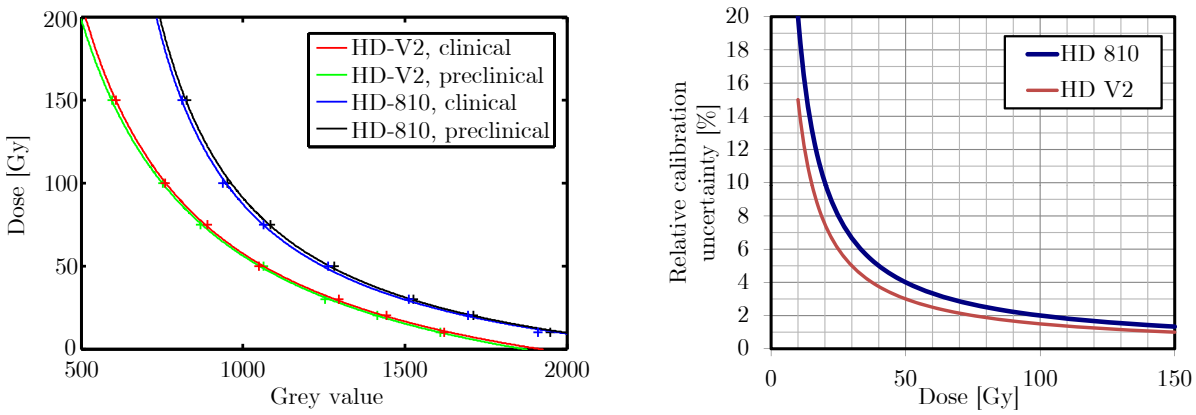

Figure 4.4 – Left: Calibration curves for HD-V2 and HD-810 films in the clinical and preclinical set-up are shown. The differences between the clinical and preclinical set-up are probably due to the energy dependence of the film sensitivity. Right: The relative calibration uncertainty is higher for HD-810 films than for HD-V2 films. Measurements should be carried out at higher doses.

with I_0 as the incident and I the transmitted beam intensity. The best linear behaviour was found between the mean grey value and the optical density (figure 4.3, right). Deviations from linearity are smaller than 7%.

Calibrations curves for the dose measurement in a homogeneous water phantom are presented in figure 4.4A. Deviations between the fit and the data are below 1.5 Gy for HD-V2 films and below 2 Gy for HD-810 films. In figure 4.4B the resulting relative calibration uncertainty is plotted over the dose. To keep the calibration uncertainty below 3% measurements should be performed at doses above 50 Gy for HD-V2 films and above 70 Gy for HD-810 films.

Interestingly the calibration curves for the clinical and preclinical set-up are not identical. The reason is probably the spectral shift towards lower energies when additional material is added into the beam path. The response of Gafchromic® films is energy dependant at low photon energies. Alternatively an inaccurate absolute dose measurement with the ionisation chambers could be considered. However, the shift from the clinical to the preclinical set-up has different directions for HD-810 and HD-V2 films. HD-V2 films seem to become more sensitive moving towards lower energies, the HD-810 films become less sensitive. The problem will be further discussed in section 4.4.3.

4.3.2 Measurement of an MRT field in a homogeneous solid water phantom

The microscope scans taken from films exposed to MRT fields had a resolution of 1.29 μm. For further processing we reduced the resolution to 5 μm perpendicular and 1 mm parallel to the beams and hence averaged over 4×775 = 3100 pixels. Doses of the clinical and the preclinical irradiation were not significantly different. The modification done to the photon spectrum by the additional ionisation chambers does not cause changes in the dose absorbed beyond the measurement uncertainties of the films. Hence averaging was performed over both measurements.

In figure 4.5 (left column) peak and valley doses are shown as depth dose curves. A value at a certain depth is obtained by averaging over the central 13 beams and 7 mm parallel to the beams. The result of the Monte Carlo calculation is shown as a solid line. The average over all 4 measurements (both films in the clinical and preclinical set-up, respectively) are presented by blue crosses. Except for the peak dose at 80 mm depth Monte Carlo calculations are within the measurement uncertainty which is determined as standard deviation from the 4 data points. Although there is no systematic difference between the clinical and preclinical beam setting, HD-V2 films measure a higher peak dose while HD-810 films measure a higher valley dose. Consequently the deduced peak to valley dose ratios (PVDRs) are higher for HD-V2 films and

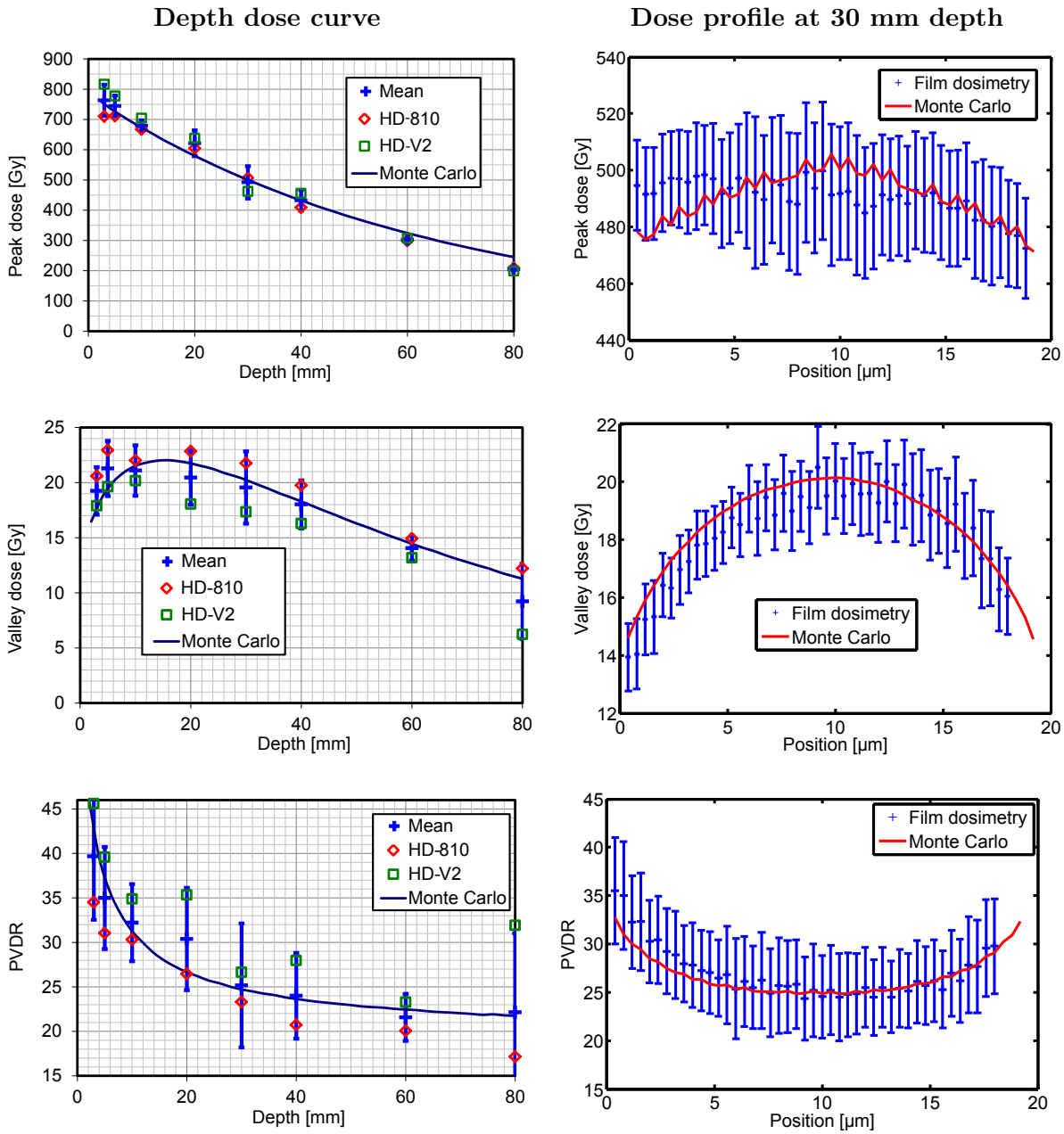

Figure 4.5 – The figures show comparisons between film dosimetry and Monte Carlo dose calculations for a 20×20 mm^2 MRT field in solid water. The beam spacing and beam width at the collimator were 400 μm and 50 μm, respectively. The left column presents depth dose curves and the right column profiles perpendicular to the microbeam planes through the field centre at 30 mm depth. From top to bottom peak dose, valley dose and PVDR are shown.

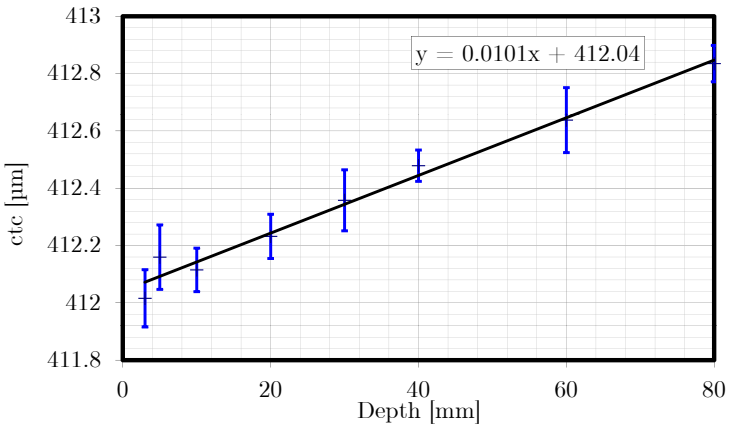

Figure 4.6 – The centre to centre distance was measured at different depth and reflects the small but measurable divergence of the synchrotron beam.

lower for HD-810 films. The differences are probably caused by different film sensitivities at low photon energies.

In contrast to the microdensitometer measurements the microscope allows a two dimensional readout of the entire microbeam fields. Therefore we were able to acquire peak dose, valley dose and PVDR as profiles across the MRT field. In the right column of figure 4.5 profiles of the microbeam field at 30 mm depth are shown. The profiles are taken from the centre of the microbeam field by averaging over 7 mm parallel to the microbeams and over both film types in the clinical and preclinical set-up (4 films). Error bars present 95% confidence intervals which were deduced from the statistical noise in the data. However, they do not include systematic errors due to calibration uncertainties or film inhomogeneities. In the field centre there are photon scattering contributions from all directions. Valley doses are therefore higher in the field centre than at the field edges. Changes in the peak dose on the contrary do not depend on the photon scattering but are only determined by the primary photon fluence and inclined incidence of the photons to the collimator (see chapter 2). Therefore the relative peak dose changes are smaller across the MRT field and the PVDR gets higher at the field edges. The measured profiles match the Monte Carlo simulated doses within the measurement uncertainties. The peak dose variations across the MRT field seen in the Monte Carlo result are less than 5% and could not be verified by film dosimetry.

Due to the high resolution of the microscope it was also possible to measure the beam divergence in the solid water phantom. To this end the average beam to beam distance was determined for the 4 measurement series in all depths. The result is plotted in figure 4.6. Error bars are gain 95% confidence intervals. Linear regression gives a beam divergence of $\tan\alpha = (1.01 \pm 0.06) \cdot 10^{-5}$, where we denote the opening angle as α. A value of $1.02 \cdot 10^{-5}$ is expected from the 39.3 m distance between wiggler source and MSC and the slit spacing of 400 μm at the MSC. The measured ctc of the microbeams at the beam entrance is $(412.04 \pm 0.02)\,\mu m$. The distance between sample and MSC is 1.2 m and consequently ctc at the goniometer should be $412.21\,\mu m$. The difference encountered can be attributed to an improper alignment of the phantom surface with the isocentre of the goniometer.

4.3.3 Dose measurements in a human head phantom

The dose calculation in the human head phantom was handled similar to that in a real treatment scenario. The peak entrance dose D_{PE} for 50 μm wide beams at 2 cm depth in a water phantom

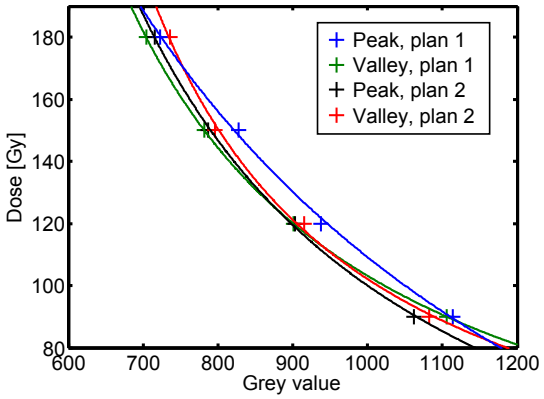

Figure 4.7 – Calibration curves for peak and valley dose measurement in plan 1 and plan 2 in the human head phantom.

determined the choice of the goniometer scanning speed v from equation 4.7. The dose calculation algorithms deliver relative dose values only and hence they need a calibration.

For the Monte Carlo dose calculation the dose of the MRT-field was initially simulated in a homogeneous solid water phantom to determine the number of photon histories required for a Monte Carlo dose of 1 Gy at 2 cm depth. This quantity α was found to be

$$\alpha = 6.526 \cdot 10^{24}\, Gy^{-1}$$

in the simulation and was used to scale the simulated dose D_{MC} in the human head phantom with N photons by

$$D = \frac{\alpha \cdot D_{PE}}{N} \cdot D_{MC}, \tag{4.9}$$

to obtain the dose D that was actually delivered in the exposure.

Figure 4.7 shows for each of the measurements (two plans with separated peak and valley measurement) calibration curves. The fitting error for all calibration data is below 2%, which is acceptable but not surprising in view of just four data points and three fitting parameters in equation 4.6. Large deviations are between the different calibration curves. If we had used a single calibration curve for all measurements the calibration error would have been roughly in the order of 10%.

A comparison between film dosimetry and dose calculation is presented in figure 4.8. Depth dose curves and profiles for peak and valley dose are presented. Measurements were unfortunately only possible in the limited depth range of the inlay in the phantom. Dose calculations are, however, performed on the whole phantom. Doses were calibrated to 100 Gy peak entrance dose. Depth dose curves were taken from the centre of the microbeam field by averaging over the central four microbeams (valleys) and 7 mm parallel to the beams. In plan 1 the agreement between measurement and Monte Carlo simulation is in the peak doses better than 4% difference and in the valley better than 9% difference. For plan 2 the peak dose at 26 and 44 mm is in the measurement 14 and 12% lower than in the Monte Carlo simulations. At the other two depths the agreement is better than 2%. Valley dose differences between measurement and Monte Carlo are below 10%.

The profiles shown in figure 4.8 were taken at the centre of the microbeam field averaging over 7 mm parallel to the microbeams. The uncertainties indicate 95% confidence intervals derived from the statistical variations on the film. They do not account for systematic errors such as calibration uncertainties or film inhomogeneities. For treatment plan 2 there are considerable deviations in the profiles at positions 1 and 2. The dose measurement was performed with an

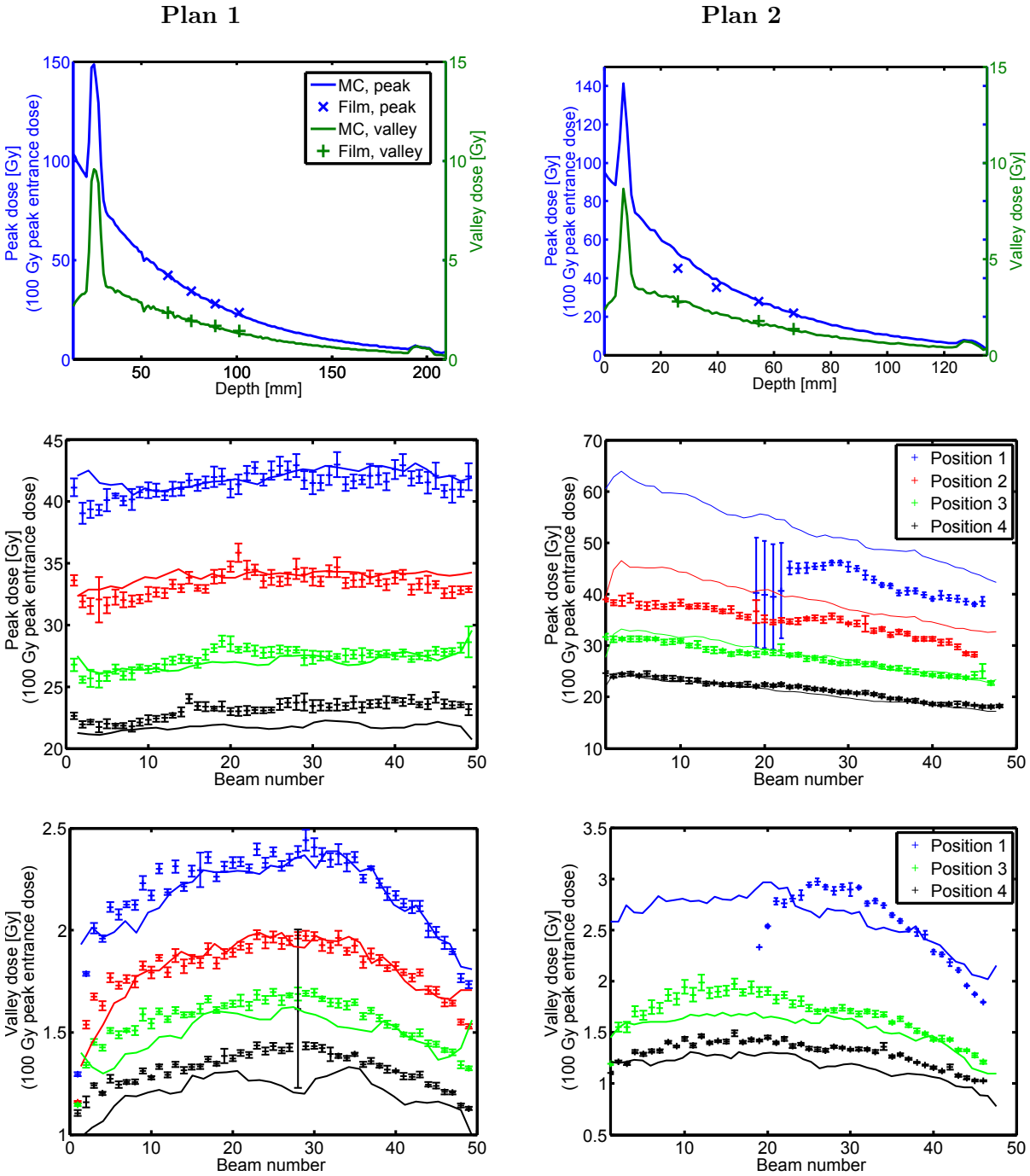

Figure 4.8 – The graphs show the measured and computed dose distribution of treatment plan 1 on the left and treatment plan 2 on the right. At the top the depth dose curves for peak and valley doses, in the middle peak dose profiles and at the bottom valley dose profiles are shown. The plotted uncertainties are 95% confidence intervals obtained from the statistical variations on the film.

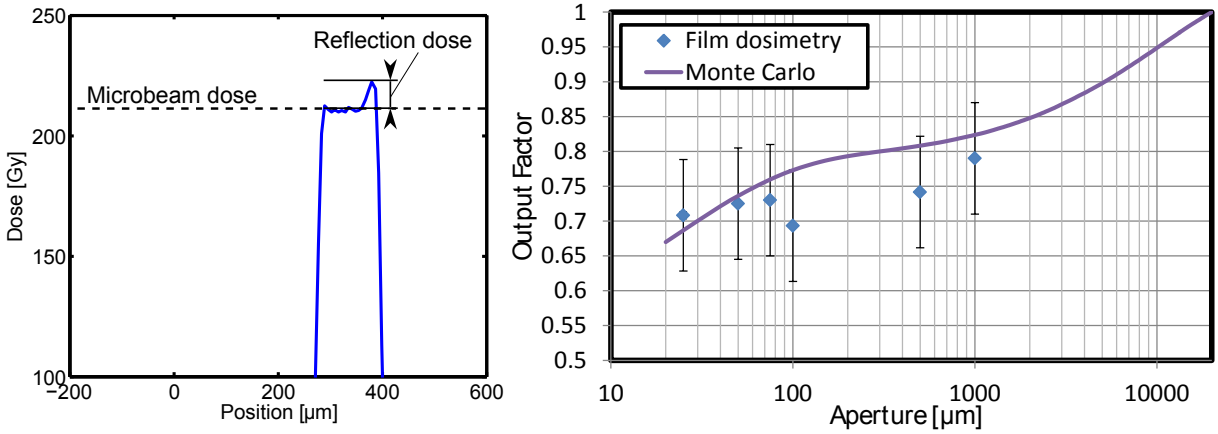

Figure 4.9 – Left: When measuring output factors the peak dose was determined ignoring the reflection at the edge of the microbeam. Right: Output factors determined by measurement and Monte Carlo simulations depending on the aperture size are shown.

angle of 45° oblique to the beam. Therefore the radiological depth for the beams at one film edge was significantly lower than for beams at the other film edge. This is reflected by a dose gradient in the data. As illustrated in figure 4.2 (right) the centre of the field at measurement position 1 was exactly at the inlay boundary and hence the measurement could only be performed from beam 20. Furthermore the measurements of the first 4 beams have larger uncertainties which were very likely caused by strain and damage when the film sheet was cut.

4.3.4 Measurement of output factors

To calibrate the measurement four films were exposed to homogeneous fields of 100, 200, 250 and 300 Gy. Equation 4.6 was used to fit these values with a calibration uncertainty of up to 3%. In the microscope scans of the microbeam films an additional dose peak is observed at one side of the microbeam. This peak was very likely caused by total external reflection (see chapter 2.4). Therefore it was subtracted in the determination of the microbeam dose as illustrated in figure 4.9 (left).

The output factors were two times independently measured. The average difference between both measurements was 0.08. The result is presented in figure 4.9 (right). The output factors for 20 mm high fields are given with respect to a 20×20 mm^2 reference field at 20 mm depth. Therefore the Monte Carlo simulation approaches one at 20 mm aperture size. The Monte Carlo result shows an increase of the output factors from 0.67 at 20 μm aperture size to 1 at 20 mm. Between 100 and 1000 μm the slope flattens creating a turning point at approximately 300 μm.

4.4 Discussion

4.4.1 Uncertainty analysis

There are three main components that contribute to the measurement uncertainty.

1. Statistical noise caused by microscopic variations in the film and detector noise of the microscope CCD camera.

2. Macroscopic Film inhomogeneities and not corrected inhomogeneous illumination.

3. Calibration uncertainties leading to systematic errors. These errors influence the whole series of film measurements that rely on the calibration. The error may express itself in a dose off-set in a certain dose-range.

We estimated the influence of the first and second uncertainty by analysing the broad beam irradiated calibration films. In the measurement films averaging was carried out over an image subset S of N = 3100 (4×775) pixels to reduce the statistical noise. A random statistic noise should consequently lead to an error of the mean μ_S of

$$\sigma_{\mu_S} = \frac{std(S)}{\sqrt{3100}}. \tag{4.10}$$

If a film is completely homogeneous and homogeneously irradiated, than for a set of subsets $\{S_i\}$ with N pixels from the image it is to expect that the standard deviation of means equals the mean of standard deviations, i.e.

$$std(mean(S_i)) \approx mean(std(S_i)/\sqrt{N}). \tag{4.11}$$

It follows directly from the law of large numbers when all the S_i are independently and identically distributed random variables. If there are inhomogeneities in the film than

$$std(mean(S_i)) > mean(std(S_i)/\sqrt{N}). \tag{4.12}$$

Here we can identify the statistical noise with

$$\sigma_{Stat} = mean(std(S_i)/\sqrt{N}) \tag{4.13}$$

and the total uncertainty with

$$\sigma_{total} = std(mean(S_i)). \tag{4.14}$$

The difference σ_{inhom} is caused by inhomogeneities and can be deduced from

$$\sigma^2_{total} = \sigma^2_{inhom} + \sigma^2_{Stat}. \tag{4.15}$$

Unfortunately the dose is even for the broad beams not quite homogeneous, which was the reason why we fitted the scanned dose with equation 4.5. How can we overcome this problem?

If the actual profile of the grey values in the film was known the problem could easily be solved. The dose profile seen by the calibration films should have several symmetries. It should have a four fold rotational symmetry and also a mirror symmetry[iii]. Therefore the information in the film contains in fact an eight fold measurement of the broad beam profile. We exploited this knowledge by averaging over all 8 orientations of the dose distribution. The resultant grey value profile was subtracted from the film scan and the statistical analysis outlined above yielded the influence of inhomogeneities, and statistical noise. Of course the method is not very accurate and yet it allows a quantitative estimate of the uncertainty contributions.

The calibration error was estimated before as $\Delta D \approx 2\,Gy$ for the HD-810 films and $\Delta D \approx 1.5\,Gy$ for the HD-V2 films. The calibration uncertainty depends of course on the dose separation of the calibration doses and whether the calibration films stem from the same film sheet. The observation made in figure 4.7 highly recommends to take the calibration and measurement series from the same row along the coating direction.

The dose dependent contribution of all the errors is depicted in figure 4.10. The graphs suggest that measurements should be carried out at higher doses. At low doses calibration errors

[iii] We ignore here an influence of the beam polarisation, which is very small when the field edges are excluded. (see chapter 2)

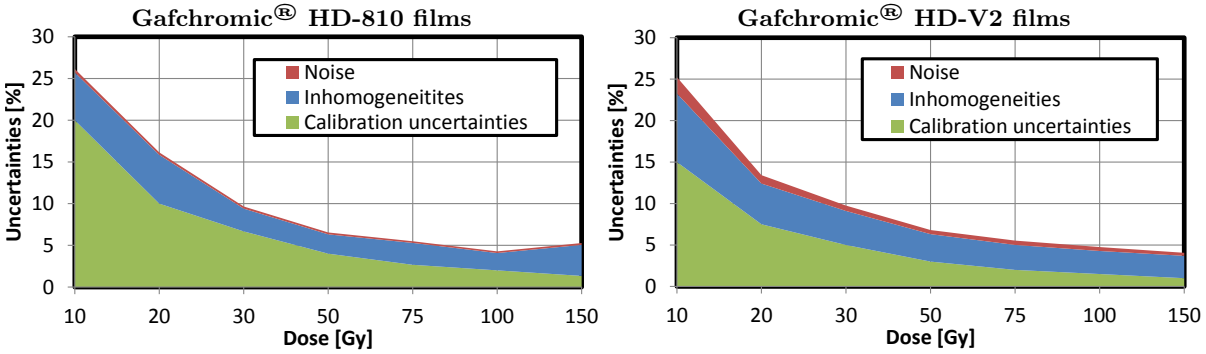

Figure 4.10 – The figures show the measurement uncertainties of radiochromic film dosimetry in MRT at a resolution of 5000 μm^2 for HD-810 (left) and HD-V2 films (right) classified according to the contributions of statistical noise, film inhomogeneities and calibration uncertainties.

have a large influence. At higher doses the effects of film inhomogeneities dominate. Statistical noise due to microstructure and granularity of the film is of minor importance. Overall the HD-V2 and HD-810 films are not very different in their performance. In HD-V2 films inhomogeneities and statistical noise are a bit higher than in HD-810 films. This is however balanced by a higher calibration accuracy. In principle 5% accuracy in dosimetry is possible when measurements are carried out at doses above 100 Gy. For that reason we chose for the dosimetry in the human head phantom a dose range of 90 to 180 Gy.

The error analysis does not take into account film-film variations or dose inhomogeneities on larger spatial scales. In view of the large variations in the calibration data presented in figure 4.7 these effects should not be underestimated. The error induced by statistical noise appears to be very small in this analysis. It should be noted, however, that this strongly depends on the resolution and scales with

$$\sigma_{Stat} \sim A^{-1/2}, \tag{4.16}$$

where A is the area of averaging which was 5 μm×1000 μm = 5000 μm^2 for all measurements in this work. If a high resolution of 5 μm is required in both directions than the statistical error is going to be between 5% at 150 Gy and 28% at 10 Gy for the HD-V2 film and between 3% at 150 Gy and 6% at 10 Gy for the HD-810 film. Here the HD-810 film has got a clear advantage over the HD-V2 film.

4.4.2 Grain Size

The resolution of the presented technique depends on the microscope and the grain size of the films. The microscope resolution is better than 1 μm and does not present a limitation. The film resolution, however, is limited by the crystal grain size. The manufacturer guarantees a resolution of at least 5 μm. We estimated the grain size by calculating the two dimensional autocovariance function as suggested by Buscombe et al.[101] for granularity measurement in sediments which was implemented in the bachelor thesis of Katrin Welsch[102] at our institute. For this purpose we Fourier transformed the mean subtracted image of a homogeneously irradiated film. The absolute value of the Fourier transform is squared to obtain the variance spectrum. The autocovariance function is normalised by its maximum. As suggested by Buscombe et al.[101] we defined the grain size as the area where the normalised autocovariance function exceeds 0.5. This led for the HD-810 films to an average grain diameter of 1.95 μm and for the HD-V2 films to a grain diameter of 2.02 μm. The autocovariance function is radially symmetric, meaning that the grains are isotropic (circular) and also isotropically spread. It can therefore be expected that the physical

imitations of the presented method is reached at around 2 μm. Both film types are comparable in terms of their granularity.

4.4.3 Energy dependence of the films

It was reported previously that Gafchromic® films are sensitive to the photon energy for energies lower than approximately 100 keV[91,103]. Butson et al.[91] investigated the energy dependence of MD-55 Gafchromic® films and observed a drop of sensitivity to 60% at 30 keV compared to 120 keV effective photon energy.

In order to assess the energy dependence of the used Gafchromic® films we exposed them to 20 Gy photon dose of an x-ray tube at tube voltages of 100, 150, 200 and 250 kV and scanned the films with the microscope. The dose rate was monitored with a semiflex and a soft x-ray chamber. Both chambers agreed within 2%. Grey values were converted to dose using the calibration curves and are plotted in figure 4.11 (left). More interesting is, however, the spectral sensitivity.

We simulated the spectrum of the x-ray tube in Monte Carlo simulations in Geant4, version 9.3.p02. Unlike in all other Monte Carlo simulations we used the PENELOPE physics libraries with an energy cut-off of 1.7 keV because they turned out to be more accurate for the simulation of the characteristic x-ray spectrum. The anode material was tungsten and the beam was filtered with an 0.1 mm copper filter. The simulated spectra can be found in appendix C. The film sensitivity η_S towards an intensity spectrum g(E) can be calculated from the monochromatic sensitivity η(E) via

$$\eta_S = \int_{E=0}^{E_{max}} g(E)\eta(E) \tag{4.17}$$

Without additional assumptions an infinite amount of measurements would be necessary to determine η(E). However, the energy dependence of the film sensitivity is mainly influenced by differences in the energy absorption between water and the film material. Since the polymeric film consists of light elements only there are no discontinuous sensitivity changes to be expected in the considered energy range.

Hence we approximated $\eta(E)$ as a quadratic function. From the four measurements a system of 4 linear equations with 3 variables (the coefficients of the polynomial) is formed. It can be used to calculate both, the coefficients of the polynomial and also the uncertainties.

Since it was shown previously that Gafchromic® films have no energy dependence above 100 keV, we normalised the efficiency at 100 keV to 1 and show the result for the spectral sensitivity in figure 4.11 (right). The HD-810 film shows a strong sensitivity decrease with decreasing energy which was also reported for MD-V2-55 films[91]. The HD-V2 film, however, has a much lower spectral dependency that slightly increases with decreasing energy. However, the increase of about 10% towards 40 keV is not significant in our data. The result corresponds to the weak energy dependence of EBT2 films which was shown by Butson et al.[104]. They found a sensitivity increase of 5% when reducing the photon equivalent energy from 95 keV to 36 keV. The different behaviour might be explained by the differences in the active materials of the two film types. Both, HD-810 and MD-V2-55 films have pentacosa-10,12-dyinoic acid (PCDA) as active material[105] whereas EBT2 and HD-V2 films use the lithiumsalt LiPCDA.

Of course the result for the spectral sensitivity is far from being accurate and only intended to give a general trend and proof of principle. Nevertheless it shows that HD-810 films have a strong sensitivity drop at low energies. At 40 keV the sensitivity is just about 50% of the sensitivity at 100 keV photon energy. HD-V2 films on the other hand are much less sensitive to photon energies. At 40 keV the sensitivity has increased by about 10% compared to 100 keV. In this respect HD-V2 films should be preferred when measuring doses at low photon energies.

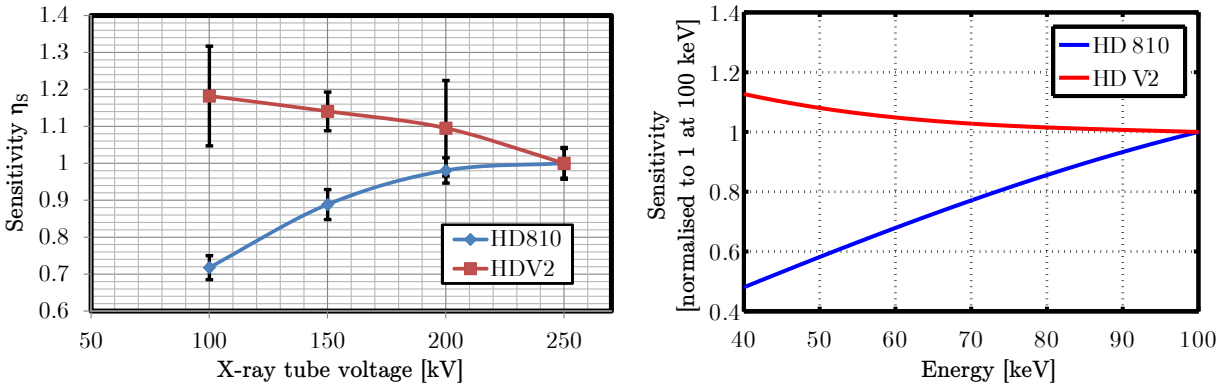

Figure 4.11 – The left graph shows the sensitivity of HD-810 and HD-V2 films to the energy spectrum of an x-ray tube operated at 100, 150, 200 and 250 kV acceleration voltage. On the right the inferred spectral sensitivity is shown.

4.5 Conclusions

In this chapter it was shown that film dosimetry in combination with microscopy is a dosimetry tool that meets the requirements set by MRT. However, the method is error prone and special care must be taken when evaluating the data. We analysed in detail the uncertainties and compared Gafchromic® HD-V2 and HD-810 films. As an example dosimetry was performed in a solid water phantom, a human head phantom and for the determination of output factors.

As three main components of measurement uncertainties we identified and quantified statistical noise, film inhomogeneities and calibration uncertainties. Calibration uncertainties dominate especially at low doses for both films and fall below 3% at doses above 50 and 70 Gy for HD-V2 and HD-810 films, respectively. Inhomogeneities are the second largest source of uncertainties. Measurement and calibration should be done on the same film sheet and ideally in one row parallel to the coating direction in the fabrication process. Otherwise uncertainties of up to 10% have to be expected. With respect to these parameters HD-V2 and HD-810 films are very similar.

Differences were, however, observed in the energy dependence and the statistical noise. HD-810 films show a strong drop of sensitivity when moving towards lower energies. At 40 keV the sensitivity is just half of that at 100 keV photon energy. HD-V2 films, on the other hand, have just a very weak energy dependence in the range between 40 and 100 keV and their sensitivity seems to slightly increase with decreasing photon energy. The effect of different film sensitivities was for example observed in the calibration curves at the clinical and preclinical set-up of the solid water phantom measurements.

The statistical noise in HD-V2 films is significantly higher than in HD-810 films. At the resolution of 5×1000 μm^2 used in this chapter the statistical noise is of minor importance and usually much less than 1%. If the resolution of 5 μm is required in two directions than the statistical noise will impair the measurements and may render the use of HD-V2 films impossible.

The dose of a microbeam field was determined in a solid water phantom. Within the measurement uncertainties the peak and valley dose measurements agree with Monte Carlo calculations. The Peak dose was determined with an accuracy of better than 5% and the valley dose with an accuracy between 10 and 15%. Problematic was, however, a systematic difference between HD-V2 and HD-810 film measurements. While valley doses were higher on HD-810 films, peak doses were higher on HD-V2 films. The additional dosimeters in the beam line in the clinical set-up did not measurably influence the dose in the phantom.

To validate doses predicted by our treatment planning system two plans were created and delivered to a human head phantom. To this end we went through the entire treatment procedure: CT scan with lead markers, planning in VIRTUOS, adjustment of orientation according to the

acquisition of projection images and finally exposure with a certain peak entrance dose. The comparison between the dose of the treatment planning system and dosimetry yielded agreement within 10% in the valley doses and 4% for 6 of 8 measuring points in the peak dose. In one of the plans two measuring points in the peak dose showed, however, differences of 12 and 14% respectively.

The dose calculation in the human head phantom exhibited a strongly enhanced dose in the skull. Especially in the valley dose the dose is increased by more than a factor of two. This may be a severe problem in a future treatment of human patients.

Finally we determined output factors and compared them to Monte Carlo simulations. Unfortunately the measurement uncertainties are still in the order of 10% and further repetitions are necessary to show that computation and measurement agree with smaller uncertainties. The dependence of the output factor on the beam size is very sensitive to the underlying physical processes. The polarisation has for example an influence of up to 2.5% (data not shown here). Two regions in the output factor course can be distinguished. For apertures that are smaller than around 300 μm electron scattering dominates the reached maximum dose. The smaller the beam the more electrons scatter out of it and thus reduce the dose in the beam. At larger field sizes the reached maximum dose is dominated by photon scattering. An equilibrium is not reach at the reference field size of 20×20 mm^2.

Chapter 5

Towards a biological understanding of MRT

5.1 Introduction

5.1.1 Basics of radiobiology

Effects of ionising radiation

[i]Ionising radiation can be classified into directly ionising radiation and indirectly ionising radiation. Directly ionising radiation such as proton or electron beams have the ability to directly ionise atoms and molecules. Indirectly ionising radiation such as x-ray or γ-rays produce secondary particles (usually electrons) that in turn ionise. In biological targets they may knock out electrons in molecules on their path and affect in particular water, as the most prevalent compound in living organisms,

$$H_2O \xrightarrow{\gamma} H_2O^+ + e^-. \tag{5.1}$$

This primary water ion has a very short lifetime and will react with water molecules to form a hydroxyl radical

$$H_2O^+ + H_2O \longrightarrow H_3O^+ + OH\cdot. \tag{5.2}$$

Free radicals are atoms or molecules with an unpaired electron. They are very reactive and will induce damage in other molecules such as proteins and the genetic material.

Deoxyribonucleic acid (DNA), the carrier of the genetic information has been proven to be the most sensitive target with respect to ionising radiation. During evolution various protection and repair mechanisms developed to shield the DNA from alteration and damage. Nevertheless already low doses of ionising radiation are able to cause, either by direct hits or indirectly by the production of free radicals, unrepairable damage to this molecule. This may lead to cell death or the inability of the cell to divide and proliferate.

The dose D_0 that creates on average in every cell 1 lethal lesion takes for most mammalian cells values between 1 and 2 Gy. D_0 creates on average 40 double strand breaks (DSBs), around 1000 single strand breaks (SSBs) and over 1000 base damages per cell. Still, most of these lesions are tackled by various DNA repair mechanisms and 37% of the cells survive this dose (Poisson statistics). Base damages and SSBs are almost completely repaired. The much more complex double strand breaks, however, were shown to decide upon cell survival.

[i]This section follows in large parts Hall and Giaccia [106].

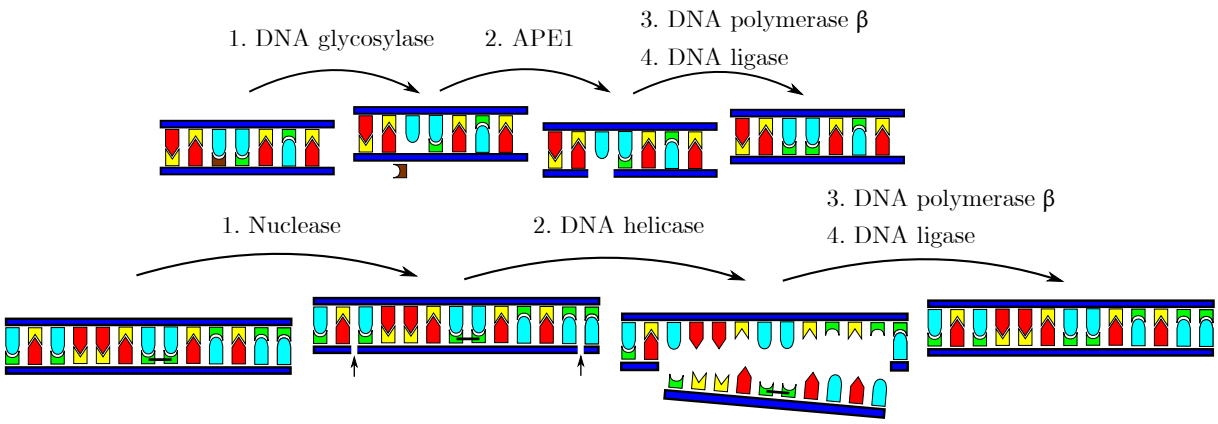

Figure 5.1 – Top: *Base excision repair* repairs mutations of single bases in four steps. Bottom: *Nucleotide excision repair* replaces for example pyrimidine dimers and other damages affecting more than one base. The figure was adapted from Hall and Giaccia [106].

DNA repair pathways

There are different DNA repair pathways working in parallel in the cell and not all of them are completely understood. Most of our knowledge on DNA repair mechanisms stems from mutations in certain genes and how they change the radiation sensitivity. Base damages are fixed by the base excision repair pathway (BER) or the nucleotide excision repair (NER).

In the *base excision repair* a single base mutation is repaired (see figure 5.1). These single base mutations can arise after chemical alteration of bases, e.g. depurination of guanin or adenin and desamination of cytosin. The repair process works in 4 steps. First the base is removed by glycosylase or DNA lyase. Afterwards the sugar residues are removed by APE1 (apurinic endonuclease 1) and the correct nucleotide is inserted by DNA polymerase β. In a last step ligation is accomplished with DNA ligase III-XRCC1 (X-ray repair cross-complementing protein 1). In the case that more than one mutation occurred the repair synthesis is performed by RFC (replication factor C), PCNA (proliferating cell nuclear antigen) or DNA polymerase δ/ε. Overhanging structures are removed by flap endonuclease 1 (FEN) and the strands are joined by ligase I.

Nucleotide excision repair (NER) removes adducts such as dimers from the DNA strand (see figure 5.1). Typical lesions tackled by this repair pathway are dimers of two bases, e.g. pyrimidindimers or covalent bonds between bases and large carbohydrates. The repair can be divided in two types, NER related to transcription (TCR, transcription coupled repair) and a general repair (GGR, general genome repair). The process is for both types very similar. The lesion is recognised and the damaged DNA strand is cut on two positions bracketing the lesion. The damaged region which typically counts between 24 and 32 nucleotides is removed and repair synthesis and DNA ligation replaces the removed part and rejoins the insert.

DNA double strand repair has two basic processes, homologous recombination repair (HRR) and nonhomologous end joining (NHEJ). Which pathway is preferred depends on the phase in the cell cycle, and they do not exclude each other. In both cases ATM (ataxia-telangiectasia mutated) and ATR (Rad3-related) are recruited to the DNA strand breaks. The proceeding of the cell in the cell cycle is stopped. HRR requires for its function a copy from an undamaged homologous chromatid or chromosome. Therefore it does only work after DNA replication in the late S- or G2-phase of the cell cycle. Its primary function is to repair and restore the functionality of replication forks with DSBs. ATM phosphorylates BRCA1 (breast cancer tumour suppressor protein) which is recruited to the DSB. The enzyme MRE11 (and perhaps others) resects one strand resulting in a 3' single strand end of the DNA which becomes the binding site for Rad51.

Endonuclease resection produces two RPA-coated single strand overhangs. BRCA2 is attracted to the DSB by BRCA1 and facilitates loading of Rad51 onto RPA-overhangs. Rad51 forms nucleofilaments and catalyses strand exchanges with the complementary strand in the undamaged chromosome. Further paralogues of Rad51 bind to RPA-coated single stranded region and recruit Rad52, which is protecting against exonucleolytic degradation. Rad54 unwinds the double strand molecule. One of the broken strands is clamped between the intact homologous strands forming so called "holiday junctions". Afterwards DNA-synthesis starts. In nonhomologous endjoining (NHEJ) ATM and ATR activate an NBS/MRE11/Rad50s protein complex for the resection of the DNA ends. This complex can be blocked and controlled by 53BP-1. At the same time H2AX is phosphorylated to γH2AX. The lesion is recognised by the KU-proteins that bind to the DNA DSB ends. DNA-PKcs (protein kinase catalytic subunit) is recruited. The ends are processed, overhangs and hair pins are removed by protein complexes summarised in the term "Artemis". Polymerases (μ or λ) bridge the DNA-ends and synthesise to fill the gaps. Finally ligation follows by the PNK/XRCC/DNA-ligase IV/XLF complex. NHEJ is a very error-prone signalling pathway. However, misrepaired double strand breaks do not necessarily affect the cell. Most of the DNA molecule consists of non-coding parts, i.e. parts that do not contain genes, or genes that are not actively expressed in the cell. Changes in these regions will not impair cell survival.

Apart from the described repair pathways there exist also *crosslink repair pathways*, that deal with DNA-DNA or DNA-protein cross links and *mismatch repair* (MMR) that remove base-base mismatches or insertion mismatches.

Cell death and cell survival curves

Un- or misrepaired DNA can cause cell death. For radiotherapy the dose dependent cell survival probability is an important quantity. However, cell death is ambiguous and can be defined in various ways. Cell dying can occur via different processes and not all of them lead consequently to a removal of the cell from the tissue.

A very controlled cell death mechanism is *apoptosis*. The word apoptosis comes from the Greek verb "αποπιπτειν" meaning falling off. It is a mechanism for a tissue to control tissue growth and is for example involved when tadpoles lose their tail. Cells round up and detach from neighbouring cells. The chromatin is condensed at the nuclear membrane and the nucleus is fragmented. The cell shrinks and separates forming membrane-bound fragments ("apoptotic bodies"), a process which is often termed "blebbing" . Many stress related signals are involved in apoptosis activation. Especially p53 was identified as a key protein in apoptosis signalling. Bcl-2 (B-cell lymphoma) is a suppressor of apoptosis.

Another stress related and very controlled mechanism that can lead to cell death is *autophagy*. The term autophagy is derived from the Greek word "αυτος", meaning self and "φαγειν", eating. This process degrades long-lived proteins and organelles in lysosomes to sustain cells under nutrient depletion. The cytoplasm and organelles are chopped and enclosed by membrane vesicles ("autophagosomes") that finally fuse with lysosomes. However, recent research has revealed that autophagy has not only a protective character but is also related to cell death. It is therefore sometimes referred to as programmed type II cell death. The mechanism is equal for all living cells and was conserved during evolution.

The most common type of cell death after radiation, however, is *mitotic death*. Un- or misrepaired lesions in the DNA manifest in different forms of chromosome aberrations. They deprive the cell from the ability to adequately distribute the DNA content to the daughter cells during cell division. Especially asymmetric exchange type aberrations seem to be the principle mechanism for radiation-induced mitotic cell death.

Other mechanisms may just lead to silencing of the cell. *Senescence* is a cellular stress

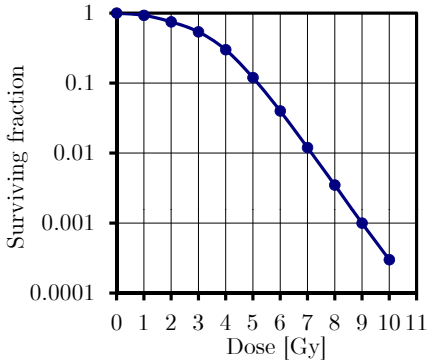

Figure 5.2 – The graph shows a typical cell survival curve.

response caused by DNA damage and oxidative stress that shortens the telomeres of the DNA. p53 and retinoblastoma proteins signal the silencing of genes required for cell cycle progression from the G1- to the S-phase. Senescence leads to permanent cell cycle arrest, however, the cell lives on and takes part in intercellular signalling pathways.

For tumour control after radiotherapy it is sufficient to achieve that tumour cells are not longer able to divide, i.e. the loss of reproductive integrity. Therefore cell survival is studied by examining the clonogenic potential of cells after irradiation. In so called clonogenic assays cells are collected after irradiation, counted and plated individually on a dish. The dish is incubated for one or two weeks. The cells divide and start to form colonies, if they maintained reproductive integrity. The outcome needs to be corrected by the plating efficiency. Even unexposed cells do not have a 100% probability to form a colony. The plating efficiency is the percentage of cells that forms colonies under control conditions in the absence of radiation. For low LET radiation the cell survival starts as a straight line on a log-linear plot, shown in figure 5.2. Then it is bending down over a range of a few Gray. At higher doses the cell survival is a straight line again. Many biophysical models have been suggested to describe the observed behaviour. However, the accuracy of the biological data is not high enough to discriminate the models. A very popular and widespread model is the *linear quadratic model* (LQM). It assumes that there are two forms of radiation actions, one leading to a linear and one to a quadratic form. The surviving fraction can be described by

$$S = e^{-\alpha D - \beta D^2}. \tag{5.3}$$

This description goes back to early work with chromosomes and the idea that the most lethal chromosome aberrations need two separate breaks, since two breaks introduce the chance of crosslinks between different parts of the DNA. This frequently leads to mitotic cell death, because the homologous chromosomes cannot be pulled apart in the anaphase of mitosis. Hence a quadratic term is added to the linear describing simple Poisson statistics. Both dose contributions are equal for a dose equal to α/β. However, the curves do not quite coincide with the observations, as the dose response becomes straight again at very high doses.

Measuring DNA strand breaks

DNA strand breaks are a measure for the damage done to a cell and especially double strand breaks can be seen as an accurate estimate for cell survival. However, as we will review in the next chapter, recent findings indicate that DSBs do not only appear as direct radiation damage but also as signalling effects from the environment.

Different techniques have been developed to measure DNA strand breaks. A standard technique is *pulse-field gel electrophoresis* (PFGE). Cells are lysed and bedded in agarose plugs. DNA

fragments are separated according to their size by electrophoresis. Another technique is the *comet assay*, also known as single cell gel electrophoresis. Unlike PFGE the Comet assay studies DNA damage on a single cell level. Cells are embedded in agarose and are lysed. The DNA forms loops that are linked to the nuclear matrix[ii]. In the following electrophoresis, comet like tails appear under the microscope in the presence of strand breaks. A completely different approach is the observation of DNA damage-induced nuclear foci. These assays use immunofluorescent staining against certain proteins employed in the DNA damage repair system. The advantage of these assays is an easy protocol and a possible application to both, tissue sections and cell culture. Most commonly the proteins γH2AX and 53BP1 are analysed.

γH2AX which was used as a damage marker throughout this work is the phosphorylated version of the histone protein H2AX. Unphosphorylated the histone is already part of the chromatin in the cells. In response to radiation (see the DNA double strand repair pathway above) the histone is phosphorylated in the vicinity of DSBs and shapes foci at the DSB.

53BP1 is also phosphorylated in response to stress and similarly forms nuclear foci. The phosphorylated and the unphosphorylated part of the histone agglomerate around DSBs. Apart from these frequently used proteins, others form foci as well (e.g. ATM, RPA, RAD51 and BRCA1).

5.1.2 Challenges and experimental contradictions

In the last years the existing radiobiological models have been challenged by several in vivo and in vitro findings. Although DNA DSBs seem to be the most relevant factor impairing cell survival, their initiators can be various. Life has developed a variety of mechanisms to react when facing life threatening situations and thus to protect the organism. Most likely these pathways are not dedicated to deal with radiation damage. However, ionising radiation affects numerous metabolic processes in cells and disturbs cellular equilibria such as that of oxidant production and scavenging. A cell hit by ionizing radiation will answer to these changes by counter-reactions. The expression of proteins may change, the progression in the cell cycle may be stopped and stress response signals may be released into the intra- and intercellular medium. The cell may undergo controlled cell death, neighbouring cells receiving signals from the hit cell may react and eventually systemic processes may activate inflammatory pathways and immune response. Since high doses of ionizing radiation are an unnatural source of endogenous hazard for a cell and an organism it is unclear whether these reactions will in the end help the cell and corresponding organism to survive or lead to further damage.

Certainly the paradigm of radiobiology – taking individual cell survival as a measure for organ survival – needs to be regarded as a strongly simplified model. The organism, intercellular signalling but also the inflammatory system play an important role. MRT is one example that shows that existing models can be misleading and are insufficient to explain all observations and treatment outcomes. In recent years overwhelming evidence has been gathered that even conventional radiotherapy might be poorly described by current radiation-damage models.

Butterworth et al. [108] have categorised biological effects that are related to irradiation but are not direct consequences of radiation damage in three groups, abscopal effects, bystander effects and cohort effects. Abscopal effects are defined as radiation-induced effects in unirradiated tissue outside the irradiated volume. The term summarises all radiation impacts observed in organs distant to the radiation side. *Bystander effects* are radiation induced effects in the same tissue but in cells that were not directly irradiated. These effects are mediated by different signalling pathways. The term "bystander" has been used by many authors. Some have, however, pointed out that the term might be misleading since not only bystander cells but also directly hit cells

[ii] The nuclear matrix is similar to the cytoskeleton a network of fibres but inside the cell nucleus. For more information see e.g. Nickerson [107].

are likely to be affected by intercellular signalling[108,109]. Therefore a third category of effects is introduced, cohort effects, that summarises biological responses in irradiated cells that are not directly evoked by energy deposition but rather intercellular communication. Plenty of experimental evidence, in vivo and in vitro indicates that these cell-signalling effects are crucial for cell and tissue survival[110–112].

Bystander effects manifests in several ways. Reported are DNA damage, cellular transformations, chromosomal aberrations and mutations[108,113,114], micronuclei[113–115] and changes in gene expression[108]. Therefore endpoints of radiation and bystander damage can be diverse, rendering comparisons problematic as remarked by McMahon et al.[109]. A commonly used endpoint is the foci formation of γH2AX and 53BP1 (e.g. Trainor et al.[112]) as a measure of DNA DSBs and the activation of double strand repair pathways. Intriguingly DSB formation is not only seen in directly hit cells, but also in bystander responding cells. Another endpoint is cell killing which is measured in clonogenic assays. This endpoint has probably the closest relation to clinical outcomes. Moreover micronuclei formation can be an endpoint (e.g. Prise[116]). The formation of micronuclei predominantly arises from non-rejoined DNA DSBs and is associated with cancer development[115]. Other authors examine the expression of stress factors such as p53 or related proteins[115].

When irradiating only a part of sparsely plated DU-145 (human prostate cancer) and AGO-1522 (human fibroblast) cells in a single culture flask with an X-Rad 225 x-ray generator, Butterworth et al.[117] observed a much lower out-of-field survival in clonogenic assays than predicted by the linear quadratic model. Only if less than 10% of the cells were exposed, the cell survival out-of-field went back to the level expected by the amount of scattered dose. Otherwise the fraction of cells irradiated did not impact the out-of-field survival. Interestingly they found that DU-145 cells show an increased in-field survival, when the in-field fraction decreases. This effect could be related to the dose volume effect seen in MRT.

Trainor et al.[112] investigated the 53BP1 and γ-H2AX foci formation with the same cells and source applying 1 Gy radiation dose. They found that in the in-field region of a modulated radiation field 30 minutes after irradation less foci can be seen than at the same dose in a homogeneously irradiated sample. A transition zone formed between irradiated and non-irradiated part, covering 8 mm in-field and 10 mm out-of-field, although the dose edge was much steeper. After 24 hours there was no difference between irradiated and unirradiated cells observable, however, in- and out-of-field the foci number remained above unirradiated controls. In statistical analysis of the foci number 24 hours post irradiation they could demonstrate that the index of dispersion σ^2/μ is larger than one. In statistics the index of dispersion or variance to mean ratio measures the dispersion of probability distributions and is one for Poisson processes. Due to the statistical nature of ionisation events one would expect that the number of DSBs per cell are Poisson distributed. Indices of dispersion which are larger than one often occur if the data is clustered suggesting here that there are two distinct entities of cells. Trainor et al.[112] inferred that these entities correspond to the bystander responding and bystander non-responding cell population. 32% of the cells were bystander responding with on average 3.1 additional foci per cell as compared to control and 68% were not responding with additional 0.82 foci per cell when irradiated.

A very remarkable observation was reported by Camphausen et al.[118]. They injected LLC-LM or T241 tumour cells to the midline dorsum of mice and irradiated the legs of the animals with 5 times 10 Gy on 5 consecutive days. Already the first day after the last fraction there was a growth difference between sham irradiated controls and irradiated animals. 3 days later the tumour size of non-irradiated mice was 3 times larger than in irradiated animals, although none of the mice received a significant dose at the tumour site. They also showed that this abscopal effect could be negated by blocking p53 or by taking p53-mutant mice.

Possibly related are dose rate and temporal fractionation effects. Although the dose rate does

not seem to have an influence on cell survival as for instance shown by Butterworth et al.[117] for dose rates between 0.25 to 4 Gy min^{-1}, interruptions during irradiation or periodic irradiations appear to be of importance. While breathing motion does not influence cell survival in homogeneous irradiations[119], significant changes occurred in the survival when only parts of the cells were irradiated. Cole et al.[120] examined survival of H460, H1299 and DU-1455 cell lines in clonogenic assays in a half-irradiated cell culture flask where they imitated respiratory motion by either moving the absorber or the cell flask. The motion perpendicular to the absorption edge had 14 to 21 cycles per minute with 3 cm amplitude and described a $\cos^2$ waveform. Only cells outside the 3 cm dose transition zone and a safety margin were taken for clonogenic assays. When comparing the survival with static conditions an increased cell survival in- and out-of-field was obtained. The out-of-field bystander effect was partially negated by the motion of the edge. Mixing effects and cell migration could be ruled out. It was also refuted that the dose gradient caused the increase in cell survival.

Clastogenic factors

The signalling mechanisms underlying the bystander effects are to date not revealed. It was suggested that soluble *clastogenic factors* are one mediator of these effects. Clastogenic means DNA breaking and clastogenic factors were first mentioned in 1954, when damage in the bone marrow was observed in children whose spleen had been irradiated because of leukaemia[113,121]. Supernatants of the blood in exposed humans and animals and the intercellular medium of exposed cells in cell culture can induce DNA damage when transferred to healthy cells. These clastogenic factors persist for a long time in the blood. They were still detected two months after an accidental gamma radiation exposure[122] and in atomic bomb survivors they were found even 31 years after exposure[113]. At the same time clastogenic activity of blood plasma from irradiated rats was already seen 15 minutes after irradiation[113,123], implying that clastogenic factors can be generated very quickly.

Transferring the medium to unexposed (undamaged) cells causes DNA DSBs, which can for example be detected with γH2AX fluorescent antibody staining. Han et al.[124] showed that the maximum fraction of cells with γH2AX foci in cells receiving medium from irradiated cells is already reached 10 minutes after irradiation. However, the clastogenic factors do not exist for long in the extracted medium or plasma. The clastogenic activity of the medium rapidly decreases[124]. Cells seem to be the origin of the clastogenic factors and they actively emit them into the intercellular medium. That is supported by the observation that blood plasma irradiations[122] or irradiations of cell culture medium[124] alone do not lead to clastogenic factors. Upon the dose dependence of clastogenic factors different observations were made. On the one hand Emerit[122] did not see any dose dependence between 4 and 50 Gy when irradiating blood in vitro. Clastogenic effects were still detectable at doses as low as 0.5 Gy. On the other hand Emerit et al.[125] observed that the amount of clastogenic factors in the blood of Chernobyl clean-up workers was dependent on the dose the workers were exposed to.

Radiation is not the only source of clastogenic factors in the organism. Clastogenic factors were also found in patients with chronic inflammatory diseases[122] and are considered to be at the origin of the accompanied spontaneous chromosome instability observed. Again it is possible to induce cell damage by transferring the supernatants of the blood of these patients to healthy cells. Very likely these clastogenic factors also explain the increased risk of cancer in patients with inflammatory diseases, e.g. a 20 times higher risk of colorectal cancer for Crohn's disease and an increased risk of liver cancer for hepatitis patients[122]. Likewise clastogenic factors are created in contact with certain chemicals. One example is asbestos. Ingestion of asbestos or its contact with the cell membrane leads to superoxide and hydrogen peroxide production[126].

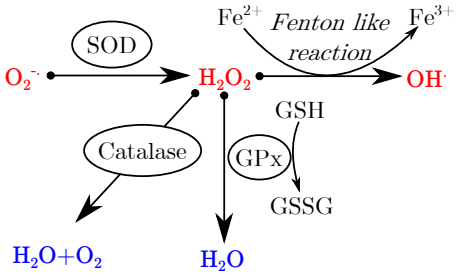

Figure 5.3 – Reactive oxygen species, their transformations and degradation in cells. In red the important ROS factors (oxidants) of the cell are shown: the superoxide anion, hydrogen peroxide and the hydroxyl radical. By SOD (superoxide dismutase) catalysation superoxide is transformed into hydrogen peroxide. Hydrogen peroxide in term can be eliminated by catalase or by glutathione (GSH) catalysed with the enzyme glutathione peroxidase (GPx). The latter reaction leads to the products water and glutathione disulfid (GSSG). However, Fenton like reactions can transform hydrogen peroxide into the very reactive hydroxyl radical. The graph is based on Robbins and Zhao [129].

Oxidative metabolism and reactive oxygen species

The exact mechanisms and chemicals underlying the clastogenic activity are still unknown. Abundant evidence links clastogenic factors with oxidative stress and oxidants. A connection between bystander effects and *reactive oxygen species* was presumed by several researchers [108,127,128]. A variety of oxidants is generated and handled by cells. Being capable of transforming and damaging proteins and DNA, they present an acute hazard to the cell and some oxidants could work as intracellular stress signals as well. One of the most important oxidants is hydrogen peroxide, a comparably long lived and widely diffusible compound that possesses a life time of more than 100 s [127,128]. Hydrogen peroxide (H_2O_2) is rather weak oxidizing, it can cross biological membranes and acts as an intracellular messenger. In the presence of transition metals it can create extremely reactive and toxic reactive oxygen species (ROS). For example hydroxyl radicals ($OH\cdot$) are produced from hydrogen peroxide in Fenton reactions[iii]. Glutathione peroxidases (GPx) act as hydrogen peroxide scavengers at low concentrations [128]. Another abundant, very unstable and short lived oxidant with a life time of a few seconds is the superoxide anion ($O_2^{-\cdot}$). It is mutated by superoxide dismutase (SOD) in the reaction [113,122]

$$2\,O_2^{-\cdot} + 2\,H^+ \xrightarrow{\text{SOD}} H_2O_2 + O_2. \tag{5.4}$$

The relation of ROS to each other is schematically shown in figure 5.3.

The main natural source of ROS in a cell is the oxidative metabolism [127]. 90% of superoxide anions are produced within mitochondria [3]. Normally there is a balance between oxidant production on the one and antioxidant defence on the other hand. If this balance is disturbed the cell falls under oxidative stress, a pathological condition that can lead to degenerative senescence and cancer. An altered redox state ("ROS level") affects the regulation of most stress-response genes, it alters the growth rate, induces the expression of specific genes and modulates ion channel activities [127]. The ROS level can be affected by various exogenous impacts. Ionising radiation is one of them.

Narayanan et al. [130] suggested that the plasma membrane bound NADPH oxidase becomes activated in response to ionising radiation and produces large amounts of $O_2^{-\cdot}$. The mechanisms that activate NADPH are not yet elucidated. However, selective blocking of NADPH oxidase by diphenyleneiodonium inhibited the generation of H_2O_2 and $O_2^{-\cdot}$. This would mean that direct

[iii] In Fenton reactions transition metals donate or accept free electrons and help to form free radicals. Especially iron is often involved and can for example produce hydroxyl radicals from hydrogen peroxide in $Fe^{2+} + H_2O_2 \longrightarrow Fe^{3+} + HO\cdot + OH^-$.

irradiation of the DNA is not necessary to induce mutations, which is supported for example by Wu et al. [131], who observed mutations after plasma irradiation with α-particles.

When cells are treated with DMSO (dimethyl sulfoxide), a potent hydroxyl radical scavenger, the mutation frequency is strongly reduced [127] and the number of observed DSBs, detected by measuring γH2AX foci, is halved [124] in irradiated cells. In bystander cells DMSO reduced the number of γH2AX foci back to the level of non-irradiated cells. Further evidence, emphasizing the role of oxidative stress in radiation damage, provide experiments in which glutathione (GSH) depleted cells show an increased mutagenicity. Glutathione is an important thiol that acts as a redox buffer in the cytosol and thus prevents oxidative stress [127,132] (see figure 5.3).

ROS participate in the expression regulation of stress-inducible proteins, for example p53 signalling and the MAPK (mitogen-activated protein kinase) pathways. They also activate superoxide dismutase (SOD) and certain catalyse enzymes [127]. SOD, given additionally up to 24 hours after irradiation, can inhibit the clastogenic factor formation. However, if SOD is added later, it does not prevent or reduce clastogenic factors. ROS were also hypothesised to stimulate cell growth by the redox-activated tumour growth factor β1 (TGF-β1) cytokine [133].

Hypothetical clastogenic factors

There is a strong link between clastogenic factors and oxidative stress, but they are not identical. Oxidative stress seems to be the precursor of clastogenic factors, since blocking ROS by SOD or DMSO prevents their formation. Once present, SOD does not influence clastogenic factor activities, though. Presumably cells amplify ROS production when irradiated and self-sustain high ROS levels afterwards by clastogenic factor signalling. Oxidants can damage the DNA molecule. They also initiate several stress related signalling processes. There is growing evidence that acute and chronic oxidative stress initiates late radiation-induced effects as well.

Clastogenic factors were found to have a low molecular weight, to be unstable at room temperature and to lose their activity overnight in a refrigerator. However, frozen they are preserved over years. Clastogenic factors induce DNA damage in living cells, but not in isolated DNA. HPLC (high-performance liquid chromatography) analysis suggests that they are comprised of several components [122]. Clastogenic factors are most effective during the S- or G2-phase of the cell cycle [113]. Three distinct groups of substances have been proposed as clastogenic factors: cytokines [108,122] (for example GF-β, interleukin-8, TNF-α), unusual nucleotides such as inosine triphosphate (ITP) [113,122] and molecules released from cell membranes by lipid peroxidation [122].

Membranes have probably an important role in bystander and ROS signalling. By activation of phospholipase A_2 arachidonic acid is released from the membrane and the genotoxic 4-hydroxynonenal is formed. For example this compound was found in most of the patients with chronic inflammatory diseases. Membranes also play an important role for the release of TNF-α.

Gap junction mediated signalling

Gap junctions are plasma membrane structures forming low resistance channels that link neighbouring cells. They consist of two connexons from each contributing cell. These connexons are multimeric assemblies of connexins [127]. Gap junctions are widely spread among most animal tissues and it is supposed that they play a central role in bystander signalling. After low dose α-particle irradiations cell populations were found to respond rather as integrated units of adjacent cells than as separate individual cells [127]. Azzam et al. [115] irradiated confluent Ag1522 cells, normal human skin fibroblasts and HLF1 cells, normal human lung fibroblasts with very low doses of α-particles and assessed the expression of $p21^{Waf1}$, a stress factor similar to p53. They found that more cells showed an increased $p21^{Waf1}$ expression than actually hit at doses as low as a few mGy. Furthermore cells with $p21^{Waf1}$ induction appeared in aggregates and lindane,

an effective gap junction inhibitor, let these aggregates disappear. Furthermore lindane reduced the number of micronuclei between 1 and 3 cGy significantly. At higher doses it didn't have a significant impact. There is also evidence that ionising radiation and ROS play a role in the activation of gap junctions and the expression of gap junction proteins such as connexin43 [127,134].

5.1.3 Motivation and criticism of the experiments in this work

There are further explanations for the observed bystander effects. For example the inflammatory system was suggested to play a role. Lorimore et al. [135] report that the recognition and clearance of radiation induced apoptotic cells can activate macrophages and lead to neutrophil infiltrations. The reaction of an organism to ionising radiation is very complex and involves many signalling pathways and systemic reactions. Probably none of these has specifically evolved to protect from radiation. A lot of further research is required to reveal the biological impact of ionising radiation in its full depth. This will complicate the optimisation of treatment strategies in radiotherapy. However, understanding might also help us to develop new, much more effective treatment strategies. MRT is a first step, showing that we can do more than classical models suggest, although we do not really understand why it works.

Apart from systemic reactions discussed for the explanation of MRT, a molecular biological explanation may also be possible. Probably the tissue sparing property of MRT is the result of a combination of various not yet understood factors. From the beam geometry in MRT it is reasonable to suppose that bystander effects play a part. In a series of experiments we analysed the response of pancreatic cancer cells to modulated radiation fields at different times after radiation exposure. As biological markers we used γH2AX staining and DNA staining with Hoechst 33342. We examined the γH2AX signal in homogeneous fields, at radiation boundaries, in exposures with dose gradients and in MRT fields. Furthermore we looked at changes in the cell cycle by analysing the Hoechst 33342 DNA-stain. We used in our experiments large screenings of cells with ten and hundred thousands of cells, with an automatised cell and foci detection system. This method yields good statistics and provides a kind of "flow cytometer" with spatial resolution. The results are surprising. We found evidence for positive and negative bystander response and some of these findings may explain the principles of MRT.

All our experiments were done in vitro only and we have to face related criticism. When working with cell cultures one has to deal with the legitimate comment of looking at a very artificial system that does not resemble at all a real organism. When the first clonogenic assays were performed in 1956, the significance of in vitro experiments were questioned and criticised. In 1957 F.G. Spear expressed his doubts in the MacKenzie Davidson Memorial Lecture to the British Institute of Radiology by saying "An isolated cell in vitro does not necessarily behave as it would have done if left in vivo in normal association with cells of other types. Its reactions to various stimuli, including radiations, however interesting and important in themselves, may indeed be no more typical of its behaviour in the parent tissue than Robinson Crusoe on his desert island was representative of social life in York in the midseventeenth century." [106] However, cell culture results are successfully applied in radiotherapy today. For example the in vitro measured cell survival curves agree very well with those obtained in vivo. Hence our results need to be confirmed in living organisms. Nonetheless, with this work we hope to add a small piece to the extremely fascinating puzzle of modern radiobiology.

5.2 Methods

5.2.1 Cell culturing and antibody staining

Throughout our experiments human pancreatic cancer cells, Panc1 were used. These cells stem from an epithelial carcinoma. They are adherent and grow in single layers. Cells were kept in a 1 g/l glucose DMEM medium[iv] (from Life Technologies) with 10% fetal bovine serum (FBS, from Life Technologies), 11% penicillin Pen/Strep Amphotericin B (from Lonza), 1% MEM NEAA non essential amino acids (from PAN Biotech GmbH) and 1% GlutaMAX (from LifeTechnologies). FBS was necessary to provide the cells with certain growth factors. The cells were grown in cell culture flasks and kept in an incubator at 37 °C, 100% humidity and 5% CO_2 level for buffering. Cells were splitted ideally every second day. That means they are treated with trypsin for 5 minutes, a peptide breaking enzyme that is found for instance in the small intestine. If cells are treated with trypsin for a short time the enzyme will not harm the cells but only break peptide bonds between cells and between the cells and the dish surface. Thus it solves and separates cells. After treatment a part of the cells is discarded, whereas the other is reseeded in the cell culture flask. For irradiation cells were grown on iBidi μ-slides[v] (iBidi GmbH, Planegg/Martinsried, Germany) or in small cell culture flasks. In most experiments confluent cells were used. The idea was to enable both, gap junctions and soluble factors mediated signalling effects. However, the cell density varies a bit from experiment to experiment. The medium was changed directly before irradiation. After irradiation the medium was kept until fixation in order to allow free diffusion of potential soluble factors in the medium.

Fixation of the cells was performed 15 minutes in 4% paraformaldehyde (PFA) solution at room temperature. Paraformaldehyde is the polymer of formaldehyde with chain lengths of up to around 100 monomers. At low pH the polymer can be decomposed in water to form a formaldehyde solution. Formaldehyde links proteins by forming methylene bridges and thereby inactivates proteins and enzymes. At the same time functional groups remain and can be recognised by antibodies during subsequent histochemical staining. After fixation cells were washed 3 times in PBS (phosphate buffered saline) to thoroughly remove the PFA again.

Immunostaining, immunohistochemical or antibody staining is a method that uses antibodies to detect certain proteins, enzymes or functional groups in tissue sections or fixed cells in cell culture. We used the indirect immunostaining method with a primary antibody, specific for an antigen of interest (in our case γH2AX) and a binding site for a secondary antibody. As primary antibody we used the Phospho-Histone H2A.X (Ser13) Rabbit (Alexa Fluor 488 Conjugate) antibody from Cell Signalling. Although this primary antibody is already coupled to a fluorophore we counterstained with a fluorophore coupled secondary anti-rabbit antibody to increase the signal strength. We followed the immunostaining protocol of the laboratory of Dr Nathan Brady.

In the first step of this protocol cells are permeabilised with 0.3% Triton X-100 (from Sigma Aldrich) solution in PBS for 10 minutes. Triton X-100 is a surfactant and is able to permeabilise cell membranes. This is necessary to allow antibodies to penetrate the cell membrane.

Specificity of antibody staining is improved by a blocking step with 3% bovine serum albuminum (BSA, from Sigma Aldrich) in a 0.3% Triton X-100 solution for 45 minutes. BSA prevents unspecific binding of antibodies. After blocking the cells are incubated over night with the primary antibody in Triton X-100 solution. The primary antibody is thoroughly removed by washing three times with PBS and the secondary antibody is added in Triton X-100 solution. Incubation time for the secondary antibody is 1 hour. By washing with PBS the secondary antibody is removed afterwards. Cell nuclei can be stained in this step by adding Hoechst 33342

[iv] For the experiments at the synchrotron 3.7 g/l glucose DMEM medium was used.

[v] Product details can be found on the company webpage, ibidi.com, catalogue number 80826 (August, 2014).

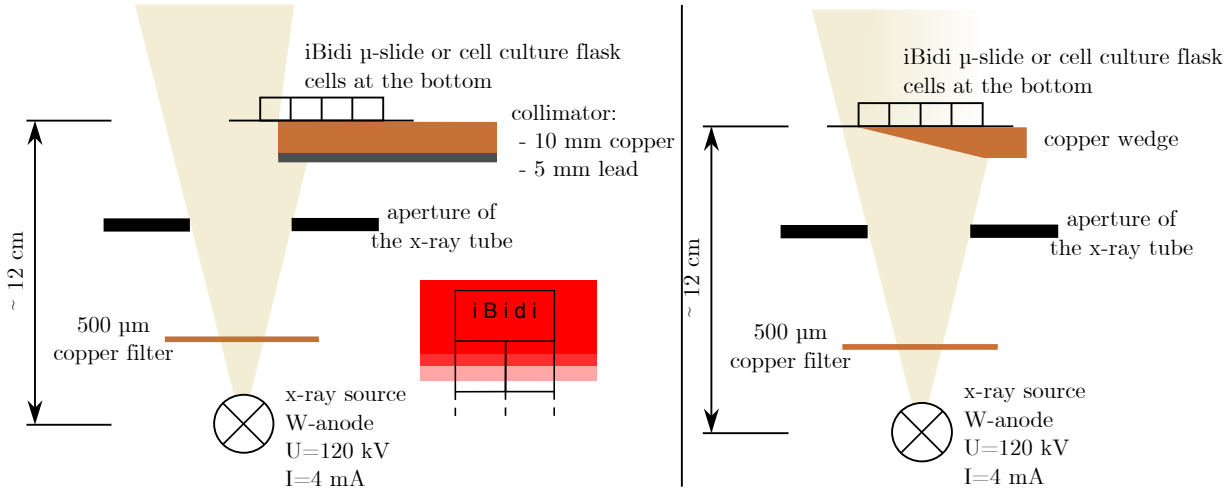

Figure 5.4 – This figure shows the experimental set-up for the step exposure (left) and gradient exposure (right) at the x-ray tube. The step exposure was achieved by exposing different parts of the two first iBidi wells for different times.

(from Sigma Aldrich) to PBS. Hoechst 33342, similar to Hoechst 33258 is an organic compound that specifically stains DNA fluorescently[136]. The molecule binds to the minor groove of double-stranded DNA and preferably to adenine and thymine rich regions[137]. The excitation of Hoechst 33342 is at 352 nm with an emission in blue light, whereas the secondary has an excitation maximum at 488 nm with an emission in green light. With appropriate excitation light and filters both signals can be analysed separately.

5.2.2 Beam application and dosimetry

Irradiation was carried out with a conventional x-ray tube and at the biomedical beamline ID17 of the European Synchrotron Radiation Facility (ESRF) in Grenoble, France. The following experiments are presented in this work:

1. Homogeneous irradiation of cells in iBidi μ-slides at the x-ray tube with doses of 1, 2, 8, 16 and 32 Gy. Cells were fixed 3 hours after exposure. The aim of this experiment was to measure the dose response of H2AX phosphorylation.

2. Homogeneous irradiation of cells in a cell culture flask at the x-ray tube with a dose of 32 Gy. Cells were fixed 24 hours after exposure. This experiment was intended to measure changes in the cell cycle after homogeneous exposure.

3. Irradiation with a dose gradient in iBidi μ-slides at the x-ray tube. The maximum dose was 48 Gy. Cells were fixed 3 and 24 hours after exposure. This experiment was carried out to investigate the cellular response in the γH2AX signal to a radiation field with a gradually changing dose.

4. Irradiation with 4 different doses in a single iBidi μ-slide well at the x-ray tube. Doses were 0, 5, 16 and 32 Gy in an approximately 3 mm wide region. Cells were fixed 3 and 24 hours after exposure. In MRT strong dose gradients play an important role. Therefore this experiment was aimed to explore the cellular reaction close to radiation boundaries.

5. Irradiation with a microbeam field (MRT-field) at the ESRF in iBidi μ-slides and in cell culture flasks. Peak entrance doses were 50, 100 and 250 Gy and cells were fixated 1 and 6 hours after exposure. Finally in this experiment we investigated the cell response after exposure in an MRT set-up.

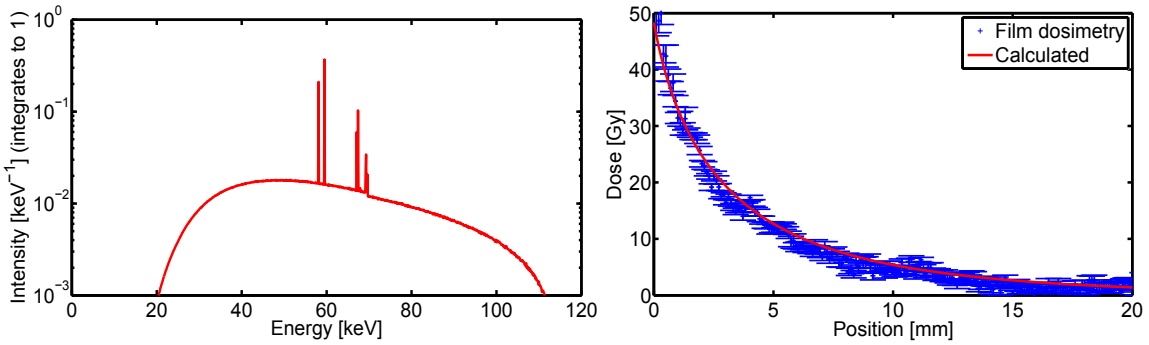

Figure 5.5 – The photon spectrum of the x-ray tube used for the cell irradiations (left) and the dose profile behind the copper wedge (right) are shown. The dose is compared between measurement and calculation.

Experiments with an x-ray tube

For experiments 1 to 4 a Siemens Powerphos medical x-ray tube was used which was operated at 4 mA cathode current and 120 kV acceleration voltage. The tube has a tungsten anode and there is an intrinsic copper filter of 500 μm. The spectrum is presented in figure 5.5. It was calculated with Monte Carlo simulations in Geant4.9.3.p02 and the PENELOPE physics libraries[56], neglecting the heel effect. The distance between sample and tube was approximately 12 cm. Absolute dosimetry was performed with a 0.125 cm^3 semiflex chamber T31010 (PTW, Freiburg). It was calibrated for photon beams between 66 keV and 5 MeV. Due to its comparably small detector volume this chamber is suitable for the small field sizes of the x-ray tube which have just a few cm in diameter. The chamber was connected to an UNIDOS electrometer (PTW). The dose rate at the position of the cells was measured[vi] as (17.9 ± 0.6) mGy/s.

Different dose distributions were achieved with different collimators and varying irradiation times. To shield parts of the cells from radiation an absorber with 5 mm lead and 10 mm copper was employed. Just $3 \cdot 10^{-7}$ of the original dose rate is transmitted by the collimator (figure 5.4). A copper wedge was used to create dose gradients. The length of the wedge was 48 mm and the opening angle was 14.9° (figure 5.4). The dose profile created by the wedge was calculated from the x-ray tube spectrum and with the x-ray absorption data from Berger et al.[64]. These results were complemented by dosimetry with MDV Gafchromic® films. The read out was done as described in chapter 4.2. The comparison between measurement and calculation is presented in figure 5.5.

For the experiments 1 and 2 doses of 1, 2, 8, 16 and 32 Gy were achieved by varying the exposure time from 56 s for 1 Gy to 30 minutes at 32 Gy. In experiment 3 cells were irradiated 45 minutes across the copper wedge. The dose steps of experiment 4 were again achieved by varying exposure times of 0, 5, 15 and 30 minutes. Due to the set-up and variations in the dose rate all dose values have an uncertainty of around 15%.

Experiments at the ID17 of the ESRF

The beam set-up for experiment 5 at the ID17 in Grenoble is shown in figure 5.6. The MSC (multislit collimator) shapes 50 μm wide parallel beams with a centre to centre distance (ctc) of 400 μm. At the sample position beam width and ctc have increased to 51.5 and 412.3 μm (see chapters 2.3.3 and 4.3.2). In order to create realistic peak and valley doses a PMMA block of 5 cm thickness was placed in front of the cells into the beam. This increases the scattered dose in the valley.

[vi] The measurement was carried out by Katrin Welsch, BSc Physics student at that time.

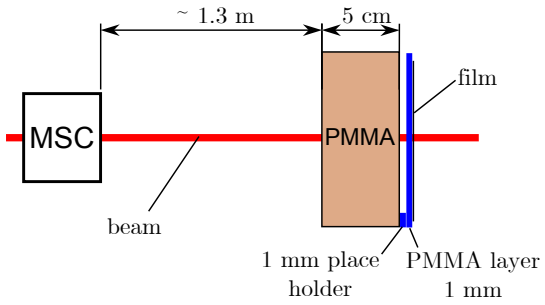

Figure 5.6 – The figure illustrates the experimental set-up used for dosimetry of the MRT cell exposure. The bottom of the cell culture flask is elevated by a 1 mm stand at the flask edge. This creates a small air-gap which needs to be considered in the dosimetry set-up. The 1 mm PMMA layer, imitating the flask bottom was separated 1 mm from the PMMA block.

Film dosimetry was performed with HD-V2 Gafchromic® films. Calibration films were exposed to homogeneous doses between 10 and 400 Gy. Three independent measurements for both peak and valley doses were carried out. The films were scanned according to the dosimetry methods discussed in chapter 4.2. We fitted the function

$$D = -51.36\,Gy + \frac{1.137 \cdot 10^5}{G - 130.1}\,Gy \tag{5.5}$$

to the calibration data with doses D and pixel grey values G. Except for the 300 Gy value the fitted calibration deviates by less than 5 Gy from the measurement. The dose was measured in a set-up as similar as possible to the cell exposure (see figure 5.6).The results of the measurement for the peak doses, valley doses and PVDRs at the three peak entrance doses used for the cell exposure are summarised in the following table[vii]:

Peak entrance dose [Gy]	Peak dose [Gy]	Valley dose [Gy]	PVDR
50	16.0 ± 0.8	0.73 ± 0.04	22.0 ± 1.6
100	32.1 ± 1.6	1.46 ± 0.08	22.0 ± 1.6
250	80.2 ± 4.0	3.64 ± 0.18	22.0 ± 1.6

Monte Carlo simulations were performed in Geant4.9.5 in the semi-adjoint modus incorporating the developed source models (see chapters 2.3.3 and 3.2.3). 10^9 photons were simulated with the ESRF spectrum and 10^7 with the collimator leakage spectrum. In figure 5.7 the Monte Carlo results and the measurement of the peak and valley doses are plotted across the MRT field for 100 Gy peak entrance dose. The peak dose is in excellent agreement between measurement and calculation. However, the valley dose measurement is approximately 15% higher than the Monte Carlo result. A likely explanation is the lack of electronic equilibrium at the film position. For the evaluation of the cell irradiation presented in the next chapters the Monte Carlo results were used.

5.2.3 Image acquisition and image processing

Microscopy was carried out with a fully automated, inverted Nikon Ti microscope for high content screening (Ti-HCS) at the Nikon Imaging Centre of Heidelberg University[viii]. The microscope was equipped with four objectives with 10, 20, 20 and 40 times magnification and a numerical

[vii] According to chapter 4.4.1 5% uncertainty was assumed for peak and valley dose measurement.
[viii] Webpage of the Nikon Imaging Centre: http://nic.uni-hd.de/

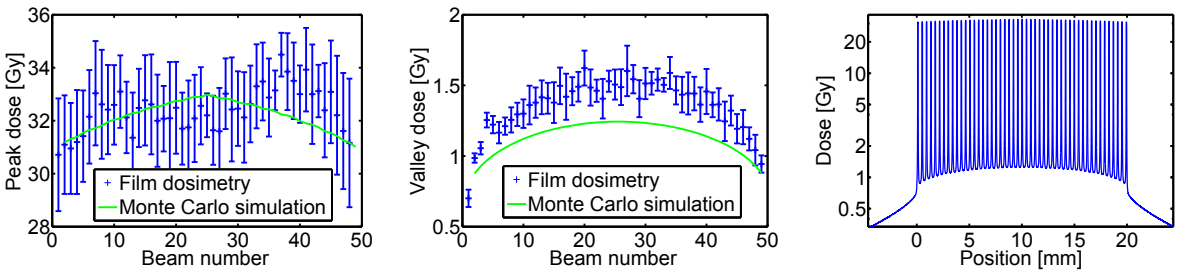

Figure 5.7 – Peak and valley doses (left and centre) measured by film dosimetry and computed in Monte Carlo calculations are shown. A dose profile across the entire MRT field was obtained by Monte Carlo simulations and is shown in the right figure.

aperture of 0.3, 0.75, 0.75 and 0.6 respectively. One of the 20x objectives was an immersion objective. In all our experiments either the 10 or the 20x objective was used without immersion oil. As camera served an Andor Clara high-sensitive interline-CCD-camera with a resolution of 1392×1040 pixels. The pixel size was 6.45×6.45 μm^2. Several wavelength for excitation were provided by a Lumencor SpectraX light engine. Available wavelengths were 395, 440, 475, 508, 560 and 640 nm. A scanning table and automatic focus allowed acquisition of large images. For some experiments they extended to a region of several cm inferring scanning times of a few hours and image sizes of up to 25 GByte.

Even the best optics cause artefacts with a negative impact on the image quality. The image acquired will suffer from aberrations, for example astigmatism or chromatic aberration by an imperfect objective. Furthermore it is very difficult to achieve a homogeneous irradiation of the sample, which is mainly a problem of the illumination system of the microscope. But also an ideal illumination and objective will only produce a sharp projection of a plane of the sample. If there is a small tilt in the sample plane, there will be some areas in the image that are sharp and others will appear blurred. To account for this problem z-stacks were acquired, i.e. the image was acquired at different sample-objective distances. For each region in the image the sharpest representation was chosen. This can easily be achieved by taking for all points the maximum intensity of the z stack. The problem is illustrated in figure 5.8. For three points in the sample the light paths and the focus created by the objective lens are shown. The highest light intensity on the image side is obtained at the image position of a sharp projection, because there the light is concentrated in a single point.

Image processing was performed in Matlab 2013. Correction of the image-illumination is usually done by acquisition of a "flat" or "white" image. This white image is acquired without a sample in the light path. We have, however, opted for another technique. Removing the sample has the disadvantage that there is no scattering or emitting object in the focal plane. This leads to dark images and the illumination inhomogeneities are poorly represented. Since we usually acquired large mosaic images made up of many acquisitions at different lateral sample positions it can be assumed that objects are on average statistically equally spread. Therefore all images from an experiment were superimposed and averaged. The result still contains some remainders of structures of the individual images as can be seen in figure 5.9 (left). Illumination inhomogeneities are expected to appear on larger scales than structures seen in the samples. Therefore the white image was filtered with a Fourier filter eliminating high frequency contributions. The filtered white image is also shown in figure 5.9 (right). This process is repeated for all fluorescent channels separately.

After image acquisition, each image is corrected by dividing the pixel grey values by the value of the corresponding pixel in the white image. Each image in the mosaic has a small overlap with its neighbouring images. This overlap needs to be regarded when fitting and stitching all images together. The overlap is calculated via autocorrelation and assumed constant all over

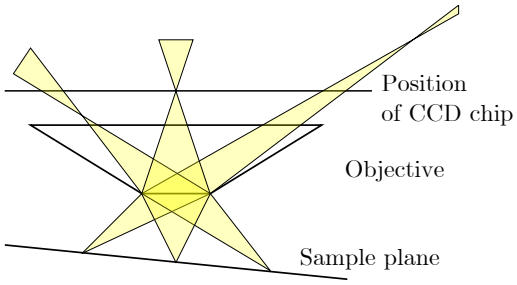

Figure 5.8 – An inclined sample plane leads to various image distances. Depending on the objective-sample distance (z) different regions of the image appear sharp. A z-stack can help to increase the depth of field.

the mosaic. The resulting mosaic is normalised to its maximum intensity value for all acquired channels and split into images of 2000×2000 pixels size (except for the edges).

The number of cells reached in some of the experiments $5 \cdot 10^5$ cells. Therefore it was impossible to manually count γH2AX foci or to individually segment cells in the images. Instead we used the software Cell Profiler[138] to perform the segmentation of the cell nuclei and to identify γH2AX foci. For nuclei recognition the Kapur method was used[139]. This method exploits the histogram of the image. It determines the grey value threshold that maximizes the sum of the entropy of a dimmer background and a brighter foreground. The entropies of the foreground F and the background B are defined as

$$\begin{aligned} H(F) &= -\sum_{i=1}^{s} \frac{n_i}{N_F} \ln \frac{n_i}{N_F} \\ H(B) &= -\sum_{i=s+1}^{m} \frac{n_i}{N_B} \ln \frac{n_i}{N_B} \end{aligned} \tag{5.6}$$

where i is the index of the grey level, m the total number of grey levels, n_i the number of pixels with grey level i, N_F the number of pixels in the foreground, i.e. $N_F = \sum_{i=1}^{s} n_i$, and N_B is the corresponding number of pixels in the background. The threshold value s was determined on a global base. Because of the image correction and homogeneous staining level across the image there was no need to adapt the threshold across the image.

Automated detection of γH2AX foci

Recognition of the γH2AX foci was more subtle. Whereas the cell nuclei were well separated and did not overlap since the cells were growing in a monolayer and not piling up, γH2AX foci agglomerated in the nuclei. They were distributed in the cell nucleus in three dimensions. Foci below and above the focal plane contributed to a background noise and therefore a simple thresholding method, such as the Kapur approach was not appropriate.

The z-stack acquisition was not extensive enough to get a sharp image of the whole cell. Some of the γH2AX foci were situated outside the focal regions and would thus not be recognised as foci throughout analysis. Nonetheless the number of detected foci will statistically be correlated to the total number of foci in the cells. As long as the focal plane is more or less at the centre of the cell nucleus the number of detected foci $N_{detected}$ will on average be the total number of foci N_{total} multiplied by a detection rate η,

$$N_{detected} \approx \eta \cdot N_{total}. \tag{5.7}$$

Not resolved foci lead, however, to a background signal. Some foci overlap or cannot be distinguished because of there close distance. Furthermore many cells exhibit a rather uniform or fibrous γH2AX background signal. These background effects should not be identified as foci,

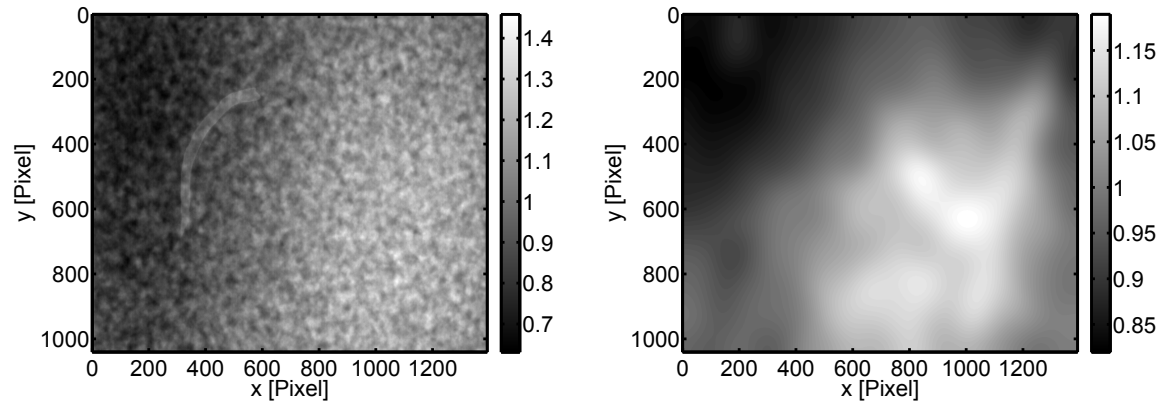

Figure 5.9 – The shading correction of the fluorescence images was performed by averaging over all images of a mosaic acquisition. The result of the averaging is shown on the left. The texture is a remainder of structures in the single images. Smoothing with a Fourier filter gives the white image (right). Shading correction is essential. The sensitivity fluctuates by approximately ±20% around the average.

though. The size of γH2AX foci varies depending on the lesion created and also on the radiation type as observed for example by Bracalente et al.[140]. They found the diameter of the γH2AX foci to vary approximately between 400 and 900 nm. Hence with a camera pixel pitch of 6.45 μm and a 20x optical magnification the foci size would be between 1.2 and 2.8 pixels. However, the limited optical resolution will blur the foci. The optical resolution Δx can be calculated from the fluorescence wavelength λ of the secondary antibody of about 500 nm and a numeric aperture NA of 0.75,

$$\Delta x = \frac{1.22\lambda}{2 \cdot \mathrm{NA}} \approx 400nm. \tag{5.8}$$

Some of the foci may still be detectable, although they are slightly out of focus. Therefore it can be expected that the foci have in the acquired images between 2 and 5 pixels diameter. Furthermore they should be more or less circular in shape and have an approximately Gaussian intensity profile (optical blurring). A selective filter would be appreciable that selectively eliminates all structures that do not meet these requirements. The wavelet transformation is an integral transformation that performs this kind of filtering. Unlike a Fourier transform the wavelet transform contains both frequency and spatial information. The continuous wavelet transform $\tilde{g}$ of a function g is defined in one dimension as

$$\tilde{g}(a,x) = \int_{-\infty}^{\infty} \left[g(x') \frac{1}{\sqrt{a}} W^* \left(\frac{x - x'}{a} \right) \right] dx' \tag{5.9}$$

and the back-transformation

$$g(x) = \frac{1}{C_W} \int_{-\infty}^{\infty} \int_{0}^{\infty} \left[\tilde{g}(a,x') \frac{1}{\sqrt{a}} W \left(\frac{x - x'}{a} \right) \right] \frac{da}{a^2} \, dx'. \tag{5.10}$$

Here the parameter a defines the size or wavelength of the wavelet. W and W^* are the wavelet and its complex conjugate that have to obey the admissibility condition in Fourier space,

$$C_W = \int_{0}^{\infty} |\hat{W}(\omega)|^2 \frac{d\omega}{|\omega|} < \infty. \tag{5.11}$$

This condition also determines the factor C_W in the back-transformation and is fulfilled if the

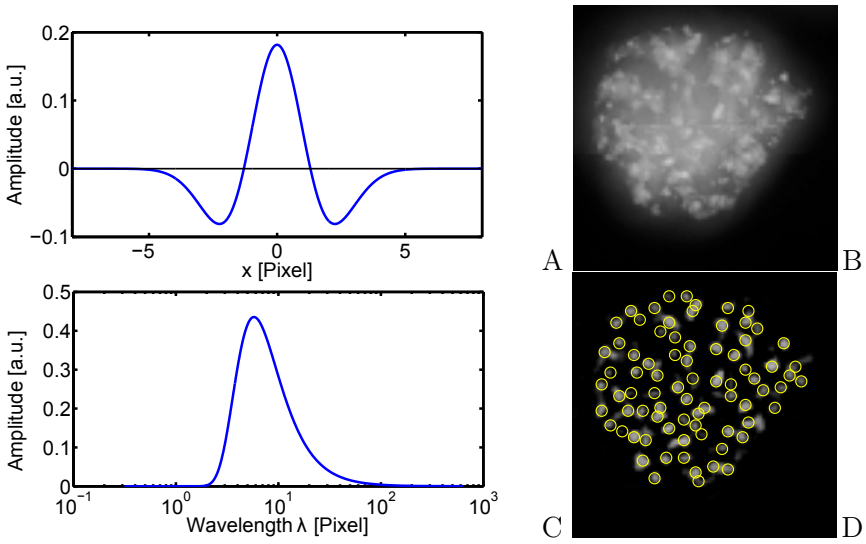

Figure 5.10 – The one dimensional Mexican hat function (A) with its spectrum (C) was used to identify γH2AX foci in the fluorescence microscope images. (B) shows the green fluorescence signal of a cell in which the phosphorylated H2AX histone was stained with an antibody emitting in green light. Whereas foci detection was difficult in (B) it was straightforward in the wavelet filtered image (D).

integral in normal space disappears, i.e.

$$\int_{-\infty}^{\infty} W(x)\,dx = 0.$$

It is simple to extend this transformation to two dimensions. The transform has four dimensions, 2 spatial and 2 wavelength dimensions. There are several wavelets in use and the wavelet transformation plays an important role in image compression and modern data processing. For our purposes a wavelet that is similar to the foci shape would be ideal. A wavelet that is fulfilling the admissibility condition and is closest to the normal distribution is the Mexican hat function. It ensues from the Laplace derivative of the two dimensional Gauss function,

$$f(x, y, \sigma_x, \sigma_y) = \frac{1}{2\pi\sigma_x\sigma_y} e^{-\frac{1}{2}\left(\frac{x^2}{\sigma_y^2}+\frac{y^2}{\sigma_y^2}\right)} \tag{5.12}$$

and reads

$$W(x, y, \sigma_x, \sigma_y) = \frac{\sigma_x^2\sigma_y^4 + \sigma_x^4\sigma_y^2 - \sigma_y^4x^2 - \sigma_x^4y^2}{2\pi\sigma_x^5\sigma_y^5} e^{-\frac{x^2}{2\sigma_x^2}-\frac{y^2}{2\sigma_y^2}}. \tag{5.13}$$

In the isotropic case when $\sigma = \sigma_x = \sigma_y$ the Mexican hat simplifies to

$$W(x, y, \sigma) = \frac{1}{2\pi\sigma^4}\left(2 - \frac{x^2+y^2}{\sigma^2}\right) e^{-\frac{1}{2}\left(\frac{x^2+y^2}{\sigma^2}\right)}. \tag{5.14}$$

The advantage of using the Mexican hat wavelet is that it is localised in frequency and space. For one dimension the Mexican hat function and its wavelength spectrum is shown in figure 5.10 with the wavelength which was also used in the foci analysis. An example of a damaged cell in the 500 nm GFP-channel is also presented in figure 5.10 together with the Mexican hat transform and the subsequently identified foci positions.

It is difficult to estimate the error-rate of this automatic detection method. A comparison with eye-based foci counting gave a detection rate of $(85 \pm 5)\%$. However, manual foci counting

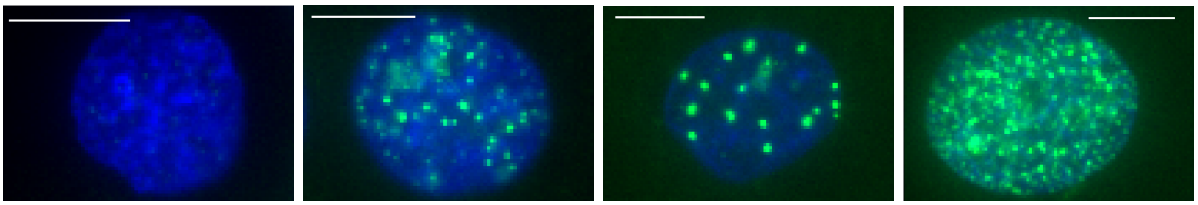

Figure 5.11 – The four images present the four different morphology types of radiation damage in the GFP-channel. The images were acquired of fluorescent stained Panc1 cells. γH2AX labelling appears in green light and the DNA (the nucleus) in blue light. From left to right examples of type I, II, III and IV cells are presented. Some cells have a mixture of type II-IV properties. The white scale bar has a length of 10 μm.

cannot be a reference since it also exhibits uncertainties. In another test we synthetically created foci in Matlab that had sizes and shapes similar to those seen in the microscope images. In these synthetic tests the detection rate tended towards 80% at high foci densities.

5.3 Results

5.3.1 Morphology of γH2AX-fluorescent stained cells after irradiation

Cells are not identical. Although the cells in a cell culture are monoclonal, i.e. they stem from a single ancestral cell, they differ in the state of the cell cycle, in age, oxidative state, mutations in the genome and many other parameters. Therefore the response of cells to a stimulus or stress such as ionising radiation will also cause individual reactions. Phosphorylation of γH2AX is a very rapid process. We fixed cells 30 minutes to 24 hours after irradiation depending on the experiment and the highest fluorescence signal was obtained shortly after irradiation. However, the signal is still measurable 24 hours after exposure. The rapid reaction of the H2AX histone following double strand break formation was observed in many experiments. The morphology of γH2AX staining varies. At doses of up to 5 Gy some cells showed no reaction at all and others were completely filled with the fluorescence signal. The distribution of the fluorescent marker can also differ from cell to cell. In some cases the marker was more or less homogeneously spread over the entire cell, in other cases foci formed in different sizes. We tried to classify the cellular reaction to radiation by γH2AX foci formation and found 4 groups (figure 5.11).

- Type I cells show no reaction at all. The γH2AX level is low and there are no foci visible.
- Type II cells have several small γH2AX foci. The foci diameter is smaller than 1.5 μm diameter. The background signal in the nucleus is low.
- Type III cells have a few large γH2AX foci. The foci diameter is larger than 1.5 μm and can measure up to 3 μm. The background signal in the nucleus is small.
- Type IV cells are completely filled with γH2AX speckle and foci. Some cells seem to emit a homogeneous, strong signal or have a high background signal.

The groups do not exclude each other. There are cells that have small and large foci at the same time with varying levels of background signal. The fraction of cells belonging to the different cell types depends on the dose. In very rare occasions apoptotic cells can be observed recognisable by blebbing and fragmentation of the cells (see chapter 5.1.1). These cells usually have a strong γH2AX fluorescence signal.

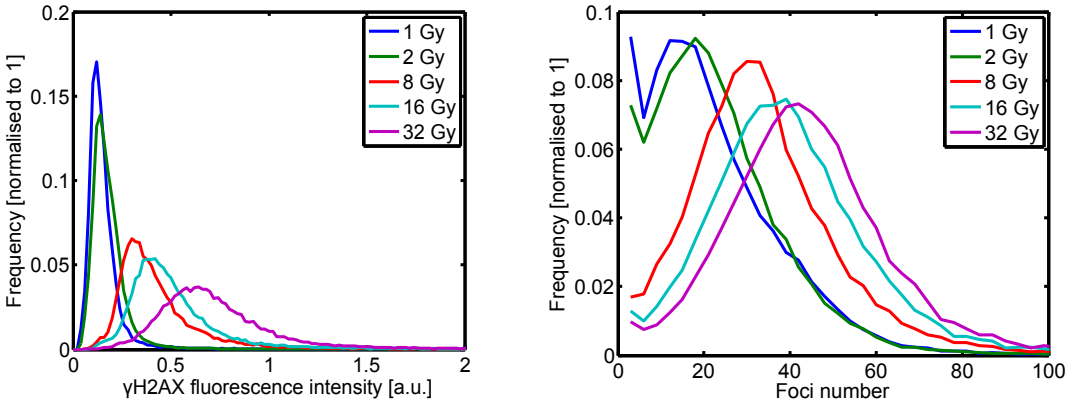

Figure 5.12 – Left: The γH2AX signal intensity histogram is shown for homogeneous irradiations with various doses 3 hours after exposure. With increasing dose the distribution becomes wider and is shifted towards higher doses. Right: γH2AX foci number histograms are shown for the same data. A shift to larger foci number is observed with increasing dose. The distributions are broader than for the signal intensity. Some cells do not show γH2AX foci at all. Especially at low doses there is a larger fraction of "non-responding cells". Peak positions and averages are plotted against dose in figure 5.13.

5.3.2 Exposure to homogeneous doses

Intensity and foci number are not linearly correlated

To assess the response of cells to homogeneous doses we plated cells in an experiment (experiment 1) 48 hours prior to irradiation onto iBidi μ-slides with a cell area density of 300 cells per square millimetre. Upon fixation 3 hours after irradiation the cell density was (630±50) mm^{-2}. Applied radiation doses were 1, 2, 8, 16 and 32 Gy. The cells were stained after fixation. The images were processed and analysed as described above. The number of γH2AX foci and the γH2AX intensity were determined for all of between 25,000 and 55,000 identified cells per dose. Figure 5.12 shows the cell frequency spectra over the γH2AX intensity and the number of γH2AX foci. In the γH2AX fluorescence intensity histogram a single peak occurs. It becomes broader and is shifted towards higher intensities with increasing dose. The foci number spectrum also shows a peak. Similarly it becomes broader and is shifted towards higher foci numbers with increasing dose. However, at low doses there is also a number of cells that do not have any foci at all. If the creation of foci was just a reaction to DSBs and each focus relates to a single DSB, one would expect a Poisson distribution of foci. All of the distributions are much broader than Poisson distributions. This can be tested by calculating the variance to mean ratio (VMR), which is 1 for Poisson distributions but between 10 and 15 in the measurement (compare Trainor et al. [112]). The differences here may be explained by counting uncertainties. Unexplained remains, however, the group of cells with no or very few foci. At low doses there seem to be responding and non-responding cells. These two types of cells are not distinguishable in the γH2AX intensity spectra. However, we found that the non-responding cells were at the low intensity end of the γH2AX intensity spectrum.

In figure 5.13 the γH2AX fluorescence signal and the average number of γH2AX foci are plotted against the applied dose. The mean and the most frequent value (peak position) are shown in the same graph. The latter is less sensitive to outliers. The uncertainty bars illustrate the peak width, which was arbitrarily defined as the set of values where the frequency is larger than 70% of the peak frequency. As described by others the number of γH2AX foci saturates at high doses. The γH2AX intensity, however, grows approximately proportional to $\sqrt{D}$ (compare black fit) and does not saturate. The reason for foci saturation could either be detection problems at high foci densities or the formation of repair centres [141]. The phosphorylation of the histone H2AX does apparently continue. A $\sqrt{D}$ behaviour could have its origin in the reaction kinetics.

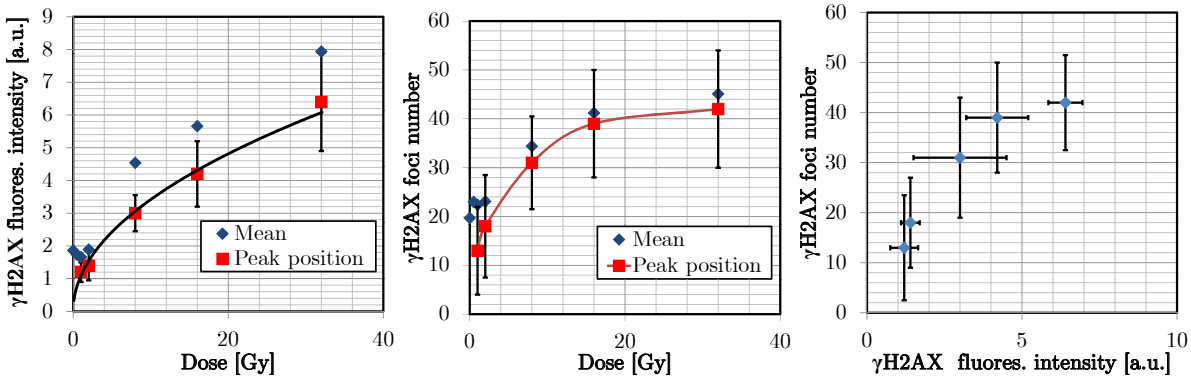

Figure 5.13 – γH2AX fluorescence intensity (on the left) and γH2AX foci numbers (in the centre) are plotted against the absorbed homogeneous dose. The distribution of foci and signal intensity is not symmetric and hence the most frequent intensity/foci number (red square) and the mean intensity/foci number (blue diamond) do not coincide. The mean is easier to compute. The peak position is, however, less sensitive to outliers. The peak position of the fluorescence intensity is approximately proportional to $\sqrt{D}$ and does not saturate with dose. The foci number saturates with dose. Hence there is no linear relationship between both quantities as shown on the right.

Although there is not enough data to reliably confirm this relation.

Radiation influences the cell cycle

Radiation has also an influence on the progression in the cell cycle. In order to study the cell cycle distribution we used the Hoechst 33342 stain and analysed the fluorescence intensity of cells in the blue channel (experiment 2). The fluorescence intensity is proportional to the amount of DNA in the cells. Cells in the G2-phase that have already replicated their DNA can be distinguished from cells in the G1-phase by a higher fluorescence intensity. The cells used for the experimental data shown in figure 5.14 were plated 48 hours before and fixed 24 hours after treatment. Some of the cells were irradiated homogeneously with 32 Gy, some of the cells were sham irradiated and some kept in the incubator throughout the whole experiment. When the cells were fixed the cell density was between 400 and 450 mm^{-2} in the irradiated iBidi wells and between 600 and 700 mm^{-2} in the unirradiated iBidi wells.

For the unirradiated cells 2 peaks at intensities I_1 and I_2 can be recognised. The ratio of I_2 to I_1 is slightly smaller than 2, which is very likely caused by a non-linearity of the microscope camera. The peak areas are approximately equal, i.e. cells are more or less equally distributed between G1- and G2-phase. Cells between both peaks can be attributed to the S-phase of DNA synthesis. After irradiation, however, the peak at intensity I_1 has almost disappeared. Instead another peak arises at an intensity I_3 which is approximately 1.8 times I_2. These are cells that have copied their DNA content 2 times. This may happen to cells that suffer from chromosome aberrations and that are consequently unable to pull the homologous pairs apart in the anaphase of mitosis. Some cells continue nevertheless with the S-phase and replicate the DNA. Probably related to the altered cell cycle distribution is an increase in the average nucleus size by around 31% from 90 to 119 μm^2.

In reaction to ionising radiation cells in the G2-phase have a stronger γH2AX signal and more foci than cells in G1-phase. At very low dose the factor is approximately 2. However it decreases with increasing dose. This is not an unexpected observation. G2-phase cells have more DNA and offer a 2 times larger target than G1-phase cells.

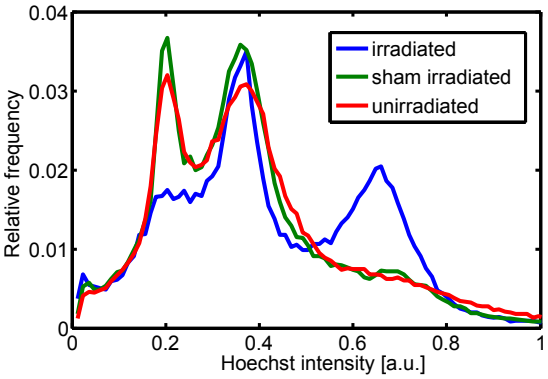

Figure 5.14 – Changes in the cell cycle visualised with Hoechst 33342. The Hoechst intensity (abscissa) is proportional to the DNA content of the nucleus. Cells in the G1-phase have a single DNA content and are represented by cells with the lowest Hoechst intensity (at 0.2). During S-phase the DNA is replicated and cells reach the G2-phase with an approximately doubled Hoechst intensity (at 0.35). Unirradiated and sham-irradiated cells distribute more or less equal between G1 and G2. Irradiated cells have almost no G1-phase cells 24 hours after irradiation with 32 Gy. Instead some cells have a signal intensity which is approximately twice the G2-phase signal. These are presumably cells which have after unsuccessful cell division doubled their DNA content twice.

5.3.3 Irradiation with modulated doses and bystander response

The γH2AX signal increases in low and decreases in high dose regions with time

We then turned towards inhomogeneous irradiations and tried to explore the role of cell-to-cell signalling in radiation fields with varying doses and finally in MRT fields. To this end we irradiated Panc1 cells through a copper wedge with a wedge angle of 14.9° to create a dose gradient across the cell population (experiment 3, see figure 5.15, left). The cells were plated 24 hours prior to irradiation. There are always two wells of the iBidi receiving the same dose. One of these wells was fixed 3 and the other 24 hours after irradiation. Cells were confluent when irradiated and had a cell density of 700 to 750 mm^{-2} 3 hours after radiation and 600 to 700 mm^{-2} 24 hours after radiation, respectively.

During irradiation a film was attached to the bottom of the iBidi μ-slide. Unfortunately there was no direct mapping between fluorescence microscopy images and dose possible. Allocating the cell position and the position on the x-ray film had an uncertainty of up to 0.5 mm.

The cells were immunostained, scanned with fluorescence microscopy and the images analysed according to the methods described before. Figure 5.15 (centre) shows the γH2AX fluorescence intensity over the position from the wedge edge. The four wells closest to the wedge edge were analysed. There is a 4 mm gap in the data at around 10 mm from the wedge edge. This is the location of the separator between the analysed wells. With growing distance from the wedge edge the intensity of γH2AX fluorescence becomes weaker. This is true for both, cells fixed 3 hours and cells fixed 24 hours after radiation exposure. However, the slope is steeper 3 hours post-irradiation. Intriguingly the two intensity curves intersect in the first well and in the second well from the wedge edge. All of the iBidi wells were stained with the same marker concentrations and imaged with the same settings of the microscope. Apparently the γH2AX activity does not simply decay with time, but they become equal. In high dose regions the activity is reduced, in low dose regions it is enhanced. In contradiction to observations by others (e.g. Schmid et al.[142]) the signal has hardly decayed after 24 hours. Equalling can also be observed in the γH2AX foci number. As seen for the homogeneous irradiations there seem to be two groups of cells – responding and non-responding cells. The fraction of these cells was dose dependent in the homogeneous case. This is also observed for the dose gradient. In figure 5.15 (right) the fraction of non-responding cells is plotted against the distance from the wedge edge. 3 hours after irradiation this fraction grows from 0.5% at the wedge edge to approximately 9% at 20

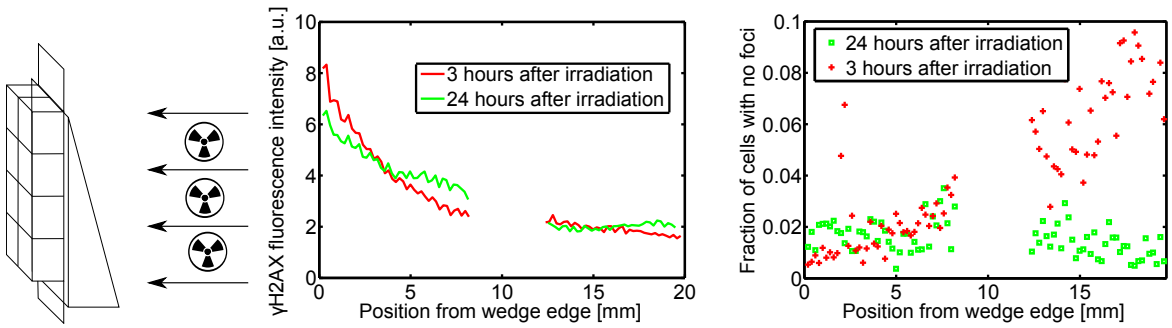

Figure 5.15 – Left: The experimental set-up to produce a dose gradient with a copper wedge is shown. The γH2AX fluorescence signal intensity is plotted in the centre as a function over wedge edge distance 3 and 24 hours after exposure. On the right the fraction of non-responding cells is shown. The gap at 10 mm is caused by the well separator. The right and the left parts of the curves stem from different wells and the medium could not mix.

mm distance from the edge. 24 hours after radiation there is, however, no dose dependency observable anymore. The fraction of non-responding cells is between 1 and 2%.

Evidence for a spatially propagating bystander signal at radiation boundaries

In another experiment we investigated the behaviour of γH2AX fluorescence intensity and number of foci at sharp irradiation boundaries (experiment 4). Cells were plated 48 hours before irradiation into iBidi μ-slides. Two wells of the μ-slide were irradiated with doses of 0, 5, 16 and 32 Gy in 4 parallel stripes (see chapter 5.2.2). The cells in one of these wells were fixed 3 hours and the cells in the other well 24 hours after radiation. 3 hours after radiation the cell density was 510 mm^{-2} and 24 hours after radiation 360 mm^{-2}. The number of foci and the γH2AX fluorescence intensity are both plotted in figure 5.16. The doses are 32 Gy from 0 to 2.1 mm, 16 Gy from 2.1 to 4.2 mm, 5 Gy from 4.2 to 7.0 mm and 0 Gy from 7 to 10 mm. Three hours after radiation the mean number of γH2AX fluorescence intensity and also the number of γH2AX foci show a step-like behaviour and there is a significant drop at each dose edge. Neither the fluorescence intensity nor the number of γH2AX foci respond, however, in a linear fashion. The number of γH2AX foci is more noisy than the fluorescence intensity data and the saturation effect of the foci number can be observed at high doses: The step size drastically increases towards lower doses. 24 hours after radiation treatment the steps have decreased in size, in both, number of γH2AX foci and γH2AX fluorescence intensity. However, the mean level of fluorescence intensity and the mean level of foci per cell has not diminished for all doses. The average number of γH2AX foci has increased in the 0 Gy step from 7 to 10 mm and the fluorescence intensity has raised in the 0 and 5 Gy steps from 4.2 to 10 mm. After 24 hours the fluorescence level of the 0 Gy step has reached the level of the 5 Gy step after 3 hours. As in the gradient dose experiment we have also analysed the fraction of cells with no foci (bottom row of figure 5.16). After 3 hours there is a strong drop observable from the 0 Gy to the 5 Gy step where the number of non-responding cells falls from 60% to approximately 10%. The fraction further decreases with increasing dose. However, there is no step-like behaviour visible anymore. This may possibly be caused by the low fraction of non-responding cells and the consequently poor statistics. More interesting is, however, the 0 Gy step itself. There is a remarkable increase of non-responding cells with increasing distance from the radiation edge from 60% to 80%. 24 hours after radiation there is not much of a difference in the non responding cells for the 5, 16 and 32 Gy steps to 3 hours post-irradiation. However, in the 0 Gy step the number of cells with no foci has fallen to 20%.

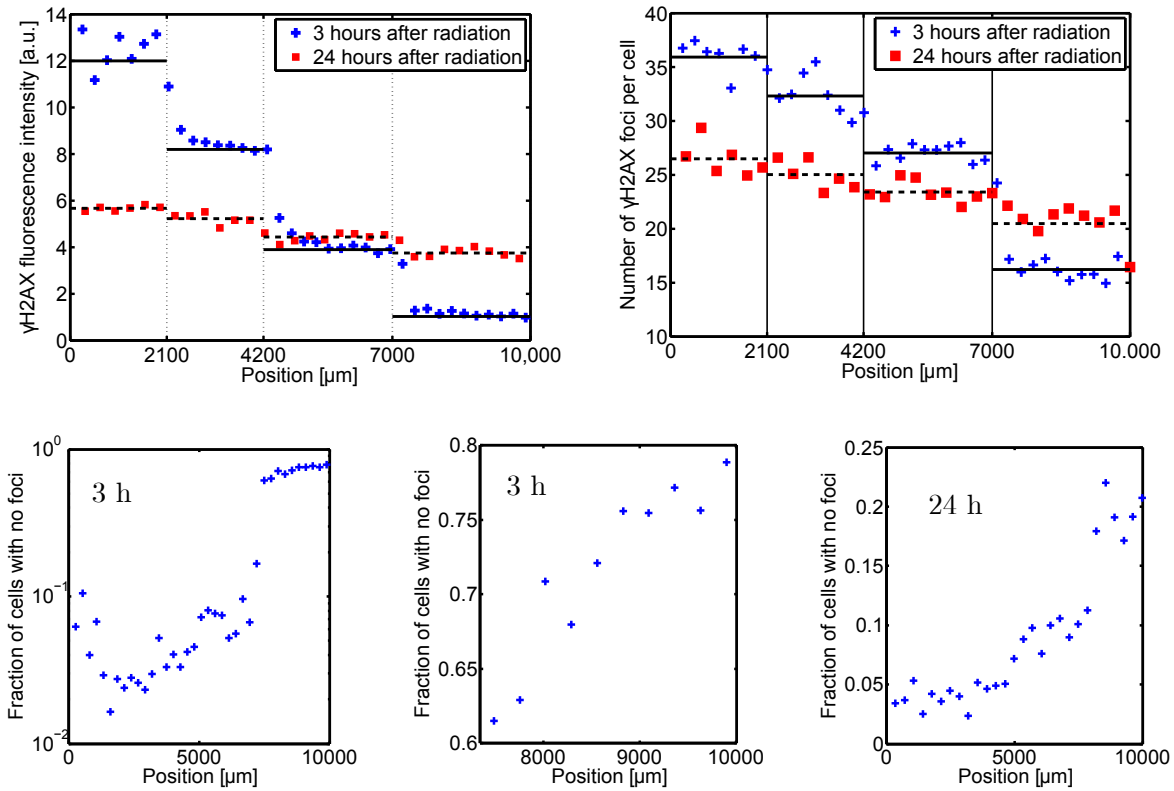

Figure 5.16 – The top left and the top right graph show the γH2AX signal intensity and foci number over the position perpendicular to the radiation boundaries 3 hours and 24 hours after exposure. The edges are indicated by lines at 2.1, 4.2 and 7 mm, separating 32, 16, 5 and 0 Gy zones. The bottom row shows the fraction of non-reacting cells with no foci: On the left 3 hours after radiation with a logarithmic ordinate. A strong drop occurs between 0 and 5 Gy. The part from 7 to 10 mm is plotted with a linear ordinate in the central plot and shows that the non-reacting cells are less frequent closer to the radiation boundary. The right graph shows the fraction of non-responding cells 24 hours after radiation exposure. In the radiated part the graph is similar to 3 hours after exposure. The fraction of non-responding cells in the 0 Gy-region has strongly decreased.

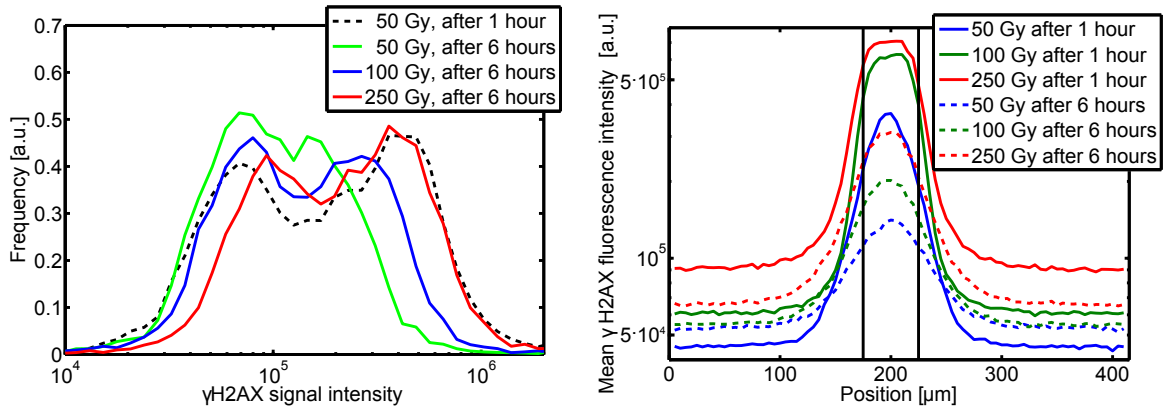

Figure 5.17 – The graph on left shows the γH2AX signal intensity histogram in the peak dose region of a 2×2 cm^2 MRT field. 6 hours after exposure for all doses and 1 hour after exposure for 50 Gy peak entrance dose, two distinct cell entities emerge. On the right a γH2AX profile (averaged over all peaks) is shown for all exposures and fixation time points.

5.3.4 Irradiation with an MRT field

Finally we investigated the γH2AX signal after irradiation with a microbeam field at the biomedical beamline ID17 of the ESRF in Grenoble. The experimental set-up for the application of microbeams is described in chapter 5.2.2. We irradiated Panc1 cells in cell culture flasks and iBidis with a 20×20 mm^2 MRT field. The adjusted beam entrance dose in water was set to 50, 100 and 250 Gy, leading to peak doses of 16, 32 and 80 Gy at the position of the cells. The PVDR (peak to valley dose ratio) in the field centre was 22 (details given in chapter 5.2.2). The cells were fixed 1 hour and 6 hours after exposure. Image acquisition for the cell culture flasks after staining was performed in a 22.5×26 mm^2 region with a resolution of 0.645 μm covering the whole MRT field. The iBidis were irradiated with the same experimental set-up, although the size of an iBidi well is just 9.4×10.7 mm^2 in size. However, we wanted to give two times the same doses. The centre of the field was aligned with the centre of the iBidi well. By imaging the central 7.6×7.6 mm^2 of the iBidi with a resolution of 0.322 μm we analysed approximately the central one seventh of the MRT field.

The lower resolution of 0.645 μm was not suitable for foci detection and only the γH2AX fluorescence intensity was evaluated. The cell densities in the culture flasks lay between 500 and 600 mm^{-2}. The higher resolution for the iBidi wells was used for foci analysis. Due to experimental difficulties the cells in the iBidis were much less homogeneously plated and the cell density was only between 220 and 280 mm^{-2}.

In the peak region a responding and a non-responding cell-entity exists

The Monte Carlo results (see chapter 5.2.2) were used to assign a dose to each cell. This way it was possible to analyse the fluorescence signal depending on the absorbed dose. In figure 5.18 γH2AX fluorescence intensity histograms are plotted against the absorbed dose in heat maps. Both, the dose and the GFP intensity are plotted on a logarithmic scale. 1 hour after irradiation cells receiving a dose smaller or equal to the valley dose show only a weak γH2AX fluorescence intensity dependence on dose. From the valley dose to approximately 2 times the valley dose the γH2AX intensity strongly increases and reaches a saturation level. Above 2 times the valley dose there is no dose dependency observable. This observation is independent of the peak entrance dose. However at 50 Gy peak entrance dose with a peak dose of 16 Gy, some cells above 1.5 Gy show a high and some a low fluorescence intensity. 6 hours after radiation there is no dose

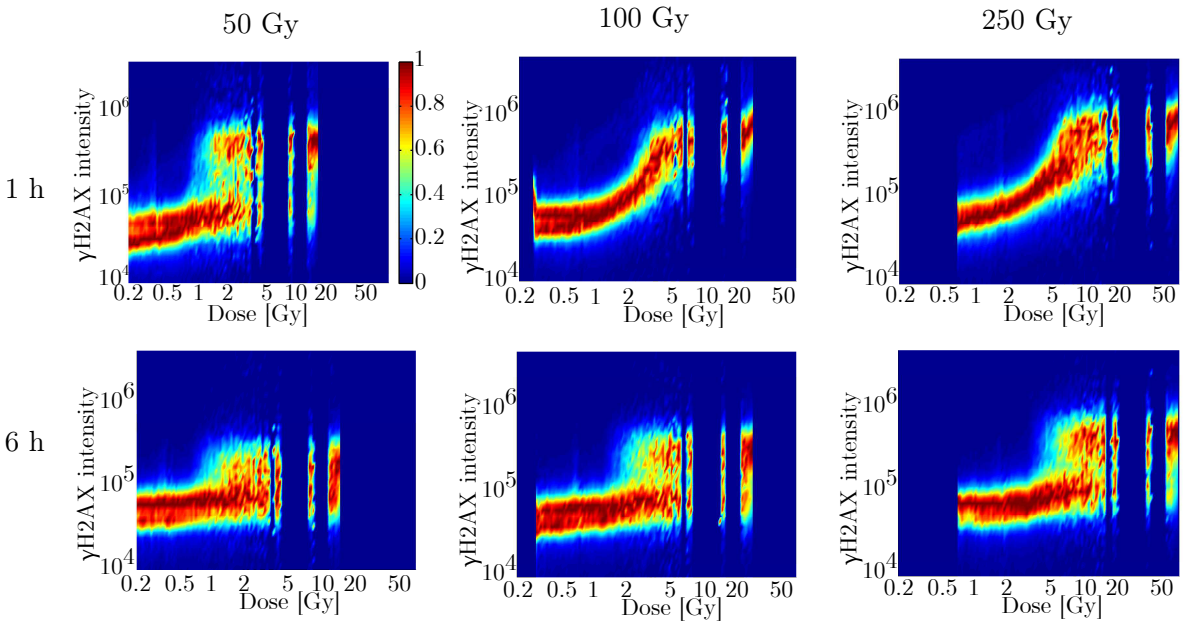

Figure 5.18 – Histograms over γH2AX fluorescence intensity and dose 1 hour after exposure (top row) and 6 hours after exposure (bottom row). The first, second and third column show the results for 50, 100 and 250 Gy peak entrance dose, respectively.

dependent behaviour observable up to approximately 2 times the valley dose. Above this dose two cell entities exist, the one having a low γH2AX fluorescence intensity (entity 1) which is only marginally higher than in the valley region and one having a high fluorescence intensity (entity 2). Figure 5.17 (left) shows the γH2AX intensity histograms for the peak region. While the γH2AX signal of entity 1 is almost dose independent, that of entity 2 depends on the dose and is higher at higher peak doses. The fraction of entity 2 cells is approximately 60% for 100 and 250 Gy 6 hours after radiation and also for 50 Gy 1 hour after radiation. This fraction falls down to approximately 30% 6 hours after radiation for 50 Gy peak entrance dose.

The γH2AX signal decay depends on the dose

The γH2AX fluorescence intensity beam profiles blur with time whereas the intensity differences in the valley dose regions decrease. A profile of the γH2AX signal intensity across a single microbeam is shown in figure 5.17 (right). The time course of the γH2AX signal intensity depends apparently on the dose. 6 hours after radiation the γH2AX signal in the valley at 50 Gy peak entrance dose has increased, whereas that of the cells in the valley at 100 Gy peak entrance dose has slightly decreased. This leads to almost equal levels of γH2AX signal in both cases. The strongest decrease of the γH2AX fluorescence is observed for the cells in the valley region at 250 Gy peak entrance dose.

The peak dose influences the cell response in the valley and vice versa

From the images with higher resolution γH2AX foci were counted. As expected the foci number per cell increases with increasing dose. Dose is not its only determining factor, though. At the same dose the number of foci in the valley region depends on the peak dose as well. 1 hour after radiation an average number of 40 foci per cell is achieved with 4 Gy at 50 Gy peak entrance dose, with 7 Gy at 100 Gy peak entrance dose and with 12 Gy at 250 Gy peak entrance dose (see table in figure 5.19). An increasing peak dose seems to make the cells in the valley more resistant to radiation. Histograms over the number of γH2AX foci are presented in figure 5.19. 1 hour

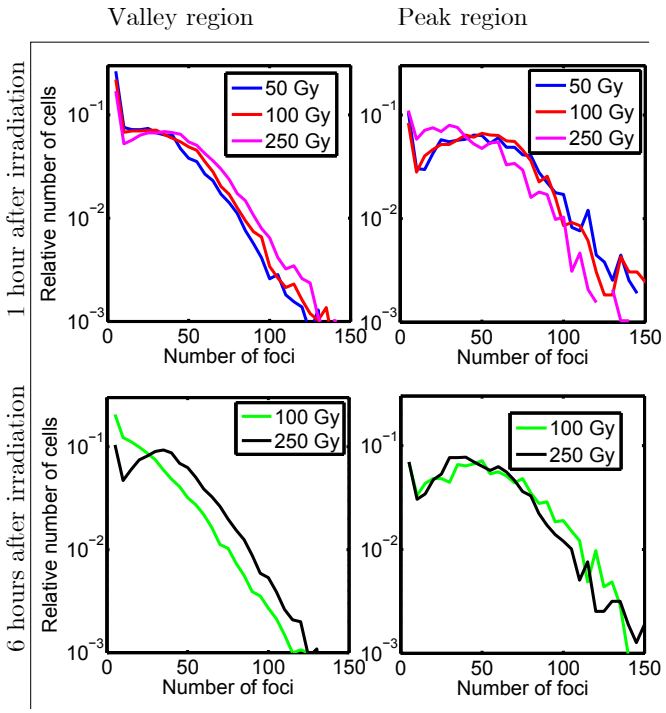

Peak:

Time	Dose	non-responding	Maximum at
1 h	50	11%	50
1 h	100	8%	50
1 h	250	11%	30
6 h	100	7%	50
6 h	250	7%	40

Valley:

Time	Dose	non-responding	Maximum at
1 h	50	17%	25
1 h	100	22%	30
1 h	250	26.5%	35
6 h	100	21%	-
6 h	250	10%	35

Figure 5.19 – The figure shows γH2AX foci number histograms in the valley and peak region 1 and 6 hours after exposure with a 2×2 cm^2 MRT field. The numerical values are tabulated on the right.

after radiation the fraction of cells with no foci is 17, 22 and 26.5% in the valley at 50, 100 and 250 Gy respectively. Surprisingly the number increases with increasing dose. For the fraction of responding cells the frequency maximum is at 25, 30 and 35 foci per cell at 50, 100 and 250 Gy. In the peak region there is still a fraction of not responding cells which is around 11% for 50 and 250 Gy and around 8% at 100 Gy peak entrance dose. The frequency maximum is at 50 foci per cell at 50 and 100 Gy. At 250 Gy the maximum number of cells is reached at around 30 foci per cell, similar to the valley dose region. The number of foci per cell is still around 50 at 100 Gy peak entrance dose in the peak dose region after 6 hours, whereas the number of foci at 250 Gy, although it has increased a bit, is still smaller at around 40 foci per cell. At 100 and 250 Gy the fraction of non-responding cells is approximately 7%. In the valley region the fraction of non-responding cells is 21% after 6 hours for 100 Gy (22% after 1 hour) and 10% for 250 Gy (26.5% before). For 100 Gy peak entrance dose there is no frequency peak over the foci number visible. For 250 Gy there is a peak at 35 foci per cell.

Two effects can be concluded from these observations. First, the time scales of foci production and degradation and also of the γH2AX signal time-lapse depend on the peak entrance dose. Secondly, there seems to be a signal from the valley region that leads to a reduction of γH2AX signal in the peak regions of the microbeams. The time scale of the latter effect is again dose dependent which can be deduced from the observation that after 50 Gy peak entrance dose the two cell entities have already formed 1 hour post-exposure. For 100 and 250 Gy this needs more time and is observed after 6 hours only. Vice versa the peak dose region seems to influence the valley as well and leads to less foci at the same valley dose with an increasing peak dose. 1 hour and 6 hours after irradiation there is clearly no linearity between γH2AX signal or foci number and dose. This might be different at time points closer to the irradiation as reported by others (e.g. Rothkamm et al.[143]).

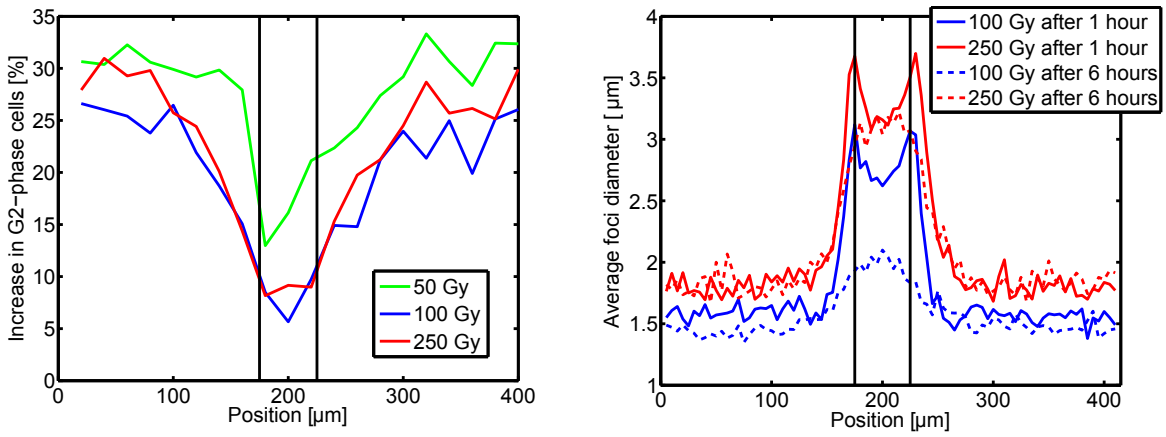

Figure 5.20 – The left graph shows the change in the fraction of G2-phase cells as an averaged profile across the microbeams for 50, 100 and 250 Gy peak entrance dose. The boundaries of the microbeam are indicated as black lines. The graph on the right shows the average foci diameter as an averaged profile across a microbeam for 100 and 250 Gy peak entrance dose 1 and 6 hours after exposure. Foci in the microbeam are much larger than in the valley. 1 hour after exposure the edges of the microbeam show the highest average foci sizes.

Irradiation changes the cell cycle distribution in the valley, but not in the peak

There is another interesting phenomenon in the cell cycle distribution. As described previously in chapter 5.3.2 cells accumulate after irradiation in the G2-phase and the fraction of G2-phase cells increases. 1 hour after radiation, independent of the peak entrance dose and cell position in the peak or valley region, $(19.0 \pm 1.5)\%$ of the cells were in G2-phase, $(48 \pm 3)\%$ in G1-phase and $(17.8 \pm 1.4)\%$ in the S-phase. A few cells had more than the doubled DNA content. However, this fraction counts just $(5.0 \pm 0.9)\%$ of the cells. 6 hours after radiation treatment the G2 fraction has grown by $(28 \pm 3)\%$ for all peak entrance doses in the valley region (see figure 5.20). However, the increase in the G2-phase fraction in the peak region is, despite the higher dose, much smaller at around $(8 \pm 3)\%$ for 100 and 250 Gy peak entrance dose. This reduction of G2-cell cycle accumulation is not constraint to the beam region, but extends to $100\,\mu m$ into the valley region approaching the valley dose value. At 50 Gy peak entrance dose the reduction is less pronounced at around 15%.

The exact quantification is difficult for several reasons. The delineation of the cell cycle phases was done by eye and is in this sense arbitrary (see appendix D). Furthermore the cell cycle distribution depends on many factors, including cell density and the culture medium. Therefore comparison between different flasks is of limited meaning although the cells were plated at the same time, with the same medium and reached a similar cell density. Even more difficult are links to other experiments. Nevertheless the reduction of a G2 fraction close to the beam is evident. Whether this means an increased cell cycle arrest in the valley or a reduced cell cycle arrest close to the peak cannot be decided.

Foci sizes vary between peak and valley and are highest at beam penumbras

Another intriguing observation indicates that the high-to-low dose interface plays an important role. It was reported by others that not only the number and intensity of foci is a useful information on DNA damage, but also the size of the foci[141]. We have therefore analysed the foci size with autocorrelation and determined a mean foci-size of the cells (for details see appendix D). In figure 5.20 (right) the mean foci size is plotted as a profile across a single microbeam. The average foci size in the valley region is $(1.6 \pm 0.1)\,\mu m$ and $(1.4 \pm 0.1)\,\mu m$ 1 and 6 hours after 100

Gy peak entrance dose and $(1.8 \pm 0.1)\,\mu m$ both, for 1 and 6 hours after 250 Gy peak entrance dose. In the peak region the average foci size is higher. In the centre of the peak the mean foci diameter is $(2.6 \pm 0.1)\,\mu m$ and $(2.0 \pm 0.1)\,\mu m$ 1 hour and 6 hours after 100 Gy peak entrance dose and $(3.1 \pm 0.1)\,\mu m$, both 1 hour and 6 hours after 250 Gy peak entrance dose. 1 hour after irradiation the foci size is at the beam penumbra much higher than in the microbeam centre. 6 hours after radiation these spikes at the beam penumbra have disappeared.

Evidence for gap junction mediated signalling

Two ways of signal transmission are discussed that may induce bystander reactions, soluble factors and gap junctions (see chapter 5.1.2). The cell cycle changes are observed in a region around the microbeam which is much broader than a single cell. Also the observed signalling in the step irradiation and equalising of γH2AX signals seen in the radiation experiments with inhomogeneous fields promote the hypothesis that a soluble signal is involved. But there is also evidence for gap junction mediated signalling in MRT fields. Figure 5.21 (left) shows the γH2AX signalling strength in dependence on the distance to the closest neighbour. The average cell nucleus diameter[ix] is $(21.3 \pm 4.0)\,\mu m$. The γH2AX signal strength is on average lower for cells with a close neighbour. Especially for nuclei that are closer to each other than the average nucleus diameter, there is a strong decrease in the average γH2AX fluorescence level.

Does the signal of neighbouring cells lead to a continuous response or is it binary, triggered by the signal of the neighbouring cell? In figure 5.21 (right) γH2AX signal strength histograms are shown for nuclei distances of 14 to 17 μm, 18 to 28 μm and 29 to 50 μm in the valley region 6 hours after treatment with a 100 Gy peak entrance dose MRT field. These histograms suggest that the response is binary. Responding cells have a lower γH2AX signalling strength and non-responding cells have a higher signalling strength. With increasing distance from the closest neighbour the fraction of cells with a higher fluorescence grows.

Unfortunately there is a large overlap of the two γH2AX intensity spectra. This is, however, not surprising looking at the method. Its main drawback is that it does not differentiate between two isolated cells and a cell which is situated in a confluent part of the cell culture flask. Furthermore it does not consider the γH2AX level of the adjacent cells. The first problem can be circumvented by analysing the γH2AX signal in dependence on the local cell density. The result is very similar. The second problem can be avoided by analysing the distribution of the difference of H2AX phosphorylation $\Delta_{i,j}$ between two cells i, j exposed to the same dose with fluorescence intensities I_i and I_j,

$$\Delta_{ij} = |I_i - I_j|. \tag{5.15}$$

If cells are not influencing each other, the distribution of $\Delta_{i,j}$ with arbitrary cells i, j and the distribution of $\Delta^n_{i,j}$ with neighbouring cells i, j should be the same. This is, however, not the case. The distribution of $\Delta^n_{i,j}$ is more concentrated at the origin than $\Delta_{i,j}$ which is broader. It can be concluded that the H2AX phosphorylation state is signalled to neighbouring cells and adapted by the cells. A comparison of the distributions $\Delta_{i,j}$ and $\Delta^n_{i,j}$ also allows to estimate the percentage of cells that move into line with close neighbours. In appendix D the two distribution are plotted for 100 Gy, 1 hour and 6 hours after radiation exposure for all cells receiving a valley dose between 1.5 and 1.6 Gy. 1 hour after exposure 9.2% of the cells are closer to their neighbours in H2AX phosphorylation levels than to other arbitrarily chosen cells receiving the same dose and 6 hours after exposure 42.7%.

[ix] This diameter was obtained by the automated cell nucleus segmentation of the Cell Profiler. The area of the detected nucleus is usually marginally larger than the actual nucleus. The diameter was calculated by assuming circular nuclei.

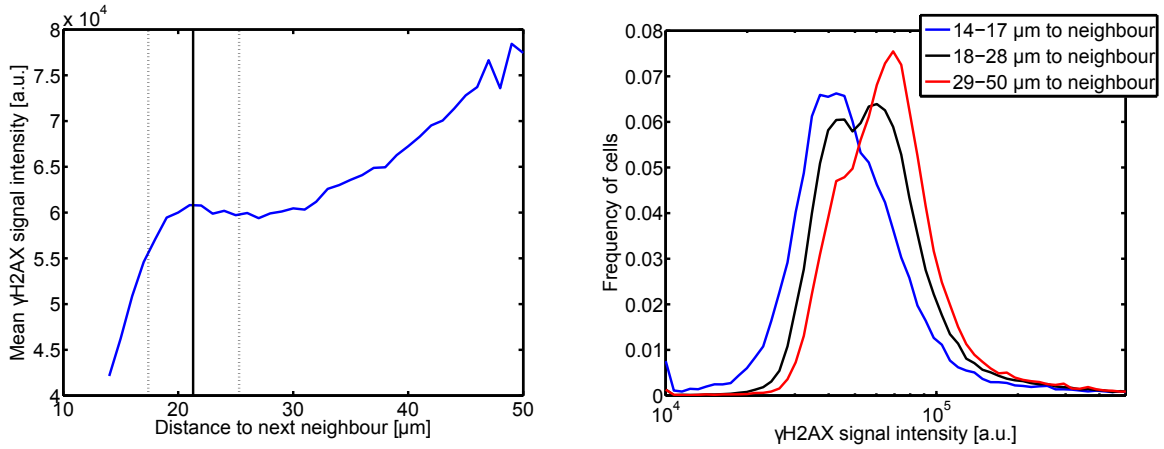

Figure 5.21 – The graph on the left shows the mean γH2AX signal intensity of cells depending on their distance to the closest neighbour. The signal intensity is lower for closely adjacent cells. The right figure shows histograms over the γH2AX signal intensity in dependence on the distance to the closest neighbour. The histograms reveal that the signal intensity does not only increase with distance, but that there is a kind of binary behaviour – either they have a low or a high signal.

5.4 Discussion

Some of the results described in the last chapter are astonishing, but an interpretation with our present knowledge on DNA DSB repair is a challenging task and cannot be satisfactory accomplished in this chapter. For sure the presented data will challenge certain paradigms and it proves our limited knowledge on cell biology. The investigations and experiments in this work are by far not exhaustive and were not intended to be. Everything they can achieve is encouraging further intensive work on the field of cell-cell communication and DNA damage repair because both will probably have a strong influence on radiotherapy outcomes.

The histone H2AX was discovered in 1980 as an isoform of the H2A histone. Its role in DNA damage repair was first suggested by William Bonner[144]. A linear dose response between foci creation and absorbed dose of ionising radiation was shown several times for low doses[140,141,143] and a direct correlation of foci with double strand breaks has been inferred. Hence γH2AX has frequently been used as a biomarker for DSBs. It was shown to be 100-fold more sensitive than the comet assay[142,145]. A matter of debate is whether the γH2AX signal intensity is similar to the number of γH2AX foci a measure of DNA damage. Several studies report linear relationship between both quantities and use the fluorescence intensity instead of the foci number[142,146,147]. Measuring fluorescence intensity is easier to accomplish and can be used in flow cytometry. Furthermore the detection of foci is not straightforward especially at high doses when several foci overlap. Very likely the here observed saturation of foci number at high doses has in part its origin in the lack of foci resolution. In particular small and dim foci are often missed in both automated and manual foci counting. The intensity of γH2AX binding per cell, however, does not only depend on the number of DSBs, but also on the H2AX substrate and the H2AX kinase activity[144]. Moreover a lower expression of γH2AX in unirradiated G1-phase cells was observed in these experiments and by others[147]. Nonetheless γH2AX was proposed as a biodosimeter with some success even in the valley region of MRT fields[143].

Phosphorylation of γH2AX

In order to judge upon the best method to evaluate cell damage and to interpret the experimental data a good knowledge of γH2AX functionality would be desirable, but is only partially present.

H2AX contributes, depending on the cell line, to 2-25% to the H2A histone pool[148]. It differs from other histones by a serine residue 4 amino acids from the COOH terminus. After DNA damage this serine becomes rapidly phosphorylated. The causes can be various, e.g. external damage, replication fork collisions, apoptosis and dysfunctional telomeres[148]. Phosphorylation itself may occur via different pathways. ATM (ataxia telangiectasia mutated) seems to be most important after ionising radiation. But there are others, such as ATR (ATM and Rad3-related) and DNA-PK (DNA dependent protein kinase). However, H2AX phosphorylation is not necessary for DNA break recognition[149]. H2AX deficient cells are still able to gather repair and signalling proteins at the DSB site. Lu et al.[150] therefore supposed that the presence of a γH2AX focus does not necessarily reflect a DSB. They showed that γH2AX is involved in apoptosis after UVA exposure and investigated the JNK-mediated phosphorylation of H2AX. They found that JNK inhibition reduces both, H2AX phosphorylation and caspase-3 activation, a hallmark of apoptosis. Although H2AX was not required in their experiments for caspase-3 activation, it was necessary for the DNA fragmentation ("ladder formation") in apoptosis. In fact H2AX deficient cells were significantly more resistant to apoptosis than wild type cells. This fits well to the observation that H2AX acts as a tumour suppressor[150,151]. The lack of H2AX in p53 deficient mice considerably accelerates the onset of lymphomas and other cancers[148]. It was also observed that H2AX deficient cells fail to arrest in the G2-phase after ionising radiation[148,152]. This is a very interesting observation with respect to our own findings. Is there a connection between the reduced percentage of cells in the G2-phase close to the microbeams and the large γH2AX foci that only occur at the microbeam site but not in homogeneous fields? Genome instability and increased radiosensitivity is both accompanied with a lack of H2AX[153,154], although its role in DNA-repair remains unclear.

Signal decay of γH2AX

Although H2AX is not essential for DNA DSB repair one observes dephosphorylation of γH2AX after DNA repair[140]. The time course of foci decay is very similar to the kinetics of DSB repair after intermediate doses[155] and an impaired DSB repair pathway leads to persistence of foci as shown in DNA-PKcs deficient[140], Ku80 deficient[156] and DNA ligase IV-deficient cells[155]. Therefore Olive and Banáth[157] proposed the use of γH2AX to measure radiosensitivity of cell lines. They measured the disappearance of γH2AX during the first few hours after exposure and found that radioresistent cell lines lose γH2AX faster than radiosensitive cell lines. From pulse field gel electrophoresis (PFGE) analysis it was found that DSBs decay exponentially with time after exposure[141,158]. Schmid et al.[142] demonstrated that the γH2AX signal decay has two exponential decay contributions, one with a halftime of 13.9 hours and one with 24 minutes. They observed that the contribution of both processes depended on the radiation type. With low LET radiation treated cells had a lower slow decay contribution than cells exposed to high LET radiation. The decay of γH2AX is also slower for p53 deficient than in p53 wt cells (5.9 vs. 3.8 hours)[153], probably because p53 is involved in the regulation of DNA repair. In our own experiments we fixed cells 1, 3, 6 and 24 hours after radiation. In contrast to the described findings we didn't see a decay half time in the order of 6 hours. The decay was much slower and sometimes even an increase was observed for γH2AX foci and H2AX phosphorylation. In the case of the gradient irradiation there was just a minor difference between the γH2AX levels after 3 and 24 hours. Furthermore the decay kinetics is dependent on the dose and the dose given to neighbouring cells. For the experiments carried out in this work doses were, however, much higher than for the majority of other experiments using γH2AX staining protocols. Several authors confirm that the number of foci per cell decreases with repair time only at low doses but not at higher doses[144,155,156,159]. Bouquet et al.[156] investigated the dose dependence of γH2AX signal loss after calicheamicin γ1 (CLM) and x-ray treatment and found that at higher doses the

level of H2AX phosphorylation remains high for hours. What is different at high dose exposures? Is the remaining high γH2AX level an indication of cellular stress and stress signalling?

The exact meaning of the γH2AX signal remains a matter of debate. The one-to-one correlation with DSBs is also questionable since most of the DSBs join within a few minutes which completely contradicts γH2AX loss half-times in the order of several hours[157]. 24 hours after a 2 Gy radiation exposure Banáth et al.[153] were not able to detect any residual DNA damage, challenging again the association of γH2AX foci with physical breaks.

Linearity of the γH2AX signal with dose

Critical for seeing a linear correlation between dose and γH2AX reaction (e.g. number of foci) seems to be the time of observation after exposure. Many experiments suggest a linear dose response up to 2 or 3 Gy (e.g. Bracalente et al.[140], Rothkamm et al.[143]) and most of them measure shortly after radiation exposure. Rothkamm and Löbrich[155] even claim linearity from 1 mGy to 100 Gy between foci count and dose. However, they count foci as early as 3 minutes after radiation exposure. Our experiments are far beyond the typical dose scale and 1 hour time between irradiation and fixation seems to be already too long to see a one-to-one response between dose and γH2AX reaction. Linearity might exist at low doses (D $<$ 10 Gy, see figure 5.13) in the experiments described here. Also the level of background foci is quite high. An explanation could give foci repair centres. It was suggested that close by foci merge to form a single focus[141]. At high LET radiation less foci were observed than DSBs predicted by Monte Carlo simulations. This clustering happens before the formation of radiation induced foci, because it was not observed in the first 30 minutes. Foci merging after longer time periods was, however, noticed giving a possible explanation of larger foci at longer time periods after radiation exposure[141].

The meaning of γH2AX foci size

The meaning of different foci sizes is another unsolved problem in γH2AX analysis. Higher foci sizes were observed after high LET radiation[140,141]. For low and intermediate LET Neumaier et al.[141] measured on average 0.64 μm diameter (FWHM) 30 minutes post-irradiation. At high LET small and large foci were found in experiments by Bracalente et al.[140]. Furthermore foci in the primary track appeared larger (0.8 μm) than those of delta rays (0.6 μm)[141]. With time after radiation foci sizes were observed to increase[140,153]. Observations in this work also suggest that foci can be classified in large and small foci. In chapter 5.3.1 we classified cells depending on the foci size into 4 groups, cells without foci, cells with small foci, cells with large foci and cells that were completely speckled and filled with γH2AX. The fraction of the different types were found to be dependent on the radiation dose. With autocorrelation we estimated the foci size. Foci sizes that we estimated with this method are larger than sizes found in the literature. This is very likely rather a methodological than empirical difference. Furthermore the autocorrelation method yields an average for all foci.

The creation of larger foci was attributed to complex non-repairable DNA damage and Bracalente et al.[140] supposes that larger foci persist whereas small foci resolve. These findings can partly be confirmed by our own observations. The higher the dose becomes the larger the average foci size gets. In the peak region much larger foci were found than in the valley region. Contradictory is, however, the reduction of the mean foci size from 1 to 6 hours after exposure and even more the observed extremely large foci at the microbeam edges. Foci size seems to indicate more than the complexity of DNA lesions. Their appearance could be connected to signalling and bystander effects at the edges of the microbeam path.

Bystander signalling by gap junctions

Rothkamm et al.[143] observed, when trying to use γH2AX foci counting for biodosimetry, that there is a higher number of foci close to the absorption edges and that this effect cannot be explained by cell movement. In fact Crosbie et al.[160] did not observe a significant cell motility after MRT exposure. They therefore already hypothesised a inter-cellular signalling between neighbouring cells. We also observed these increased γH2AX levels in the step irradiation experiments close to the step edges (see figure 5.16). There is an increase of the level close to the edge on the low dose site, at the 16 to 32 Gy and the 5 to 16 Gy edge. Between 0 and 5 Gy this increase is not observed, however we see a reduction of non-responding cells with decreasing distance to the radiation boundary. But there are also several observations in the microbeam field that indicate cell communication. An increasing peak dose leads to the same number of foci at higher doses in the valley and there is a slight increase in the number of foci in the valley dose 6 hours compared to 1 hour after radiation. The latter observation seems to be typical for inhomogeneous radiation fields: While high dose regions lose γH2AX levels, levels raise in low dose regions.

What mediates the signal transduction between cells then? Banáth et al.[153] observed that neighbour cells often show similar foci numbers and sizes and inferred that these are daughter cells from one irradiated mother cell and that the damage is inherited. In our observation we also see equal damage in adjacent cells. After 1 hour 9.2% and after 6 hours 42.7% of neighbouring cells have a more similar H2AX phosphorylation level than two randomly selected cells at the same dose. It is unlikely that this originates in cell division and inherited damage. The importance of cell-to-cell contact was emphasised by experiments of Mitchell et al.[161]. In their experiments they irradiated C3H 10T1/2 mouse fibroblast cells with a high and a low plating density by a 5.3 MeV α-particle microbeam. Bystander effects were observed for both, low and high density cells. However, the effects were several times stronger in densely plated cells.

Changes in the cell cycle two cell entities

Remarkable is the change in the G2-phase fraction of the cell population across the microbeam. That the cell cycle is influenced by cell-cell communication after radiation exposure is not new. Shao et al.[162] demonstrated that the G1 cell cycle arrest is influenced in bystander cells and that cell-cell contact is important. In view of these observations the question is whether the reduced G2-phase fraction in and close to the microbeams results from an induced G1-arrest. This, however, is unlikely, because it is well known that the G1 arrest is mediated by $p53^2$. Panc1 cells are p53 mutants and should therefore not arrest in G1-phase. This is also confirmed by the presented experimental results of homogeneous irradiations, where the G2 fraction is increased 24 hours after exposure (see figure 5.14). Another hypothesis would be that the cells get stuck in the S-phase due to the high damage caused in the peak. However, there is an increase in the G1-phase observable compared to the valley (data not shown) and the S-phase fraction remains more or less unaffected. Furthermore the change in the cell cycle distribution is also seen at 50 Gy peak entrance dose. Here the peak dose is even lower than for the homogeneous exposure with the cell cycle distribution shown in figure 5.14.

A possibly related observation is the formation of two cell entities with very different levels of H2AX phosphorylation. In case that the cell cycle progression is accelerated in the microbeams, one could argue that the entity 1 (with a lower H2AX phosphorylation level) is generated by fast proliferation and quickly created daughter cells that were not exposed to radiation. The fraction of entity 1 cells after 6 hours at 100 and 250 Gy is 40%. Hence within 6 hours 25% of a cell population that received a very high dose would have divided, which is very unlikely. Even more astonishing would be that 25% of the cell population in the peak region of the 50 Gy peak entrance dose MRT field would have already replicated within 1 hour. Although cell density is

a difficult measure, because it cannot be measured prior to irradiation, there is no evidence that there was an increased cell density at the microbeam site which would support the theory that enhanced proliferation created the low γH2AX level cell entity. Fact is that the splitting of the cell population in a high and low γH2AX signal fraction happens at the microbeam edge (see appendix D). Furthermore there is a time dependence observable. Apparently the splitting is delayed by higher doses and occurs faster at low doses, since we see the two cell entities already after 1 hour at 50 Gy peak entrance dose but not before 6 hours after irradiation for 100 and 250 Gy peak entrance dose. In the case of 50 Gy peak entrance dose the fraction of high γH2AX level cells has decreased 6 hours after exposure. Does that imply a repair process? Further experiments are required to probe this hypothesis.

Bystander signalling by a small soluble factor

Apart from observations indicating a gap junction mediated signalling there is also evidence in the performed experiments for bystander signalling by soluble factors. The equalisation of γH2AX response after a dose gradient and dose steps irradiation is one of them and the increased levels of γH2AX signal in the valley 6 hours compared to 1 hour after MRT field irradiation another. Also the changing fraction of non-responding cells with the distance to the radiation edge in the 0 Gy step of the step-irradiation experiment indicates signalling by soluble factors. McMahon et al.[109] suggested a model for bystander response assuming a diffusible small molecule. The basic points of their model are:

- Hit cells and responding cells generate a signal for a certain time to reach a local equilibrium. The time depends on the DNA damage.
- The signal decays with a certain decay constant λ.
- Not the intensity of the signal, but the time of influence above a certain concentration threshold on a bystander cell decides upon reaction probability.
- The response is binary.
- The propagation of the signal with concentration ρ is described by the diffusion equation with a decay term, where D is the diffusion coefficient:

$$\frac{\partial \rho}{\partial t} = D\Delta\rho(r,t) - \lambda\rho(r,t).$$

They presume that diffusion is usually much faster than signal production. Therefore we consider the stationary problem with $\partial\rho/\partial t = 0$ and try to find a solution for an experiment where half of the cells are irradiated and half of the cells are shielded. The stationary solution for ρ in the unirradiated half space, if the irradiated half space has a constant concentration c_0, sustained by the cells after damage detection and if the unirradiated half space does not have any signal production at all, is

$$\rho = c_0 e^{-\sqrt{\lambda/D}d}, \tag{5.16}$$

where d is the distance from the radiation boundary. Mastro et al.[163] measured the diffusion coefficient of small molecules in the cytoplasm and found on average $3.3 \cdot 10^{-4}\ mm^2/s$. McMahon et al.[109] found for λ a value of $3.2 \cdot 10^{-4} s^{-1}$ when fitting experimental data. This implies that the spatial signal decay is in the order of 1 mm. That fits well to the ranges observed in our experiments[x].

[x]Important in the model of McMahon et al.[109] is of course the time a cell is subjected to a certain signal strength. However, the cells in the irradiated part will at a certain point stop emitting a signal. Because of

Of course the data presented here is still too sparse and subjected to too high uncertainties for a quantitative evaluation. However, our results do in principal support a soluble factor mediated bystander effect. Definitely this bystander effect is important in MRT, where valley dose regions have just a few hundred micrometre distance from the closest dose peak.

5.5 Conclusions

In this chapter we tried to find explanations for the principles behind MRT tissue sparing by looking at effects in the double strand break repair and changes in the cell cycle in pancreatic cancer cells under cell culture conditions, i.e. in vitro. The attempt to exhaustively explain the rational behind MRT with these experiments was not intended. Cell culture can hardly simulate the complex processes in real tissue as part of an even more complex organism. Inflammatory response, immune reaction, cell migration and the effects of the vascular system are not present in this simple model. Cell culture is another model in science that has its strengths and weaknesses. Scientific models do not represent the reality they are just reflecting some parts of it. The strength of a model is at the same time its weakness: the simplification of reality. It is the principle of science to simplify and abstract and at the same time not to forget about the differences to reality. Still, the model of cell culture is very complex and we understand but very little about the cellular response towards ionising radiation.

Within the model of cell culture we were, however, able to show that the secret of tissue sparing in MRT is likely to be found in molecular biology. This shall not exclude other explanatory approaches. We showed that at high doses neither the creation of γH2AX foci nor the phosphorylation level of H2AX are proportional to dose. Furthermore both measures are not proportional to each other. As already observed by others we confirm that at high doses the reduction of the γH2AX level with time does not follow the DNA-repair kinetics any more. Instead we demonstrated an adjustment of γH2AX fluorescence levels and foci numbers with time after exposure. High dose regions decrease, low dose regions increase their H2AX phosphorylation. We attributed these adjustment to bystander responses and provided evidence for both, cell-to-cell communications via gap junctions and soluble factors. It was shown that our results are in agreement with the idea of a dispersive propagating signal molecule transferring the bystander information. We were also able to show that close neighbours react alike as opposed to arbitrary cells receiving the same dose.

In an MRT field we were able to reveal that the distribution of the cell cycle is changed at and close to the microbeams. This presumably promotes cell proliferation replacing damaged cells. Accompanied with these changes in the cell cycle is the appearance of a group of less damaged cells in the peak region between 1 and 6 hours after exposure. Furthermore large γH2AX foci go along with these changes at the edges of the microbeams. Hitherto associated with more complex DNA double strand breaks this observation raises the question whether these larger foci are rather involved in a faster repair process. They appear at the edges of the microbeams close to low dose regions. To risk an adventurous hypothesis one could suggest a support in the DNA repair from less damaged adjacent cells. Unlike most reports on bystander effects we do not only observe negative effects, i.e. damaging of unirradiated cells, but particularly bystander positive effects, in the sense of a reduction of H2AX phosphorylation levels. Although we must admit that our observations question the conventional interpretation of the γH2AX signal after radiation exposure.

build-up and decay, cells with a lower stationary signal will experience different durations with a signal over the threshold value. Therefore the static signal concentration is in our case a suitable measure of bystander probability.

Chapter 6

Conclusions

MRT is a multidisciplinary research field and involves a complex interplay between physical and biological factors. The main focus of this work was pointed at the prediction of dose in an MRT treatment, its dosimetric validation and the biological effect of an MRT dose distribution on a cellular level.

Treatment planning is an essential component of radiotherapy. In MRT it is assumed that the peak dose determines the tumour control and the valley dose the normal tissue sparing. An accurate prediction of dose prior to an MRT treatment is indispensable when moving on to a clinical application. One of the main outcomes of this work was therefore an MRT treatment planning system (TPS) based on the interface VIRTUOS, a planning software which is currently used at the German Cancer Research Centre (DKFZ) for conventional therapy planning. The dose calculation is based on the definition of treatment parameters in VIRTUOS, a CT image of the patient acquired prior to the treatment and a model of the radiation source in the form of phase space information. To the latter a separate chapter, chapter 2, was dedicated.

The source phase space is distinctly different to that of other radiation sources. In particular the photon beams are polarised and highly parallel. In chapter 2 we investigated the effect of polarisation and developed a simple source model.

The polarisation sensitive Compton effect preferentially scatters photons perpendicular to the polarisation direction and leads to an unisotropic energy absorption. It was found that the polarisation has a strong influence on the scattered dose outside the radiation field, but little effect on the dose inside the radiation field. Within the microbeam field the linear polarisation perpendicular to the microbeams reduces the valley dose by less than 3%. The effect on the peak dose is even less and does not exceed 0.1%. Therefore the assumption of unpolarised beams leads to reasonable dose estimates. Nonetheless polarised photon interactions were regarded for all Monte Carlo simulations throughout this thesis.

From the simulation of the entire phase space by Martínez-Rovira et al.[13] we extracted a couple of essential parameters to create an accurate, but simple source model. The model is tailored for the ID17 biomedical beam line at the ESRF in Grenoble, but may be adapted to beamlines at other synchrotrons as well. The most important feature of the model is that the beams can be assumed as parallel when the change in the beam width and ctc (centre to centre distance) from the MSC to the sample caused by the tiny beam divergence is regarded. Collimator scattering can be neglected, but there is a considerable amount of leakage radiation which increases the dose by around 10%. The photon flux varies slightly from beam to beam due to the broad synchrotron beam profile and geometric absorption at the collimator edges. Some effects are not regarded by Monte Carlo simulations, such as total external reflection, diffraction and rough collimator surfaces. In chapter 2.4 we showed that total external reflection at the MSC walls affects more than 4% of the photons entering a 50 μm wide slit at the edge of a 20×20 mm^2 MRT field. Reflections from the collimator walls were also experimentally observed

while measuring output factors.

Apart from the source model the material composition of the phantom (or patient) serves as an input for the dose prediction in MRT. The conversion of Hounsfield units (HU) to material parameters is presented in chapter 3.4 and based on the method of Schneider et al. [45]. Unfortunately the transformation is not unique and two different materials can have the same HU representation in a CT. The resulting uncertainties were estimated to be between 0.5 and 5% for the attenuation coefficient μ and around 2% for the dose absorption in the tissue.

Three different dose calculation methods, forward Monte Carlo, convolution (CPKA) and superposition point kernel algorithm (SPKA), were presented in chapter 3 which are linked to VIRTUOS. The forward Monte Carlo dose calculation method in chapter 3.2.2 can be assumed as most accurate. However, it requires a considerable amount of computation time. Without parallelisation the calculation time is in the order of weeks. Therefore two kernel based dose calculation methods were developed and integrated into the TPS. In these methods analytically calculated photon and electron dose kernels are used to estimate the scatter dose around primary interaction points on the microbeam paths.

The fastest and most simple point kernel approach is the convolution based algorithm (CPKA) which calculates the dose by convolving the scatter kernels with the primary interaction density ("interaction strength") on the beam. The dose calculation took in calculations on a standard PC 5 to 10 minutes. The disadvantage of the method is that homogeneous material is assumed around the interaction point. At material interfaces considerable deviations between CPKA and Monte Carlo simulations arise.

This disadvantage is compensated by a superposition point kernel algorithm in curved space (SPKA). Material inhomogeneities are regarded by deforming the point kernel in a projection into curved space. The metric is derived from the absorption coefficient around the primary interaction point. The differences between Monte Carlo and SPKA are considerably reduced close to the material interfaces. The price for this modification is a two to three times longer calculation time than for the CPKA depending on the irradiation geometry.

Overall the CPKA, forward Monte Carlo and SPKA agree within 15% accuracy with the exception of regions close to material boundaries in CPKA dose calculations. The first veterinarian patient was already planned with the new TPS.

For lateral homogeneous detector geometries we presented another very efficient dose calculation method: semi-adjoint Monte Carlo. The accuracy is comparable to that of forward Monte Carlo, but much less particle histories are required for the same statistical noise level.

In chapter 4 we presented an MRT dosimetry procedure with radiochromic films associated with a readout at an optical microscope. Unlike film scanners this method has a sufficiently high resolution and in contrast to readouts with a microdensitometer the method has a better reproducibility, provides two dimensional dose maps and is still higher resolving. Moreover the microscope scanning time is much shorter than with the microdensitometer. However, care must be taken with inhomogeneous illuminations.

An uncertainty analysis was carried out and two film types, Gafchromic® HD-V2 and HD-810 films, were compared to each other. It turned out that the total uncertainty results from a combination of film inhomogeneities, statistical noise and calibration errors. The total uncertainty decreases with dose. At low doses the calibration uncertainty dominates, while at high doses inhomogeneities are most important. The statistical noise contribution was small for the resolution of 5×1000 μm^2 required for the planar microbeams in this work. However, for higher resolutions these uncertainties become significant. The physical limitation for the resolution is the grain size which is 2 μm in both film types.

Gafchromic® HD-V2 and HD-810 films are in principle very similar in their performance. However, HD-V2 films exhibit a higher statistical noise rendering them less suitable if higher dose resolutions are required than the 5×1000 μm^2 examined here. HD-810 films are on the

other hand sensitive to the photon energy. The film sensitivity at 50 keV photon energy is approximately half of the sensitivity at 100 keV.

The dosimetry method was applied to measure the dose in a homogeneous water phantom, an anthropomorphic human head phantom and for the determination of output factors. The measurements were compared to the TPS predictions and semi-adjoint Monte Carlo simulations. In the case of the anthropomorphic human head phantom the complete treatment planning process was carried out from the acquisition of the CT image, over the calibration with ionisation chambers, alignment with projection images and exposure. Planning and measurement agreed within 10% measurement uncertainties in the valley region and except for two outliers within 4% uncertainty in the peak region.

We finally tried to connect the dose to a biological damage inflicted on cells in cell culture in chapter 5. To this end human pancreatic cancer cells Panc1 were cultivated and exposed at an x-ray tube and at the ID17 beamline of the ESRF in Grenoble. Cells were irradiated with a homogeneous, a gradient and a step dose pattern at the x-ray tube with doses of up to 48 Gy. At the synchrotron the cells were irradiated with microbeam fields with peak doses between 16 and 80 Gy and valley doses between 0.7 and 3.6 Gy.

For analysis cells were fixed between 1 and 24 hours after radiation. They were stained for the phosphorylated histone γH2AX and with the DNA stain Hoechst 33342. Under γH2AX staining various cell morphologies were observed. Cell nuclei with smaller or larger foci and different levels of background staining could be distinguished. Large screening with fluorescence microscopy in combination with automated foci counting and nuclei contouring allowed a spatially resolved cell signal analysis with a large number of cells. The technique is comparable to flow cytometry but provides also spatial information.

From these cell irradiations we found a non-linearity between fluorescence intensity, foci number and dose. A binary cell response was measured for the number of formed foci – either cell nuclei contained a high number of foci or no foci at all. This observation contradicts the theory that there is a one to one correlation between double strand breaks and foci formation.

Apart from the dose the cell response crucially depends on the dose given to neighbouring cells. A levelling off with time was observed in all conducted experiments with spatially varying dose. In the gradient and step exposure the number of foci and the γH2AX signal intensity increased in low and decreased in high dose regions from 3 to 24 hours after exposure. In microbeam exposures the dose in the valley that lead to an equal level of γH2AX signal was peak dose dependent. If the peak dose is increased, the same number of foci is reached at a higher valley dose.

The experimental results support the idea of a small diffusing molecule that conveys a bystander signal. In the step exposure at the interface between unirradiated and irradiated cells we found that the fraction of non-responding cells in the unirradiated part depended on the distance to the radiation boundary and that this fraction decreased with time. The signal decay observed would match that of a diffusive signal. However, the data did not suffice for a detailed quantitative analysis.

Comparing the γH2AX signal differences between adjacent cells and arbitrarily selected cells receiving the same dose in the valley region of a microbeam field revealed that close neighbours tend to react alike. A quantitative analysis showed that over 40% of the cells were influenced by close neighbours. This observation would support a gap junction mediated bystander signalling. In future experiments one could test this dependence by inhibiting gap junctions, for example with lindane.

There were remarkable findings in cells exposed to MRT fields. Within the microbeam paths there are cells with a low (entity 1) and with a high (entity 2) level of γH2AX. The formation of these two cell entities was observed to be time and dose dependent. Only the response of entity 2 cells depended on the dose. Potentially associated to these two responses is the formation of

large foci at the beam penumbras observed shortly after radiation exposure. The foci size in the penumbras exceeded that of the anyway increased foci size in the peak region by 15 to 20% 1 hour after exposure but went back to an unobtrusive level 6 hours after exposure.

Apart from γH2AX we also analysed the Hoechst 33342 staining signal which allowed conclusions to be drawn about the cell cycle distribution. In homogeneous irradiations we observed the well known fact that radiation influences the cell cycle distribution. The fraction of G1 cells is reduced and that of G2 cells increased. Furthermore some multiploid cells appeared. Panc1 cells are p53 mutants and do not arrest in G1. In a microbeam field we observed that the change in the cell cycle distribution did mainly affect the valley regions. From 1 hour to 6 hours after exposure an 28% increase in the G2 fraction of valley region cells was measured, but in peak region cells the increase was just between 5 and 15%.

Dose is obviously not the only determining factor in MRT. Our results suggest that intercellular signalling is a crucial factor in tissue survival and especially dose interfaces could be extremely important for the cell survival. While most research in the field of bystander signalling supported a negative bystander effect, i.e. a signalling that causes damage, we conclude from our observations that it is not easy to predict whether bystander effects are protective or detrimental. Most likely the bystander response is a protective mechanism that is activated in response to hazard, against which it did actually not evolve. Probably it is one explanation for the tissue sparing effect of MRT. Further basic research may unravel the importance of intercellular signalling in MRT. Moreover there is a chance to effectively use the knowledge on bystander effects in cancer therapy and medicine.

This way MRT presents a fascinating research field which may contribute to radiotherapy in general by unveiling the influence of cell signalling and refining the still simple dose-damage relationships as they are in use in clinical practice today. MRT as a treatment modality itself is promising. However, its use is limited by the dependence on large synchrotrons. The clinical use in a research facility is difficult, expansive and can therefore only be provided to a very small number of patients. Hence an important focus in MRT research should be on the development of compact and powerful x-ray sources.

Inverse Compton compact light sources[164] present one alternative to synchrotrons, where x-rays are created by inverse Compton scattering of photons in a laser field at electrons that have a few tens of MeV kinetic energy and are produced in small storage rings. An example is the Munich compact light source (MuCLS)[165]. However, the photon energy is lower than at a third generation synchrotron such as the ESRF and also the photon flux is 3 to 4 orders of magnitude smaller. But this may change in the future.

Another approach is the carbon nanotube field emission x-ray technology. Schreiber and Chang[166] performed a Monte Carlo study for MRT and came to the conclusion that a maximum dose rate of 700 Gy/min would be reachable in the centre of a 3 cm diameter target and suggest the use for small animal MRT experiments. However, the maximal acceleration voltage of the tube is 160 kV, leading to a mean photon energy of 40 to 50 keV. Therefore both, dose rate and photon energy are lower than desirable for MRT.

Bibliography

[1] Robert Koch-Institut and Gesellschaft der epidemiologischen Krebsregister in Deutschland e.V. Berlin. Krebs in Deutschland 2009/2010, 2013. URL `http://www.krebsdaten.de/Krebs/DE/Home/homepage_node.html`.

[2] G. G. Steel. *Basic clinical radiobiology*. Arnold, London, 3rd edition, 2002.

[3] B. Alberts, A. Johnson, P. Walter, J. Lewis, M. Raff, and K. Roberts. *Molecular Biology of the Cell*. Taylor & Francis Ltd., New York, 5th revised edition, November 2007. ISBN 9780815341055.

[4] A. Köhler. Röntgentiefentherapie mit Metallnetzschutz: Praktische Erfolge. *Strahlentherapie*, 1:121–131, 1912.

[5] J. A. Laissue, H. Blattmann, and D. N. Slatkin. Alban Köhler (1874-1947): Erfinder der Gittertherapie. *Zeitschrift für Medizinische Physik*, 22(2):90–99, June 2012. ISSN 0939-3889. doi: 10.1016/j.zemedi.2011.07.002.

[6] W. Zeman, H. J. Curtis, E. L. Gebhard, and W. Haymaker. Tolerance of mouse-brain tissue to high-energy deuterons. *Science*, 130(3391):1760–1761, December 1959. ISSN 0036-8075, 1095-9203. doi: 10.1126/science.130.3391.1760-a.

[7] J. M. Ordy, H. W. Barnes, T. Samorajski, H. J. Curtis, L. Wolin, and W. Zeman. Pathologic and behavioral changes in mice after deuteron irradiation of the central nervous system. *Radiation Research*, 18(1):31–45, January 1963. ISSN 0033-7587. doi: 10.2307/3571423.

[8] H. J. Curtis. The use of a deuteron microbeam for simulating the biological effects of heavy cosmic-ray particles. *Radiation Research Supplement*, 7:250, 1967. ISSN 04858611. doi: 10.2307/3583718.

[9] H. Rodney Withers, J. M. G. Taylor, and B. Maciejewski. Treatment volume and tissue tolerance. *International Journal of Radiation Oncology*Biology*Physics*, 14(4):751–759, April 1988. ISSN 0360-3016. doi: 10.1016/0360-3016(88)90098-3.

[10] R. Serduc, E. Bräuer-Krisch, E. A. Siegbahn, A. Bouchet, B. Pouyatos, R. Carron, N. Pannetier, L. Renaud, G. Berruyer, C. Nemoz, T. Brochard, C. Rémy, E. L. Barbier, A. Bravin, G. Le Duc, A. Depaulis, F. Estève, and J. A. Laissue. High-precision radiosurgical dose delivery by interlaced microbeam arrays of high-flux low-energy synchrotron x-rays. *PLoS ONE*, 5(2):e9028, February 2010. doi: 10.1371/journal.pone.0009028.

[11] E. Bräuer-Krisch, H. Requardt, T. Brochard, G. Berruyer, M. Renier, J. A. Laissue, and A. Bravin. New technology enables high precision multislit collimators for microbeam radiation therapy. *Review of Scientific Instruments*, 80(7):074301, July 2009. ISSN 0034-6748, 1089-7623. doi: 10.1063/1.3170035.

[12] A. Bouchet, B. Lemasson, G. Le Duc, C. Maisin, E. Bräuer-Krisch, E. A. Siegbahn, L. Renaud, E. Khalil, C. Rémy, C. Poillot, A. Bravin, J. A. Laissue, E. L. Barbier, and R. Serduc. Preferential effect of synchrotron microbeam radiation therapy on intracerebral 9L gliosarcoma vascular networks. *International Journal of Radiation Oncology*Biology*Physics*, 78 (5):1503–1512, 2010. ISSN 0360-3016. doi: 10.1016/j.ijrobp.2010.06.021.

[13] I. Martínez-Rovira, J. Sempau, and Y. Prezado. Development and commissioning of a monte carlo photon beam model for the forthcoming clinical trials in microbeam radiation therapy. *Medical Physics*, 39(1):119–131, January 2012. ISSN 0094-2405. doi: 10.1118/1.3665768.

[14] D. N. Slatkin, P. Spanne, F. A. Dilmanian, and M. Sandborg. Microbeam radiation therapy. *Medical Physics*, 19(6):1395–1400, November 1992. ISSN 0094-2405. doi: 10.1118/1.596771.

[15] E. A. Siegbahn, J. Stepanek, E. Bräuer-Krisch, and A. Bravin. Determination of dosimetrical quantities used in microbeam radiation therapy (MRT) with monte carlo simulations. *Medical Physics*, 33(9):3248–3259, September 2006. ISSN 0094-2405. doi: 10.1118/1.2229422.

[16] H. Requardt, A. Bravin, Y. Prezado, E. Bräuer-Krisch, M. Renier, T. Brochard, P. Berkvens, F. Estève, H. Elleaume, J.-F. Adam, H. Blattmann, J. A. Laissue, B. Kaser-Hotz, C. Nemoz, and G. Berruyer. The clinical trials program at the ESRF biomedical beamline ID17: status and remaining steps. In *AIP Conference Proceedings*, volume 1234, pages 161–164. AIP Publishing, June 2010. doi: 10.1063/1.3463164.

[17] Y. Prezado, M. Vautrin, I. Martínez-Rovira, A. Bravin, F. Estève, H. Elleaume, P. Berkvens, and J. F. Adam. Dosimetry protocol for the forthcoming clinical trials in synchrotron stereotactic radiation therapy (SSRT). *Medical Physics*, 38(3):1709–1717, March 2011. ISSN 0094-2405. doi: 10.1118/1.3556561.

[18] M. Miura, H. Blattmann, E. Bräuer-Krisch, A. Bravin, A. L. Hanson, M. M. Nawrocky, P. L. Micca, D. N. Slatkin, and J. A. Laissue. Radiosurgical palliation of aggressive murine SCCVII squamous cell carcinomas using synchrotron-generated x-ray microbeams. *The British Journal of Radiology*, 79(937):71–75, January 2006. ISSN 0007-1285. doi: 10.1259/bjr/50464795.

[19] C. P. Baker, H. J. Curtis, W. Zeman, and R. G. Woodley. The design and calibration of a deuteron microbeam for biological studies. *Radiat. Res.*, 15:489–495, 1961.

[20] H. J. Curtis. Limitations on space flight due to cosmic radiations. *Science*, 133:312–316, 1961.

[21] H. J. Curtis. The microbeam as a tool in radiobiology. *Advances in Biological and Medical Physics*, 175:207–224, 1963.

[22] J. A. Laissue, H. Blattmann, M. Di Michiel, D. N. Slatkin, N. Lyubimova, R. Guzman, W. Zimmermann, S. Birrer, T. Bley, P. Kircher, R. Stettler, R. Fatzer, A. Jaggy, H. Smilowitz, E. Brauer, A. Bravin, G. Le Duc, C. Nemoz, M. Renier, W. C. Thomlinson, J. Stepanek, and H.-P. Wagner. Weanling piglet cerebellum: a surrogate for tolerance to MRT (microbeam radiation therapy) in pediatric neuro-oncology. *Proc. SPIE*, 4508:65–73, 2001. doi: 10.1117/12.450774.

[23] R. Serduc, P. Vérant, J.-C. Vial, R. Farion, L. Rocas, C. Rémy, T. Fadlallah, E. Brauer, A. Bravin, J. Laissue, H. Blattmann, and B. van der Sanden. In vivo two-photon microscopy

study of short-term effects of microbeam irradiation on normal mouse brain microvasculature. *International Journal of Radiation Oncology*Biology*Physics*, 64(5):1519–1527, April 2006. ISSN 0360-3016. doi: 10.1016/j.ijrobp.2005.11.047.

[24] R. Serduc, Y. v. d. Looij, G. Francony, O. Verdonck, B. v. d. Sanden, J. Laissue, R. Farion, E. Bräuer-Krisch, E. A. Siegbahn, A. Bravin, Y. Prezado, C. Segebarth, C. Rémy, and H. Lahrech. Characterization and quantification of cerebral edema induced by synchrotron x-ray microbeam radiation therapy. *Physics in Medicine and Biology*, 53(5):1153, March 2008. ISSN 0031-9155. doi: 10.1088/0031-9155/53/5/001.

[25] D. N. Slatkin, P. Spanne, F. A. Dilmanian, J.-O. Gebbers, and J. A. Laissue. Subacute neuropathological effects of microplanar beams of x-rays from a synchrotron wiggler. *Proc. Natl. Acad. Sci. USA*, 92, 1995.

[26] G. J. M. J. van den Aardweg, J. W. Hopewell, E. M. Whitehouse, and W. Calvo. A new model of radiation-induced myelopathy: A comparison of the response of mature and immature pigs. *International Journal of Radiation Oncology*Biology*Physics*, 29(4): 763–770, July 1994. ISSN 0360-3016. doi: 10.1016/0360-3016(94)90564-9.

[27] E. Bräuer-Krisch, R. Serduc, E. A. Siegbahn, G. Le Duc, Y. Prezado, A. Bravin, H. Blattmann, and J. A. Laissue. Effects of pulsed, spatially fractionated, microscopic synchrotron x-ray beams on normal and tumoral brain tissue. *Mutation Research/Reviews in Mutation Research*, 704(1–3):160–166, April 2010. ISSN 1383-5742. doi: 10.1016/j.mrrev.2009.12.003.

[28] J. A. Laissue, G. Geiser, P. O. Spanne, F. A. Dilmanian, J.-O. Gebbers, M. Geiser, X.-Y. Wu, M. S. Makar, P. L. Micca, M. M. Nawrocky, D. D. Joel, and D. N. Slatkin. Neuropathology of ablation of rat gliosarcomas and contiguous brain tissues using a microplanar beam of synchrotron-wiggler-generated x rays. *International Journal of Cancer*, 78(5): 654–660, November 1998. ISSN 1097-0215. doi: 10.1002/(SICI)1097-0215(19981123)78:5<654::AID-IJC21>3.0.CO;2-L.

[29] P. Regnard, G. L. Duc, E. Bräuer-Krisch, I. Troprès, E. A. Siegbahn, A. Kusak, C. Clair, H. Bernard, D. Dallery, J. A. Laissue, and A. Bravin. Irradiation of intracerebral 9L gliosarcoma by a single array of microplanar x-ray beams from a synchrotron: balance between curing and sparing. *Physics in Medicine and Biology*, 53(4):861, February 2008. ISSN 0031-9155. doi: 10.1088/0031-9155/53/4/003.

[30] E. Schültke, B. H. J. Juurlink, K. Ataelmannan, J. Laissue, H. Blattmann, E. Bräuer-Krisch, A. Bravin, J. Minczewska, J. Crosbie, H. Taherian, E. Frangou, T. Wysokinsky, L. D. Chapman, R. Griebel, and D. Fourney. Memory and survival after microbeam radiation therapy. *European Journal of Radiology*, 68(3, Supplement):S142–S146, 2008. ISSN 0720-048X. doi: 10.1016/j.ejrad.2008.04.051.

[31] R. Serduc, A. Bouchet, E. Bräuer-Krisch, J. A. Laissue, J. Spiga, S. Sarun, A. Bravin, C. Fonta, L. Renaud, J. Boutonnat, E. A. Siegbahn, F. Estève, and G. L. Duc. Synchrotron microbeam radiation therapy for rat brain tumor palliation—influence of the microbeam width at constant valley dose. *Physics in Medicine and Biology*, 54(21):6711, November 2009. ISSN 0031-9155. doi: 10.1088/0031-9155/54/21/017.

[32] S. Sabatasso, J. A. Laissue, R. Hlushchuk, W. Graber, A. Bravin, E. Bräuer-Krisch, S. Corde, H. Blattmann, G. Gruber, and V. Djonov. Microbeam radiation-induced tissue damage depends on the stage of vascular maturation. *International Journal of Ra-*

*diation Oncology*Biology*Physics*, 80(5):1522–1532, August 2011. ISSN 0360-3016. doi: 10.1016/j.ijrobp.2011.03.018.

[33] H. Blattmann, J. O. Gebbers, E. Bräuer-Krisch, A. Bravin, G. Le Duc, W. Burkard, M. Di Michiel, V. Djonov, D. N. Slatkin, J. Stepanek, and J. A. Laissue. Applications of synchrotron x-rays to radiotherapy. *Nuclear Instruments and Methods in Physics Research Section A: Accelerators, Spectrometers, Detectors and Associated Equipment*, 548(1–2): 17–22, August 2005. ISSN 0168-9002. doi: 10.1016/j.nima.2005.03.060.

[34] M. Fuss, F. Wenz, R. Scholdei, M. Essig, J. Debus, M. V. Knopp, and M. Wannenmacher. Radiation-induced regional cerebral blood volume (rCBV) changes in normal brain and low-grade astrocytomas: quantification and time and dose-dependent occurrence. *International Journal of Radiation Oncology*Biology*Physics*, 48(1):53–58, August 2000. ISSN 0360-3016. doi: 10.1016/S0360-3016(00)00590-3.

[35] B. van der Sanden, E. Bräuer-Krisch, E. A. Siegbahn, C. Ricard, J.-C. Vial, and J. Laissue. Tolerance of arteries to microplanar x-ray beams. *International Journal of Radiation Oncology*Biology*Physics*, 77(5):1545–1552, August 2010. ISSN 0360-3016. doi: 10.1016/j.ijrobp.2010.02.019.

[36] M. A. Reidy and S. M. Schwartz. Endothelial regeneration. III. time course of intimal changes after small defined injury to rat aortic endothelium. *Laboratory investigation; a journal of technical methods and pathology*, 44(4):301–308, 1981.

[37] A. Merrem. Modeling of damage to the vasculature of the cerebral cortex after microbeam radiation therapy. Master thesis, Department of Physics and Astronomy, Ruprecht-Karls-University, Heidelberg, Germany, 2013.

[38] L. Risser, F. Plouraboué, A. Steyer, P. Cloetens, G. Le Duc, and C. Fonta. From homogeneous to fractal normal and tumorous microvascular networks in the brain. *Journal of Cerebral Blood Flow & Metabolism*, 27(2):293–303, 2007.

[39] J. Folkmann. Seminars in medicine of the Beth Israel Hospital, Boston. Clinical applications of research on angiogenesis. *N. Engl. J. Med.*, 333:1757–1763, 1995.

[40] G. D. Yancopoulos, S. David, N. W. Gale, J. S. Rodge, S. J. Wiegand, and J. Holash. Vasculature specific growth factors and blood vessel formation. *Nature*, 407:242–248, 2000.

[41] K. M. Prise, M. Folkard, and B. D. Michael. Radiation-induced bystander and adaptive responses in cell and tissue models. *Dose-response*, 4(4):263–276, 2006.

[42] C. Mothersill, C. Bucking, R. W. Smith, N. Agnihotri, A. O'Neill, M. Kilemade, and C. B. Seymour. Communication of radiation-induced stress or bystander signals between fish in vivo. *Environmental Science & Technology*, 40(21):6859–6864, November 2006. ISSN 0013-936X. doi: 10.1021/es061099y.

[43] R. W. Smith, J. Wang, E. Schültke, C. B. Seymour, E. Bräuer-Krisch, J. A. Laissue, H. Blattmann, and C. E. Mothersill. Proteomic changes in the rat brain induced by homogenous irradiation and by the bystander effect resulting from high energy synchrotron x-ray microbeams. *International Journal of Radiation Biology*, 89(2):118–127, September 2012. ISSN 0955-3002. doi: 10.3109/09553002.2013.732252.

[44] R. Bendl, A. Hoess, M. Keller, J. Pross, and W. Schlegel. VIRTUOS - a program for VIRTUal radiOtherapy simulation and verification. In *Proceedings of the Eleventh International*

Conference on the Use of Computers in Radiation Therapy, pages 226–227, Manchester, 1994.

[45] W. Schneider, T. Bortfeld, and W. Schlegel. Correlation between ct numbers and tissue parameters needed for monte carlo simulations of clinical dose distributions. *Phys. Med. Biol.*, 45 (2000):259–278, 1998.

[46] S. Bartzsch, M. Lerch, M. Petasecca, E. Bräuer-Krisch, and U. Oelfke. Influence of polarization and a source model for dose calculation in MRT. *Medical Physics*, 41(4):041703, March 2014. ISSN 0094-2405. doi: 10.1118/1.4867858.

[47] J. Stepanek, H. Blattmann, J. A. Laissue, N. Lyubimova, M. D. Michiel, and D. N. Slatkin. Physics study of microbeam radiation therapy with PSI-version of monte carlo code GEANT as a new computational tool. *Medical Physics*, 27(7):1664–1675, July 2000. ISSN 0094-2405. doi: 10.1118/1.599034.

[48] M. De Felici, R. Felici, C. Ferrero, A. Bravin, A. Tartari, and M. Gambaccini. Monte carlo assessment of peak-to-valley dose ratio for MRT. *Nuclear Instruments and Methods in Physics Research Section A: Accelerators, Spectrometers, Detectors and Associated Equipment*, 580(1):489–492, 2007.

[49] I. Orion, A. B. Rosenfeld, F. A. Dilmanian, F. Telang, B. Ren, and Y. Namito. Monte carlo simulation of dose distributions from a synchrotron-produced microplanar beam array using the EGS4 code system. *Phys. Med. Biol.*, 45:2497–2508, 2000.

[50] M. De Felici, E. A. Siegbahn, J. Spiga, A. L. Hanson, R. Felici, C. Ferrero, A. Tartari, M. Gambaccini, J. Keyriläinen, and E. Bräuer-Krisch. Monte carlo code comparison of dose delivery prediction for microbeam radiation therapy. In *Journal of Physics: Conference Series*, volume 102, page 012005, 2008.

[51] H. Nettelbeck, G. J. Takacs, M. L. F. Lerch, and A. B. Rosenfeld. Microbeam radiation therapy: A monte carlo study of the influence of the source, multislit collimator, and beam divergence on microbeams. *Med. Phys.*, 36 (2), 2009.

[52] B. H. Nelson, A. F. Bielajew, H. Hirayama, W. R. Nelson, D. W. O. Rogers, K. R, and W. C. Fields. *History, overview and recent improvements of EGS4*. SLAC-PUB-6499 (NRC-PIRS-0436, KEK Internal 94-4), Revised June 1, 1994.

[53] M. De Felici, R. Felici, M. S. del Rio, C. Ferrero, T. Bacarian, and F. Dilmanian. Dose distribution from x-ray microbeam arrays applied to radiation therapy: An egs4 monte carlo study. *Med. Phys.*, 32 (8):2455–2459, 2005.

[54] R. P. Hugtenburg, A. S. Adegunloye, and D. A. Bradley. X-ray microbeam radiation therapy calculations, including polarisation effects, with the monte carlo code EGS5. *Nuclear Instruments and Methods in Physics Research Section A: Accelerators, Spectrometers, Detectors and Associated Equipment*, 619(1–3):221–224, July 2010. ISSN 0168-9002. doi: 10.1016/j.nima.2010.01.018.

[55] Geant4 collaboration, homepage. Physics reference manual, June 2014. URL `geant4.cern.ch/support/userdocuments.shtml`.

[56] F. Salvat, J. M. Fernández-Varea, and J. Sempau. PENELOPE-2006: a code system for monte carlo simulation of electron and photon transport. In *Workshop Proceedings*, volume 4, page 7, 2006.

[57] O. Klein and Y. Nishina. Über die Streuung von Strahlung durch freie Elektronen nach der neuen relativistischen Quantendynamik von Dirac. *Zeitschrift für Physik*, 52(11-12), 1929.

[58] W. Heitler. *The Quantum Theory of Radiation*. Courier Dover Publications, 1954. ISBN 9780486645582.

[59] B. Lai and F. Cerrina. SHADOW: a synchrotron radiation ray tracing program. *Nuclear Instruments and Methods in Physics Research Section A: Accelerators, Spectrometers, Detectors and Associated Equipment*, 246(1):337–341, 1986.

[60] J. Baro, J. Sempau, J. M. Fernández-Varea, and F. Salvat. PENELOPE: an algorithm for monte carlo simulation of the penetration and energy loss of electrons and positrons in matter. *Nuclear Instruments and Methods in Physics Research Section B: Beam Interactions with Materials and Atoms*, 100(1):31–46, 1995.

[61] P. Andreo, D. T. Burns, K. Hohlfeld, M. S. Huq, T. Kanai, F. Laitano, V. G. Smythe, and S. Vynckier. Absorbed dose determination in external beam radiotherapy. Technical Reports Series No. 398, International Atomic Energy Agency, Vienna, Austria, 2000.

[62] E. Bräuer-Krisch. Experimental dosimetry for microbeam radiation therapy. PhD thesis, University College London, London, United Kingdom, April 2012.

[63] J. Spiga, E. A. Siegbahn, E. B. Krisch, P. Randaccio, and A. Bravin. The GEANT4 toolkit for microdosimetry calculations: Application to microbeam radiation therapy (MRT). *Med. Phys.*, 34:4322–4330, 2007.

[64] M. Berger, J. Hubbel, S. Steltzer, J. Chang, J. Coursey, R. Sukumar, and D. Zucker. Xcom: photon cross section database. National Institute of Standards and Technology, Gaithersburg, MD, November 2010. (version 3.1) [online available: http://www.nist.gov/pml/data/xcom/index.cfm, March 2011].

[65] S. Kuznetsov. X-ray optics calculator, June 2014. URL `http://www.ipmt-hpm.ac.ru/xcalc/xcalc/intro.php`.

[66] I. Lux and L. Koblinger. *Monte Carlo PARTICLE Transport Methods: Neutron and Photon Calculations*. CRC Press, Boca Raton, USA, 2000.

[67] D. J. H. Ahrens and D. U. Dieter. Computer methods for sampling from gamma, beta, poisson and bionomial distributions. *Computing*, 12(3):223–246, September 1974. ISSN 0010-485X, 1436-5057. doi: 10.1007/BF02293108.

[68] G. I. Marchuk. Сопряженные уравнения и их применения. *Труды Института Математики и Механики*, 12(1), 2006.

[69] D. C. Irving. The adjoint Boltzmann equation and its simulation by monte carlo. *Nuclear Engineering and Design*, 15:273–292, 1971.

[70] L. K. Iván Lux. *Monte Carlo PARTICLE Transport Methods: Neutron and Photon Calculations*. CRC Press, 2000.

[71] E. Schültke, M. Trippel, E. Bräuer-Krisch, M. Renier, S. Bartzsch, H. Requardt, M. D. Döbrössy, and G. Nikkhah. Pencilbeam irradiation technique for whole brain radiotherapy: Technical and biological challenges in a small animal model. *PLoS ONE*, 8(1):e54960, January 2013. doi: 10.1371/journal.pone.0054960.

[72] J. A. Laissue, S. Bartzsch, H. Blattmann, E. Bräuer-Krisch, A. Bravin, D. Dalléry, V. Djonov, A. L. Hanson, J. W. Hopewell, B. Kaser-Hotz, J. Keyriläinen, P. P. Laissue, M. Miura, R. Serduc, A. E. Siegbahn, and D. N. Slatkin. Response of the rat spinal cord to x-ray microbeams. *Radiotherapy and Oncology*, 106(1):106–111, January 2013. ISSN 0167-8140. doi: 10.1016/j.radonc.2012.12.007.

[73] J. E. O'Connor. The variation of scattered x-rays with density in an irradiated body. *Phys. Med. Biol.*, 1:352, 1957.

[74] J. S. Pruitt and R. Loevinger. The photon-fluence scaling theorem for compton-scattered radiation. *Medical Physics*, 9(2):176–179, March 1982. ISSN 0094-2405. doi: 10.1118/1.595080.

[75] S. Bartzsch. Dose calculation for synchrotron microbeams. Diploma thesis, Friedrich Schiller-Universität, Jena, Germany, March 2011.

[76] S. Bartzsch and U. Oelfke. A new concept of pencil beam dose calculation for 40–200 keV photons using analytical dose kernels. *Medical Physics*, 40(11):111714, October 2013. ISSN 0094-2405. doi: 10.1118/1.4824150.

[77] H. Bethe. Zur Theorie des Durchgangs schneller Korpuskularstrahlen durch Materie. *Ann. Physik*, 397(3):325–400, 1930.

[78] A. Ahnesjö, P. Andreo, and A. Brahme. Calculation and application of point spread functions for treatment planning with high energy photon beams. *Acta Oncologica*, 26 Fasc. 1:49–56, 1987.

[79] C. Debus. Development of a treatment planning system for microbeam radiation therapy. Master thesis, Department of Physics and Astronomy, Ruprecht-Karls-University, Heidelberg, Germany, 2012.

[80] J. Kieselmann. A differential geometric approach to heterogeneities in dose calculations applied to microbeam radiation therapy. Master thesis, Department of Physics and Astronomy, Ruprecht-Karls-University, Heidelberg, Germany, July 2014.

[81] CIRS Tissue Simulation & Phantom Technology. Electron density reference phantom, user guide & technical information, March 2008. URL `http://www.cirsinc.com`.

[82] A. Badal and A. Badano. Accelerating monte carlo simulations of photon transport in a voxelized geometry using a massively parallel graphics processing unit. *Med. Phys.*, 36: 4878–4880, 2009.

[83] X. Jia, X. Gu, J. Sempau, D. Choi, A. Majumdar, and S. B. Jiang. Development of a gpu-based monte carlo dose calculation code for coupled electron–photon transport. *Physics in Medicine and Biology*, 55:3077–3086, 2010.

[84] X. Jia, H. Yan, X. Gu, and S. B. Jiang. Fast monte carlo simulation for patient-specific CT/CBCT imaging dose calculation. *Physics in Medicine and Biology*, 57:577–590, 2012.

[85] E. Bräuer-Krisch, A. Rosenfeld, M. Lerch, M. Petasecca, M. Akselrod, J. Sykora, J. Bartz, M. Ptaszkiewicz, P. Olko, A. Berg, M. Wieland, S. Doran, T. Brochard, A. Kamlowski, G. Cellere, A. Paccagnella, E. A. Siegbahn, Y. Prezado, I. Martinez-Rovira, A. Bravin, L. Dusseau, and P. Berkvens. Potential high resolution dosimeters for MRT. *AIP Conference Proceedings*, 1266(1):89–97, July 2010. ISSN 0094243X. doi: doi:10.1063/1.3478205.

[86] M. Petasecca, A. Cullen, I. Fuduli, A. Espinoza, C. Porumb, C. Stanton, A. H. Aldosari, E. Bräuer-Krisch, H. Requardt, A. Bravin, V. Perevertaylo, A. B. Rosenfeld, and M. L. F. Lerch. X-tream: a novel dosimetry system for synchrotron microbeam radiation therapy. *Journal of Instrumentation*, 7(07):P07022, July 2012. ISSN 1748-0221. doi: 10.1088/1748-0221/7/07/P07022.

[87] M. Lerch, M. Petasecca, A. Cullen, A. Hamad, H. Requardt, E. Bräuer-Krisch, A. Bravin, V. Perevertaylo, and A. Rosenfeld. Dosimetry of intensive synchrotron microbeams. *Radiation Measurements*, 46(12):1560–1565, 2011. ISSN 1350-4487. doi: 10.1016/j.radmeas.2011.08.009.

[88] S. J. Doran, T. Brochard, J. Adamovics, N. Krstajic, and E. Bräuer-Krisch. An investigation of the potential of optical computed tomography for imaging of synchrotron-generated x-rays at high spatial resolution. *Physics in Medicine and Biology*, 55(5):1531, March 2010. ISSN 0031-9155. doi: 10.1088/0031-9155/55/5/018.

[89] S. J. Doran, A. T. A. Rahman, E. Bräuer-Krisch, T. Brochard, J. Adamovics, A. Nisbet, and D. Bradley. Establishing the suitability of quantitative optical CT microscopy of PRESAGE® radiochromic dosimeters for the verification of synchrotron microbeam therapy. *Physics in Medicine and Biology*, 58(18):6279, September 2013. ISSN 0031-9155. doi: 10.1088/0031-9155/58/18/6279.

[90] MEDI-TEST S.A.S. Gafchromic® MD-55 radiochromic dosimetry film for high energy photons configuration, specifications and performance data, August 2014. URL `http://www.meditest.fr/pdf/MD-55.pdf`.

[91] M. J. Butson, P. K. Yu, T. Cheung, and P. Metcalfe. Radiochromic film for medical radiation dosimetry. *Materials Science and Engineering: R: Reports*, 41(3–5):61–120, September 2003. ISSN 0927-796X. doi: 10.1016/S0927-796X(03)00034-2.

[92] Ashland Inc. Product information sheet: Gafchromic® dosimetry media, type HD-V2, January 2014. URL `http://www.ashland.com/products/gafchromic-radiotherapy-films`.

[93] J. F. Dempsey, D. A. Low, S. Mutic, J. Markman, A. S. Kirov, G. H. Nussbaum, and J. F. Williamson. Validation of a precision radiochromic film dosimetry system for quantitative two-dimensional imaging of acute exposure dose distributions. *Medical Physics*, 27(10):2462–2475, 2000. doi: 10.1118/1.1290488.

[94] A. Niroomand-Rad, C. R. Blackwell, B. M. Coursey, K. P. Gall, J. M. Galvin, W. L. McLaughlin, A. S. Meigooni, R. Nath, J. E. Rodgers, and C. G. Soares. Radiochromic film dosimetry: Recommendations of AAPM radiation therapy committee task group 55. *Medical Physics*, 25(11):2093–2115, 1998. doi: 10.1118/1.598407.

[95] J. C. Crosbie, I. Svalbe, S. M. Midgley, N. Yagi, P. a. W. Rogers, and R. A. Lewis. A method of dosimetry for synchrotron microbeam radiation therapy using radiochromic films of different sensitivity. *Physics in Medicine and Biology*, 53(23):6861, December 2008. ISSN 0031-9155. doi: 10.1088/0031-9155/53/23/014.

[96] N. Nariyama, K. Umetani, K. Shinohara, T. Kondoh, A. Kurihara, and M. Fukumoto. Micro-scale dose distribution of microplanar x rays from synchrotron radiation: measurement and monte carlo calculation. *Prog. Nucl. Sci. Technol*, 2:312–317, 2011.

[97] A. Niroomand-Rad, S.-T. Chiu-Tsao, C. G. Soares, A. S. Meigooni, and A. S. Kirov. Comparison of uniformity of dose response of double layer radiochromic films (MD-55-2) measured at 5 institutions. *Physica medica: PM: an international journal devoted to the applications of physics to medicine and biology: official journal of the Italian Association of Biomedical Physics (AIFB)*, 21(1):15–21, March 2005. ISSN 1120-1797. doi: 10.1016/S1120-1797(05)80015-8.

[98] D. F. Lewis. Practical guide to radiochromic film EBT2/EBT3. Presentation, Ashland Advanced Materials Group, July 2011. URL `http://www.filmqapro.com/Documents/Lewis%20-%20Europe%2011-2011.pdf`.

[99] P. Berkvens, E. Brauer-Krisch, T. Brochard, C. Nemoz, M. Renier, P. Fournier, H. Requardt, and M. Kocsis. Highly robust, high intensity white synchrotron beam monitor. In *2013 IEEE Nuclear Science Symposium and Medical Imaging Conference (NSS/MIC)*, pages 1–3, 2013. doi: 10.1109/NSSMIC.2013.6829691.

[100] E. Bräuer-Krisch, A. Bravin, M. Lerch, A. Rosenfeld, J. Stepanek, M. D. Michiel, and J. A. Laissue. MOSFET dosimetry for microbeam radiation therapy at the European Synchrotron Radiation Facility. *Medical Physics*, 30(4):583–589, April 2003. ISSN 0094-2405. doi: 10.1118/1.1562169.

[101] D. Buscombe, D. Rubin, and J. Warrick. An automated and universal method for measuring mean grain size from a digital image of sediment. *2nd Joint Federal Interagency Conference, Las Vegas, NV*, January 2010.

[102] K. Welsch. Hochpräzise ortsaufgelöste Filmdosimetrie für Anwendungen in der Mikro-Strahlentherapie. Bachelorarbeit, Ruprecht-Karls-Universität, Heidelberg, Germany, 2012.

[103] P. J. Muench, A. S. Meigooni, R. Nath, and W. L. McLaughlin. Photon energy dependence of the sensitivity of radiochromic film and comparison with silver halide film and LiF TLDs used for brachytherapy dosimetry. *Medical Physics*, 18(4):769–775, July 1991. ISSN 0094-2405. doi: 10.1118/1.596630.

[104] M. J. Butson, P. K. Yu, T. Cheung, and H. Alnawaf. Energy response of the new EBT2 radiochromic film to x-ray radiation. *Radiation Measurements*, 45(7):836–839, August 2010. ISSN 1350-4487. doi: 10.1016/j.radmeas.2010.02.016.

[105] D. J. Kirby. Radiation dosimetry of conventional and laser-driven particle beams. PhD thesis, University of Birmingham, United Kingdom, July 2011.

[106] E. J. Hall and A. J. Giaccia. *Radiobiology for the Radiologist*. Lippincott Williams&Wilki, Philadelphia, 7th edition, June 2011. ISBN 9781608311934.

[107] J. Nickerson. Experimental observations of a nuclear matrix. *Journal of Cell Science*, 114 (3):463–474, February 2001. ISSN 0021-9533, 1477-9137.

[108] K. T. Butterworth, S. J. McMahon, A. R. Hounsell, J. M. O'Sullivan, and K. M. Prise. Bystander signalling: Exploring clinical relevance through new approaches and new models. *Clinical Oncology*, 25(10):586–592, 2013. ISSN 0936-6555. doi: 10.1016/j.clon.2013.06.005.

[109] S. J. McMahon, K. T. Butterworth, C. Trainor, C. K. McGarry, J. M. O'Sullivan, G. Schettino, A. R. Hounsell, and K. M. Prise. A kinetic-based model of radiation-induced intercellular signalling. *PLoS ONE*, 8(1):e54526, January 2013. doi: 10.1371/journal.pone.0054526.

[110] S. J. McMahon, K. T. Butterworth, C. K. McGarry, C. Trainor, J. M. O'Sullivan, A. R. Hounsell, and K. M. Prise. A computational model of cellular response to modulated radiation fields. *International Journal of Radiation Oncology*Biology*Physics*, 84(1):250–256, September 2012. ISSN 0360-3016. doi: 10.1016/j.ijrobp.2011.10.058.

[111] N. Suchowerska, M. A. Ebert, M. Zhang, and M. Jackson. In vitro response of tumour cells to non-uniform irradiation. *Physics in Medicine and Biology*, 50(13):3041, July 2005. ISSN 0031-9155. doi: 10.1088/0031-9155/50/13/005.

[112] C. Trainor, K. T. Butterworth, C. K. McGarry, S. J. McMahon, J. M. O'Sullivan, A. R. Hounsell, and K. M. Prise. DNA damage responses following exposure to modulated radiation fields. *PLoS ONE*, 7(8):e43326, August 2012. doi: 10.1371/journal.pone.0043326.

[113] C. Lindholm, A. Acheva, and S. Salomaa. Clastogenic plasma factors: a short overview. *Radiation and Environmental Biophysics*, 49(2):133–138, May 2010. ISSN 0301-634X, 1432-2099. doi: 10.1007/s00411-009-0259-3.

[114] W. F. Morgan. Non-targeted and delayed effects of exposure to ionizing radiation: I. radiation-induced genomic instability and bystander effects in vitro. *Radiation Research*, 159(5):567–580, 2003. ISSN 0033-7587. doi: 10.1667/0033-7587(2003)159[0567:NADEOE]2.0.CO;2.

[115] E. I. Azzam, S. M. d. Toledo, and J. B. Little. Direct evidence for the participation of gap junction-mediated intercellular communication in the transmission of damage signals from α-particle irradiated to nonirradiated cells. *Proceedings of the National Academy of Sciences*, 98(2):473–478, January 2001. ISSN 0027-8424, 1091-6490. doi: 10.1073/pnas.98.2.473.

[116] K. M. Prise. Studies of bystander effects in human fibroblasts using a charged particle microbeam. *International Journal of Radiation Biology*, 74(6):793–798, January 1998. ISSN 0955-3002. doi: 10.1080/095530098141087.

[117] K. T. Butterworth, C. K. McGarry, C. Trainor, S. J. McMahon, J. M. O'Sullivan, G. Schettino, A. R. Hounsell, and K. M. Prise. Dose, dose-rate and field size effects on cell survival following exposure to non-uniform radiation fields. *Physics in Medicine and Biology*, 57(10):3197, May 2012. ISSN 0031-9155. doi: 10.1088/0031-9155/57/10/3197.

[118] K. Camphausen, M. A. Moses, C. Ménard, M. Sproull, W.-D. Beecken, J. Folkman, and M. S. O'Reilly. Radiation abscopal antitumor effect is mediated through p53. *Cancer Research*, 63(8):1990–1993, April 2003. ISSN 0008-5472, 1538-7445. PMID: 12702593.

[119] A. J. Cole, C. K. McGarry, K. T. Butterworth, K. M. Prise, J. M. O'Sullivan, and A. R. Hounsell. Development of a novel experimental model to investigate radiobiological implications of respiratory motion in advanced radiotherapy. *Physics in Medicine and Biology*, 57(22):N411, November 2012. ISSN 0031-9155. doi: 10.1088/0031-9155/57/22/N411.

[120] A. J. Cole, C. K. McGarry, K. T. Butterworth, S. J. McMahon, A. R. Hounsell, K. M. Prise, and J. M. O'Sullivan. Investigating the influence of respiratory motion on the radiation induced bystander effect in modulated radiotherapy. *Physics in Medicine and Biology*, 58(23):8311, December 2013. ISSN 0031-9155. doi: 10.1088/0031-9155/58/23/8311.

[121] W. B. Parsons, C. H. Watkins, G. L. Pease, and D. S. Childs. Changes in sternal marrow following roentgen-ray therapy to the spleen in chronic granulocytic leukemia. *Cancer*, 7

(1):179–189, January 1954. ISSN 1097-0142. doi: 10.1002/1097-0142(195401)7:1<179::AID-CNCR2820070120>3.0.CO;2-A.

[122] I. Emerit. Reactive oxygen species, chromosome mutation, and cancer: possible role of clastogenic factors in carcinogenesis. *Free Radical Biology and Medicine*, 16(1):99–109, January 1994. ISSN 0891-5849. doi: 10.1016/0891-5849(94)90246-1.

[123] G. B. Faguet, S. M. Reichard, and D. A. Welter. Radiation-induced clastogenic plasma factors. *Cancer Genetics and Cytogenetics*, 12(1):73–83, 1984. ISSN 0165-4608. doi: 10.1016/0165-4608(84)90010-4.

[124] W. Han, L. Wu, B. Hu, L. Zhang, S. Chen, L. Bao, Y. Zhao, A. Xu, and Z. Yu. The early and initiation processes of radiation-induced bystander effects involved in the induction of DNA double strand breaks in non-irradiated cultures. *British Journal of Radiology*, 80 (Special Issue 1):S7–S12, September 2007. ISSN 0007-1285. doi: 10.1259/bjr/44550200.

[125] I. Emerit, A. Levy, L. Cernjavski, R. Arutyunyan, N. Oganesyan, A. Pogosian, H. Mejlumian, T. Sarkisian, M. Gulkandanian, M. Quastel, J. Goldsmith, E. Riklis, E. Kordysh, S. Poliak, and L. Merklin. Transferable clastogenic activity in plasma from persons exposed as salvage personnel of the chernobyl reactor. *Journal of Cancer Research and Clinical Oncology*, 120(9):558–561, September 1994. ISSN 0171-5216, 1432-1335. doi: 10.1007/BF01221035.

[126] I. Emerit, M. C. Jaurand, L. Saint-Etienne, and A. Levy. Formation of a clastogenic factor by asbestos-treated rat pleural mesothelial cells. *Agents and Actions*, 34(3-4):410–415, November 1991. ISSN 0065-4299, 1420-908X. doi: 10.1007/BF01988737.

[127] E. I. Azzam, S. M. de Toledo, and J. B. Little. Oxidative metabolism, gap junctions and the ionizing radiation-induced bystander effect. *Oncogene*, 22(45):7050–7057, 2003. ISSN 0950-9232. doi: 10.1038/sj.onc.1206961.

[128] W. Zhao, D. I. Diz, and M. E. Robbins. Oxidative damage pathways in relation to normal tissue injury. *British Journal of Radiology*, 80(Special Issue 1):S23–S31, September 2007. ISSN 0007-1285. doi: 10.1259/bjr/18237646.

[129] M. E. C. Robbins and W. Zhao. Chronic oxidative stress and radiation-induced late normal tissue injury: a review. *International Journal of Radiation Biology*, 80(4):251–259, January 2004. ISSN 0955-3002. doi: 10.1080/09553000410001692726.

[130] P. K. Narayanan, E. H. Goodwin, and B. E. Lehnert. α particles initiate biological production of superoxide anions and hydrogen peroxide in human cells. *Cancer Research*, 57(18):3963–3971, September 1997. ISSN 0008-5472, 1538-7445. PMID: 9307280.

[131] L.-J. Wu, G. Randers-Pehrson, A. Xu, C. A. Waldren, C. R. Geard, Z. Yu, and T. K. Hei. Targeted cytoplasmic irradiation with alpha particles induces mutations in mammalian cells. *Proceedings of the National Academy of Sciences*, 96(9):4959–4964, April 1999. ISSN 0027-8424, 1091-6490. doi: 10.1073/pnas.96.9.4959. PMID: 10220401.

[132] A. Meister and M. E. Anderson. Glutathione. *Annual Review of Biochemistry*, 52(1): 711–760, 1983. doi: 10.1146/annurev.bi.52.070183.003431. PMID: 6137189.

[133] R. Iyer and B. E. Lehnert. Factors underlying the cell growth-related bystander responses to α particles. *Cancer Research*, 60(5):1290–1298, March 2000. ISSN 0008-5472, 1538-7445. PMID: 10728689.

[134] P. D. Lampe and A. F. Lau. Regulation of gap junctions by phosphorylation of connexins. *Archives of Biochemistry and Biophysics*, 384(2):205–215, 2000. ISSN 0003-9861. doi: 10.1006/abbi.2000.2131.

[135] S. A. Lorimore, P. J. Coates, G. E. Scobie, G. Milne, and E. G. Wright. Inflammatory-type responses after exposure to ionizing radiation in vivo: a mechanism for radiation-induced bystander effects? *Oncogene*, 20(48), 2001.

[136] Cell Signaling Technology. Hoechst 33342. product information sheet, 2010. URL `http://media.cellsignal.com/pdf/4082.pdf`.

[137] J. Portugal and M. J. Waring. Assignment of DNA binding sites for 4′,6-diamidine-2-phenylindole and bisbenzimide (hoechst 33258). a comparative footprinting study. *Biochimica et Biophysica Acta (BBA) - Gene Structure and Expression*, 949(2):158–168, February 1988. ISSN 0167-4781. doi: 10.1016/0167-4781(88)90079-6.

[138] A. E. Carpenter, T. R. Jones, M. R. Lamprecht, C. Clarke, I. H. Kang, O. Friman, D. A. Guertin, J. H. Chang, R. A. Lindquist, J. Moffat, P. Golland, and D. M. Sabatini. CellProfiler: image analysis software for identifying and quantifying cell phenotypes. *Genome Biology*, 7(10):R100, October 2006. ISSN 1465-6906. doi: 10.1186/gb-2006-7-10-r100. PMID: 17076895.

[139] J. N. Kapur, P. K. Sahoo, and A. K. C. Wong. A new method for gray-level picture thresholding using the entropy of the histogram. *Computer Vision, Graphics, and Image Processing*, 29(3):273–285, 1985. ISSN 0734-189X. doi: 10.1016/0734-189X(85)90125-2.

[140] C. Bracalente, I. L. Ibañez, B. Molinari, M. Palmieri, A. Kreiner, A. Valda, J. Davidson, and H. Durán. Induction and persistence of large γH2AX foci by high linear energy transfer radiation in DNA-Dependent protein kinase–Deficient cells. *International Journal of Radiation Oncology*Biology*Physics*, 87(4):785–794, November 2013. ISSN 0360-3016. doi: 10.1016/j.ijrobp.2013.07.014.

[141] T. Neumaier, J. Swenson, C. Pham, A. Polyzos, A. T. Lo, P. Yang, J. Dyball, A. Asaithamby, D. J. Chen, M. J. Bissell, S. Thalhammer, and S. V. Costes. Evidence for formation of DNA repair centers and dose-response nonlinearity in human cells. *Proceedings of the National Academy of Sciences*, 109(2):443–448, October 2012. ISSN 0027-8424, 1091-6490. doi: 10.1073/pnas.1117849108. PMID: 22184222.

[142] T. E. Schmid, G. Dollinger, W. Beisker, V. Hable, C. Greubel, S. Auer, A. Mittag, A. Tarnok, A. A. Friedl, M. Molls, and B. Röper. Differences in the kinetics of γ-H2AX fluorescence decay after exposure to low and high LET radiation. *International Journal of Radiation Biology*, 86(8):682–691, June 2010. ISSN 0955-3002. doi: 10.3109/09553001003734543.

[143] K. Rothkamm, J. C. Crosbie, F. Daley, S. Bourne, P. R. Barber, B. Vojnovic, L. Cann, and P. A. W. Rogers. In situ biological dose mapping estimates the radiation burden delivered to 'Spared' tissue between synchrotron x-ray microbeam radiotherapy tracks. *PLoS ONE*, 7(1):e29853, January 2012. doi: 10.1371/journal.pone.0029853.

[144] E. P. Rogakou, D. R. Pilch, A. H. Orr, V. S. Ivanova, and W. M. Bonner. DNA double-stranded breaks induce histone H2AX phosphorylation on serine 139. *Journal of Biological Chemistry*, 273(10):5858–5868, March 1998. ISSN 0021-9258, 1083-351X. PMID: 9488723.

[145] G. Speit and A. Hartmann. The comet assay (single-cell gel test). In *DNA Repair Protocols*, number 113 in Methods in Molecular Biology™, pages 203–212. Humana Press, January 1999. ISBN 978-0-89603-802-8, 978-1-59259-675-1.

[146] S. H. MacPhail, J. P. Banath, T. Y. Yu, E. H. M. Chu, H. Lambur, and P. L. Olive. Expression of phosphorylated histone H2AX in cultured cell lines following exposure to x-rays. *International journal of radiation biology*, 79(5):351–359, 2003.

[147] S. H. MacPhail, J. P. Banáth, Y. Yu, E. Chu, and P. L. Olive. Cell cycle-dependent expression of phosphorylated histone H2AX: reduced expression in unirradiated but not x-irradiated g1-phase cells. *Radiation research*, 159(6):759–767, 2003.

[148] O. Fernandez-Capetillo, A. Lee, M. Nussenzweig, and A. Nussenzweig. H2AX: the histone guardian of the genome. *DNA Repair*, 3(8–9):959–967, August 2004. ISSN 1568-7864. doi: 10.1016/j.dnarep.2004.03.024.

[149] A. Celeste, O. Fernandez-Capetillo, M. J. Kruhlak, D. R. Pilch, D. W. Staudt, A. Lee, R. F. Bonner, W. M. Bonner, and A. Nussenzweig. Histone H2AX phosphorylation is dispensable for the initial recognition of DNA breaks. *Nature Cell Biology*, 5(7):675–679, July 2003. ISSN 1465-7392. doi: 10.1038/ncb1004.

[150] C. Lu, F. Zhu, Y.-Y. Cho, F. Tang, T. Zykova, W.-y. Ma, A. M. Bode, and Z. Dong. Cell apoptosis: Requirement of H2AX in DNA ladder formation, but not for the activation of caspase-3. *Molecular Cell*, 23(1):121–132, July 2006. ISSN 1097-2765. doi: 10.1016/j.molcel.2006.05.023.

[151] C. H. Bassing, H. Suh, D. O. Ferguson, K. F. Chua, J. Manis, M. Eckersdorff, M. Gleason, R. Bronson, C. Lee, and F. W. Alt. Histone H2AX: a dosage-dependent suppressor of oncogenic translocations and tumors. *Cell*, 114(3):359–370, August 2003. ISSN 0092-8674. doi: 10.1016/S0092-8674(03)00566-X.

[152] O. Fernandez-Capetillo, H.-T. Chen, A. Celeste, I. Ward, P. J. Romanienko, J. C. Morales, K. Naka, Z. Xia, R. D. Camerini-Otero, N. Motoyama, P. B. Carpenter, W. M. Bonner, J. Chen, and A. Nussenzweig. DNA damage-induced G2–M checkpoint activation by histone H2AX and 53BP1. *Nature Cell Biology*, 4(12):993–997, 2002. ISSN 1465-7392. doi: 10.1038/ncb884.

[153] J. P. Banáth, S. H. MacPhail, and P. L. Olive. Radiation sensitivity, H2AX phosphorylation, and kinetics of repair of DNA strand breaks in irradiated cervical cancer cell lines. *Cancer Research*, 64(19):7144–7149, October 2004. ISSN 0008-5472, 1538-7445. doi: 10.1158/0008-5472.CAN-04-1433. PMID: 15466212.

[154] A. Celeste, S. Difilippantonio, M. J. Difilippantonio, O. Fernandez-Capetillo, D. R. Pilch, O. A. Sedelnikova, M. Eckhaus, T. Ried, W. M. Bonner, and A. Nussenzweig. H2AX haploinsufficiency modifies genomic stability and tumor susceptibility. *Cell*, 114(3):371–383, August 2003. ISSN 0092-8674. doi: 10.1016/S0092-8674(03)00567-1.

[155] K. Rothkamm and M. Löbrich. Evidence for a lack of DNA double-strand break repair in human cells exposed to very low x-ray doses. *Proceedings of the National Academy of Sciences*, 100(9):5057–5062, April 2003. ISSN 0027-8424, 1091-6490. doi: 10.1073/pnas.0830918100. PMID: 12679524.

[156] F. Bouquet, C. Muller, and B. Salles. Report the loss of γH2AX signal is a marker of DNA double strand breaks repair only at low levels of DNA damage. *Cell Cycle*, 5(10):1116–1122, 2006.

[157] P. L. Olive and J. P. Banáth. Phosphorylation of histone H2AX as a measure of radiosensitivity. *International Journal of Radiation Oncology*Biology*Physics*, 58(2):331–335, February 2004. ISSN 0360-3016. doi: 10.1016/j.ijrobp.2003.09.028.

[158] B. Stenerlöw, K. H. Karlsson, B. Cooper, and B. Rydberg. Measurement of prompt DNA double-strand breaks in mammalian cells without including heat-labile sites: Results for cells deficient in nonhomologous end joining. *Radiation Research*, 159(4):502–510, April 2003. ISSN 0033-7587. doi: 10.1667/0033-7587(2003)159[0502:MOPDDS]2.0.CO;2.

[159] O. A. Sedelnikova, E. P. Rogakou, I. G. Panyutin, and W. M. Bonner. Quantitative detection of 125IdU-Induced DNA double-strand breaks with γ-H2AX antibody. *Radiation Research*, 158(4):486–492, 2002. ISSN 0033-7587. doi: 10.1667/0033-7587(2002)158[0486:QDOIID]2.0.CO;2.

[160] J. C. Crosbie, R. L. Anderson, K. Rothkamm, C. M. Restall, L. Cann, S. Ruwanpura, S. Meachem, N. Yagi, I. Svalbe, R. A. Lewis, B. R. G. Williams, and P. A. W. Rogers. Tumor cell response to synchrotron microbeam radiation therapy differs markedly from cells in normal tissues. *International Journal of Radiation Oncology*Biology*Physics*, 77 (3):886–894, July 2010. ISSN 0360-3016. doi: 10.1016/j.ijrobp.2010.01.035.

[161] S. A. Mitchell, G. Randers-Pehrson, D. J. Brenner, and E. J. Hall. The bystander response in C3H 10T$\frac{1}{2}$ cells: The influence of cell-to-cell contact. *Radiation Research*, 161(4):397–401, April 2004. ISSN 0033-7587. doi: 10.1667/RR3137.

[162] C. Shao, Y. Furusawa, M. Aoki, and K. Ando. Role of gap junctional intercellular communication in radiation-induced bystander effects in human fibroblasts. *Radiation Research*, 160(3):318–323, September 2003. ISSN 0033-7587. doi: 10.1667/RR3044.

[163] A. M. Mastro, M. A. Babich, W. D. Taylor, and A. D. Keith. Diffusion of a small molecule in the cytoplasm of mammalian cells. *Proceedings of the National Academy of Sciences*, 81 (11):3414–3418, June 1984. ISSN 0027-8424, 1091-6490. PMID: 6328515.

[164] E. Bulyak, P. Gladkikh, A. Zelinsky, I. Karnaukhov, S. Kononenko, V. Lapshin, A. Mytsykov, Y. Telegin, A. Khodyachikh, A. Shcherbakov, V. Molodkin, V. Nemoshkalenko, and A. Shpak. Compact x-ray source based on compton backscattering. *Nuclear Instruments and Methods in Physics Research Section A: Accelerators, Spectrometers, Detectors and Associated Equipment*, 487(3):241–248, July 2002. ISSN 0168-9002. doi: 10.1016/S0168-9002(02)00904-X.

[165] K. Burger, E. Eggl, K. Achterhold, F. Pfeiffer, and J. Wilkens. The munich compact light source towards microbeam radiation therapy with a compact synchrotron (poster), 2014. URL `http://www.munich-photonics.de/fileadmin/media/MuCLS_Poster.pdf`.

[166] E. C. Schreiber and S. X. Chang. Monte carlo simulation of a compact microbeam radiotherapy system based on carbon nanotube field emission technology. *Medical Physics*, 39(8):4669–4678, August 2012. ISSN 0094-2405. doi: 10.1118/1.4728220.

Appendix A

Supplementary material to chapter 2

Geometrical of beams at the edge of the MSC

At the edge of the MSC the incidence of the primary synchrotron beam is inclined by a small angle ϕ. Consequently some of the photons will hit the walls and therefore not contribute to the microbeam. Some of them might be absorbed or reflected by total external reflection (see chapter 2.4). If one assumes a 100% absorbing material, the change in the photon flow in the microbeams resulting from the inclined incidence can be determined from the following geometry:

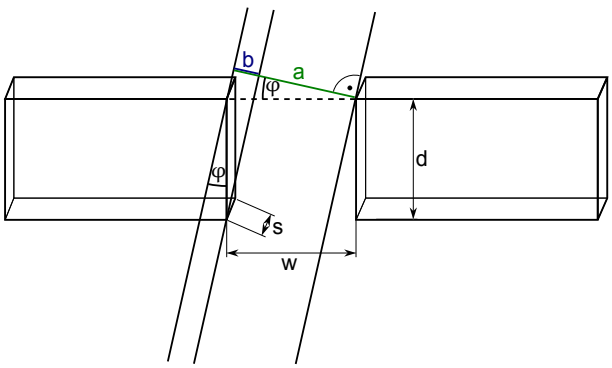

The number of photons in the case of normal incidence ($\phi = 0$) in the microbeam in a certain time interval is

$$N_0 = \Phi w s, \tag{A.1}$$

where Φ is the fluence in front of the MSC. From the drawing we read

$$a = w \cos\phi \tag{A.2}$$

$$b = d \sin\phi \tag{A.3}$$

The effective aperture area in the beams eye view can therefore be calculated

$$A = (w \cos\phi - d \sin\phi)s \approx (w - \phi d)s. \tag{A.4}$$

The latter approximation is valid for small incidence angles, which is reasonable with regard to the small beam divergence. The angle ϕ can furthermore be calculated as the ratio between the distance of the slit from the central beam $|x|$ and the distance of the collimator from the wiggler h,

$$\phi = \frac{|x|}{h}. \tag{A.5}$$

Thus the effective aperture area is

$$A = (w - \frac{|x|d}{h})s \tag{A.6}$$

From that the number of photons that pass the collimator aperture in a certain time can be obtained in

$$\frac{N}{N_0} = \frac{\Phi A}{\Phi w s} = 1 - \frac{d}{hw}|x|. \tag{A.7}$$

This yields a factor of $\beta = 0.041\,cm^{-1}$ in equation 2.28 in section 2.3.3 for the geometry at the ESRF. However, the absorption of the collimator material is not 100%. Therefore the effective coefficient was determined as $\beta = 0.030\,cm^{-1}$

Appendix B

Supplementary material to chapter 3

Calibration of the CT-device

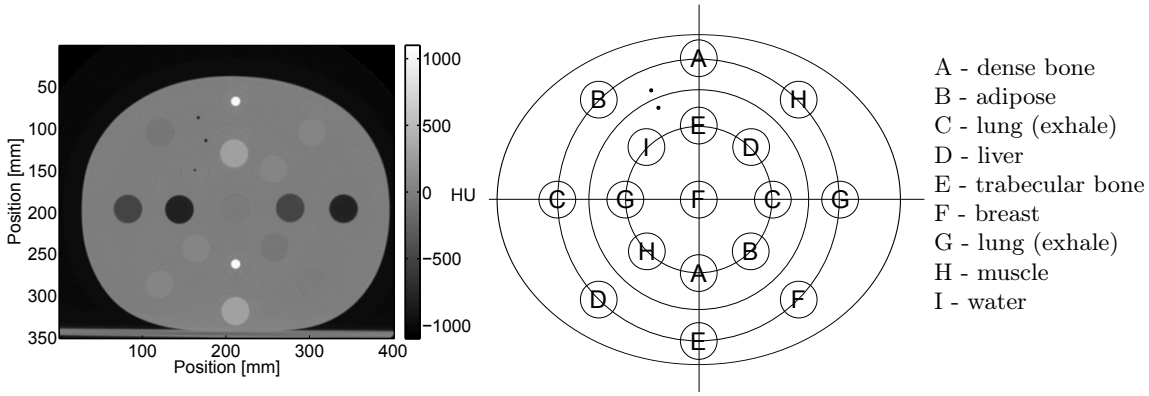

Figure B.1 – The figure shows on the left a CT image of the CIRS electron density reference phantom, model 62. It was acquired at the AOI in Hünenburg (Switzerland). The right figure is a schematic view of the phantom (adopted from CIRS Tissue Simulation & Phantom Technology [81]). The letters in the cylindrical inlets denote the imitated materials.

The calibration of the CT conversion is performed by assigning Hounsfield units (HU) to the base materials, cortical bone, red/yellow marrow, adipose tissue, adrenal gland, small intestine, connective tissue and air. We calibrated the CT with the CIRS electron density reference phantom, model 62 (figure B.1) and determined the HU such that mass density and RED of the converted HU match those stated by the manufacturer closest. The result is presented in the two graphs of figure B.2 for mass density on the left and RED on the right. The blue curve shows the calibration presented in Schneider et al. [45]. This comparison is made to demonstrate that calibration is absolutely essential for any dose calculation. Especially for materials with higher HU the two calibration curves differ substantially.

The differences between the HU in the CT image and the calibration curve values are smaller than 18 HU with an average of 8.8 HU. For the materials of the electron density reference phantom the following table compares the measured HU (Exp.), the HU that would be expected from the calibration (Calibr.) and the difference $|\Delta HU|$:

Tissue	Exp.	Calibr.	$\lvert\Delta HU\rvert$	Tissue	Exp.	Calibr.	$\lvert\Delta HU\rvert$
Dense bone	1044	1029	15	Breast	-33.2	-25	8.2
Adipose	-69.2	-59	10.2	Lung (inhale)	-792.5	-791	1.5
Lung (exhale)	-489.5	-504	14.5	Muscle	48.2	48	0.2
Liver	56.2	55	1.2	Water	-5.0	-13	8
Trabecular bone	286	298	12	Air	-998.5	-981	17.5

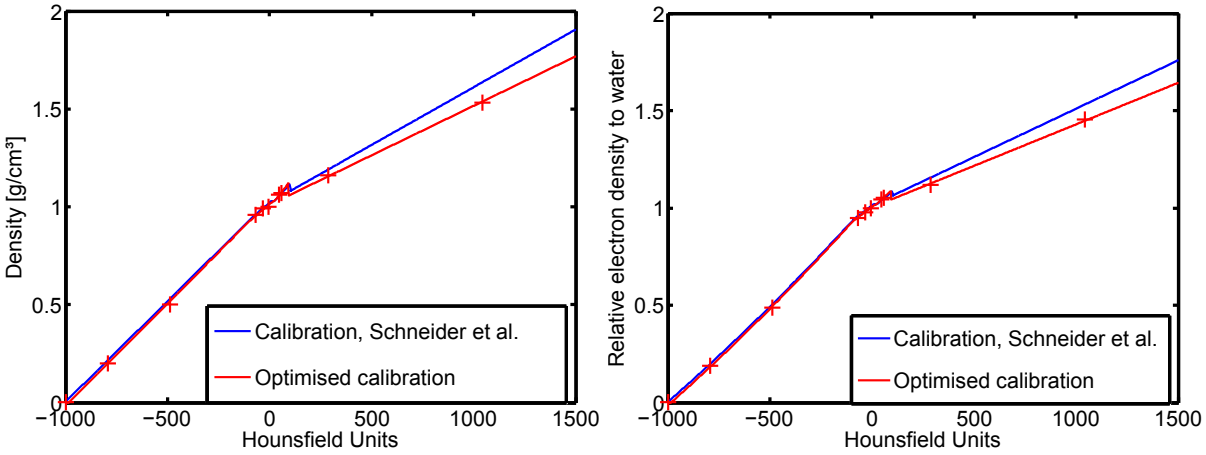

Figure B.2 – Density and RED calibration curves are shown. The "+" illustrate data points obtained with the CIRS electron density reference phantom. The resulting calibration is shown as red lines and compared with the calibration in Schneider et al. [45]

Schneider et al. [45] analysed a more comprehensive set of materials. Table B.1 on the next page shows the deviations from their calibration curve. Although the calibration is different in our case, the table gives a good impression on the error for various materials. It also highlights, that certain materials, such as connective tissue differ vastly from the CT-calibration and others less. The reason is that the conversion is based on interpolation between base materials. For some tissues with a very different composition this can be a poor approach. The HU standard deviation for all the listed materials is 17 HU.

Taking into account the uncertainties from the calibration and the scattering of materials an uncertainty of 20 HU seems to be a reasonable value. Figure B.3 illustrates the consequences for the absorption coefficients.

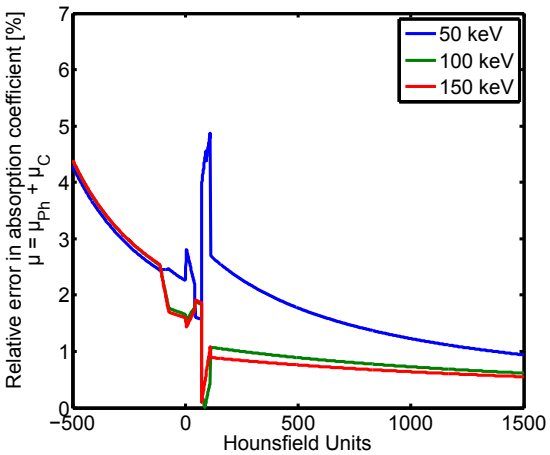

Figure B.3 – The figure shows the uncertainty for the absorption coefficient of photoelectric absorption and Compton scattering if an average HU uncertainty of 20 HU is assumed.

Tissue	HU	ΔHU	Tissue	HU	ΔHU
Lung	-750	40	Liver 2	53	-5
Lung, blood-filled	-741	-8	Trachea	54	-6
Fat	-108	0	Spleen	54	-6
Adipose tissue	-98	0	Heart, blood filled	56	-8
Adipose tissue	-77	1	Blood, whole	56	-8
Adipose tissue	-55	1	Liver 3	63	-6
Yellow marrow	-49	7	Skin 1	72	32
Mammary gland	-37	6	Skin 2	74	30
Yellow/red marrow (1:1)	-22	2	Skin 3	77	27
Mammary gland	-1	3	Connective tissue	100	79
Red marrow	11	2	Cartilage	102	27
Brain, cerospinal fluid	13	-22	Spongiosa	262	-49
Adrenal gland	14	-1	Sternum	385	13
Small intestine (wall)	23	-10	Sacrum	454	11
Urine	26	-24	D6, L3 incl. Cartilage (male)	466	16
Gallbladder bile	27	-14	Whole vertebral column (male)	514	18
Lymph	29	-16	D6, L3 excl. Cartilage (male)	526	6
Pancreas	32	-1	Humerus, spherical head	538	-6
Prostate	34	-3	Femur, spherical head	538	-6
Brain, white matter	34	-3	Femur, conical trochanter	586	-4
Testis	36	-5	C4 incl. Cartilage (male)	599	17
Brain, grey matter	40	-9	Sacrum (female)	621	12
Muscle, skeletal 1	40	0	Humerus, whole specimen	636	-3
Stomach	41	-1	Ribs 2nd, 6th (male)	657	9
Heart 1	41	-1	Innominate (male)	658	8
Kidney 1	41	-1	C4 excl. Cartilage (male)	672	11
Muscle	41	-1	Femur total bone)	688	-5
Thyroid	42	-2	Femur (whole specimen)	702	-2
Aorta	43	-3	Innominate (female)	742	8
Heart 3	43	-3	Clavicle, scapula	756	-6
Kidney 2	43	-3	Humerus (total bone)	756	-6
Liver 1	43	-3	Humerus, cylindrical shaft	805	-4
Muscle, skeletal 2	43	-3	Ribs 10th (male)	843	8
Muscle, skeletal 3	44	-4	Cranium	999	4
Heart 3	45	-5	Mandible	1113	7
Mammary gland 3	45	3	Femur, cylindrical shaft	1239	-1
Kidney 3	46	-6	Compact bone	1454	-65
Ovary	46	-6	Cortical bone	1524	-24
Eye, lens	49	8			

Table B.1 – This table was taken from the data in Schneider et al.[45]. It states the measured HU and the differences to the calibration therein.

A treatment planning example for Betty

The following image B.4 is a screen shot from the therapy planning system virtuos. It shows CT slices from the first veterinarian patient, cat "Betty", which suffered from a carcinoma at its nose. The target volume is at the tip of the nose. The field size is adjusted to 26×30 mm^2 in the collimator window on the right. It is visualised as a yellow square in the top left, sagittal view. At the bottom left the gantry, couch and collimator angle can be adjusted for the exposure. In this treatment plan no contouring of target organs or organs at risk was carried out.

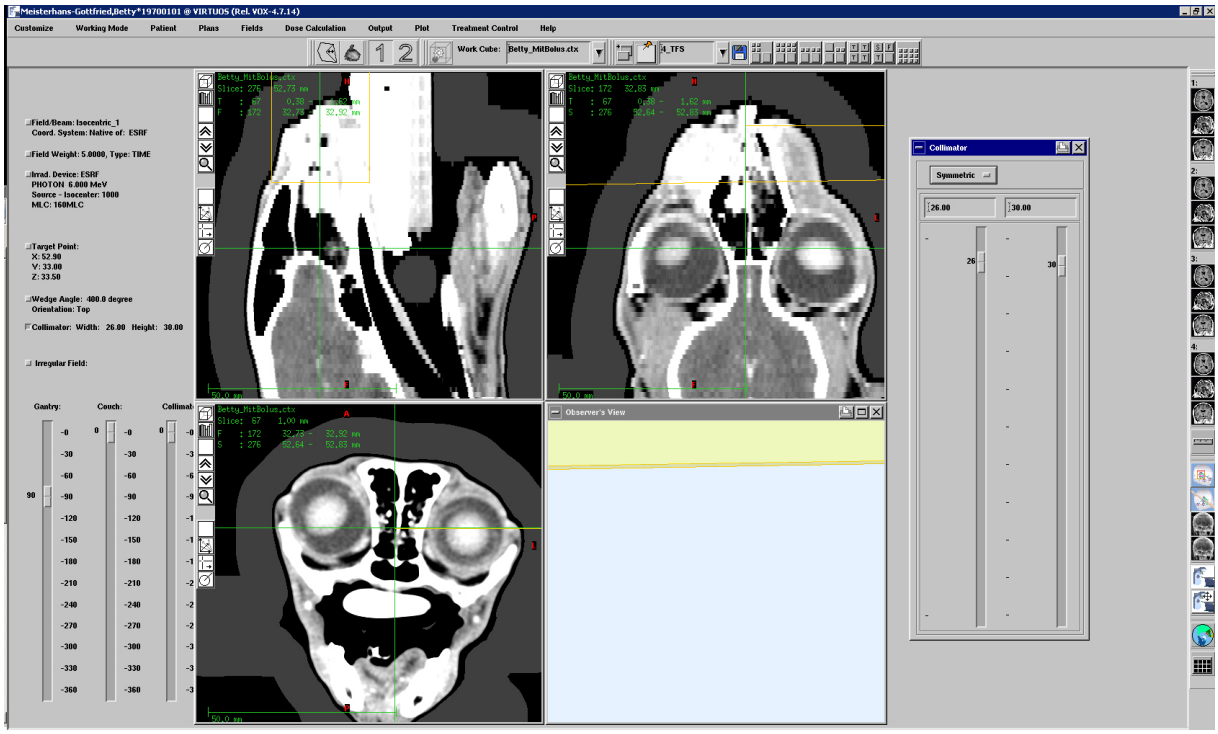

Figure B.4 – Screenshot of the TPS VIRTUOS.

The result of the Monte Carlo dose calculation is presented in figure B.5 as peak dose (left) and valley dose (right) and in figure B.6 as PVDR. In all figures the contours of the CT image are overlaid (black iso-HU curves). The water bolus is clearly visible which was placed around the nose in order to protect the tissue from too high peak entrance doses.

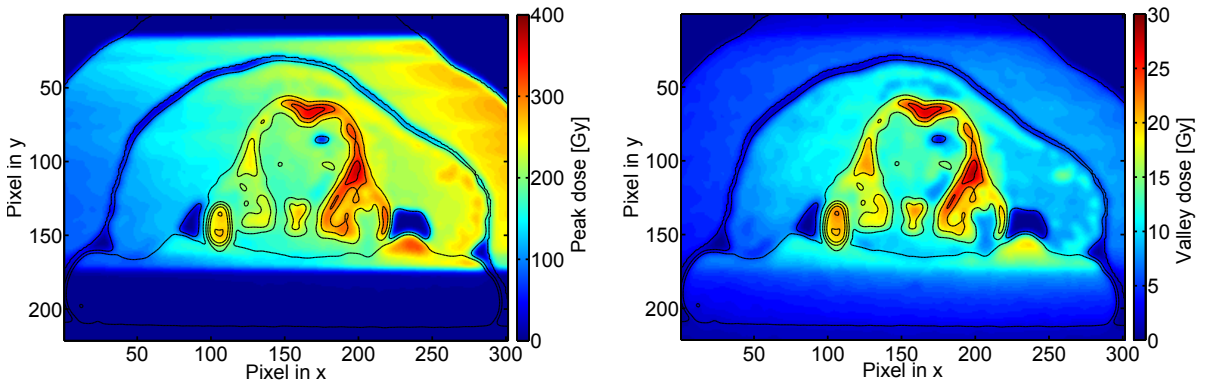

Figure B.5 – Peak dose (left) and valley dose (right) in the MRT treatment plan for the first "patient", cat Betty.

The voxel size is approximately 0.2×0.2×1.25 mm. Hence there are some voxels in the field

without microbeam. Furthermore the small voxel size leads to relatively high noise level in the Monte Carlo simulations. Therefore the data was smoothed with a flattening filter. Nevertheless the peak dose (right image) shows still some regions with a lower value, which is an artefact from the small voxel size. Very high dose levels are reached in the bone in both, peak and valley regions. These levels could potentially be hazardous. A shift to slightly higher photon energies could significantly reduce the dose level (see chapter 3.6). The PVDR is computed in the following image.

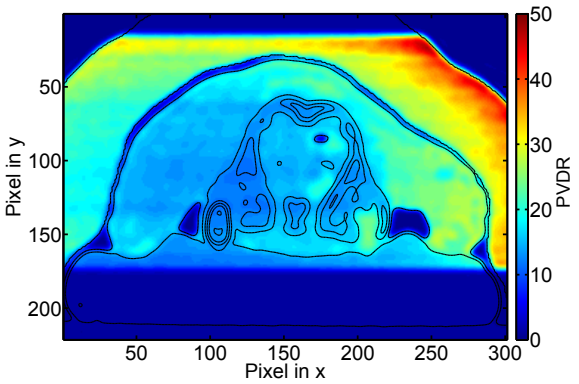

Figure B.6 – PVDR in the MRT-treatment plan for Betty

Appendix C

Supplementary material to chapter 4

X-ray tube spectra simulated in Geant4

In order to determine the spectral sensitivity of radiochromic films we irradiated films with an x-ray tube operated at 100, 150, 200 and 250 keV acceleration voltage. The anode material was tungsten.

The tube spectrum was simulated in Monte Carlo calculations in Geant4 (version 9.3.p02) with the PENELOPE physics libraries. The energy cut-off was set at 1.7 keV. A monoenergetic, electron pencil beam was simulated to impinge onto the centre of a tungsten block under an angle of 45°.

A hollow cylinder (inner radius 2 mm, outer radius 10 mm) was defined around the electron incidence on the tungsten surface and was placed on the block surface. The following figure shows a sketch of the detector and scoring symmetry.

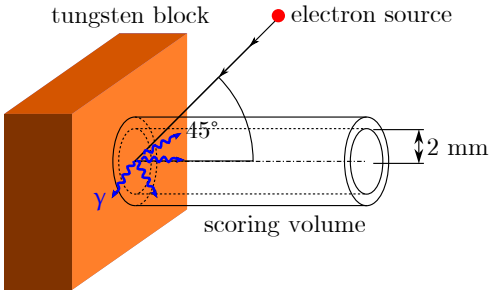

All photon energies of photons that crossed the boundaries of the hollow cylinder were scored. Due to the heel effect the photon energies slightly depend on the emission angle. We did not take account of this effect. The filtering of the raw tube spectrum $S_{raw}(E)$ with the build-in 0.1 mm copper plate was computed with the aid of the photon absorption coefficients from Berger et al.[64]. The final spectrum follows from

$$S(E) = e^{-\mu_{0.5mm,Al}(E)\cdot 0.1mm} S_{raw}(E), \tag{C.1}$$

and is presented for the tube voltages 100, 150, 200 and 250 kV in the following graph:

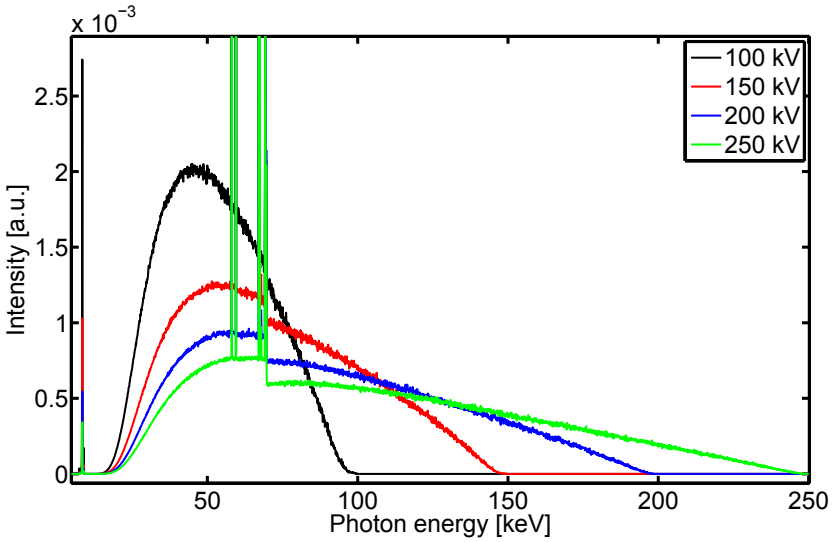

Figure C.1 – X-ray tube spectra are shown for 100, 150, 200 and 250 kV acceleration voltage, a tungsten anode and 0.1 mm aluminium filtering. Apart from the continuous bremsstrahlung spectrum the K lines of the characteristic spectrum are visible and at the very low energy end of the spectrum the L lines can be seen.

Appendix D

Supplementary material to chapter 5

Cell cycle distribution of cells irradiated with an MRT field

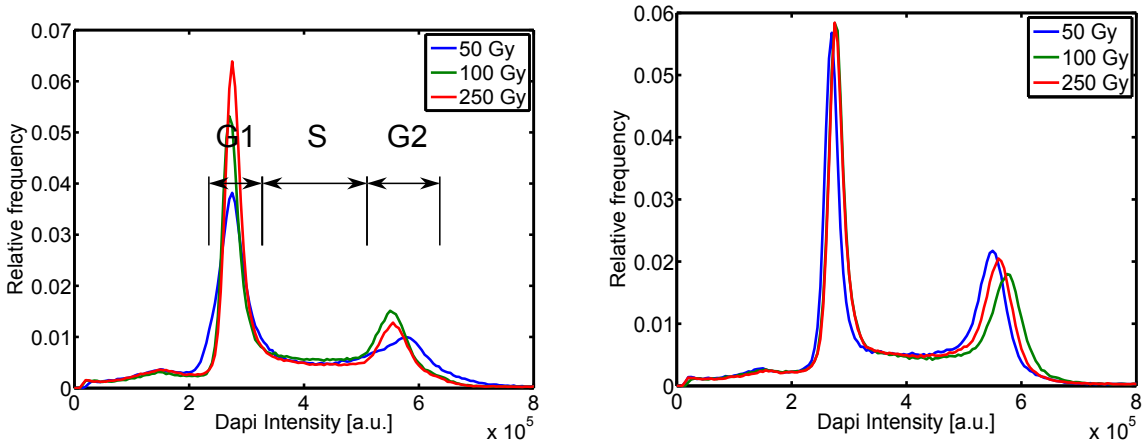

Figure D.1 – Histograms of cells over their DNA content 1 hour (left) and 6 hours (right) after microbeam exposure.

The graphs (figure D.1) show histograms of the fluorescence intensity of Hoechst 33342 in the Dapi channel 1 hour after radiation on the left and 6 hours after radiation on the right for the cell culture flasks irradiated with an MRT field (experiment 5). The cell phases are clearly distinct from each other and can be easily assigned (see left figure). Nevertheless there are fluctuations in the signal intensity. Therefore the delineation of cell phases has to be made manually for each histogram. Quantitative comparisons between different experiments are therefore difficult.

Determination of foci sizes with autocorrelation

Foci sizes were determined from the fluorescence images in the green channel (GFP-channel). The foci size was not determined individually for each focus but an average value was attributed to each cell with autocorrelation. After segmentation of the nuclei the GFP-channel image of the cell was taken for analysis. First the background was determined by convolution with a Gauss filter of 10 pixel width. The background was subtracted from the image. From the background subtracted image of the cell $I(x, y)$ the autocorrelation $I_{AC}(x, y)$ was computed

using the equation

$$I_{AC}(x,y) = \int_x \int_y I(x',y') \cdot I(x-x', y-y')\, dy'\, dx'. \tag{D.1}$$

The autocorrelation has an unavoidable background level. We define a threshold value as one half of the maximum autocorrelation intensity above the background level. The background level was determined as the average $< I_{AC} >$ over x and y. The area of the foci is than the number of pixels that have an intensity above the threshold intensity in the autocorrelation image.

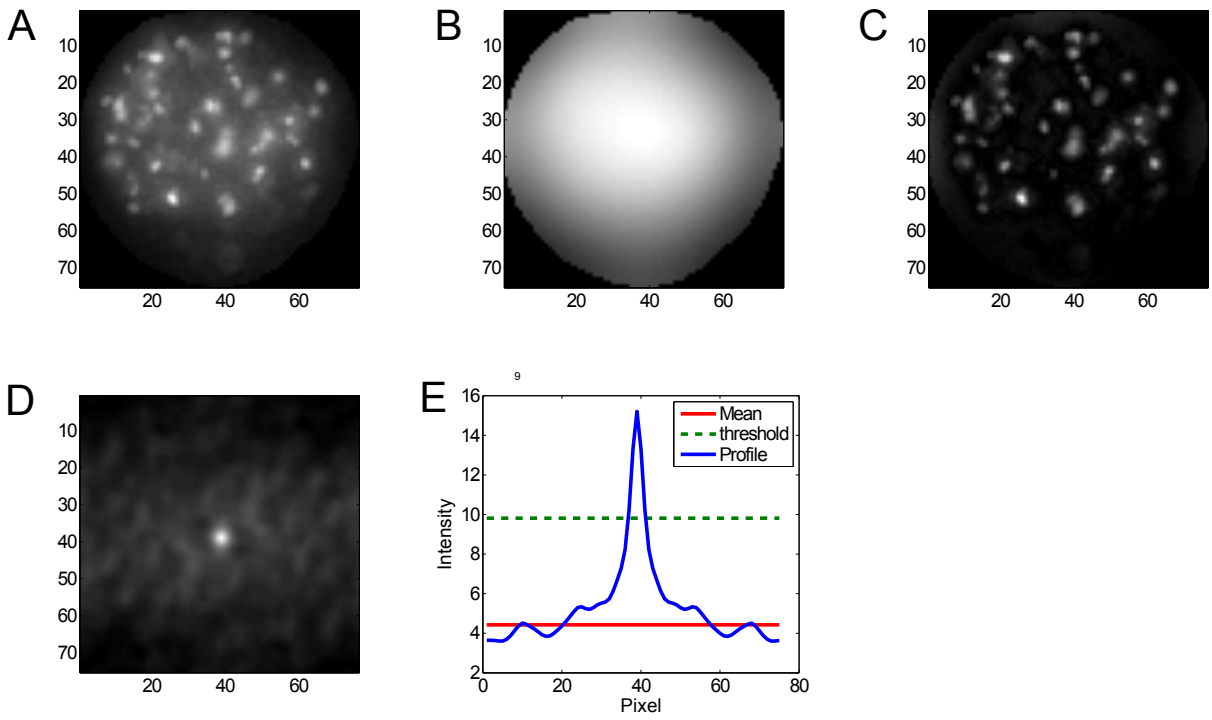

Figure D.2 – Steps for the determination of the foci size: A: GFP-channel image of the cell, B: Background signal, C: Background subtracted image, D: Autocorrelation of the background subtracted image, E: Profile, threshold value and mean of the autocorrelation.

Distribution of H2AX phosphorylation differences between closest neighbours $\Delta^n_{i,j}$ and arbitrarily selected cells $\Delta_{i,j}$ at the same dose

In order to assess whether closely neighbouring cells influence each other in the phosphorylation of the histone H2AX the distribution of γH2AX fluorescence intensity differences $\Delta_{i,j} = |I_i - I_j|$ between 2 cells i, j was analysed at a fixed dose. The two graphs in figure D.3 show for 1 hour (left) and 6 hours (right) after exposure with an MRT field of 100 Gy peak entrance dose these histograms. The red graph is the distribution $\Delta_{i,j}$ for arbitrarily chosen cells in a dose range from 1.5 to 1.6 Gy. The blue curve shows this distribution $\Delta^n_{i,j}$ for close neighbour cell-pairs i, j at a dose between 1.3 and 1.8 Gy. The second range of doses was taken a bit larger, to increase the number of pairs in the statistics. The disadvantage is that the distribution may be made a bit wider. Nonetheless the distribution of neighbour cell pairs is in both cases more concentrated

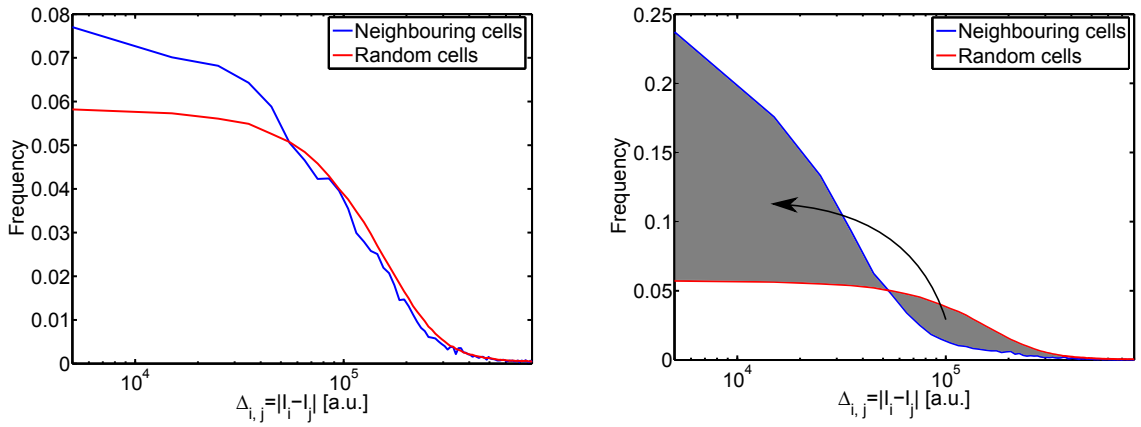

Figure D.3 – The two figures show histograms of cell pairs over their γH2AX fluorescence signal difference.

at low intensity differences. This means that cells in close neighbourhood tend to react alike in terms of H2AX phosphorylation. The effect is more pronounced 6 hours after exposure. From the $\Delta_{i,j}$ distributions it is possible to estimate the fraction of γH2AX bystander cells. This is illustrated in the right figure. The grey fraction moves from $\Delta_{i,j}$ to $\Delta^n_{i,j}$ towards low intensity differences. This fraction is 9.2% 1 hour post-exposure and 42.7% 6 hours post-exposure.

Histograms over γH2AX fluorescence intensity and position

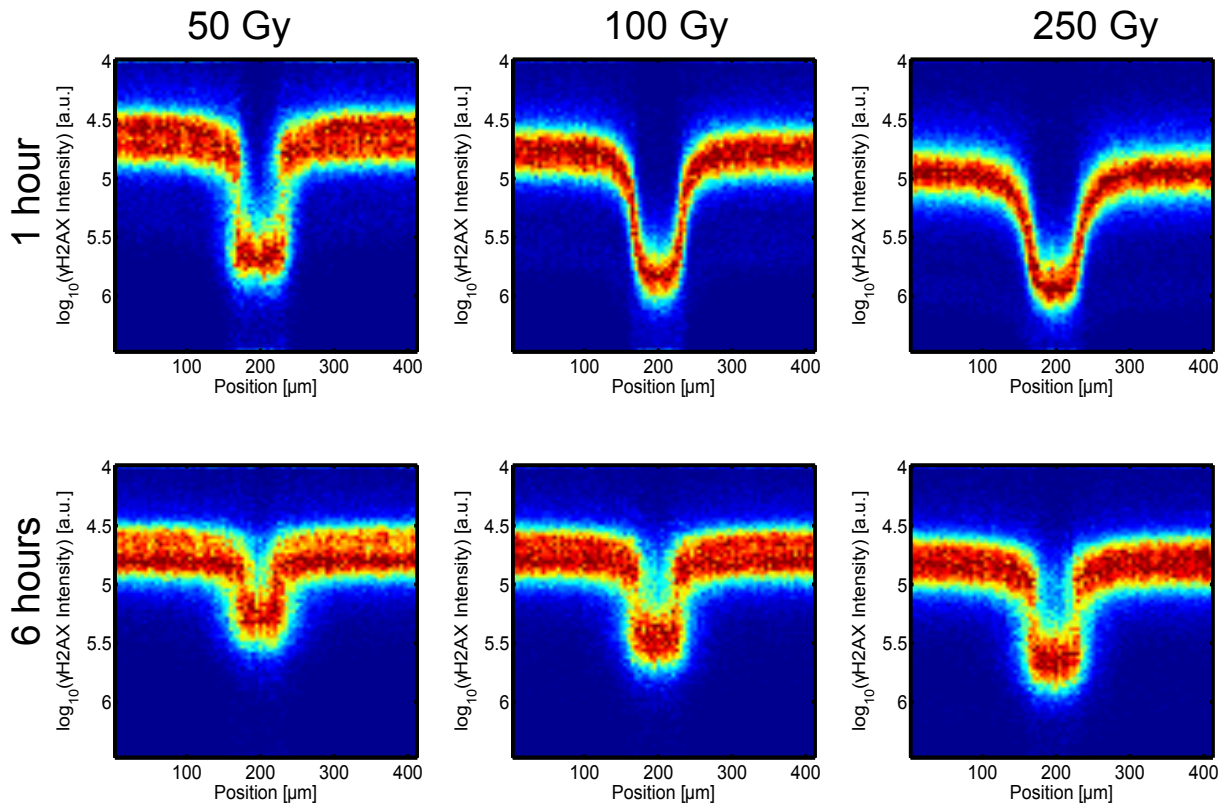

These figures show γH2AX signal intensity histograms, normalised to the maximum in dependence on the position across the microbeam. They were created by averaging over all microbeams

in the field. The colour code shows red for a high and blue for a low frequency. The top row shows the cells 1 hour after exposure and the bottom row 6 hours after exposure. The peak entrance doses of 50, 100 and 250 Gy are shown in the first, second and third column.

Appendix E

List of abbreviations

ATM ataxia-telangectasia mutated

ATR ATM and Rad3-related

BER base excision repair

53BP-1 tumour suppressor p53-binding protein 1

BRCA1, 2 breast cancer 1, 2 (tumour suppressor protein)

BSA bovine serum albuminum

ctc centre to centre distance

CPKA convolution based point kernel algorithm

DMEM eagle's minimal essential medium

DMSO dimethyl sulfoxide

DNA-PKcs DNA protein kinase catalytic subunit

DSB double strand break

ESRF European Synchrotron Radiation Facility

FWHM full width at half maximum

GFP green fluorescent protein

GPx glutathione peroxidase

GSH glutathione

HPLC high-performance liquid chromatography

HRR homologous recombination repair

HU Hounsfield units

KU-protein protein that binds DNA DSB ends, required in NHEJ

LED Light emitting diode

LET linear energy transfer

LQM linear quadratic model

MMR mismatch repair

MRT Microbeam Radiation Therapy

MSC multi slit collimator

NADPH nicotinamide adenine dinucleotide phosphate

NER nucleotide excision repair

NHEJ nonhomologous end joining

NSLS National Synchrotron Light Source (in Brookhaven, USA)

OAR organs at risk

OF output factor

PBS phosphate buffered saline

PET positron emission tomography

PFGE pulse-field gel electrophoresis

PVDR peak to valley dose ratio

Rad50,51,54 DNA repair protein 50, 51, 54

RED relative electron density to water

ROS reactive oxygen species

RPA replication protein A

SOD superoxide dismutase

SPKA superposition point kernel algorithm in curved space

SSB single strand break

TGF tumour growth factor

TNF-α tumour necrosis factor-α

TPS Therapy planning system

XRCC1 X-ray repair cross-complementing protein 1

Index